ERRATUM

The caption of Fig(5-5) at page 81 should read;

Distribution of the rms deviation from the fitted line in track reconstruction for side 1 and side 2 .

THE PROBLEM OF THE ω MESON NEAR ITS PRODUCTION THRESHOLD

A thesis presented for the

degree of Doctor of Philosophy of

the University of London

by

HOUSHANG KARAMI

Department of Physics,

Imperial College of Science and Technology,

London, S.W.7.,

December, 1977

ABSTRACT

π^-p elastic scattering and ω meson production near the ω threshold have been investigated.

Various properties of the ω meson from its production threshold to a centre of mass momentum, p^*, of 200 Mev/c were studied using a missing mass technique.

The mass and width of the ω were found to be independent of p^*, having mean values of 783.0 ± 0.35 Mev/c^2 and 9.9 ± 0.42 Mev/c^2 respectively. The angular distribution was found to be isotropic from threshold to the highest centre of mass momentum investigated.

In the elastic channel the cross-sections were measured for pion momenta from 1000 to 1700 Mev/c, in the range COS $\theta^* \simeq -0.6$ to COS $\theta^* \simeq +0.8$, using a system of drift chambers surrounding a liquid hydrogen target. No structure has been observed in the elastic differential cross-section across the ω threshold or anywhere else in the momentum range covered.

It has been shown that the well-established N* resonance in the $P_{11}(1780)$, state can explain both the rapid rise of the ω production cross-section and its angular distribution. Therefore, it is very likely that the ω meson is produced mainly through the P-wave decay of this P_{11} resonance.

CONTENTS

		Page
Abstract.		i
1. Introduction.		
1-1	Aims of the experiments.	1
1-2	Motivation.	1
1-3	Theory.	
1-3-1	Scattering length theory.	4
1-3-2	Resonance model.	9
1-3-3	Threshold effect.	12
1-3-4	Angular distribution.	15
2. Kinematics and general consideration.		
2-1	Production experiment.	
2-1-1	Production of the ω meson.	20
2-1-2	Missing mass spectra.	22
2-2	$\pi^- p$ elastic scattering.	24
3. Apparatus and technique.		
3-1	Beam and momentum spectrometer.	31
3-2	Liquid hydrogen target.	32
3-3	Interaction.	
3-3-1	Neutron detection.	33
3-3-2	Detection system for $\pi^- p$ elastic scattering.	34
3-4	Electronics and logic.	37

Page

4. Performance.

4-1 Missing mass experiment timing and resolution. 53

4-2 The resolution of the elastic scattering experiment. 55

4-3 Data collection 55

5. Data analysis.

5-1 Data enriching. 61

5-2 The method of analysis used in the missing mass experiment.

5-2-1 Time of flight measurement. 62

5-2-2 Neutron selection. 62

5-2-3 Missing mass spectra. 63

5-2-4 Monte-Carlo simulation. 64

5-3 Analysis of the elastic scattering data.

5-3-1 Event track reconstruction. 66

5-3-2 Event selection. 66

6. Results.

6-1 ω production results.

6-1-1 Mass of the ω . 86

6-1-2 Width of the ω. 87

6-1-3 The ω Cross-sections. 88

6-1-4 Differential Cross-sections. 89

6-2 $\pi^- p$ elastic scattering results. 91

6-2-1 Differential Cross-sections. 92

page

7. Analysis of the results.

7-1 Behaviour of the ω cross-section. 146

7-2 Angular distribution of the ωn system. 149

7-3 Analysis of the π^-p elastic scattering results.

7-3-1 Cusp effect 152

7-3-2 The effect of the opening of the ω threshold on the elastic channel. 153

7-4 Conclusion. 158

Appendix. 169

Acknowledgements. 172

References. 173

1. INTRODUCTION

(1-1) Aims Of The Experiments.

This thesis describes two experiments concerned with different aspects of ω production near threshold, carried out by the author as part of the Imperial College Counter group, working at the Rutherford Laboratory.

The first experiment was concerned with studies of the ω meson in the reaction $\pi^- + p \rightarrow \omega + n$ near its production threshold, in which the mass of the ω was determined by missing mass techniques. The main aims were to measure the cross-section and angular distribution of the ω n system very close to the production threshold.

The second experiment was an investigation of the elastic scattering reaction $\pi^- + p \rightarrow \pi^- + p$ at very closely spaced momentum intervals through the ω threshold.

(1-2) Motivation.

Consider ω meson production in the reaction $\pi^- + p \rightarrow \omega + n$. Close to the threshold of ω production, where p^*, the final state momentum in the centre of mass system (CMS), is low, the angular momentum barrier strongly inhibits all final state partial waves other than S-wave. If in addition the matrix element is only slowly dependent on the total energy $\sqrt{s}$, then one would expect that the ω production cross-section would rise linearly with p^* i.e., ($\sigma \simeq p^*$ or $\sigma/p^* = \text{constant}$), and also that the angular distribution of the final state would be isotropic.

Previously the Imperial College counter group investigated various properties of the ω meson in the same reaction, this experiment will

be refered to as "π7" from the name of the beam line in which it was carried out[1,2]. The behaviour of the cross-section as a function of p* up to 300 Mev/c from this experiment is shown in Fig (1 - 1).

In this experiment data were collected by two concentric rings of neutron counters at angles near 0° in the laboratory frame. Each ring detected neutrons emitted at both forward and backward CMS angles which could be distinguished by different times -of-flight. The differential cross-section was therefore measured at two points near $\theta^* = 0^{\circ}$ and $\theta^* = 180^{\circ}$, where θ^* is the CMS production angle.

If only S and P waves are present in the final state then the angular distribution can be expanded in terms of Legendre Polynomials as;

$$\frac{d\sigma}{d\Omega}(\theta^*) = A_0 + A_1 P_1(\cos\theta^*) + A_2 P_2(\cos\theta^*) \qquad (1\text{-}1)$$

The results of the fits to the data (from the π7 experiment) are shown in Fig(1-2) and indicates that the $P_1(\cos\theta^*)$ term is consistent with zero. The data concerning the A_2/A_o ratio however is not sufficienly accurate to establish that the $P_2(\cos\theta^*)$ term is also not significant.

The most striking feature of the data is the drop of nearly a factor 3 in the ratio σ/p^* between $p^*=120$ and $p^*=20$ Mev/c which is incompatible with the expected constant value. However, it is conceivable that the rise could be the manifistation of an N* resonance in the S-channel.

The production of the ω in an S-wave implies that the initial $\bar{\pi}$ p system is in an S_{11} or D_{13} state ($\ell_{2I,2J}$). The total energy of the $\bar{\pi}$ p system at the ω threshold, in the reaction $\bar{\pi} + p \rightarrow \omega + n$ is 1722 Mev, and resonances in both the above waves near this mass have been reported.

These are the S_{11} observed in elastic scattering data and D_{13} observed in the inelastic channels $\pi\Delta$ and σN (σ is a I=0, J=0 $\pi\pi$ resonance)[3].

The S_{11} state is well-established, but there is little evidence of D_{13} in the elastic scattering data and the only clear evidence is from the inelastic channel ($\pi \pi N$). One phase shift solution, Berkeley Path 2, does show a rapid increase in the inelasticity of S_{11} near the ω threshold.

If we now allow a $P_2(\text{COS } \theta^*)$ term to be present in the angular distribution but keep the prohibition on a $p_1(\text{COS } \theta^*)$ term, as the data from the $\pi 7$ experiment requires, a possible N* resonance which could satisfy these requirement is the $F_{15}(1688)$. However the F_{15} resonance would produce a large $P_2(\text{COS } \theta^*)$ term in the angular distribution[4] and the result from the $\pi 7$ experiment can not rule this out. A further point is that within the framework of an $SU(6)_W$ decay scheme for baryon decay, there is strong support in favour of the ω n system coupling to $F_{15}(1688)$[5].

In order to investigate these possibilities further, the ω meson production cross-section and angular distribution needed to be studied in an experiment that covered the whole CMS angular region over a range of p* from threshold up to at least 200 Mev/c.

In addition it was decided that a study of the differential elastic scattering cross-section over a series of closely spaced momentum intervals through the ω threshold might show threshold effects or a narrow N* resonance which could possibly throw light on our understanding of the ω meson behaviour.

(1-3) Theory.

The ω meson was first observed in the study of the proton-anti proton annihilations (Maglic et al, 1961), and ever since has been a subject of several experiments. Its main properties are well known. The world average values for the ω mass and width are 782.6±0.3 Mev/c2 and

10.0±0.3 Mev/c2 respectively[6]. Its quantum numbers were found to be $I^G(J^P)C_n=0^-(1^-)$- and its main decay modes are $\pi^+\pi^-\pi^o$(90%), $\pi^+\pi^-$(1.3%) and $\pi^o\gamma$(8.7%).

The ω meson is a member of the vector nonet in the quark model having a mixing angle $\theta=45^o$ with the ϕ meson.

Since the main concern of this work is the study of the behaviour of the Cross-section for ω production near its threshold, a brief review of the production Cross-section , the behaviour of the angular distribution of an inelastic channel and the effect of its opening on the elastic channel is presented.

(1-3-1) Scattering Length Theory.

The asymptotic wave function describing the relative motion of two particles in a given channel i, with orbital angular momentum ℓ, and wave number k, is represented by;

$$\psi_{\ell_i}^{(i\to i)}(r) = \frac{-1}{2i\,k_i\,r}\left\{ e^{-i(k_i r-\ell_i\pi/2)} - S_{ii}\, e^{i(k_i r-\ell_i\pi/2)} \right\} \qquad (1\text{-}2)$$

This expression represents the ingoing and outgoing spherical waves in the same channel i. However, with an ingoing wave in the channel i, there will be outgoing waves also in all the other different channels which are open. The outgoing wave in the f channel is written as;

$$\psi_{\ell_i}^{(i\to f)}(r) = \frac{1}{2i\,\sqrt{k_f k_i}\,r}\, S_{fi}\, e^{i(k_f r-\ell_f\pi/2)} \qquad (1\text{-}3)$$

The Cross-section for the transition of a given initial channel i, to a final channel f, is obtained by the ratio of the flux of the outgoing wave in the channel f to the incident plane wave flux;

$$\sigma_{\ell_i}^{(i\to f)} = (2\ell_i+1)\frac{\pi}{k_i^2}\left|\delta_{fi} - S_{fi}\right|^2 \qquad (1\text{-}4)$$

The quantities S_{fi} are in general complex numbers and the elements of n×n matrix S(i,f=1,2,...n), n=number of channels open.

We now consider a simple system (a+b), having only two possible reaction channels (say, a+b and c+d). In this case, using both the unitarity and the symmetry of the S matrix, then S can be represented as;

$$S_\ell = \begin{pmatrix} \eta_\ell\, e^{2i\delta_\ell(1)} & i\sqrt{1-\eta_\ell^2}\, e^{i\{\delta_\ell(1)+\delta_\ell(2)\}} \\ i\sqrt{1-\eta_\ell^2}\, e^{i\{\delta_\ell(1)+\delta_\ell(2)\}} & \eta_\ell\, e^{2i\delta_\ell(2)} \end{pmatrix} \qquad (1\text{-}5)$$

Where quantities $\delta_\ell(1)$, $\delta_\ell(2)$ are phase shifts and η_ℓ is the absorption parameter. Substituation into Eq(1-4), yield;

$$\sigma_{el} = \sigma_\ell^{(i\to i)} = (2\ell+1)\frac{\pi}{k_i^2}\left|1-\eta_\ell e^{2i\delta_\ell(1)}\right|^2 \qquad (1\text{-}6)$$

$$\sigma_{inel} = \sigma_\ell^{(i\to f)} = (2\ell+1)\frac{\pi}{k_i^2}\left|1-\eta_\ell^2\right| \qquad (1\text{-}7)$$

A new matrix (T) is introduced such as to satisfy the condition;

$$S_{fi} = \delta_{fi} + 2i\sqrt{k_i k_f}\cdot T_{fi}$$

Where T is;

$$T = k^{-1/2}\,\frac{S-1}{2i}\cdot k^{-1/2}$$

In terms of the element T, Eq(1-4), and Eq(1-6), become;

$$\sigma_{el} = 4\pi(2\ell+1)\frac{1}{k_i^2}\left|T_{el}\right|^2 \qquad (1\text{-}8)$$

$$\sigma_{inel} = 4\pi(2\ell+1)\frac{k_f}{k_i}\left|T_{inel}\right|^2 \qquad (1\text{-}9)$$

From a comparison of Eq(1-6), and Eq(1-8), one can write;

$$T_{el} = \frac{\eta\, e^{2i\delta} - 1}{2i} = e^{i\Delta}\ \mathrm{SIN}\ \Delta = \frac{1}{\mathrm{COT}\ \Delta - i} \qquad (1\text{-}10)$$

Where $\eta = e^{2\gamma}$, and $\Delta = \delta + i\gamma$.

In general $k^{2\ell+1}\ \mathrm{COT}\ \Delta$ can be expanded as a series in k as;

$$k^{2\ell+1}\ \mathrm{COT}\ \Delta = \frac{1}{A} + \frac{1}{2}\, r\, k^2 + \ldots\ldots$$

Where r is the effective range of the interaction[22].

In the zero range approximation (i.e., r=0), in the one-channel case, one can define a scattering length A by;

$$k^{2\ell+1}\ \mathrm{COT}\ \Delta = \frac{1}{A}$$

Then Eq(1-10) becomes;

$$T = \frac{Ak^{2\ell+1}}{1 - iAk^{2\ell+1}} \qquad (1\text{-}11)$$

Where A is a real number and a function of energy.

A generalization of Eq(1-11), for the multi-channel case has been made by Dalitz and Taun[7], and Ross and Shaw[8].

They define a K matrix by a matrix equation similar to the relation between T and A in Eq(1-11). i.e.;

$$T = \frac{K}{1 - iQK} \qquad (1\text{-}12)$$

Where Q is the momentum matrix and is given by; $\begin{pmatrix} k_1 & 0 \\ 0 & k_2 \end{pmatrix}$, and the K matrix, for the two channel system which incorporates the

requirements of unitarity and time reversal invariance, is represented by:

$$K = \begin{pmatrix} \alpha k_1^{2\ell} & \beta(k_1k_2)^{\ell} \\ \beta(k_1k_2)^{\ell} & \gamma k_2^{2\ell} \end{pmatrix} \qquad (1\text{-}13)$$

Where α, β, γ, are real numbers and k_1, k_2 are centre of mass momenta for the elastic and inelastic channels respectively. The energy dependence of the K matrix is the result of centrifugal barrier penetration.

Matrix elaments T_{11}, T_{12}, T_{21}, and T_{22} representing the scattering amplitudes for channels;

$$a + b \rightarrow a + b$$

$$c + d \rightarrow a + b$$

$$a + b \rightarrow c + b$$

$$c + d \rightarrow c + d$$

are given by;

$$T_{11} = \frac{A}{1-ik_1A}$$

$$T_{12} = \tilde{T_{21}} = \frac{B}{1-ik_2C} \qquad (1\text{-}14)$$

$$T_{22} = \frac{C}{1-ik_2C}$$

Where the quantities A, B, and C are;

$$A = \alpha k_1^{2\ell} + \frac{i\beta^2(k_1k_2)^{2\ell}\, k_2}{1-i\gamma k_2^{2\ell+1}}$$

$$B = \frac{\beta(k_1 k_2)^{\ell}}{1-i\alpha k_1^{2\ell+1}}$$

$$C = \gamma k_2^{2\ell} + \frac{i\beta^2(k_1 k_2)^{2\ell} k_1}{1-i\alpha k_1^{2\ell+1}}$$

Therefore the Cross-sections for the elastic and inelastic channels are;

$$\sigma_{el} = 4\pi(2\ell+1) \frac{|A|^2}{1 + k_1^2|A|^2 + 2k_1 \, Im(A)} \qquad (1\text{-}15)$$

$$\sigma_{inel} = 4\pi \frac{k_2}{k_1} (2\ell+1) \frac{|B|^2}{1 + k_2^2|C|^2 + 2k_2 \, Im(C)} \qquad (1\text{-}16)$$

Rewriting $C = k_2^2 (a+ib)$, where the quantities a, and b are;

$$a = \gamma - \frac{\alpha\beta^2 k_1^{4\ell+2}}{1 + (\alpha k_1^{2\ell+1})^2} \qquad b = \frac{\beta^2 k_1^{2\ell+1}}{1 + (\alpha k_1^{2\ell+1})^2}$$

Then Eq(1-16), becomes;

$$\sigma_{inel} = \frac{4}{k_1^2} \cdot \frac{g b k_2^{2\ell+1}}{(1+bk_2^{2\ell+1})^2 + (ak_2^{2\ell+1})^2} \qquad (1\text{-}18)$$

Where a is the real part and b is the imaginary part of the complex scattering length for the inelastic channel, and g is a positive number less than one which measures the coupling for the transition from the initial state to final state.

It is seen from Eq(1-18), that a and b are only functions of k_1, the initial state centre of mass momentum and as k_1 , varies by

only 2% over the range of momentum covered by this experiment, they can be taken as constants.

(1-3-2) Resonance Model.

An alternative approach to the direct production described by the scattering length theory, is the "Resonance Model".

The interaction between two particles, at energy $E=E_R$ may be said to be "resonant" with quantum numbers ℓ, J^P, I, if the total Cross-section contribution from that partial wave has a maximum at that energy.

It is seen from Eq(1-10), that the Cross-section is proportional to $SIN^2\ \Delta$, this implies at resonance $\Delta_{E_R} = \pi/2 + n\pi$.

The expansion of COT Δ in a Taylor series around the resonance energy is given;

$$COT\ \Delta(E) = COT\ \Delta(E_R) + (E-E_R)\left\{ \frac{d}{dE} COT\ \Delta(E) + \cdots\cdots \right\}_{E=E_R}$$

At resonance energy $COT\ \Delta(E_R) = 0$, and by defining;

$$\frac{2}{\Gamma} = -\left\{ \frac{d}{dE} COT\ \Delta(E) \right\}_{E=E_R}$$

One has;

$$T_{el} = \frac{\Gamma/2}{(E-E_R) - i\Gamma/2} \qquad (1\text{-}19)$$

Thus the elastic Cross-section is;

$$\sigma_{el} = \frac{\pi}{k^2} \frac{(2\ell+1)\cdot\Gamma^2}{(E-E_R)^2 + \Gamma^2/4} \qquad (1\text{-}20)$$

So far the spins of the particles have not been considered. In the case of $\pi^- p$ scattering, for a given ℓ, there are two total angular momenta $J = \ell \pm 1/2$, and correspondingly there are two outgoing waves amplitudes $\eta_\ell^{\pm} e^{2i\delta_{\ell\pm}}$. Eq(1-19) is summed over two states of each ℓ, and the factor $(2\ell+1)$ is replaced by $(2J+1)/2$ and Eq(1-20), is modified as;

$$\sigma_{el} = \frac{\pi}{k^2} (J+1/2) \frac{\Gamma^2}{(E-E_R)^2 + \Gamma^2/4} \qquad (1\text{-}21)$$

This is the non-relativistic Briet-Wigner equation for a resonating partial wave amplitude and Γ is the full width at half height (f.w.h.h.) at the resonance.

Let us consider the general case where there are severals channels into which a resonance can decay; the total width (Γ_{Tot}) of a resonance can be written as the sum of the elastic(Γ_{el}), and inelastic(Γ_{inel}) width.

$$\Gamma_{Tot} = \Gamma_{el} + \Gamma_{inel}$$

We define the following parameters;

$$x_i = \Gamma_{el}/\Gamma_{Tot}$$

$$x_f = \Gamma_{inel}/\Gamma_{Tot}$$

The generalisation of Eq(1-21), is obtained as follows;

The probability of formation of a resonance in the elastic channel will be proportional to x_i; the probability that the resonance will decay into an elastic or an inelastic channels is proportional to x_i, and x_f, respectively. Therefore the elastic, inelastic and total Cross-section will be proportional to x_i^2, $x_i x_f$, and x_i respectively;

$$\sigma_{el} = \frac{4\pi}{k^2} (J+1/2) \frac{x_i^2}{\{(E_R-E).2/\Gamma\}^2 + 1}$$

$$\sigma_{inel} = \frac{4\pi}{k^2} \quad (J+1/2) \quad \frac{x_i\, x_f}{\{(E_R-E).2/\Gamma\}^2 + 1}$$

$$\sigma_{Tot} = \frac{4\pi}{k^2} \quad (J+1/2) \quad \frac{x_i}{\{(E_R-E).2/\Gamma\}^2 + 1}$$

The Cross-section behaviour of ω production in $\pi^- p$ collisions is therefore given by;

$$\sigma_{(\pi^- p \to \omega n)} = \frac{2/3\pi}{k^2} \quad \frac{(J+1/2)\ \Gamma_{\pi p}\ \Gamma_{\omega n}}{(E-E_R)^2 + \frac{1}{4}(\Gamma_{\pi p} + \Gamma_o + \Gamma_{\omega n})^2} \qquad (1\text{-}22)$$

Where k is the centre of mass momentum for the elastic channel and $\Gamma_{\pi p}$, $\Gamma_{\omega n}$, and Γ_o are the partial widths to the elastic, ω-n, and all the other channels, respectively.

The energy dependence of the width is usually expressed using the non-relativistic potential theory expression;

$$\Gamma(E) = \gamma \frac{(qr)^{2\ell+1}}{D_\ell(qr)} \qquad (1\text{-}23)$$

where ℓ is the orbital angular momentum of the decay, γ is the reduced partial width, q is the centre of mass momentum, r is an effective interaction radius and $D_\ell(qr)$ is a barrier factor[22].

The values of D corresponding to $\ell = 0,1,2$ are

$$D_0 = 1$$

$$D_1 = 1 + (qr)^2$$

$$D_2 = 9 + 3(qr)^3 + (qr)^9$$

Eq(1-13) represents the K matrix in the zero range approximation. It has been suggested that the effect of the radius of the interaction can be introduced in the K matrix by replacing the quantities k_1, and k_2 by $k_1/(1+k_1^2\, r^2)^{1/2}$, and $k_2/(1+k_2^2\, r^2)^{1/2}$, respectively in Eq(1-13), where r is the radius of the interaction[9]. Thus k_1 and k_2 in Eq(1-18) have been replaced by these new values.

(1-3-3) Threshold Effect.

One of the interesting effects resulting from the general properties of the S-Matrix, is the behaviour of the reaction Cross-section at an energy corresponding to the threshold of a new channel. Such an effect, manifested as discontinuties in the curves of the Cross-section versus energy, was first discussed by Wigner, Adair, Baz, and Akun[10-13].

For the moment we consider a simple system (a+b), having only two possible reaction channels (say, a+b, and c+d) . The scattering matrix as given by Eq(1-5), described both the elastic scattering procces;

$$a + b \rightarrow a + b \qquad (1\text{-}24a)$$

$$c + d \rightarrow c + d \qquad (1\text{-}24b)$$

As well as the inelastic reactions;

$$a + b \rightarrow c + d \qquad (1\text{-}24c)$$

$$c + d \rightarrow a + b \qquad (1\text{-}24d)$$

We aim to investigate the effect of the opening of reaction (1-24c), on the Cross-section for the elastic channel Eq(1-24a) . Near the threshold, the dominent term in the amplitude for reaction Eq(1-24c) assuming an S-wave production, can be written;

$$1-\eta^2 = 2aq$$

Where a is a constant and q is the centre of mass momentum for the inelastic channel.

Let k be the centre of mass momentum of the initial state, then the elastic and inelastic Cross-sections are;

$$\sigma_{el}\ (E>E_t) = \frac{4\pi}{k^2} = \left| \frac{(1-aq)\ e^{2i\delta(1)} - 1}{2i} \right|^2 \simeq \frac{4\pi}{k^2}\ (1-aq)\ \mathrm{SIN}^2\ \delta(1)$$

$$\sigma_{inel} = \frac{2\pi aq}{k^2} \qquad (1\text{-}25)$$

In terms of the centre of mass energy E, and the threshold energy E_t, the values k and q are given by;

$$k^2 = 2\mu_a E$$
$$q^2 = 2\mu_b (E-E_t) \qquad (1\text{-}26)$$

Where μ's are appropriate reduced masses.

As the energy is approached from above ($q \to 0$), $\sigma_{inel} \to 0$, and $\sigma_{el} \to \sigma_o = \frac{4\pi}{k^2} \text{SIN}^2\ \delta_o(1)$, but the derivative $\frac{d\sigma_{el}}{dE} \to -\infty$, indicating that there is a discontinuity in the elastic Cross-section at $E=E_t$. It is also necessary to consider the behaviour of δ_{el} as $E \to E_t$ from below. Of course for $E<E_t$ we require $\eta=1$ but in the immediate vicinity of the threshold, the effects of the inelastic channel are still present; these may be derived by noting that q becomes imaginary for $E<E_t$ in Eq(1-26).

$$q \to iq = i(2\mu_b)^{1/2}\ (E_t-E)^{1/2}$$

and the phase shift for (S-wave) scattering of reaction Eq(1-24b) also becomes imaginary;

$$\delta(2) \to i\delta(2)$$
$$\delta(1) \to \delta(1)$$

Substitution into Eq(1-25) yield;

$$\sigma_{el}\ (E<E_t) = \frac{4\pi}{k^2} \text{SIN}^2\ \delta(1) - aqe^{2\eta q} \text{SIN}\ \delta(1)\ \text{COS}\ \delta(1) \qquad (1\text{-}27)$$

Eq(1-27) joins in to Eq(1-25) at $E=E_t$, but not smoothly; rather approaching the threshold from below, $\frac{d\sigma_{el}}{dE} \to \infty$ for δ(1) lying in the first or third quadrant. These two possible forms of the scattering Cross-section anomaly are shown in Fig(1-3a,b).

So far we have considered the situation where only two channels

are allowed. In the more general case, where the reaction of interest is coupled to more than one channel (as, is the case in ω production by $\pi^- p$ interactions), the threshold anomaly can have other shapes, in addition to those shown in Fig(1-3a,b).

Below the threshold of a new inelastic channel, assuming no dependence on spin, the differential cross-section is given by;

$$\frac{d\sigma_o}{d\Omega} = \frac{1}{4k^2} \Sigma_\ell \left| S_\ell P_\ell(\cos\theta^*) \right|^2 = \left| F(\theta^*) \right|^2 = \left| f(\theta^*) e^{i\delta} \right|^2 \qquad (1\text{-}28)$$

Where the subscript ℓ, symbolizes all the quantum numbers characterizing a given combination of initial and final channels and δ is phase shift.

Near the threshold for a new channel, (say a+b $\rightarrow$ e+f), the only amplitude whose alteration we need to consider is that corresponding to the set of channels L which leads to an S-wave production of the products (e+f) for this amplitude one can write;

$$S_L = So_L - aq\, e^{i\alpha}$$

Accordingly, near the threshold Eq(1-28), becomes;

$$\frac{d\sigma}{d\Omega} = \left| f(\theta^*) e^{i\delta} - \frac{aq\, e^{i\alpha} P_L(\theta^*)}{2ik} \right|^2$$

or

$$\frac{d\sigma}{d\Omega} \simeq \frac{d\sigma o}{d\Omega} - \frac{aq}{k} f(\theta^*) P_L(\theta^*) \,\mathrm{SIN}\,(\alpha-\delta) \qquad \text{for } E>E_t$$

and

$$\frac{d\sigma}{d\Omega} \simeq \frac{d\sigma o}{d\Omega} - \frac{aq}{k} f(\theta^*) P_L(\theta^*) \,\mathrm{COS}\,(\alpha-\delta) \qquad \text{for } E<E_t$$

The threshold anomalies have the form of (a or b) of Fig(1-3), if $0 < (\alpha-\delta) < \pi/2$ or $\pi/2 < (\alpha-\delta) < \pi$ respectively. For $(\alpha-\delta)$ in the third and fourth quadrants, the shapes are shown in Fig(1-3c,d).

(1-3-4) Angular Distribution.

In this section the qualitative behaviour of the ω angular distribution is discussed. At an energy just above the threshold, the angular momentum barrier inhibits all final state partial waves other than S-wave. Eq(1-18), shows that the contribution to the Cross-section from each ℓ^{th} partial wave behaves almost as $\sigma/p^* = (p^*)^{2\ell}$, e.g., constant for S-wave production.

The rapid rise in σ/p^* Fig(1-1), suggests that P-wave is important. However, some S-wave is definitely required as σ/p^* behaviour is inconsistent with parobolic rise from zero.

The scattering amplitudes are labelled by L L' (2J)(2s'), where L and L' are the orbital angular momenta for initial and final states, s' is the spin of the final state and J is the total angular momentum. The values of L at the threshold energy of the ω production for $\pi^- p$ system could be L=0,1,2,3 and let the L' at energy around the threshold, has values L'=0,1 as the angular momentum barrier requires. The conservation rules of the total angular momentum and parity allow only the following 7 amplitudes;

(SS11),(DS33),(PP11),(PP31),(PP33),(PP13),(FP53)

In the appendix (I) we present table of coefficients of the differential Cross-section calculated for the reaction $0^- + 1/2^+ \rightarrow 1^- + 1/2^+$. Then the angular distribution for the reaction $\pi^- p \rightarrow \omega\, n$ can be expanded as;

$$\begin{aligned}\frac{d\sigma}{d\Omega} = {} & \{ (SS11)(SS11)^* + 2(DS33)(DS33)^* + (PP11)(PP11)^* + (PP13)(PP13)^* \\ & + 2(PP31)(PP31)^* + 2(PP33)(PP33)^* + 3(FP53)(FP53)^* \} P_0 (\cos\theta^*) \\ & + \mathrm{Re}\{ 2(SS11)(PP11)^* + 4(SS11)(PP31)^* - 2.828(DS33)(PP13)^* \\ & + 1.789(DS33)(PP33)^* + 6.573(DS33)(FP53)^* \} P_1 (\cos\theta^*) +\end{aligned}$$

$$\text{Re}\ \{\ 4(PP11)(PP31)^{*} - 1.265(PP13)(PP33)^{*} - 1.6(PP33)(PP33)^{*} + 2.939(PP33)(FP53)^{*} - 4.648(PP13)(FP53)^{*} + 2(PP31)(PP31)^{*} + 2.4(FP53)(FP53)^{*}\ \}\ P_2\ (\text{COS}\ \theta^{*}) \qquad (1\text{-}29)$$

The above expansion suggests that, of the possible final S and P-wave combinations of the final state, the following amplitudes;

$$(SS11) + (PP13)$$

or

$$(PP11) + (DS33)$$

lead to an isotropic angular distribution, whilst the combinations;

$$(SS11) + (PP13) + (PP33) + (FP53)$$

or

$$(DS33) + (PP31) + (PP11)$$

produce no P_1 (COS θ^{*}) term in the angular distribution although they produce P_2 (COS θ^{*}) term. Thus, there is a possibility that , there could be a substantial P-wave amplitude even if the angular distribution is isotropic, as the ω particle is a vector meson.

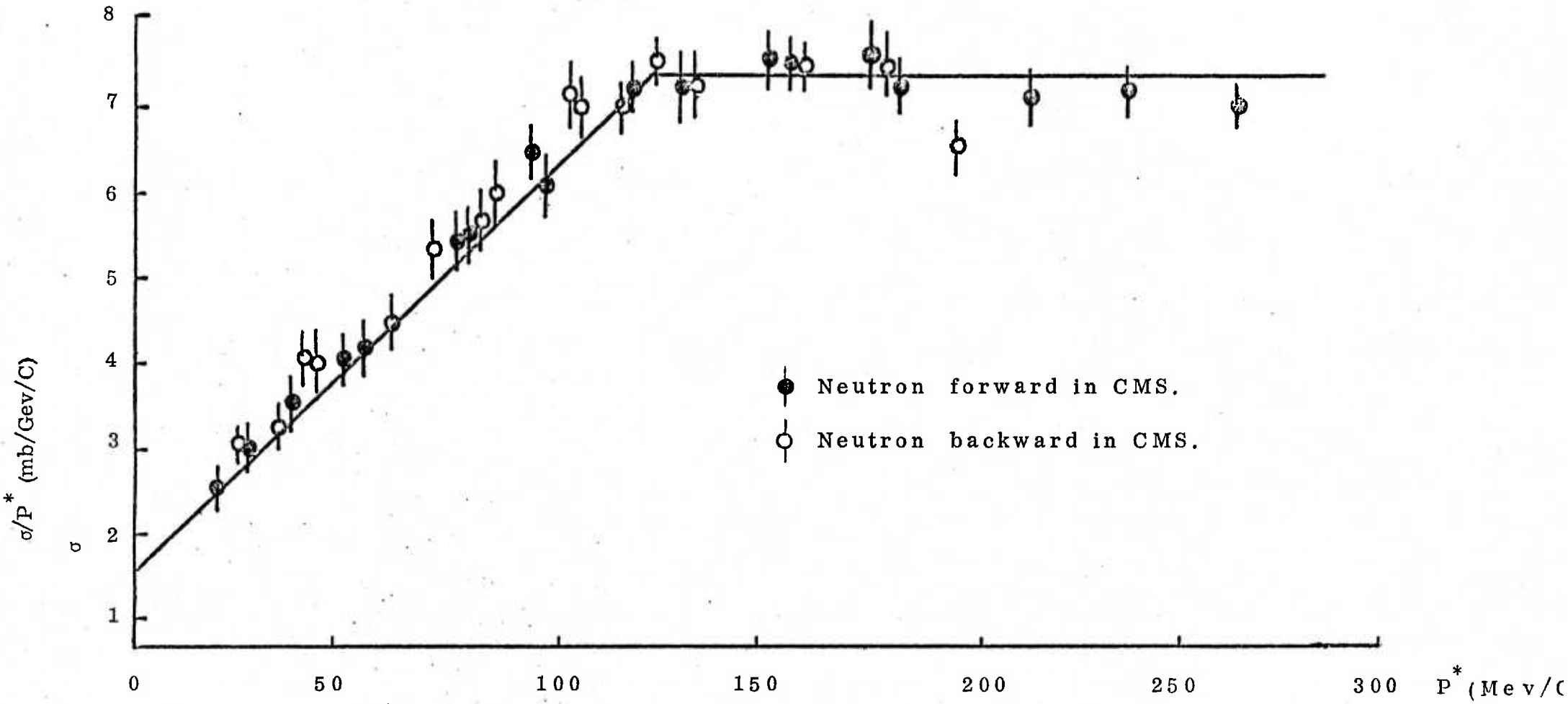

The cross section σ/P^* as a function of P^*. The solid line is the shape of the cross section used in the Monte Carlo.

This plot is reproduced from the reference (2).

FIG. (1-1)

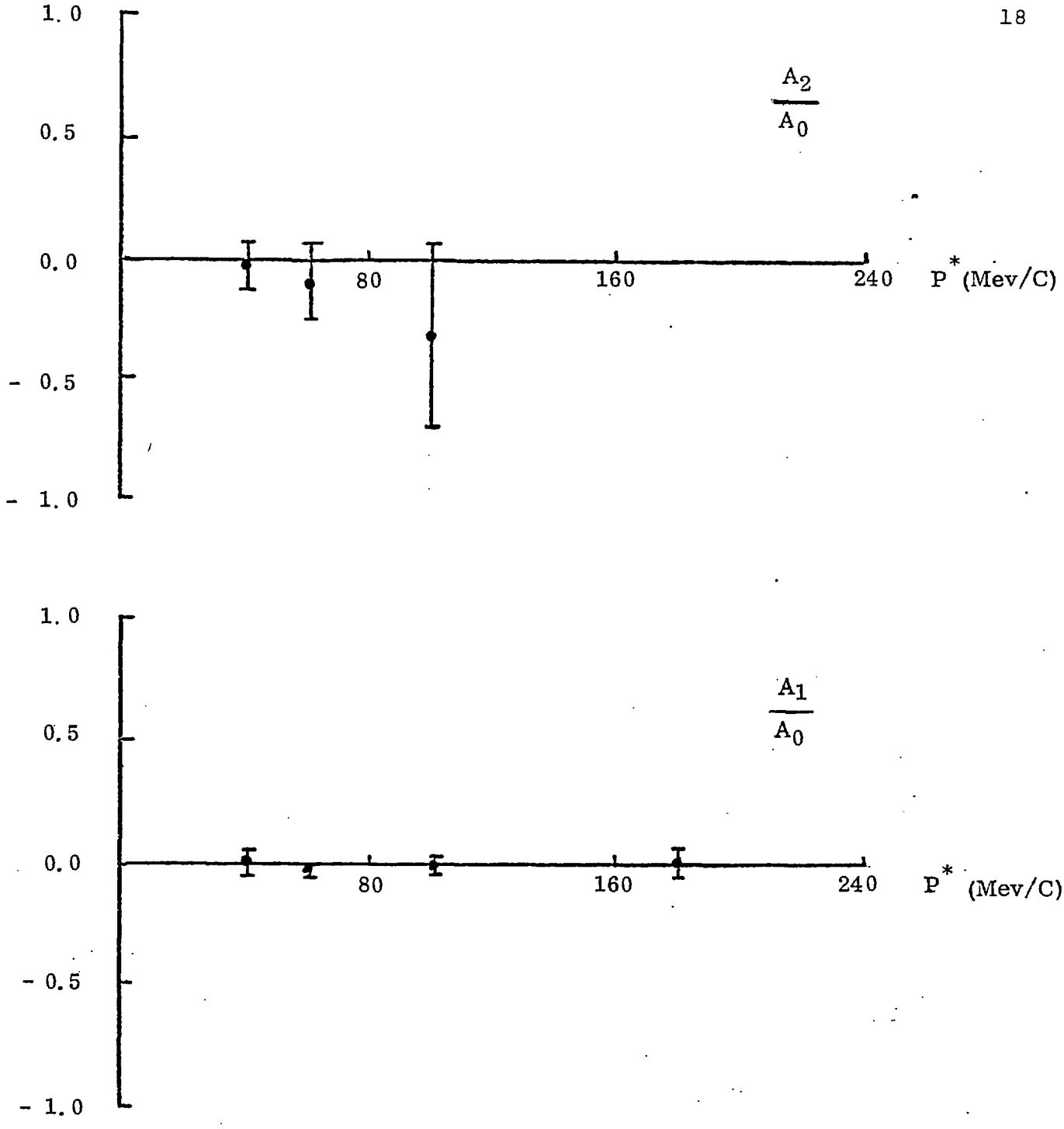

The values of the ratios of the polynomial coefficients from the fit to the angular distribution, as function of P^*.

This plot is reproduced from the reference (2).

FIG. (1-2)

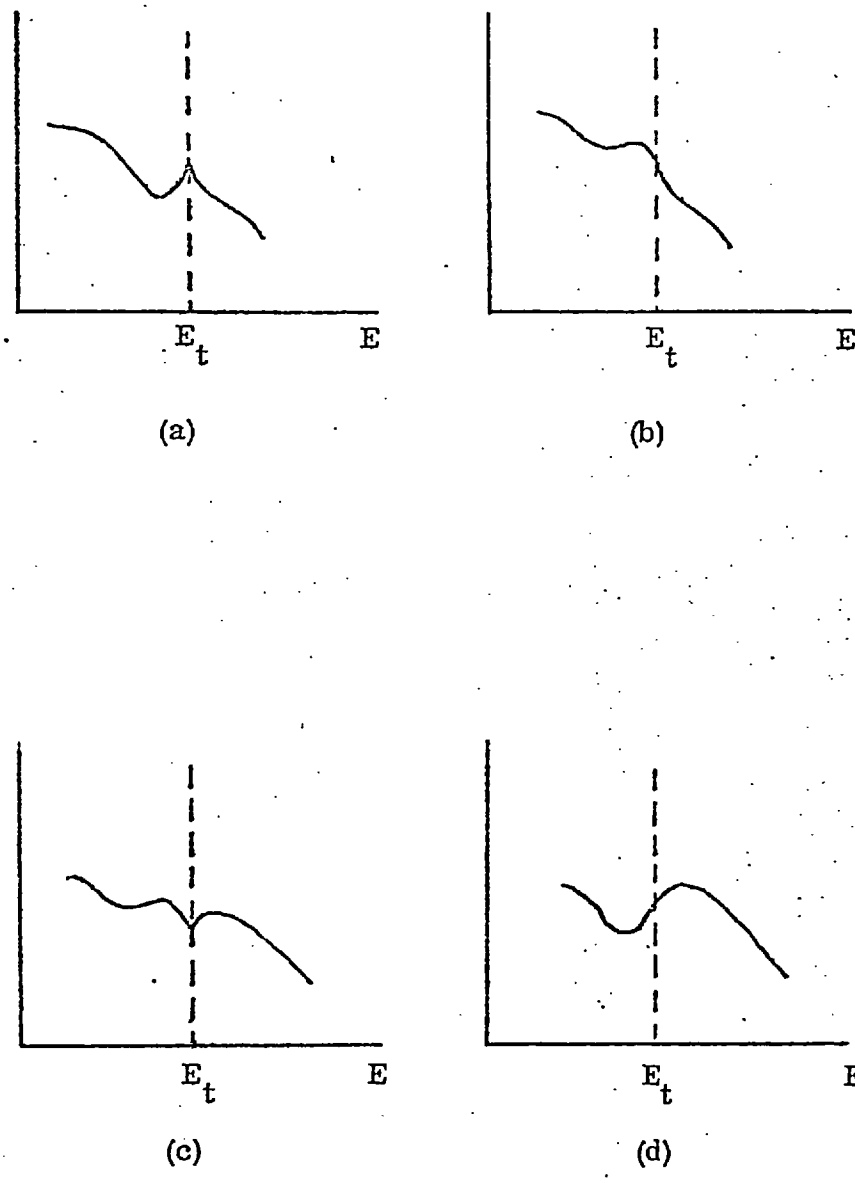

Possible cusp anomalies exibited by elastic scattering at the threshold of an inelastic channel.

Fig (1- 3)

2. KINEMATICS AND GENERAL CONSIDERATION

Cosider the reaction $1 + 2 \rightarrow 3 + 4$

The following notations are defined for different quantities;

P = momentum

E = total energy

M = rest mass

T = kinetic energy

β = velocity

γ = Lorentz factor = $(1-\beta^2)^{-1/2}$

s = total centre of mass energy squared in two-particle collision

θ = polar angle with Z-axis

Ω = solid angle

c = velocity of light, c=1

$\nearrow$ = 4-vector of momentum-energy

Subscripts refer to particle indices, starred quantities refer to the values these quantities have in the centre of mass system(CMS), and unmarked, to the value they have in the laboratory system(LS).

(2-1-1) Production Of The ω Meson.

The reaction studied was;

$$\underset{1}{\pi^-} + \underset{2}{p} \rightarrow \underset{3}{\omega} + \underset{4}{n} \qquad (2\text{-}1)$$

The invariant mass of particle 3, using energy and momentum conservation, is given by;

$$M_3^2 = M_1^2 + M_2^2 + M_4^2 + 2(E_1M_2 - E_1E_4 - M_2E_4 + P_1P_4 \cos\theta_4) \qquad (2\text{-}2)$$

Where particle 1 is the beam particle, particle 2 is assumed to be initially at rest and the measured variables are p_1, θ_4, and τ_n. The latter is defined by $\tau_n = \tau_4 - \tau_o$ where τ_4 is the time of flight (t.o.f.) of the neutron over a fixed distance d, and τ_o is the reference t.o.f. of particles with $\beta=1$.

Thus $$\tau_n = \frac{d}{c}\left(\frac{1}{\beta_4} - 1\right) \qquad (2\text{-}3)$$

The uncertainty in the determination of M_3 can be derived from equation(2-2);

$$\frac{\partial M_3}{\partial p_1} = \frac{1}{M_3} \cdot \{ p_4 \cos\theta_4 - \beta_1(E_4 - M_2) \} \qquad (2\text{-}4)$$

$$\frac{\partial M_3}{\partial p_4} = \frac{1}{M_3} \cdot \{ p_1 \cos\theta_4 - \beta_4(E_1 + M_2) \} \qquad (2\text{-}5)$$

$$\frac{\partial M_3}{\partial \theta_4} = \frac{1}{M_3} \cdot (-p_1 p_4 \sin\theta_4) \qquad (2\text{-}6)$$

Using $p_4 = \gamma_4 M_4 \beta_4$ and Eq(2-3) one can show;

$$\frac{\partial M_3}{\partial \tau_n} = \frac{\partial M_3}{\partial p_4} \cdot \frac{\partial p_4}{\partial \tau_n} = \frac{1}{M_3} \left\{ p_1 \cos\theta_4 - \beta_4(E_1 - M_2) \cdot \frac{-p_4 E_4^2}{\tau_n M_4^2} \right\} \qquad (2\text{-}7)$$

Let Δp_1, $\Delta\theta_4$ and $\Delta\tau_n$ be the uncertainties in the measurement of p_1, θ_4 and τ_n respectively. The mass resolution of the experiment ΔM_3, to first order would be;

$$\Delta M_3 = \left\{ \left(\frac{\partial M_3}{\partial p_1} \cdot \Delta p_1\right)^2 + \left(\frac{\partial M_3}{\partial \theta_4} \cdot \Delta\theta_4\right)^2 + \left(\frac{\partial M_3}{\partial \tau_n} \cdot \Delta\tau_n\right)^2 \right\}^{1/2} \qquad (2\text{-}8)$$

Eq(2-8) assumes that Δp_1, $\Delta\theta_4$, and $\Delta\tau_n$ are uncorrelated.

(2-1-2) Missing Mass Spectra.

For each event the time taken by the recoil neutron to travel from the liquid hydrogen target to a neutron counter was measured. The momentum of the neutron p_4, was then calculated and hence the missing mass calculated as p_1, and θ_4 are known.

The kinematics corresponding to two arbitrary neutron angles are shown in Fig(2-1) which illustrates lines of constant missing mass on a plot of p_1, the beam momentum, versus τ_n, the neutron time of flight over a distance of 615 cm. The lines of constant p_4^* are also shown.

The time of flight behaviour of the neutron as a function of beam momentum is also plotted for the ω mass at various laboratory angles and is shown in Fig(2-2a), and the relation between neutron laboratory angle θ_4, and centre of mass system angles θ^*, for various momenta of the final state in the centre of mass system, p^*, is also plotted in Fig(2-2b).

For a fixed incident pion momentum p_π, the number of events/ incident beam particle into a solid angle $\Delta\Omega$ and momentum interval Δp_4, will be given by;

$$R = N_H \int_{\Delta\Omega} \int_{\Delta p_4} \frac{d^2\sigma}{d\Omega\, dp_4} \, d\Omega \, dp_4$$

Where N_H, is the number of target particles/unit area. If J_p, is the Jacobian for the transformation of the variables(COS θ_4,p_4) to (t,M_3) which are Lorantz invariants, we have;

$$R = \frac{N_H}{2\pi} \int \int \frac{d^2\sigma}{dt\, dM} \, J_p \, d\Omega \, dp_4 \qquad (2\text{-}9)$$

$$\text{Where } J_p = 2\, p_1\, M_2\, p_4^2 \,/\, M_3\, E_4 \qquad (2\text{-}10)$$

and t (four momentum transfer squared) is given by;

$$t = (p_2 - p_4)^2 = (M_4 - M_2)^2 - 2 T_4 M_2 \qquad (2\text{-}11)$$

For a narrow resonance such as the ω meson, it is reasonable to assume that as p^* and θ^* are varied the cross-section behaviour of each mass interval within the resonance is the same. In terms of t, this implies that one can factorize the M_3 and t dependence of the double-differential cross-section in Eq(2-9) as;

$$\frac{d^2\sigma}{dt\, dM_3} = \frac{\Gamma/2}{(M_3 - M_0)^2 + (\Gamma/2)^2} \cdot \frac{d\sigma}{dt} \qquad (2\text{-}12)$$

Where M_o and Γ are the central mass and width of the resonance respectively.

The four-momentum transfer squared t, in the CMS is given by ;

$$t = M_2^2 + M_4^2 - 2 E_2^* E_4^* + 2 p_2^* p_4^* \cos \theta_4^* \qquad (2\text{-}13)$$

Since $p_1^* = p_2^*$ and $p_3^* = p_4^*$, we define;

$$K^* = p_1^* = p_2^* \qquad \text{and} \qquad p^* = p_3^* = p_4^*$$

hence at fixed p_1, we have;

$$dt = 2 k^* p^* d(\cos \theta_4^*) \qquad (2\text{-}14)$$

Using Eq(2-12) and Eq(2-14), we have;

$$\frac{d^2\sigma}{dt\, dM_3} = \frac{\Gamma/2}{(M_3 - M_0)^2 + (\Gamma/2)^2} \cdot 2 K^* p^* \frac{d\sigma}{d(\cos \theta^*)} \qquad (2\text{-}15)$$

The general expression for the number of detected events can be obtained by combining Eq(2-9) and Eq(2-15).

$$N = \frac{N_H}{2\pi} \int \int \int d\Omega \, dp_1 \, dp^* \cdot \frac{\Gamma/2}{(M_0-M_3)^2 + (\Gamma/2)^2} \times$$

$$J_p \cdot 2 K^* p^* \cdot \frac{d\sigma}{d(\cos\theta^*)} \cdot n(p_1) \cdot \varepsilon(p^*) \qquad (2\text{-}16) \cdot$$

$\varepsilon(p^*)$ is the neutron counter efficiency and the factor $n(p_1)$ represents the momentum distribution of the incident beam particle over a range of momentum bins.

The value K^* varies very slowly over the available range of p^* so that if we hold costant the final state parameters, p^*, and COS θ^* , and scan through M_3, by scanning p_1, we will be able to trace out the shape of the resonance independent of any assumptions about cross-section behaviour. Then,by integrating over p_1 and therefore M_3, the values of the differential cross-section and the angular distribution of the ω meson can also be determined.

2-2 $\pi^- p$ Elastic Scattering.

In the reaction

$$\underset{1}{\pi^-} + \underset{2}{p} \rightarrow \underset{3}{\pi^-} + \underset{4}{p}$$

there is the same initial state as in the reaction involving ω production.

The two scattered charged particles in the final state were detected by a system of drift chambers as explained in more detail in chapter 3.

Consider an event in the final state having scattering angles θ_π and θ_p for the pion and proton in the laboratory frame. Fig(2-3) shows the behaviour of the θ_π and θ_p for a fixed incident pion momentum p_π, of 1.1 Gev/c in laboratory frame. Curve A is the variation

of θ_p with θ_π and curve B is the reverse. The dashed lines represent approximately the effect of the experimental angular resolution.

On detection of an event by the drift chambers, a distinction between the π and p was made using kinematic constraints on the final state scattering angles. Fig(2-3) shows that π and p can not be distinguished at scattering angles $\theta_\pi \simeq \theta_p \simeq 45^\circ$ in the laboratory system.

In this ambiguity region, more information in addition to the measurement of scattering angles is required. The problem can be resolved by using information from the pulse height in the two thin scintillation counters placed at each side of the target immediately behind the drift chambers.

Having determined the two scattering angles θ_π and θ_p, and the incident pion momentum p_1 in the laboratory system, the pion and proton momenta are uniquely defined.

The total energy squared s, is;

$$s = M_1^2 + M_2^2 + 2\, E_1\, M_2$$

where

$$E_1 = (M_1^2 + p_1^2)^{1/2}$$

The final state momentum p^*, in the CMS can be given as;

$$p^{*2} = \frac{\{ s - (M_3 + M_4)^2 \}\{ (s - (M_3 - M_4)^2 \}}{4s} \qquad (2\text{-}17)$$

and the CMS angles of each final state particles are;

$$\theta_\pi^* = \cos^{-1} \left\{ \frac{\gamma_c^2\, \beta_c \pm \{\gamma_c^4\, \beta_c^2 - (\gamma_c^2 + \cot^2 \theta_3)\, (\gamma_c^2\, \beta_c^2 - \beta_3^{*2} \cot^2 \theta_3)\}^{1/2}}{\beta_3^* (\gamma_c^2 + \cot^2 \theta_3)} \right\}$$

$$+ \text{ for } \theta_3 \leqslant 90^\circ \qquad (2\text{-}18)$$

$$- \text{ for } \theta_3 > 90^\circ$$

Similarly the CMS scattering angle θ^*_p, is given by;

$$\theta^*_p = \cos^{-1}\left\{ \frac{\gamma_c^2\,\beta_c - \{\gamma_c^2\,\beta_c^2 - (\gamma_c^2 + \cot^2\theta_4)(\gamma_c^2\,\beta_c^2 - \beta_4^{*2}\cot^2\theta_4)\}^{1/2}}{\beta_4^*(\gamma_c^2 + \cot^2\theta_4)} \right\} \tag{2-19}$$

Where;

$$\beta_c = \frac{p_1}{E_1 + M_2} \qquad \gamma_c = \frac{E_1 + M_2}{\sqrt{s}}$$

$$\beta_3^* = \frac{p_3^*}{E_3^*} \qquad \beta_4^* = \frac{p_4^*}{E_4^*}$$

Assuming that the errors in the measurements of θ_π and θ_p are uncorrolated, then the best value for CMS scattering angle θ^*, can be written as;

$$\theta^* = \frac{\{\theta_\pi^*(\frac{\partial\theta^*}{\partial\theta_p}\Delta\theta_p)^2 + \theta_p^*(\frac{\partial\theta_\pi^*}{\partial\theta_\pi}\Delta\theta_\pi)^2\}}{\{(\frac{\partial\theta_p^*}{\partial\theta_p}\Delta\theta_p)^2 + (\frac{\partial\theta_\pi^*}{\partial\theta_\pi}\Delta\theta_\pi)^2\}} \tag{2-20}$$

Where;

$$\left(\frac{\partial\theta_p^*}{\partial\theta_p}\right) = \frac{1 + \cot^2\theta_4}{\gamma_c\left\{\frac{\cos\theta_p^*(\beta_c + \beta_4^*\cos\theta_p^*)}{\beta_4^*\sin^2\theta_4^*} - 1\right\}} \tag{2-21}$$

and

$$\left(\frac{\partial\theta_\pi^*}{\partial\theta_\pi}\right) = \frac{1 + \cot^2\theta_3}{\gamma_c\left\{\frac{\cos\theta_\pi^*(\beta_c + \beta_3^*\cos\theta_\pi^*)}{\beta_3^*\sin^2\theta_\pi^*} + 1\right\}} \tag{2-22}$$

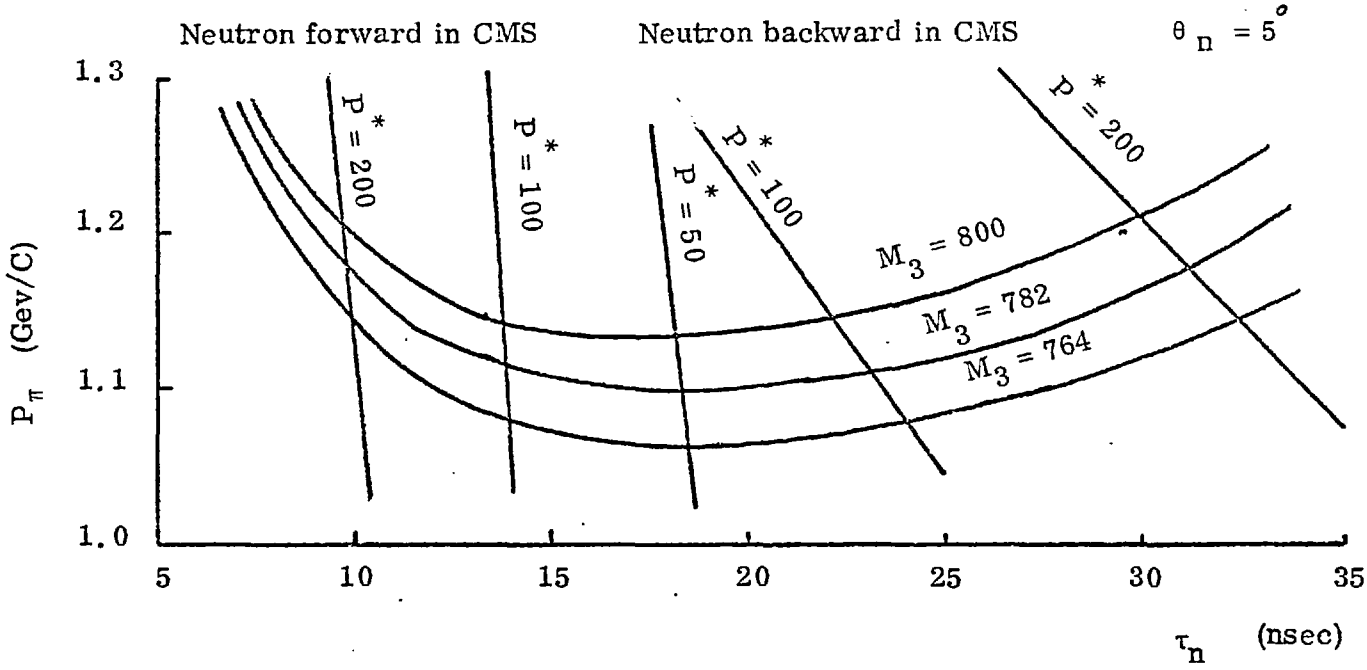

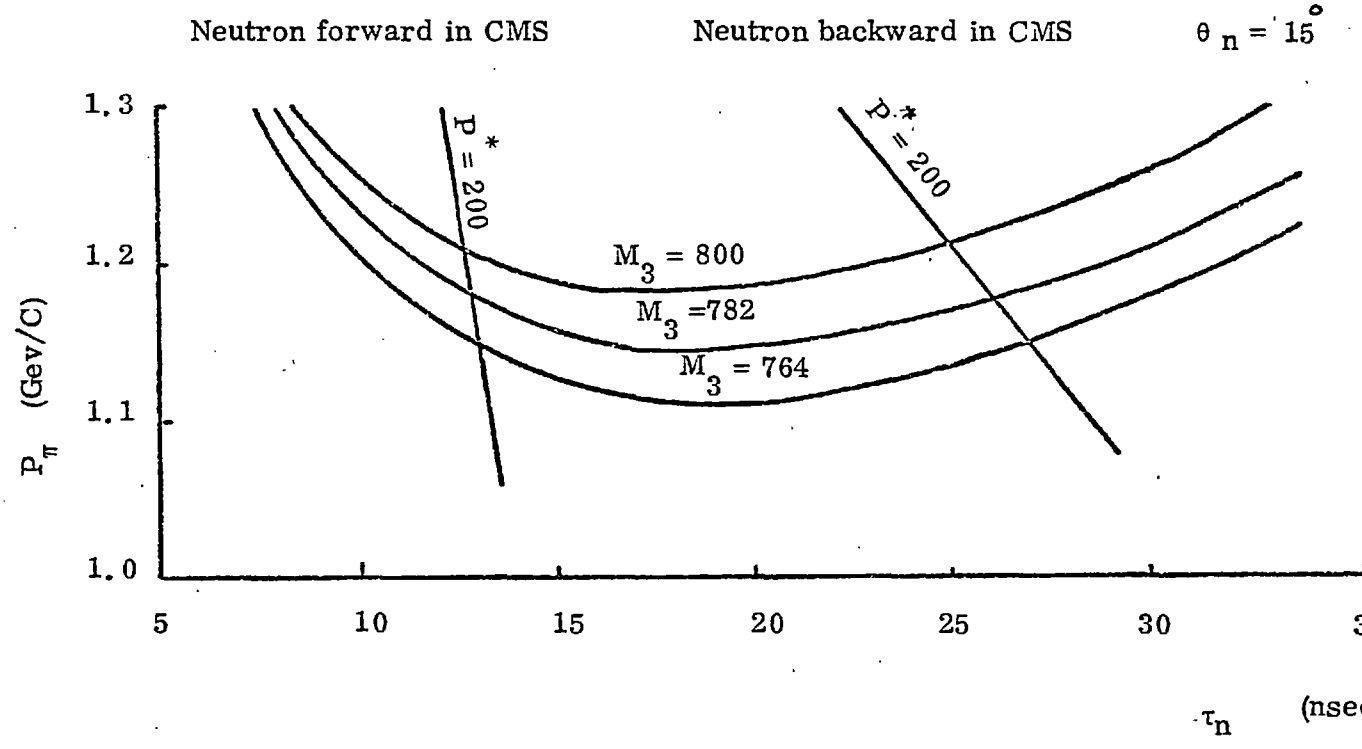

The relationship between P_π and τ_n at different laboratory angles for various values of missing mass M_3 , and centre of mass system momentum P^* .

Fig (2 - 1)

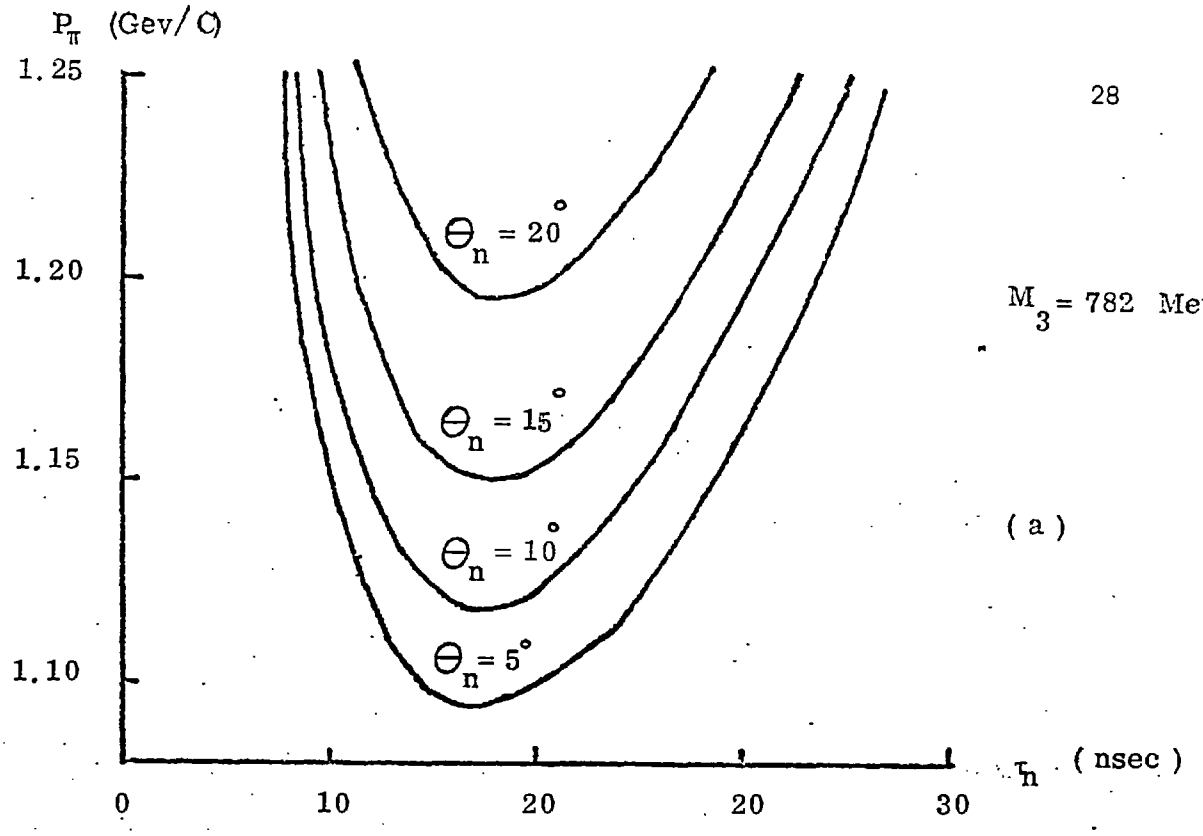

The relationship between beam momentum P_π, and neutron time of flight τ_n, at various laboratory angles θ_n, for ω mass.

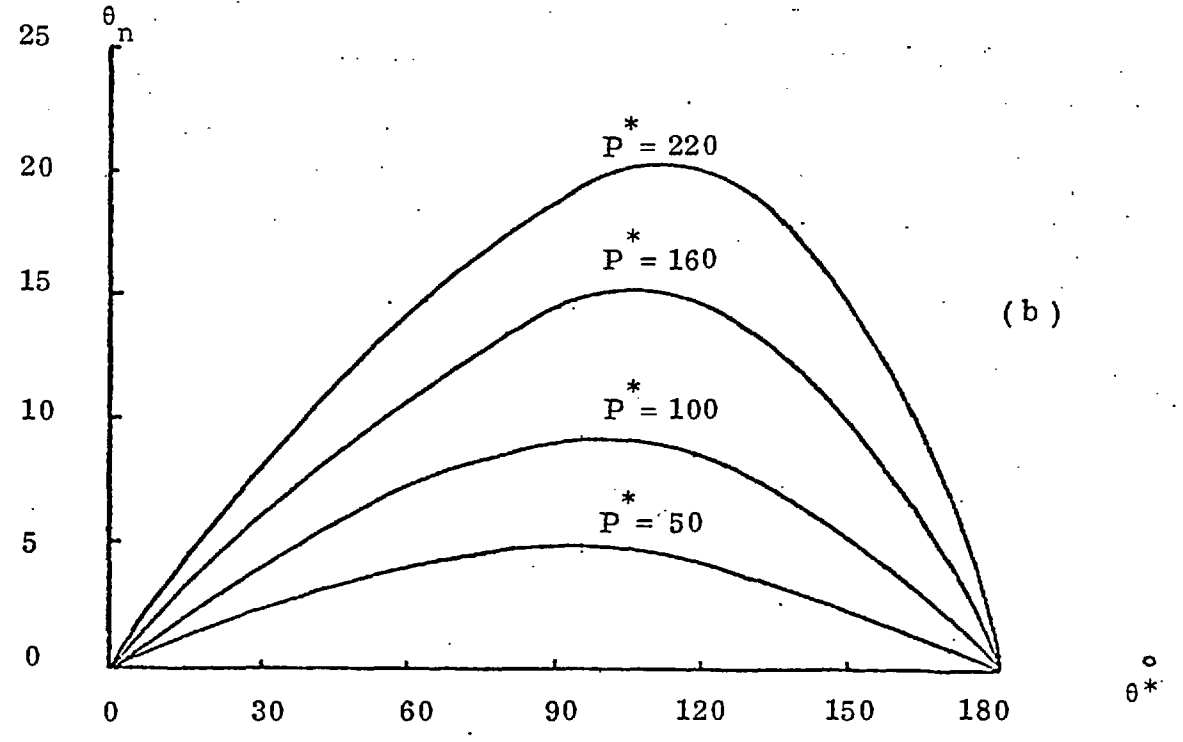

The relationship between neutron angle in laboratory system θ_n, and in centre of mass system θ^*, for various values of P^*.

Fig (2 - 2)

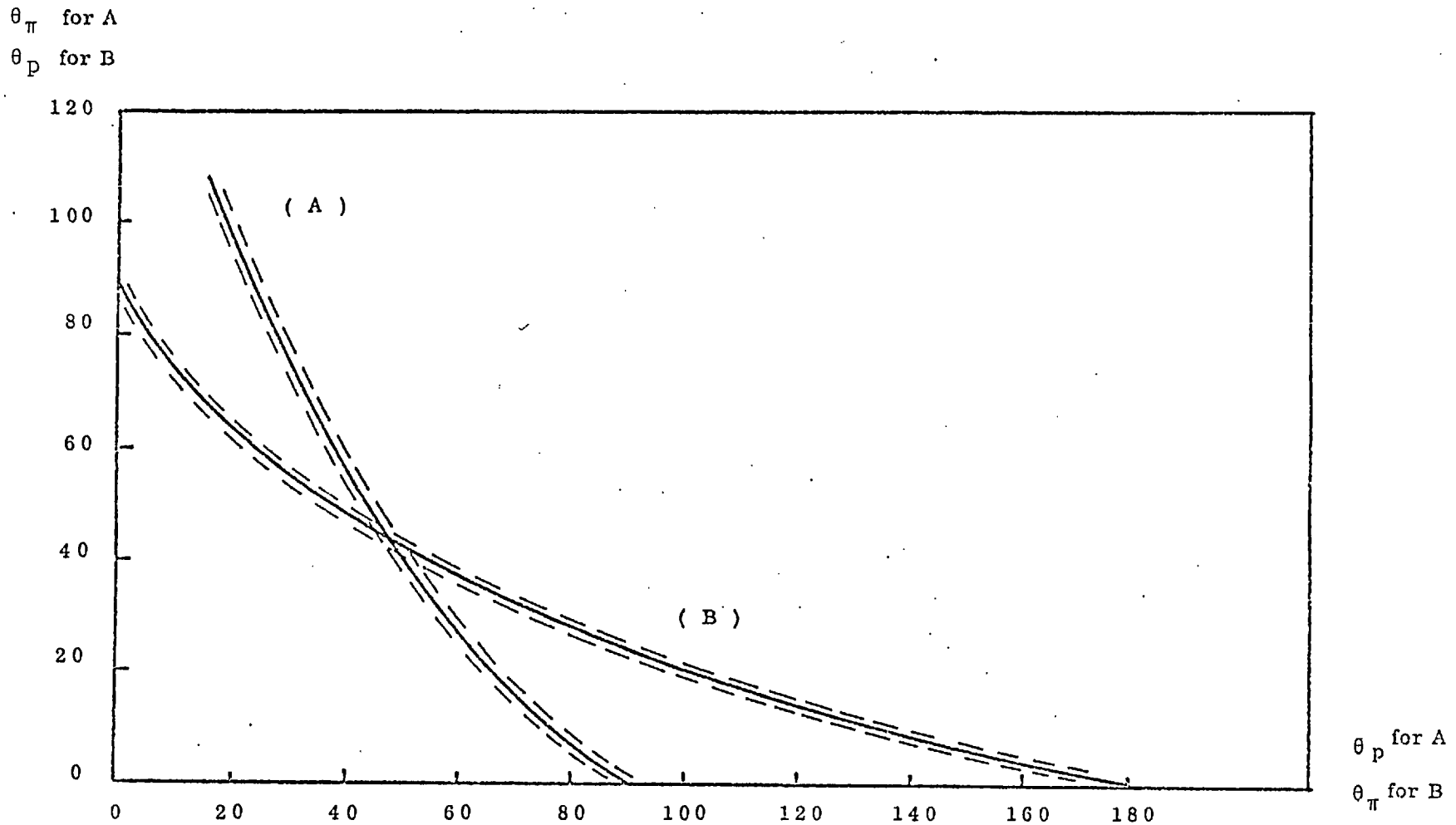

Variation of pion scattering angle θ_π with proton scattering angle θ_p, in the LS for pion beam momentum P_π of 1.1 Gev/C for curve A. Curve B is the reverse relationship. The dashed lines represent the effect of angular resolution.

Fig (2 - 3)

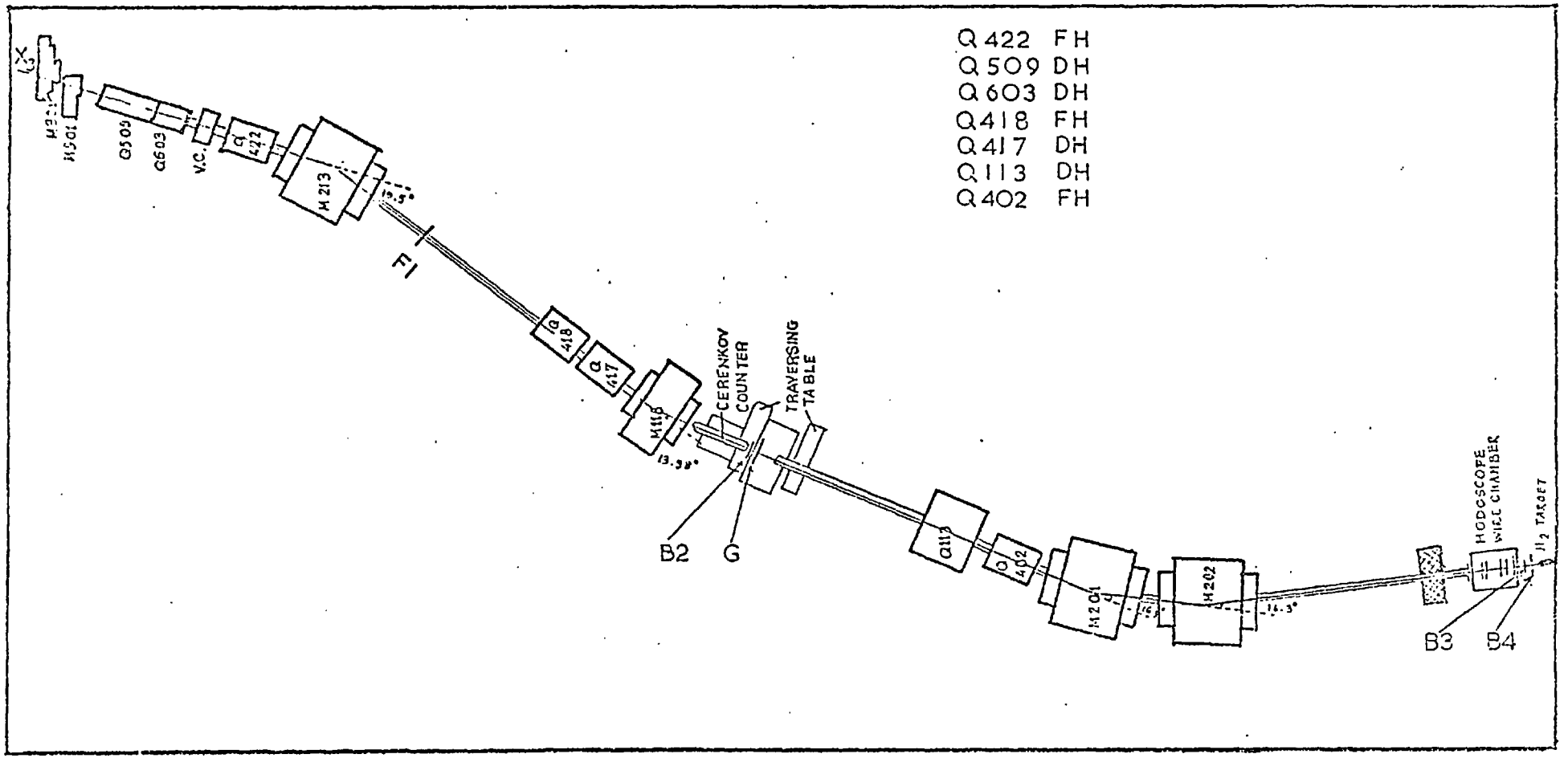

Plan of π 8A beam line .

Fig (3 - 1)

3 APPARATUS AND TECHNIQUE

(3-1) Beam And Momentum Spectrometer.

A pion beam was generated at an external target, in an extracted proton beam from Nimrod, and ultimately focussed on a liquid hydrogen target by the elements shown in Fig(3-1). Negative particles were brought to a first focus F1, by magnets M801, M901, M213, and quadrupoles Q509, Q603, and Q422.An intermediate horizontal focussing quadrupole Q418, and vertical focussing quadrupole Q417, together with the bending magnet M118 focussed the image of F1, on to a plane at G, where the required momentum bite was defined by a collimator. Electrons in the beam were rejected by a threshold gas Čerenkov counter C, the beam was then refocussed through a vertical focussing quadrupole Q113, and horizontal focussing Q402, together with bending magnets M201, and M202, on to a plane at H, which was conjugate to the G plane with unit magnification.

Five multi wire proportional chambers Fig(3-2),G,H (1 mm wire spacing) J,K and L (2 mm wire spacing) were used for the accurate momentum and angle determination of a beam particle.

The H, and K, wire chambers determined the horizontal geometry of a beam particle and the two J, and L, wire chambers measured the vertical positions. The G, and H, chambers measured the momentum of a beam particle crossing these two conjugate planes. The overall momentum dispersion at H, was 40.5 mm/1% momentum variation.

In addition to the wire chambers, two sets of thin scintillation counter hodoscopes in the G, and H, planes were used. The G, hodoscope consisted of eight fingers of scintillation counters each of width 7.5 mm and the H, hodoscope had six fingers of width 7.5 mm. The function of the G, and H, hodoscopes was to give the total number of incident

beam pions Σp_{π}, and also to rescue those events in which their momenta could not be determined because several wires had fired in the chambers. A check on the consistency of the wire chambers and hodoscope information was also made.

The liquid hydrogen target was immediately downstream of the L-wire chamber.

The beam profile at the target had a f.w.h.h. of 2.5 cm in both the horizontal and vertical directions. The beam divergence had a f.w.h.h. of about 15 mrads horizontally and 5 mrads vertically.

The spectrometer magnets were investigated individually using search coils and appropriate shims added to give a uniform magnetic field. The dipole fields were monitored by means of NMR probes, and the quadrupole fields by current in the windings. During the data taking the currents and NMR frequencies were monitored via a television screen. Their values were quite stable and only occasional adjustments to them were necessary. The currents were cycled to remove hysteresis effects when they were set to new currents.

The magnet supplies were stable to better than 1 part in 10^3 and for the spectrometer magnets much better than 1 part in 10^4. The spectrometer was calibrated using the floating wire technique[14].

(3-2) Liquid Hydrogen Target.

Liquid hydrogen was contained in a cylindrical flask, 60 mm in diameter and 200 mm in length, with its axis parallel to the beam direction. The effective density of the boiling hydrogen was held at 0.07 gm/cc by means of a constant pressure device. An outer casing of aluminum enclosed the target and enabled it to be thermally insulated by a Vacuum. The beam passed through two melinex window in the outer

casing with 0.12 mm thickness. The target system is shown in Fig(3-3)

The momentum loss of a π^- in liquid hydrogen at 1.1 Gev/c is about 0.0289 Mev/mm. In the missing mass experiment the incident pion momenta were corrected for energy loss assuming they interacted at the mid-point of the target, and in the elastic scattering experiment the correction was made using the calculated interaction point.

(3-3) Interaction.

(3-3-1) Neutron Detection.

The apparatus was designed to detect a recoil neutron produced in association with an ω meson near the threshold.

Recoil particles were detected and identified by means of the 60 neutron counters N_{1-60} , the 12 charged particle counters A_{1-12} , and the proton counter P.

Neutron Counters.

60 neutron counters were arranged as shown in Fig(3-4). Neutron counters N_{1-45} and N_{46-60}, were positioned downstream from the target at distances 615 cm and 435 cm respectively.

Each neutron counter was 32 cm long, 6.7 cm wide and 30 cm deep, Particles were detected when they interacted in the scintillators producing charged products which themselves caused the emission of scintillation light. Photons were collected at the back of the counters by a conical light guide, 30 cm long leading to RCA 8575 photo-multiplier. During the experiment, the voltage supplies on the photo-multiplier tubes were held constant to ±1 volt. The gains of the tubes were equalised between the counters before data taking commenced. On detection of a recoil particle, a pulse height measurement was also made.

The detection efficiency for a neutron is energy dependent , Fig(3-5) shows the behaviour of the neutron detection efficiency as a

function of neutron energy for the neutron counters used in the π7 experiment, but for most of the energy range of the experiment the efficiency was between 24% and 26% [15]. Since the neutron counters used in this experiment were very similar to those of the π7 experiment, the value 25% was used in our analysis.

A-Counters.

In front of each group of 5 neutron counters were placed thin scintillation counters A_{1-12}, to enable a neutron to be distinguished from a charged particle.

Proton Counter.

The proton counter was a circular thin scintillation counter of diameter 60 mm and thickness 2 mm situated 14 cm downstream of the centre of the liquid hydrogen target.

Recoil particles from interactions in the hydrogen target passed through this counter, before being detected in the neutron counters. A cross-check on the charge of the recoil particle was applied on the data in the off-line analysis using the information from this counter.

(3-3-2) Detection System For π^- p Elastic Scattering.

A system of drift chambers surrounding the liquid hydrogen target was used to detect elastically scattered particles and an extrapolation of their trajectories enabled a determination of the interaction point in the hydrogen target to be made and this enabled an accurate determination of the momentum of the beam pion.

Fig(3-6) illustrates the drift chamber arrangement used in this experiment. A detailed description of the drift chamber has been given elsewhere [16], and thus only a brief outline will be presented here.

In a drift chamber the electrons liberated in the gas by ionizing collisions drift under an electric field with constant velocity

towards the signal wire where they are detected Fig(3-7).

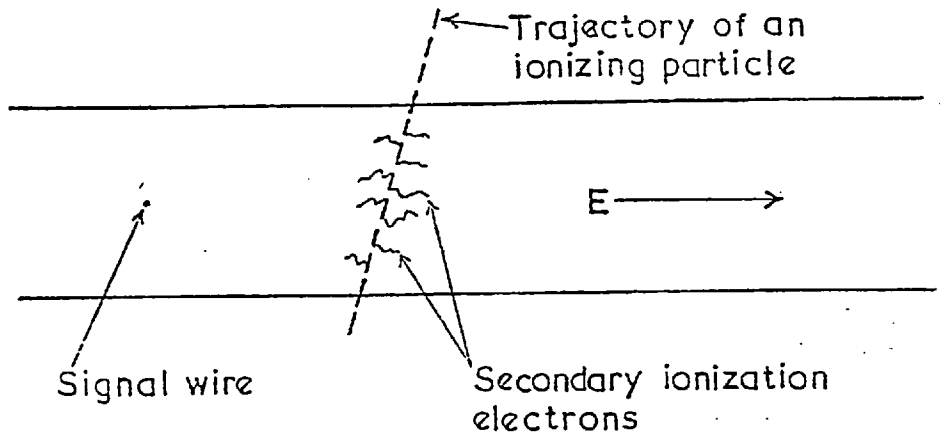

Fig (3 - 7)

Knowing the drift velocity in the chamber, the measurement of the time that elapses between a particle's passage and the avalanche pulse appearing on the signal wire enables a determination of the position where the charged particle passed through the drift chamber.

Drift chambers of 428 x 400 mm^2 sensitive area were constructed for the experiment and details are shown in Fig(3-8), andFig(3-9). The frame is made of Tufnol sheets of 12 mm thickness. The cathode plane was made from Polyseter sheets(5 mil) deposited with copper (0.5 mil) and etched into strips with a pitch of 5 mm. A chain of resistances of 1 MΩ linked the ends of each strip forming the graduated drift field of about 500/cm along the length of the chamber. A -12.0 Kv voltage was applied on the cathode wires at the centre of the chamber and the gain of the chamber could be adjusted by a variable -3.0 Kv voltage applied to the cathode wires nearest to the signal wires, Fig(3-8).

Cathode wires and signal wires were made of gold plated tungsten wires of diameters 100 μm and 20 μm respectively.

In order to determine the position (X,Y) of a particle, two such

chambers were mounted together, each rotated through an angle of 5^{o} with the vertical direction in opposite directions Fig(3-10).The distances between chamber centers was 31 mm; such a two chamber set is named a "Module". Three modules at each side of the target were used to determine elastically scattered particle tracks.

The accuracy of the measurement of the trajectory depends on the range of the primary electrons in addition to other factors e.g., electric field, gas mixture etc. The drift velocity varies with the composition of the gas mixture and its nature. The drift time of electrons to the signal wire is used to determine the position of the particles within the chamber. A gas mixture is therefore required which gives a constant drift velocity independent of the electric field along the length of chamber. The best gas mixture found to satisfy this requirement was a mixture of 25% Methane and 75% Argon.With thismixture a -12.0 Kv voltage was applied at the cathode resulting in a drift velocity of 70 mm/μsec.

The time needed for an electron to drift from the cathode wires to the signal wire was about 3.2 μsec, and if two particles passed through the chamber within this time there could be a confusion between the two if the second particle passed through the chamber closer to the signal wire than the first one. To overcome this problem an electronic circut was designed to reject events if they were within a 3.2 μsec time interval.

The drift time measurement relied on recording a number of pulses from a 200 MHZ oscillator in a Camac scaler that was allowed to count during the drift time. A "Start" signal from thin scintillation counters (D_{1-4}) positioned immediately after the chambers initiated the clock and a "Stop" signal from the drift chamber signal wire terminated it. The drift velocities were calculated for each side of a drift chamber from the distribution of those events which triggered the signal wires on both

sides. Fig(3-12) shows the distributions of such events for 24 signal wires in a typical run.

The linearity between drift distance and drift time was tested by means of a well collimated beam and a finger scintillation counter. The linearity found to be very good and only a slight deviation of about 1 mm was found at distances less than 2.5 cm from the cathode plane for perpendicular tracks. The linearity was also found to be very good for tracks at angles of 45° to the chamber plane. A small correction was made for angled tracks due to the finite thickness of the chamber.

The stability of the drift speed depends on the stability of gas mixture,pressure,voltage,temperature,etc.The change of drift speed was found to be less than 1% from run to run.

The uncertainty in the measurement of the drift time was 5 nsec which corresponds to an uncertainty of about 0.37 mm in the determination of the position.

(3-4) Electronics and Logic.

A simplified diagram of the tunnel diode electronics and logic is shown in Fig(3-11).

The trigger logic system can be grouped as follows;

(i) Beam Trigger; A beam particle was assigned to one of the four momentum channels by grouping a number of selected G, and H , combinations in each coincidence circut. An "or" of the four momentum channel coincidences was designed to give the total number of the beam pions refered to as Σp_{π} .

The logic accepted beam particles when one finger only of the G hodoscope, and one finger only of the H hodoscope were in coincidence, otherwise they were rejected. Electrons in the beam were vetoed by a threshold gas Cerenkov counter. Two thin B_2, and B_3, scintillation counters

were positioned immediately upstream of the G, and H, hodoscopes, and a scintillation counter B_4, with a circular hole of 7 cm diameter, was placed immediately upstream of the liquid hydrogen target. It was used to reduce the number of non- hydrogen events by demanding no pulse from this counter. A circut called the "Interference remover" was designed to veto events if there were two signals from either B_2,B_3 or B_4, within 40 nsec. Thus a beam trigger was defined as;

$$T_B = B_2 \cdot 1G \cdot 1H \cdot B_3 \cdot \overline{C} \cdot \overline{B_4}$$

(ii) Interaction Trigger; Non-interacting beam particles were eliminated from the final trigger if there was a pulse from either of two circular scintillation counters V1(130 mm in diameter), and V2(320 mm in diameter) situated downstream of the liquid hydrogen target at distances 2m and 6m respectively. So an interaction was defined as;

$$T_I = T_B \cdot \overline{(V_1 + V_2)}$$

A good event could be vetoed by a noise signal from V_1, or V_2. The rate at which this happened, called occupancy, was a function of the beam intensity and was monitored during data taking. In this experiment the rate was less than 2% so no correction for this was needed in the analysis.

A small thin scintillation counter, the P counter, positioned immediately after the liquid hydrogen target, could be set in coincidence (for proton) or veto (for neutron) in the off-line analysis.

(iii) Neutron Trigger; Pulses from the last dynodes of the neutron counters N_{1-60}, were delayed, and "or"ed together to form a single "neutron" pulse.

Three timing gates were introduced in the logic as follows;

The first gate was called "The fast peak gate" and was used to

collect events caused by particles having $\beta \simeq 1$, e.g., elastically scattered beam particles. The distribution of events in this gate provided the accurate time zero reference (τ_0). The fast peak gate was opened from (τ_0 - 3) to (τ_0 + 3) nsec and accepted a 1% random sample of such events by means of 1 MHZ oscillator to reduce the high rate of events in this gate.

The second gate called "The accidental gate", could accept pulses in a time of flight region which was inaccessible to physical particles from the interaction. Its timing, relative to the fast peak, was from -15 nsec to -5 nsec. Its purpose was to investigate the rate of accidental coincidences between neutron counter pulses and interaction triggers.

The event gate was opened 3 nsec after fast peak and extended to 40 nsec, it accepted all recoil particles of interest.

The three timing gates are shown diagramatically in Fig(3-13)

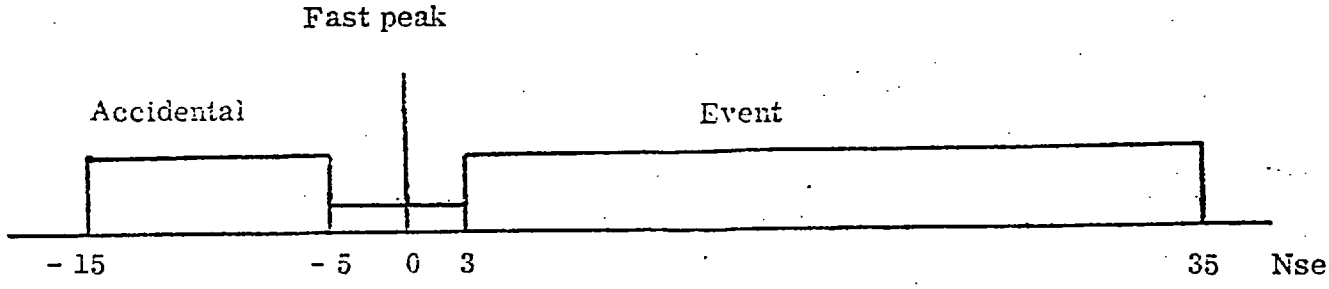

Timing gates .

Fig (3-13)

A pulse from a neutron counter that arrived during one of the three timing gates, together with an interaction trigger, formed an event trigger. For an event trigger two strobes, S_I, and S_N, were used to read the state of the all the neutron counters, A-counters, beam counters, hodoscope and wire chambers data into Camac scalers.

This information was then stored in the on-line computer.

S_I was in time with the beam counter B_3, and S_N, with the neutron counters.

The neutron counter pulse heights were also digitised and recorded, to enable a correction to be made in the off-line analysis as there was a dependence of the t.o.f. upon the pulse height.

(iv) Elastic Trigger; The scintillation counters D_1, and D_2, covered those drift chambers which were on one side of the hydrogen target, and D_3, and D_4, covered the drift chambers on the other side. A pulse either from D_1, or D_2 which coincided with a pulse from either D_3, or D_4, was used to define a pair of charged particles which passed through the drift chambers simultaneously. A further combination of such a coincidence and interaction trigger formed the drift chamber trigger.

Pulses from the D counters were timed with the gate from the drift chamber trigger and formed a coincidence, called the elastic trigger which was used to strobe all counters. The information from all the beam counters, hodoscope, wire chambers, the digitised drift time of the drift chambers and the digitised pulse heights from the D counters were read and then recorded using the on-line computer.

In order to record the beam momentum distribution a beam trigger was collected after every fifth event and named "Beam sample event".

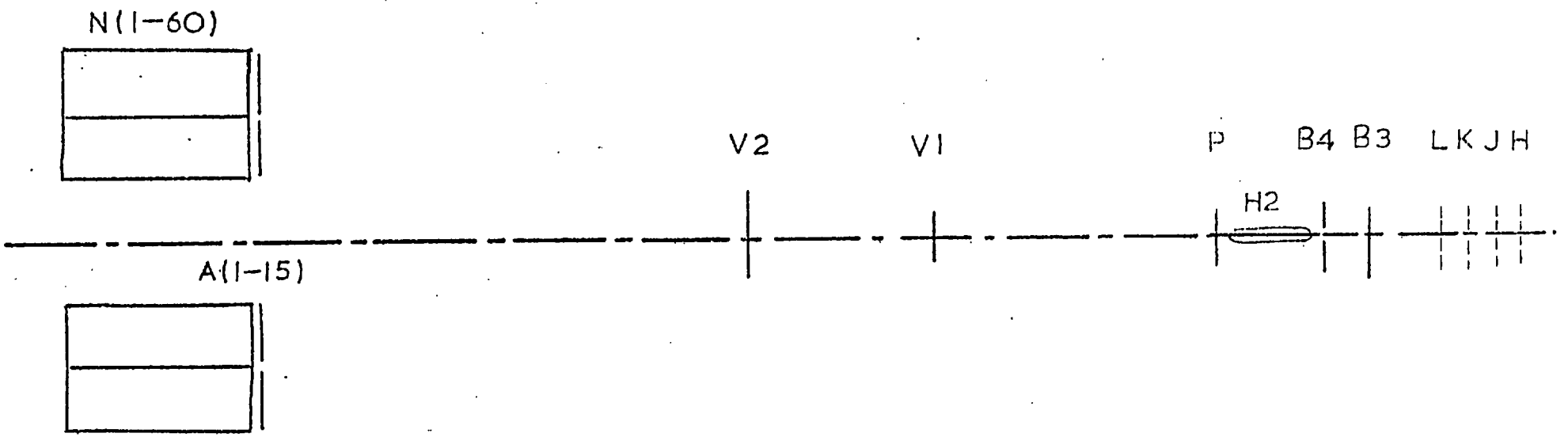

Plan of π 8A beam line .

Fig (3 - 1)

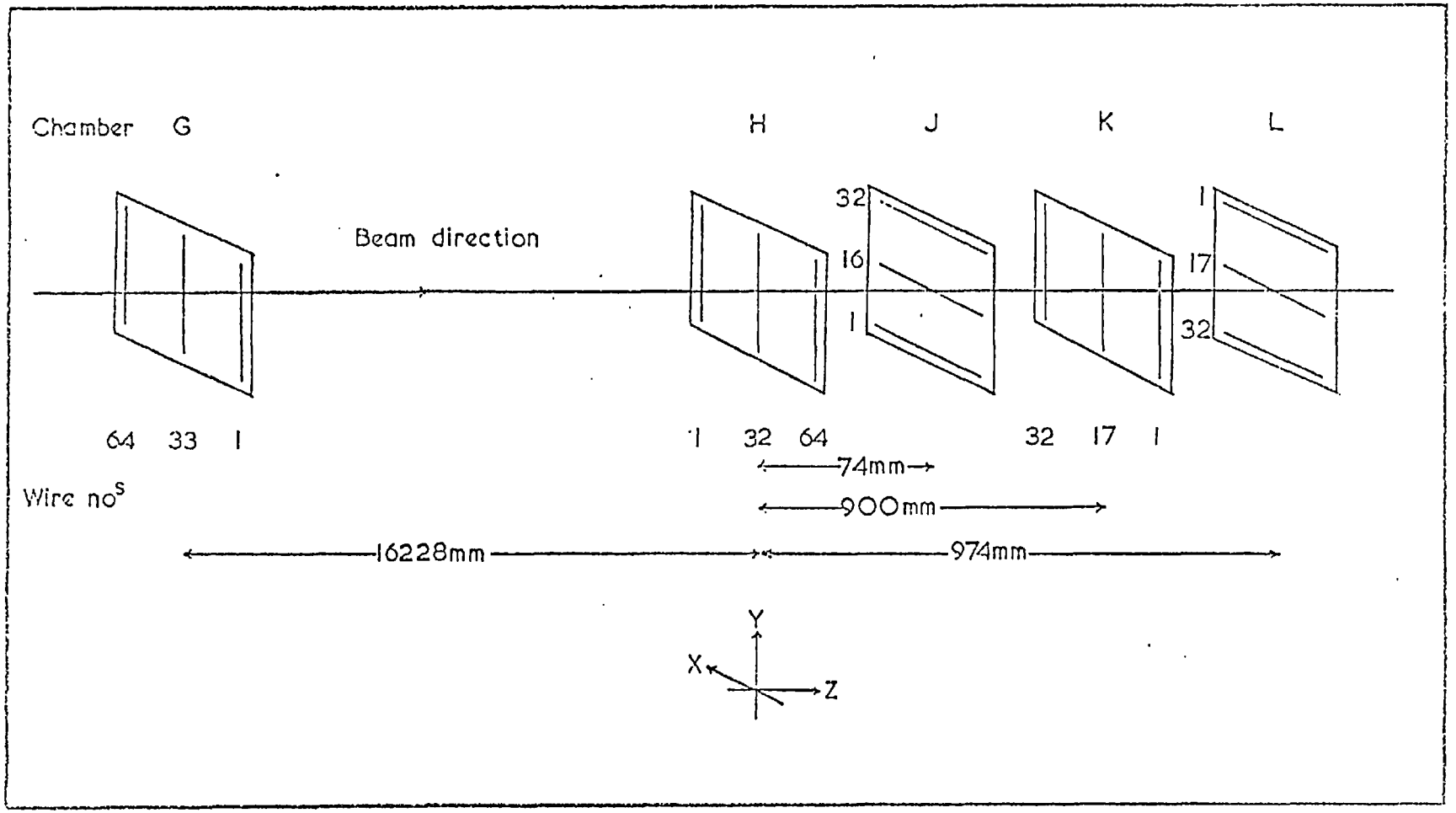

Arrangement of the wire chambers in the π8A beam line.

Fig(3-2)

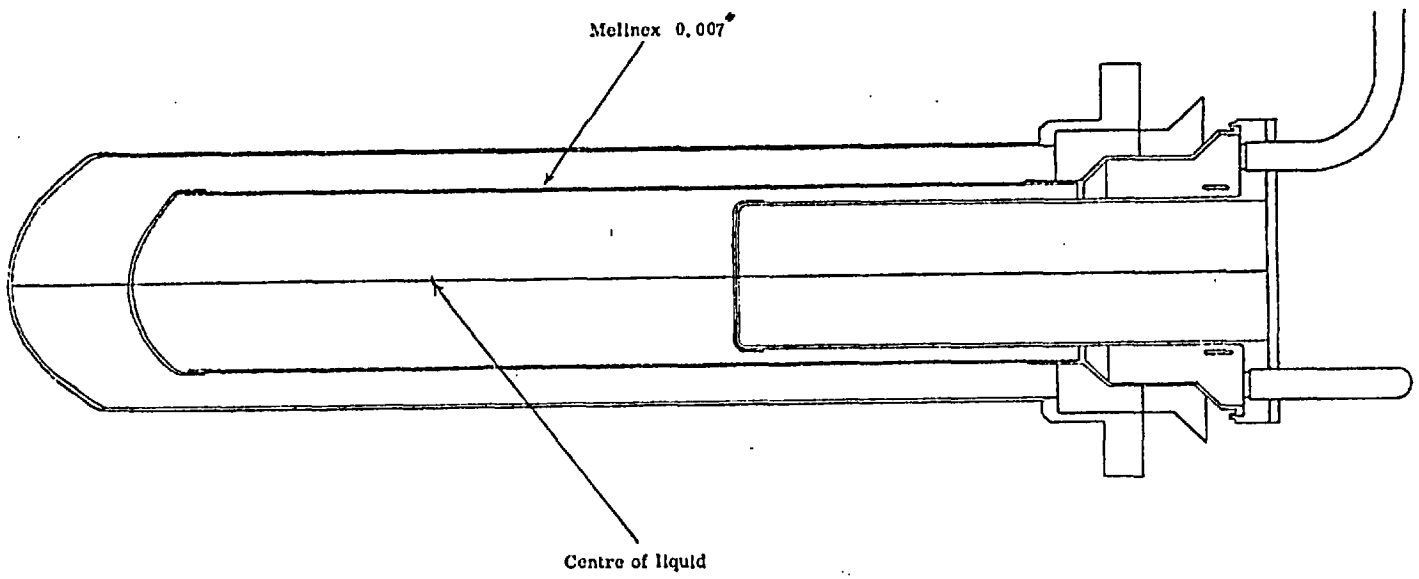

Liquid Hydrogen Target.

Fig (3 - 3)

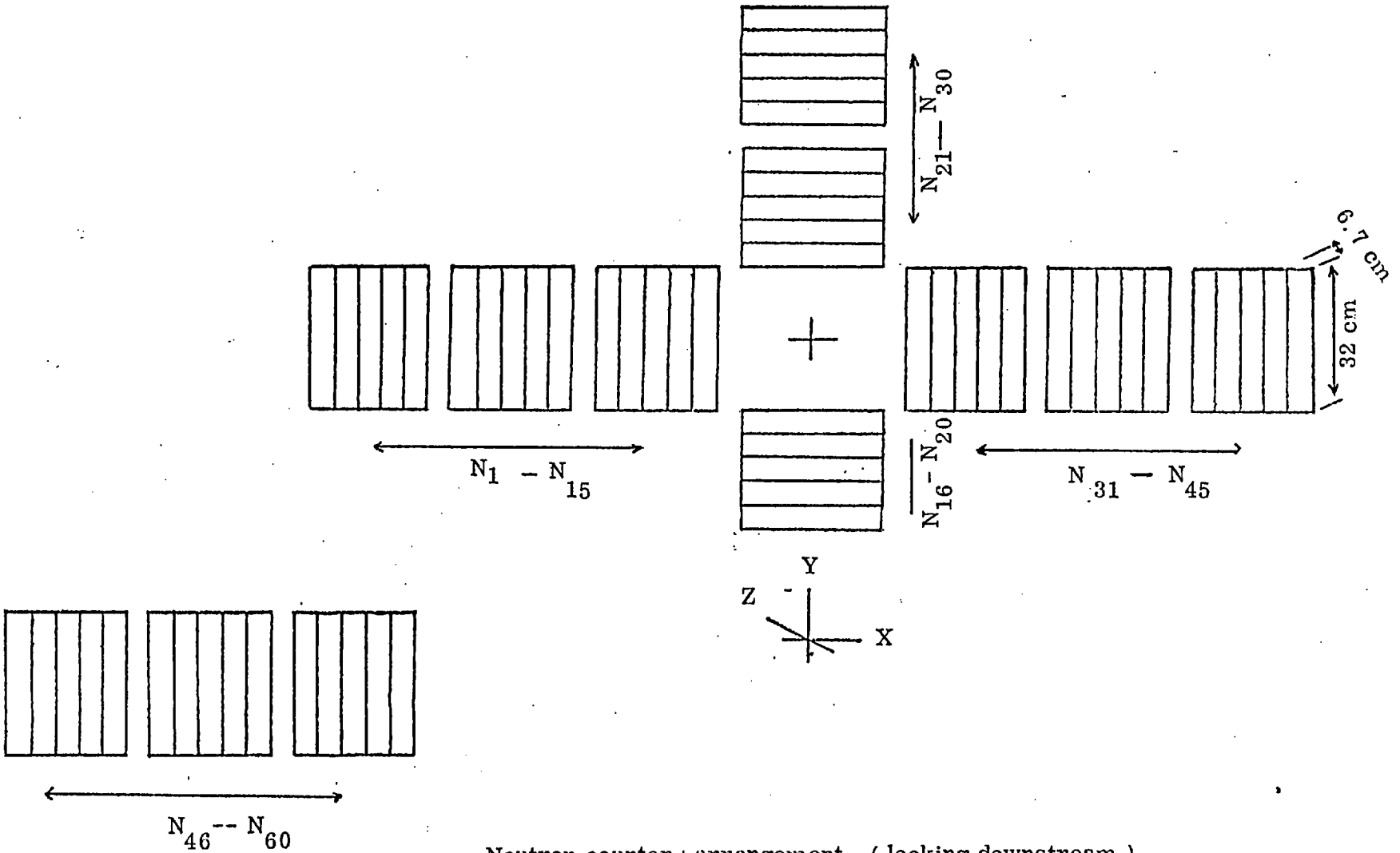

Neutron counter arrangement (looking downstream).

Fig (3 - 4)

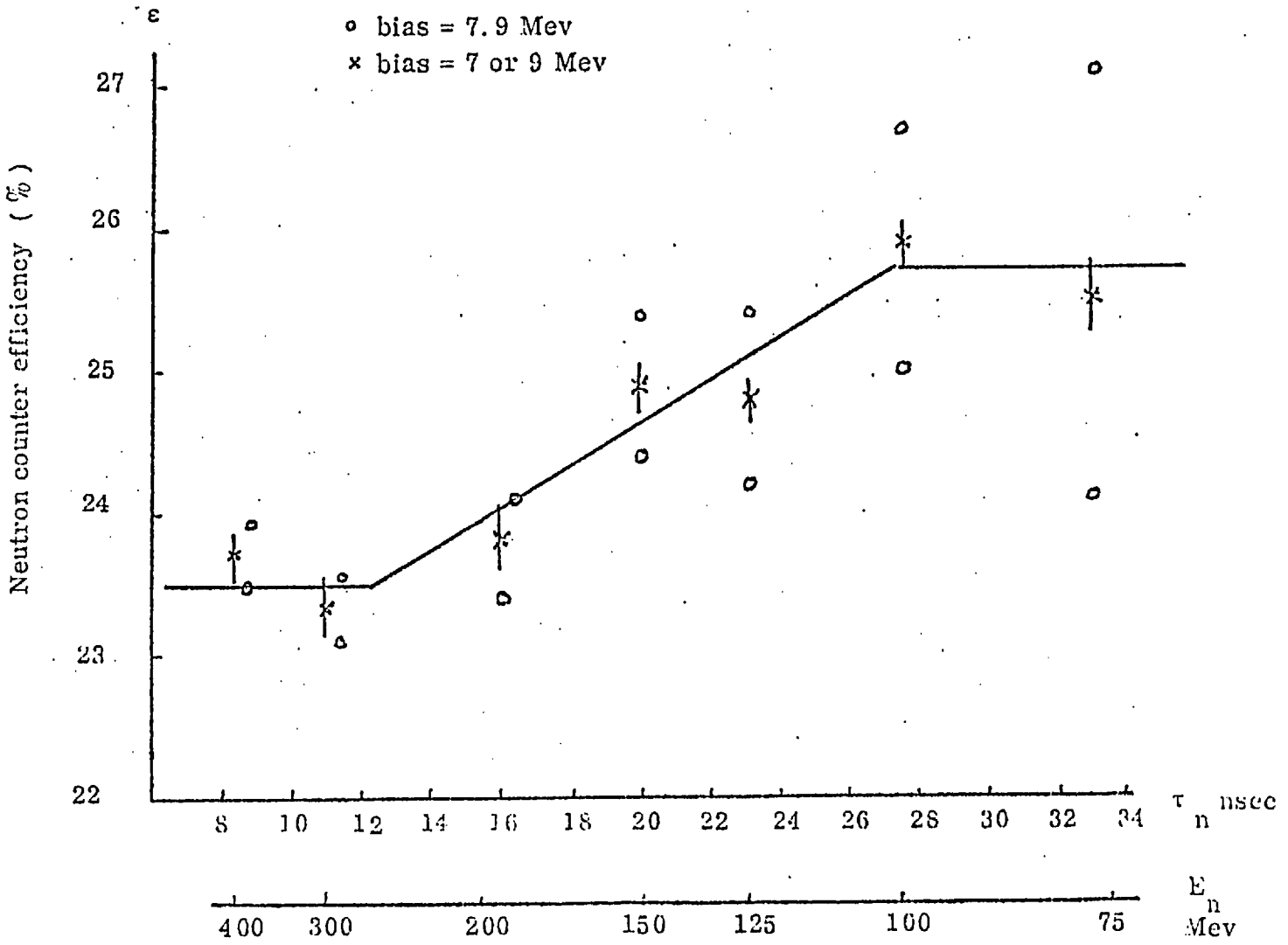

This plot is reproduced from the reference (15) .

Fig(3-5)

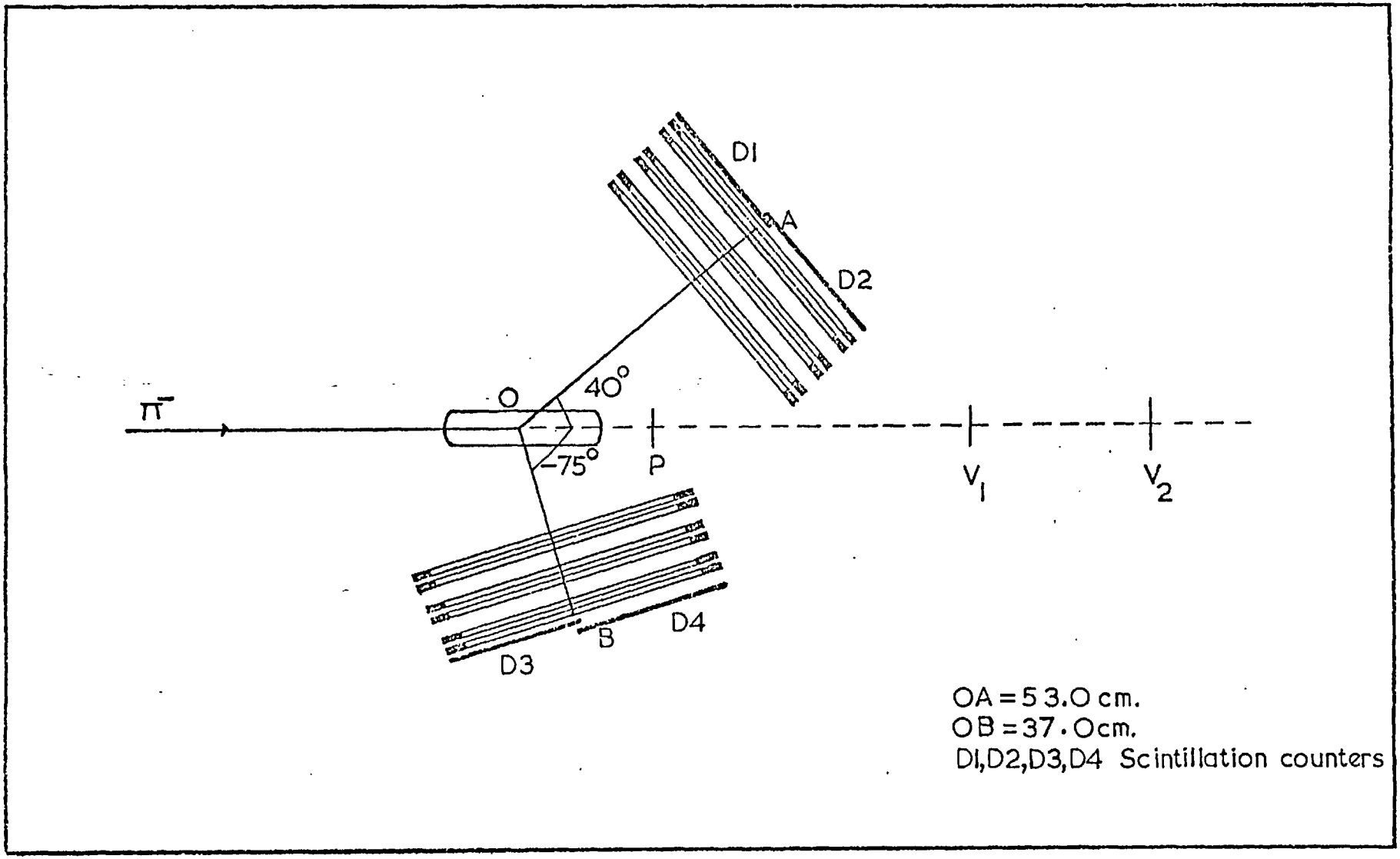

Schematic arrangement of drift chambers around the liquid hydrogen target (not to scale) .

Fig (3 - 6)

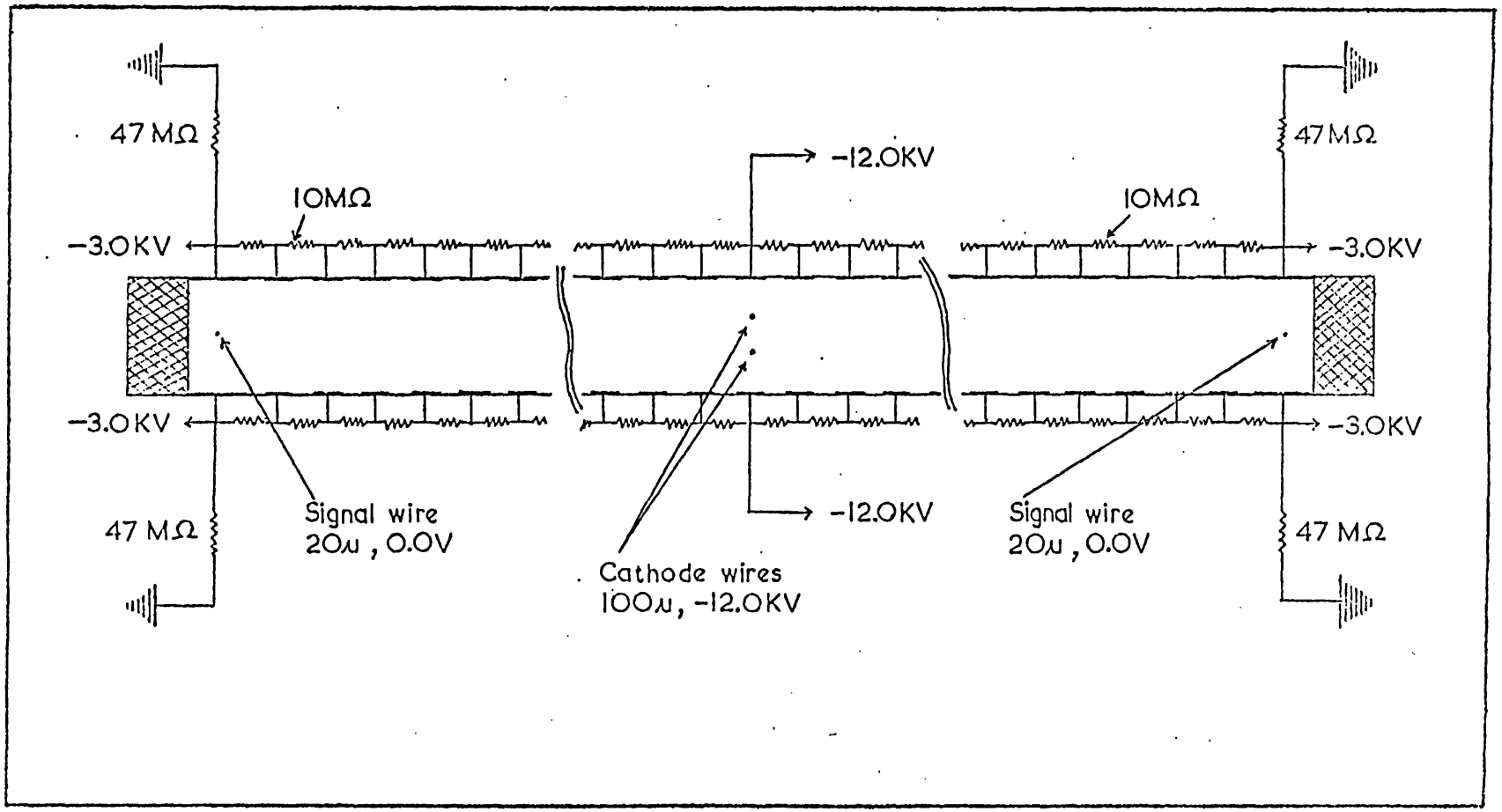

Schematic diagram of drift chamber .

Fig (3 - 8)

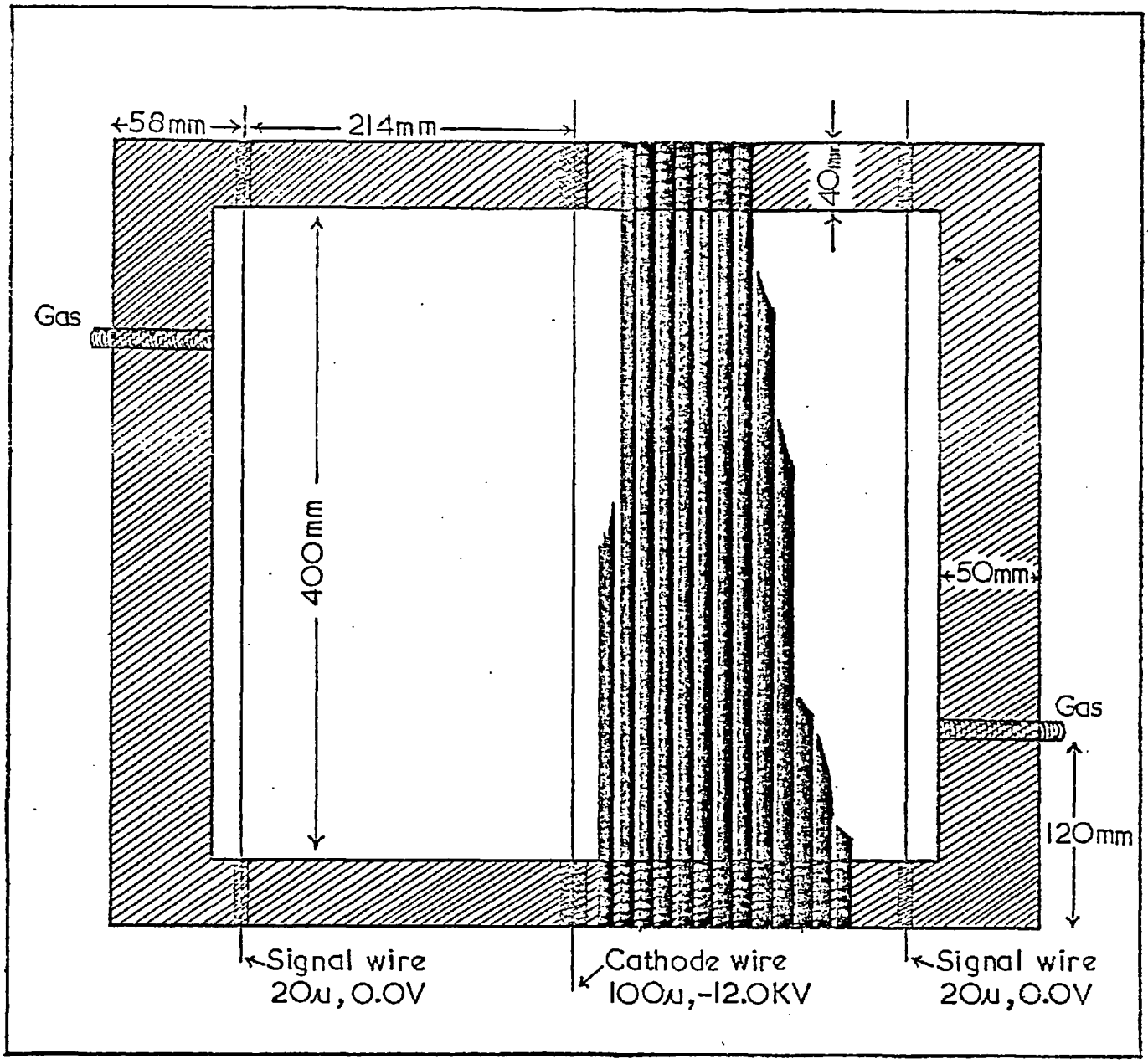

Fig (3 - 9)

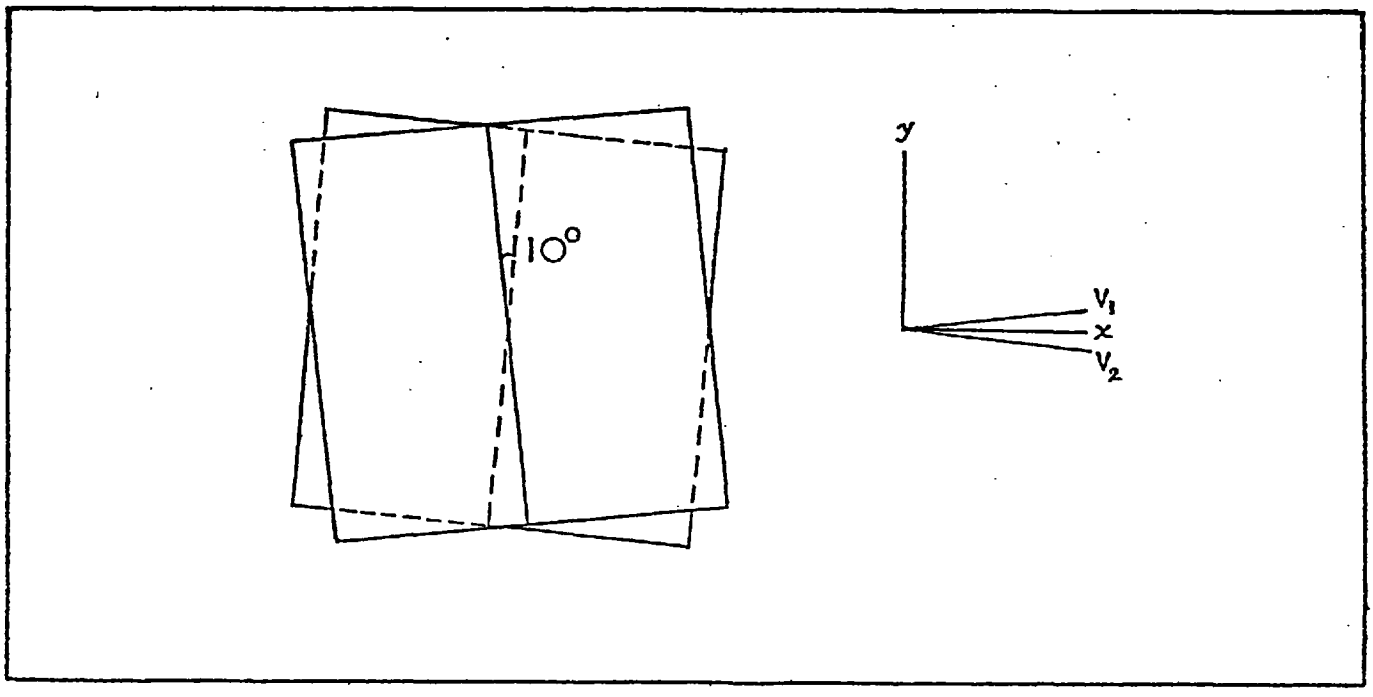

Fig (3 - 10)

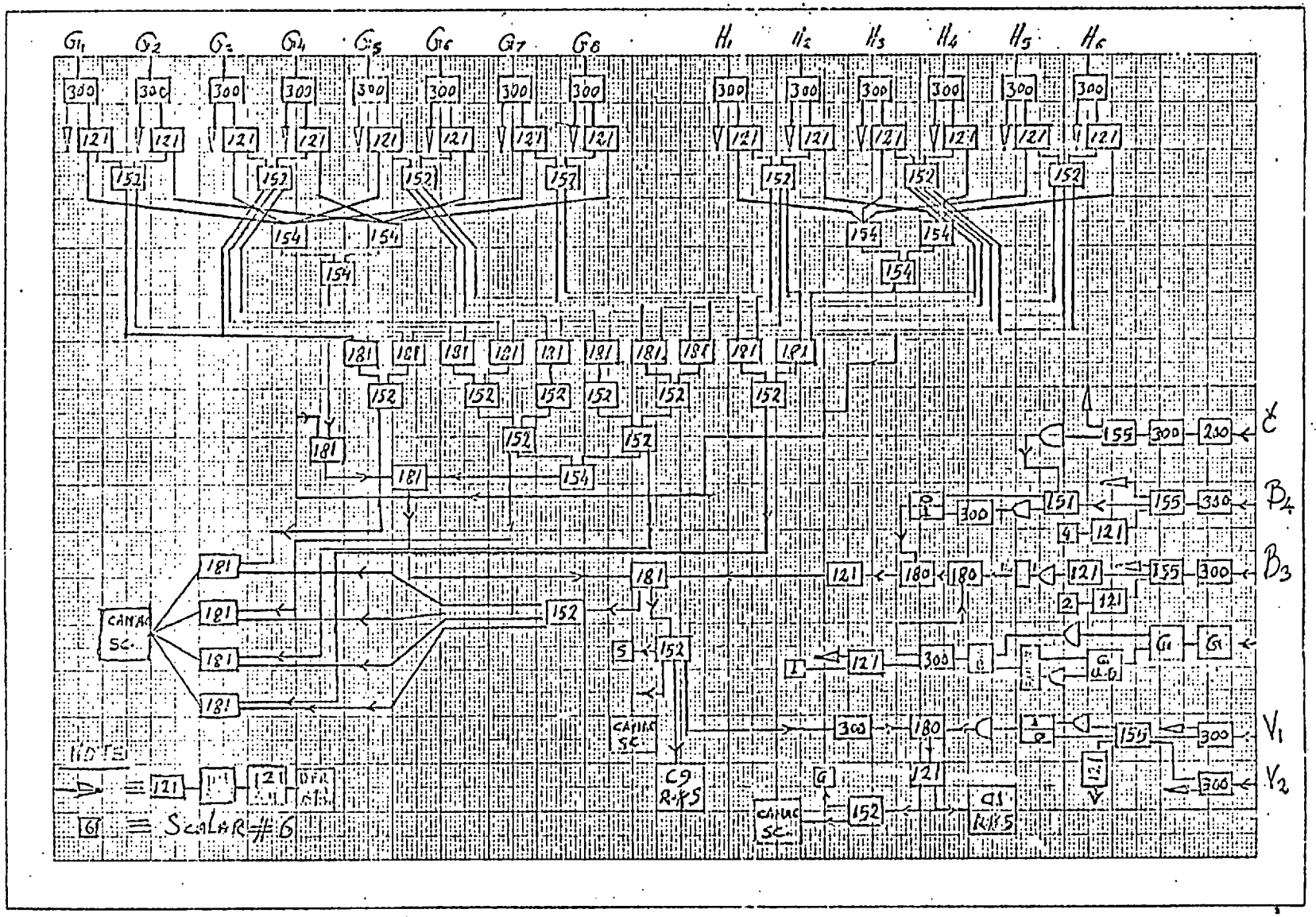

Diagram of logic system (first stage)

Fig (3 - 11)

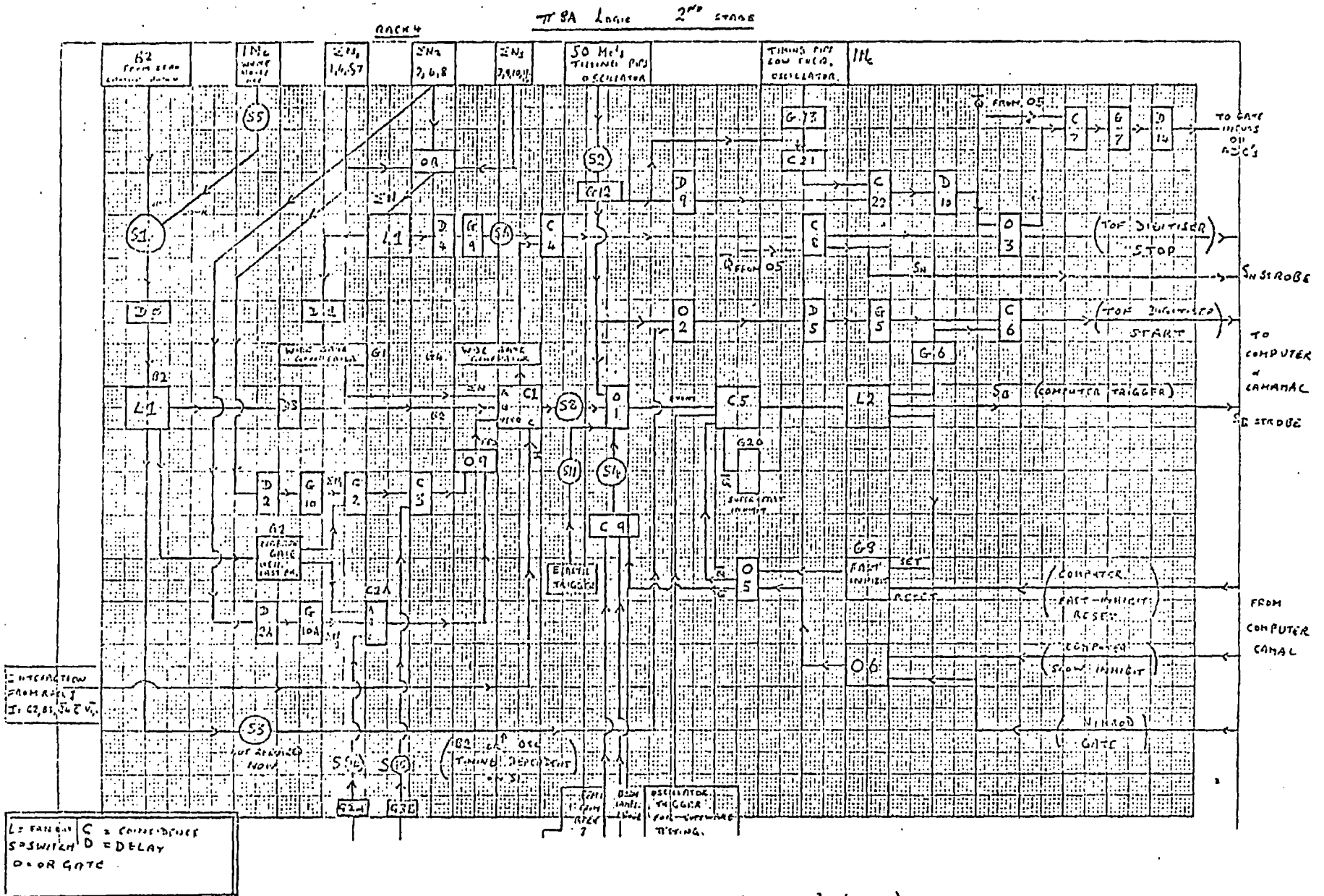

Diagram of logic system (second stage)

Fig (3 - 11)

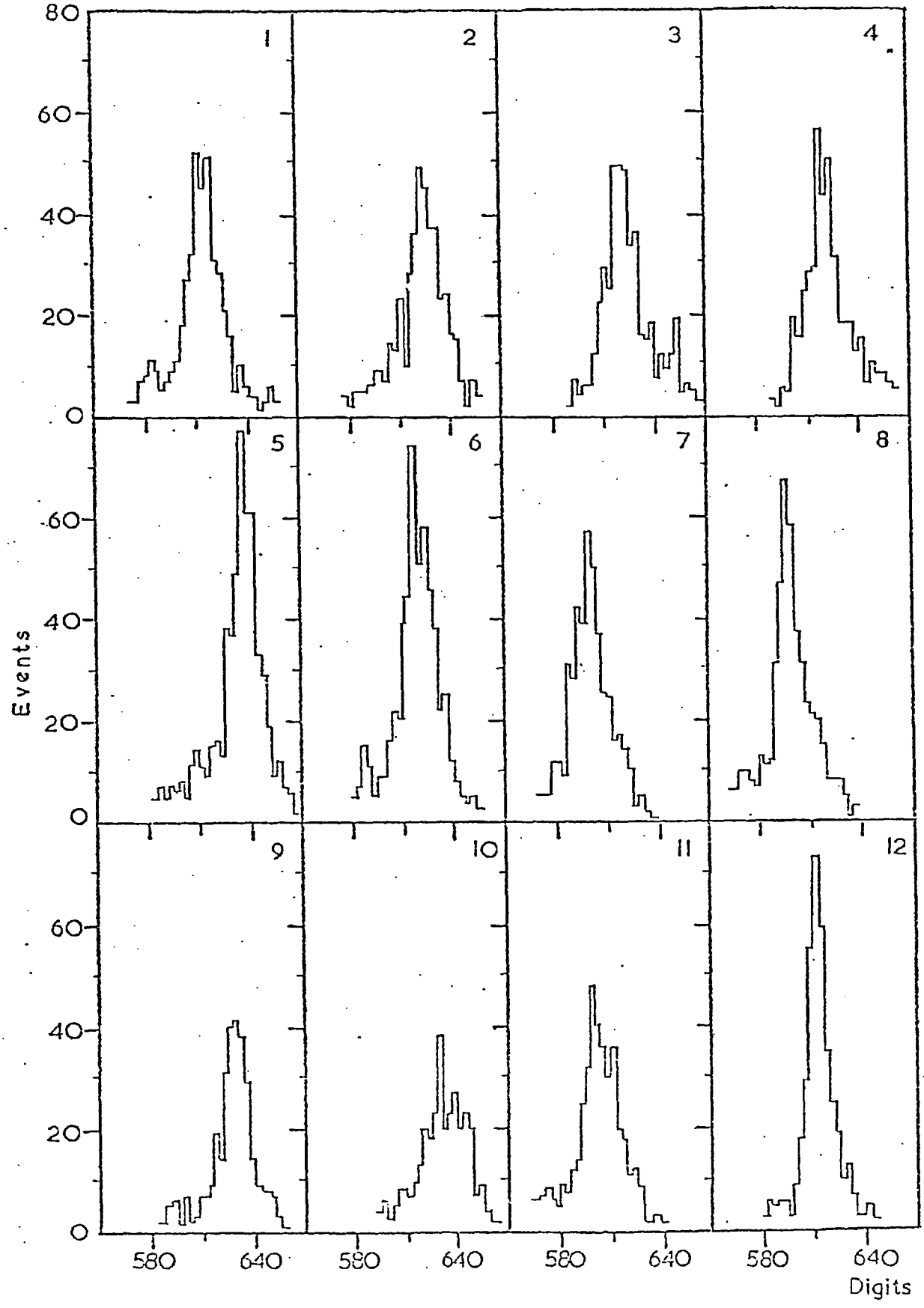

The distribution of events which triggered both sides of the signal wire .

Fig (3-12)

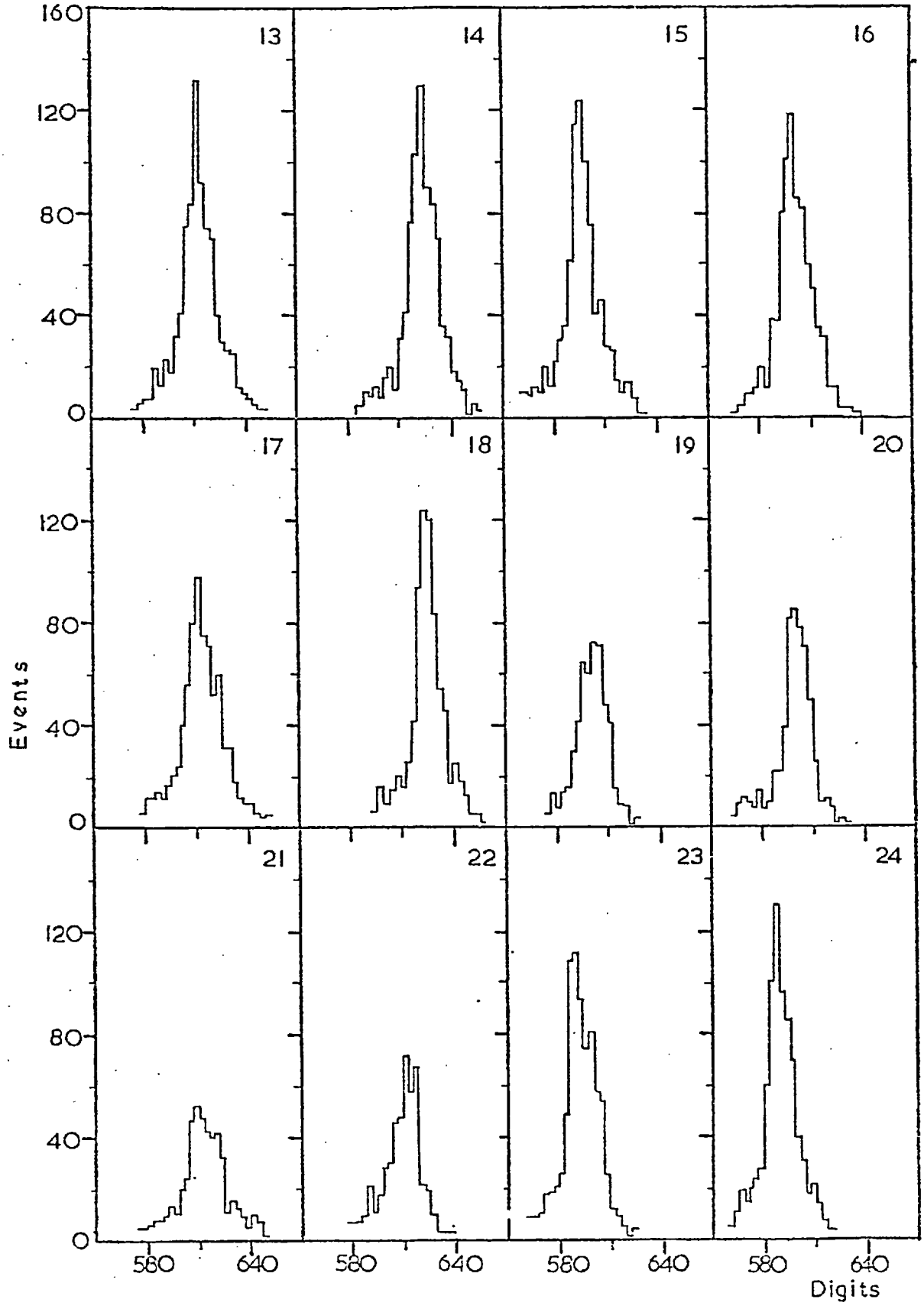

The distribution of events which triggered both side of the signal wire .

Fig (3-12)

4 PERFORMANCE

(4-1) Missing Mass Experiment-Timing and Resolution.

The quantities that were measured in the missing mass experiment were, incident pion momentum p_π, neutron scattering angle θ_n, and neutron time of flight τ_n, with uncertainties of Δp_π, $\Delta\theta_n$, and $\Delta\tau_n$, respectively.

(i) Δp_π; As has been mentioned the momentum scale was determined by floating wire measurements. The uncertainty in the measurement of the beam pion momentum, relative to the central momentum of the run, results from the uncertainty in the position of the pion in the wire chambers and also the effect of the uncertainty, ΔX, in the point of the interaction in the liquid hydrogen target. Taking the momentum spectrometer resolution to be 0.025% and the momentum loss, through ionization in the hydrogen, to be 0.25% Mev/c/cm, we have;

$$\Delta p_\pi = \{ (0.00025\ p_\pi)^2 + (0.25\ \Delta X)^2 \}^{1/2} \qquad (4\text{-}1)$$

Where p_π, is the central momentum of the run and ΔX, was taken as 10 cm (half the length of the target).

(ii) $\Delta\tau_n$; For each event a t.o.f. corresponding to the time a neutron took to travel between the beam counter B_3, and the neutron counters $N_{1\text{-}60}$, was measured and digitised. Each pulse from the neutron counters passed through a zero crossing discriminator to minimise the dependence of the time of flight upon the pulse height of neutron counters. The time of flight scale was approximately $\frac{1}{4}$ nsec per digit.

In the electronics, the reference time zero for each the different neutron counters were made equal to within ±0.1 nsec.

Fast peak events were sampled throughout data taking and the maximum of this distribution defined the time zero reference, τ_0 . The intrinsic timing resolution of the electronics was

measured from the widthof this distribution which was found to be about 0.5 nsec and was stable during data taking.

(iii) $\Delta\theta_n$: Knowing the position of the centre of the neutron counter for an event, the neutron scattering angle is given by;

$$\cos\theta_n = \left(\frac{Z^2}{X^2 + Y^2 + Z^2} \right)^{1/2} \qquad (4\text{-}2)$$

Where X, Y, and Z, are the coordinates of the centre of the neutron counter with respect to the centre of hydrogen target. Then for the angular resolution one has;

$$\Delta\theta_n = 1/d^2 \cdot \{ (\cot\theta_n \cdot X \cdot \Delta X)^2 + (\cot\theta_n \cdot Y \cdot \Delta Y)^2 + (\tan\theta_n \cdot Z \cdot \Delta Z)^2 \}^{1/2} \qquad (4\text{-}3)$$

Where $\Delta X, \Delta Y, \Delta Z$ are the uncertainties in the measurement of X,Y, and Z respectively and d, is the distance from the centre of neutron counter to the centre of the liquid hydrogen target, and is $(X^2 + Y^2 + Z^2)^{1/2}$

From the above measured quantities the missing mass of the ω meson M_3, the final state momentum in CMS,p^*, and the CMS angle of the ω meson θ^*_ω, were calculated.

The uncertainty in the determination of the ω mass is given by Eq(2-8). Fig(4-1) shows the behaviour of the missing mass resolution as a function of the time of flight of the neutron for different incident momenta at different angles. The variation of Δp^*, as a function of p^* is shown in Fig(4-2).

(4-2) The Resolution Of The Elastic Scattering Experiment.

The accuracy of the measurement of the scattered particle tracks depends on the accuracy of the determination of the drift velocity in the drift chambers. The uncertainty in the determination of the position resulting from the error in the drift velocity measurement was about 0.37 mm which resulted in a maximum of 2° uncertainty in the measurement of the CMS scattering angle, θ^{*}.

The uncertainty in the incident pion momentum was improved by determining the point of the interaction in the liquid hydrogen target and this resolution was better than 0.3 Mev/c.

(4-3) Data Collection.

The experiment were performed in the π8A beam line of the Rutherford laboratory during 1974.

In the missing mass experiment there were, on average, about 150K beam triggers with approximately 40 events per burst and in the elastic scattering experiment, the beam triggers were about 80K per burst with about 90 events read in to the computer.

Data was transfered into the DDP-516 computer after each burst. After a number of bursts, when 216 (or nearly 216) events had been recorded, the data in a set of blocks was written on to a 7-track magnetic tape.

At the end of each burst the DDP-516 performed an on-line preliminary analysis of this set of blocks in order to investigate the behaviour of the experiment.

A full tape held approximately 11000 blocks for the missing mass experiment and about 7600 blocks for the elastic scattering experiment.

The data contained on a full tape is called a "Run", and a run contained approximately 200 million and 50 million beam triggers for the

first and second experiment respectively.

Each run was characterised by its central momentum and covered a range of 4 momentum bins corresponding to the different G, and H, hodoscope combinations.

The momentum spread for each run was about 1% of its central momentum (f.w.h.h. of 11 Mev/c at 1.1 Gev/c, the threshold of ω production).

The data covered a range of momentum from 1.000 Gev/c to 1.256 Gev/c, where the central momenta of two consecutive runs were separated by 0.7% (i.e.,≈7 Mev/c). In the first experiment data was more concentrated aroundthe ω threshold, while in the second an equal number of runs were taken at each central momenta over the above range of momentum. The distribution of the total number of incident pions that were accumulated for both experiments are shown in Fig(4-3), and Fig(4-4).

Before each run commenced, the currents in the spectrometer magnets were set to the proper values corresponding to the central momentum of the run, determined by the floating wire measurements. The magnetic fields of M201, and M202 were accurately adjusted using a nuclear magnetic resonance (NMR) method. The stability of the fields was checked by monitoring the position of the signals from the NMR probes throughout the data taking period. The stability of M201, and M202, was better than 1 part in 10^4.

The currents in the quadrupoles Q113, and Q422, were set at the values which had been found by optimising the beam intensity at a series of momenta and then interpolating. The currents were always cycled towards the final values in order to remove a hysteresis effect. The current in the M213, was adjusted so as to make the beam particles symetrically distributed about the beam axis.

At the end of each run, the run summary was checked in the

on-line analysis for signs of malfunctions of the wire chambers, drift chambers, or electronics. The run summary contained histograms of various distributions, such as the neutron t.o.f., pulse height spectra, distribution of the number wires firing in each chamber and values of beam scalers.

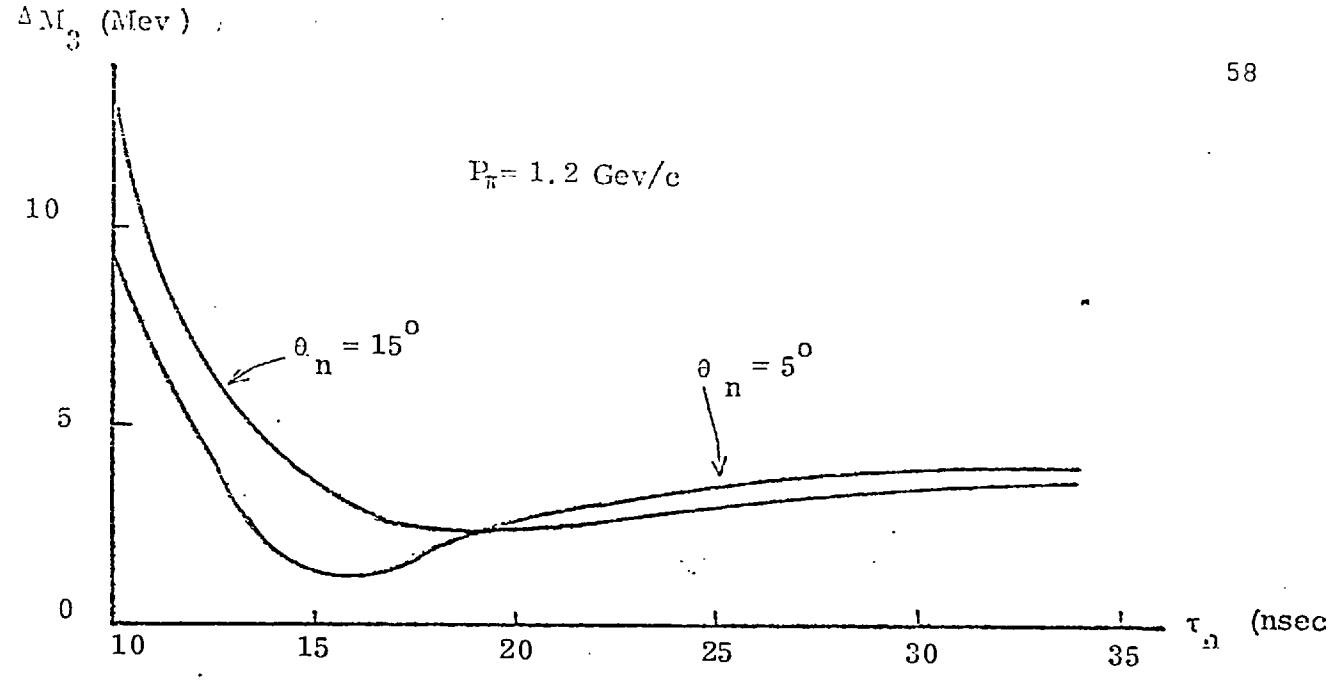

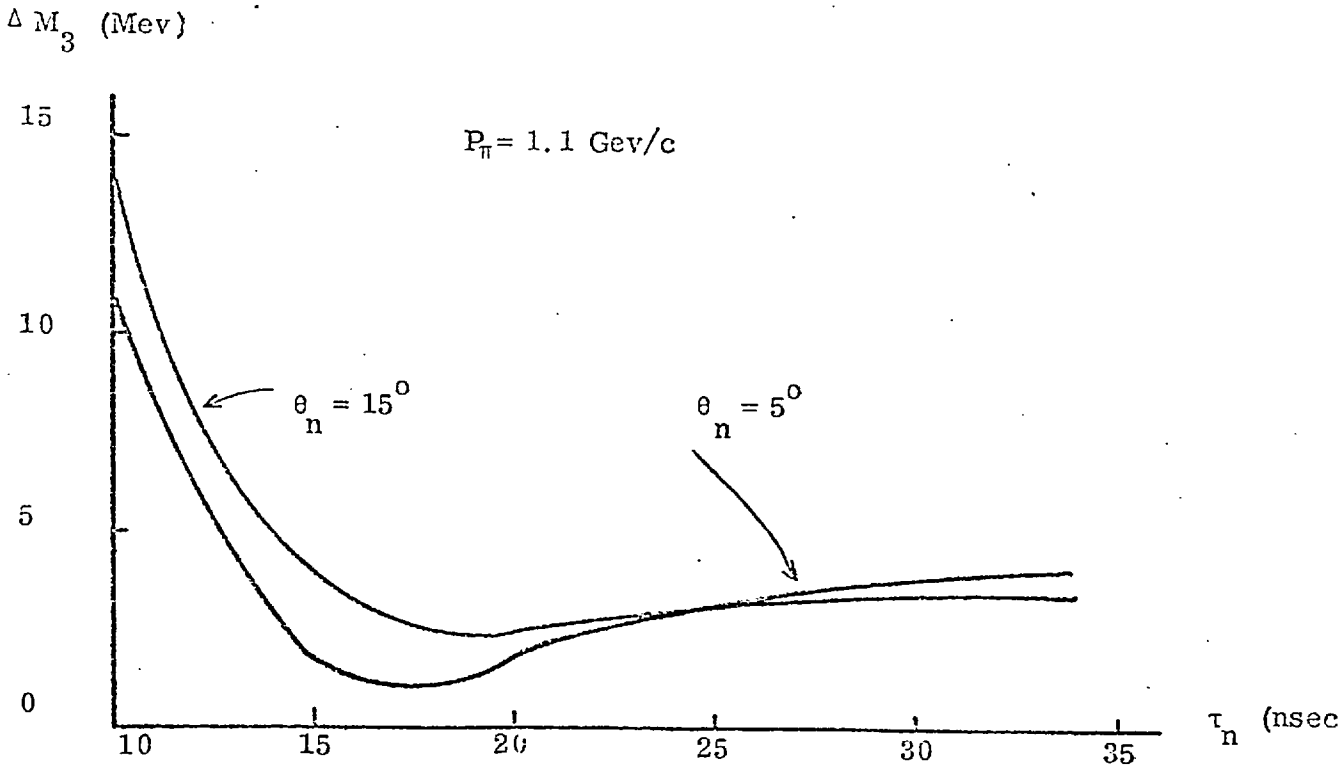

Missing mass resolution as a function of the neutron time of flight.

Fig(4-1)

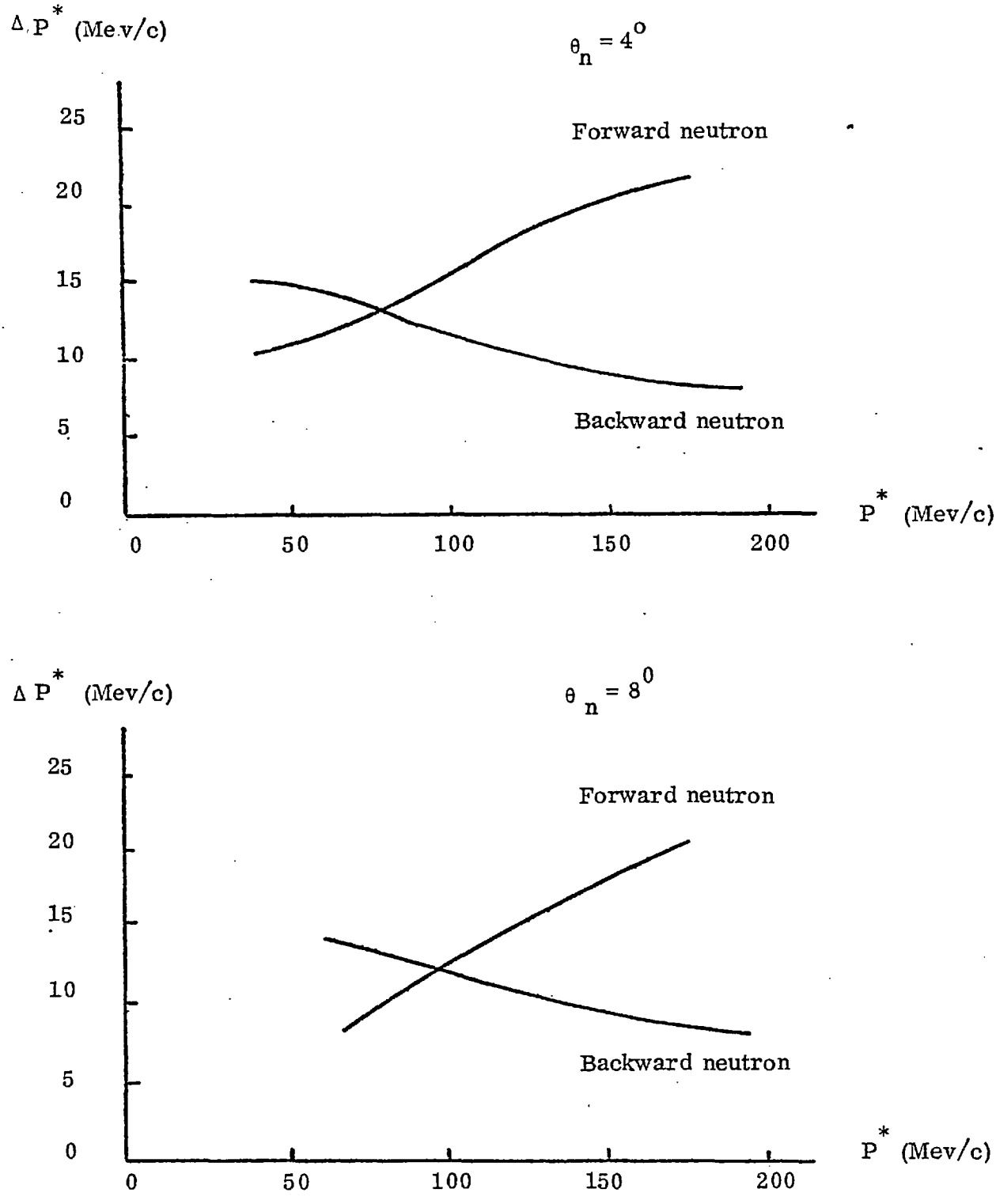

CMS momentum resolution of the ω meson as a function of P^* at different laboratory angles .

Fig (4 - 2)

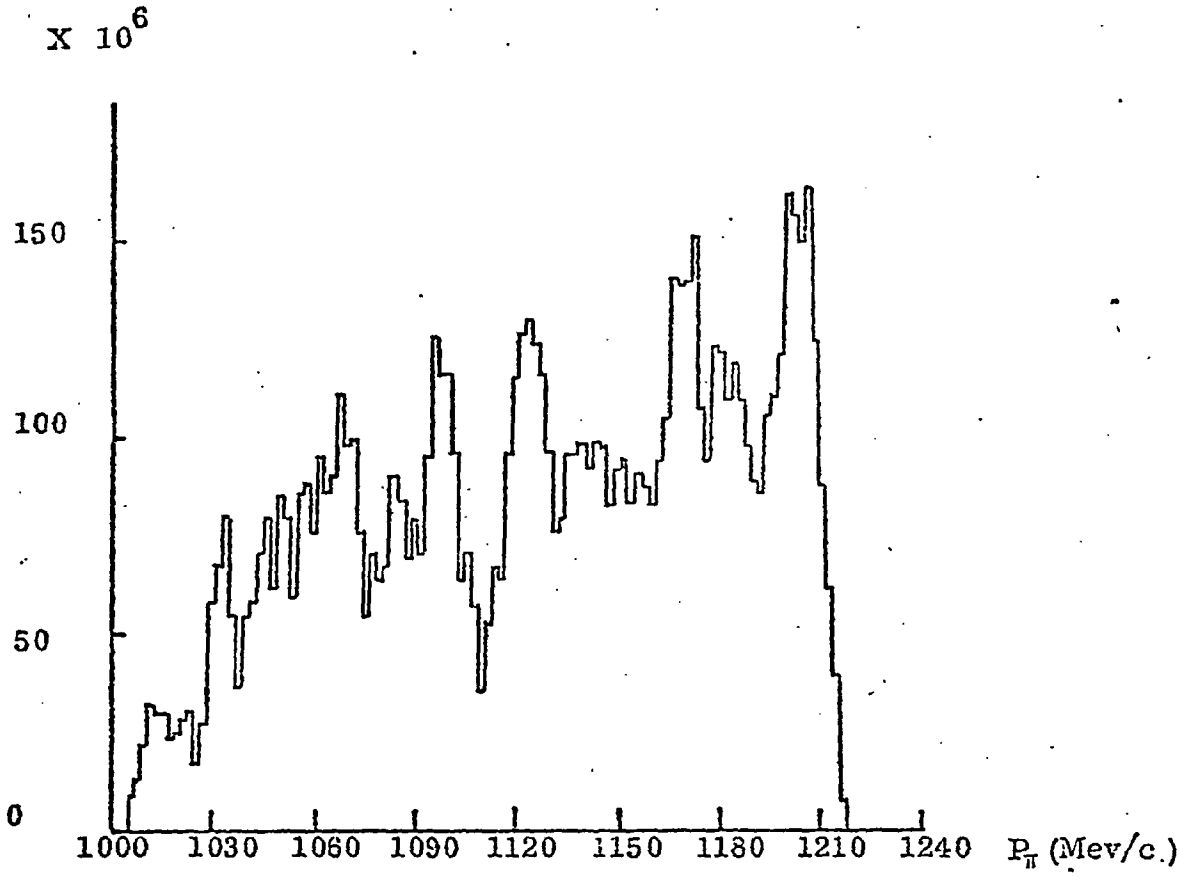

Total number of incident pions in 2 Mev/c bins for the ω production experiment.

Fig(4-3)

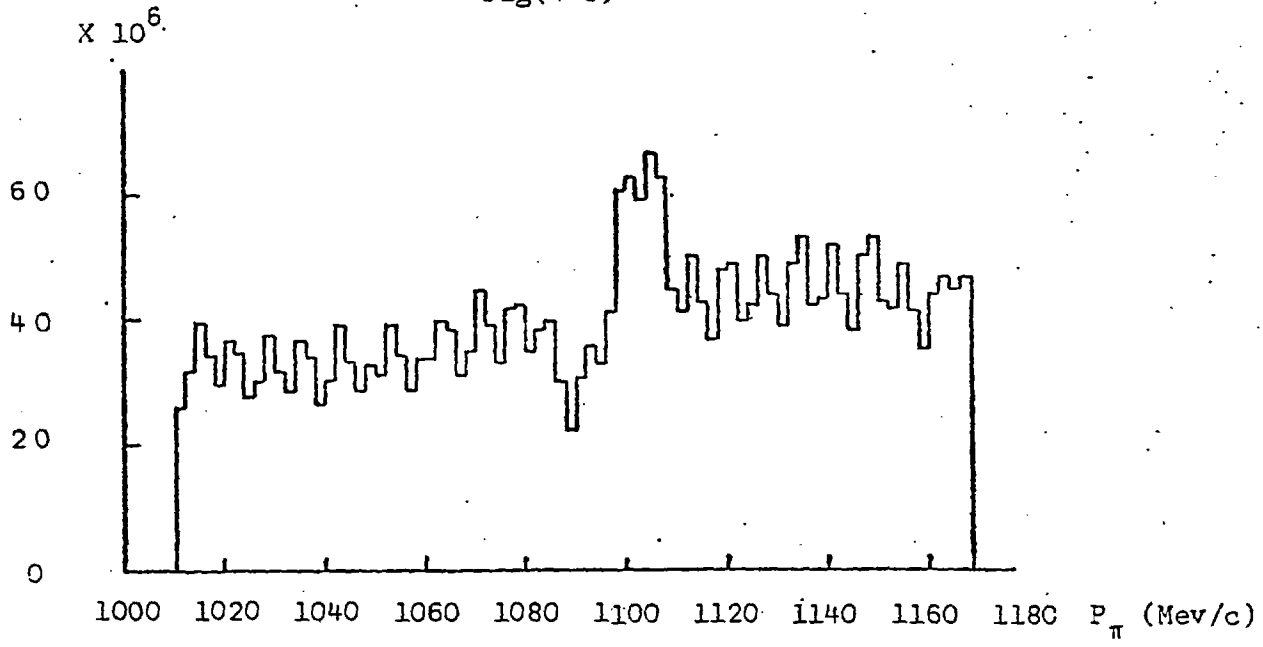

Total number of incident pions in 2 Mev/c bins for the $\pi^- p$ elastic scattering experiment.

Fig(4-4)

5 DATA ANALYSIS

This chapter describes the off-line analysis of data for each of the two experiments. The description follows the chronological order in which the work was carried out.

(5-1) Data Enriching.

The raw data was written on 7-track tapes as a set of blocks. These were copied directly on to 9-track tapes each of which could contain the data from 4 7-track tapes.

A block contained 18 events and a number of these were self-contained i.e., they contained all the information for each event, beam sample events and various scalers which enabled a normalisation to the number of incoming beam particles to be made.

In the missing mass experiment unwanted events were rejected such as those falling in to the following categories;

(i) Proton events;

(ii) Neutron events possessing a time of flight values out of the range of interest i.e., $\tau_n < 3$ nsec or $\tau_n > 40$ nsec;

(iii) Beam sample events.

All the remaining events were arranged in a set of new blocks and written on to a tape called "The enriched tape". The information which was required for normalisation such as, total number of beam triggers, the momentum distribution of the beam sample events, and the percentage of events which were rejected together with the fast peak position for each neutron counter, were written separately on to a disk to be used at the normalisation stage.

In the elastic scattering experiment, beam sample events and

ambiguous events, such as those where more than one or two adjacent wires in the chambers had triggered, were not copied on to the enriched tape. The information required for normalisation, as mentioned for the first experiment, together with the drift velocities of the drift chambers needed for track reconstruction of the scattered events in the analysis stage, were calculated and recorded on to a separate disk.

(5-2) The Method Of Analysis Used In The Missing Mass Experiment.

(5-2-1) Time Of Flight Measurement.

In the missing mass experiment the time of flight measurements in the 60 neutron counters were corrected to bring them into agreement. The required corrections were determined from data collected in a special run. For this run a 100 mm thickness lead was placed in the beam. Beam pions were scattered into the neutron counters, and were accepted by the fast timing gate. Correction were found and applied in the off-line analysis.

As has been mentioned there was some time of flight dependence upon neutron counter pulse height. This was investigated by studying at a time of flight-pulse height scatter plot. A correction rule was found which was applied in the off-line analysis programme.

The position of the fast peak, which defined time zero τ_0, was measured for each neutron counter and for each individual run. Fig(5-1) shows for a single neutron counter the variation of the central position of the fast peak for each run as a function of the central momentum of the run. At each central momentum the positions were distributed within standard deviation of ±0.15 nsec. The width of the peak is a measurement of the experimental timing resolution and was about 0.5 nsec at full width half height.

A 50 MHZ crystal oscillator was used to calibrate the scale of the time of flight digitizer by a method descrined in Ref(17). This calibration was repeated several times during the experiment. The time of flight scale was found to be 0.256 nsec per digit. A very slight departure from linearity was observed and a correction rule was found which was applied in the analysis.

The following corrections, therefore, to the digitised raw time of flight for each event were applied;

(i) A correction for individual neutron counter timing;

(ii) A correction for time of flight pulse height dependence;

(iii) A conversion of the digitised time of flight to a nsec scale, and a slight correction for a non-linearity in the the scale;

(iv) A subtraction of the time of flight of the fast peak.

(5-2-2) Neutron Selection.

Neutron events were classified into two classes. The first class satisfying the following requirements;

(i) A single neutron counter or two adjacent neutron counters having fired;

(ii) No A-counter fired;

(iii) No signal from the P-counter;

(iv) One wire or two adjacent wires fired in each of the wire chambers.

Events which failed on any of the above conditions were put in to the second class and called "Ambiguous events".

Ambiguous events contained 8% of the total events. The source of the ambiguous events could have been noise in the neutron counters, A-counters, P-counters, a neutral particle produced from an interaction of one of the scattered particles with an air molecule as it travelled from the liquid hydrogen target to the neutron counters or noise in the wire chambers.

(5-2-3) Missing Mass Spectra.

In this experiment all the information is contained in missing mass spectra as has already been mentioned, and the resonance properties can be directly extracted by fitting a resonance signal plus a smoothly varying background.

For each unambiguous event, the missing mass M_3, the final state CMS momentum p^*, and CMS angle of missing mass θ^*, were calculated and, together with the incident momentum p_π, all were binned and stored in a 4-dimension array. Such an array for each run was written on to a data summary tape (D.S.T.).

The number of events within a missing mass interval normalised to a certain number of incident beam pions for each beam momentum bin, when plotted as a function of missing mass, is called "The missing mass spectrum".

Normalised missing mass spectra were obtained by combining runs on the D.S.T. in conjunction with information placed on the disk at the enriching stage such as the total number of beam triggers, beam sample momentum distribution, and efficiency factors. Fig(5-2) shows the missing mass spectra normalised to 100 million beam pions, for all events and for various p^* and θ^* intervals.

(5-2-4) Monte-Carlo Simulation.

In order to extract various properties of the ω meson production from the missing mass spectra, a computer simulation of the experiment was written which incorporated the behaviour of the neutron counters.

Since the aims of the experiment were to study the Cross-section behaviour and the angular distribution of the ω production at low p^*, the following assumptions were made in the Monte-Carlo programme.

(i) The Cross-section rises linearly with p^*;

(ii) The ω meson is produced isotropically in the CMS;

(iii) The ω mass distribution was taken to be a simple non-relativistic Briet-Wigner of the form;

$$\frac{\Gamma^2/4}{(M_3 - M_o)^2 + \Gamma^2/4} \qquad (5\text{-}1)$$

Where Γ, f.w.h.h. and M_o, the central mass of the ω meson were taken to be 10 Mev/c^2, and 782 Mec/c^2 respectively.

(iv) The beam momentum was simulated in the programme by a triangular distribution with f.w.h.h. of 11 Mev/c [15].

The beam pion lost 1.8 Mev/c by ionization in the beam scintillation counters before entering the liquid hydrogen target. The energy loss in the hydrogen target was calculated for a random point of interaction along the length of the hydrogen target and was given a Landau fluctuation.

The neutron counter efficiency was taken to be 25% independent of the time of flight of the neutron.

For each event generated having the above properties, the neutron laboratory angle was calculated and ,if it was incident upon a neutron counter,the t.o.f. was calculated. Neutrons were assumed to interact in a a random point inside the neutron counters and light from this point, travelling at a velocity of 0.67c, reached the back face. The neutron time of flight was defined with respect to the time of flight of beam pions to the neutron counters as this difference was measured accurately in the experiment.

The time of flight error was given a gaussian distribution with a standard deviation of 0.6 nsec (experimental timing resolution).

A Monte-Carlo D.S.T. from the computer simulation programme, in the same format as the data D.S.T.,was produced. By analysing this simulated data in the same manner as the experimental data, the resonance properties could be extracted.

Since neutrons and protons triggered the neutron counter by a different mechanism a check was made on the time zero position, τ_0. This was done by studying the position of the ω signal in the region where $dM_3/D\tau_n$ was most sensitive.

The Monte-Carlo was run with different time zero shifts, $\Delta\tau_o$ (i.e., $\tau_n' = \tau_n + \Delta\tau_o$) and compared with the data, Fig(5-3) shows the variation of the peak position of the ω meson as function of the neutron time of flight shift for angular region $-1<\cos\theta^*<-0.8$. The dashed lines represent the experimental values. As a result of this comparision a value of $\Delta\tau_0$ = 0.1 nsec were used in all subsequent Monte-Carlo runs.

(5-3) Analysis Of The Elastic Scattering Data.

(3-3-1) Event Track Reconstruction.

To analyse events from the enriched tapes, the drift velocity information, which was written on a disk, was used to calculate the co-ordinates of the scattered pion and proton tracks for each event. A least squares fitting programme was used to obtain the bestfitted line for the three pairs of points forming each track. This fit was carried out in the XZ, and XY, planes independently. An extrapolation of the two fitted tracks in to the liquid hydrogen target determined the point of interaction in the target.

A distinction between π and p tracks was made by kinematic constraints as mentioned in chapter (2-2) and the problem of distinction in the ambiguity region was resolved using the pulse height distribution in the D counters. Fig(5-4) shows the corresponding pulse height distribution.

(5-3-2) Event Selection.

In selecting elastically scattered events the following requirements were imposed;

(i) At least two modules on each side must be triggered by each event. 11% of the events failed by this test;

(ii) For each event the r.m.s. deviation of the data from the two fitted tracks were calculated. Fig(5-5) shows this distribution for both sides for a typical run.
The standard deviation for side 1 and side 2 are σ_1 = 2 mm and σ_2 = 1.5 mm respectively. Events with more than a 3 cm deviation were rejected. The fraction of events failed was 12%.

(iii) The difference of the intersection of the horizontal projection of each track with the incident beam direction was calculated. Fig(5-6) illustrates this distribution which has a r.m.s. deviation of 5 mm. Applying a 3-cm cut, 13% of the events failed to satisfy this condition;

(iv) The point of interaction in the liquid hydrogen target was taken as the average value of the two intersecting points of the horizontal projection of the each track with the incident beam direction, and the event was rejected if it lay outside the hydrogen target. 9% of the events were of this type, Fig(5-9) shows this distribution.

(v) The angle between the projection of the two tracks in the XY plane was measured and distribution is shown in Fig(5-7), where the angular resolution was about 4°. Any event having an accoplanarity of more than 10° was rejected, and this resulted in an 11% failure rate;

(vi) The CMS scattering angle for each scattered particle, θ^*_π, and θ^*_p, were independently calculated. Fig(5-8) shows the distribution of the difference of these angles, i.e., $(\theta^*_\pi - \theta^*_p)$. The CMS angular resolution was about 2°. Events with a difference of more than 10° were rejected and the rate of failure was again about 11%.

Each event which satisfied the above tests was classified as a good event and for each such event, the incident momentum p_π, the average CMS scattering angle θ^*, and the average point of interaction in the liquid hydrogen target were recorded in a 3-dimension array. For each run such an

array was written on to a D.S.T.

A Monte-Carlo simulation programme was written to calculate the acceptanceof the drift chambers for different regions of CMS angle. The acceptance that was found hardly changed with the momentum range of this experiment, (from 1.020 Gev/c to 1.180 Gev/c). The acceptance calculated for p_π = 1.1 Gev/c was the one used throughout the range of momentum.

The acceptance for a CMS angular region of $0.84 > \cos\theta^* > 0.74$ was about 17% declining to about 14% for the region $-0.66 < \cos\theta^* < -0.56$.

A D.S.T. was made combining the results of all runs. Using the information from each individual run such as, the total beam trigger, the beam sample event momentum distribution and various efficiency factors, which were stored on a disk, together with the acceptance factors, the normalised number of events in each momentum channels was calculated.

The cross-section was then calculated from the following expression;

$$\frac{d\sigma}{d\Omega} = \frac{\text{. NE . ACC}}{2\pi.10^8 \text{ . HTL . } \Delta(\cos\theta^*) \text{ . HC}} \qquad (5\text{-}2)$$

Where;

NE = Number of events normalised to 100 million incident pions, in the CMS angular range $\Delta(\cos\theta^*)$.

ACC = The drift chambers acceptance factor.

HTL = Hydrogen target length.

HC = Hydrogen concentration = density of hydrogen/weight of one atom of hydrogen.

Having a length of 200 mm liquid hydrogen target and 0.0703 gm/cc for density of the liquid hydrogen , we have;

$$\frac{d\sigma}{d\Omega} = \frac{\text{. NE . ACC}}{8.4 \times 10^4 \text{ . } \Delta(\cos\theta^*) \cdot 2\pi} \text{ mb/sr} \qquad (5\text{-}3)$$

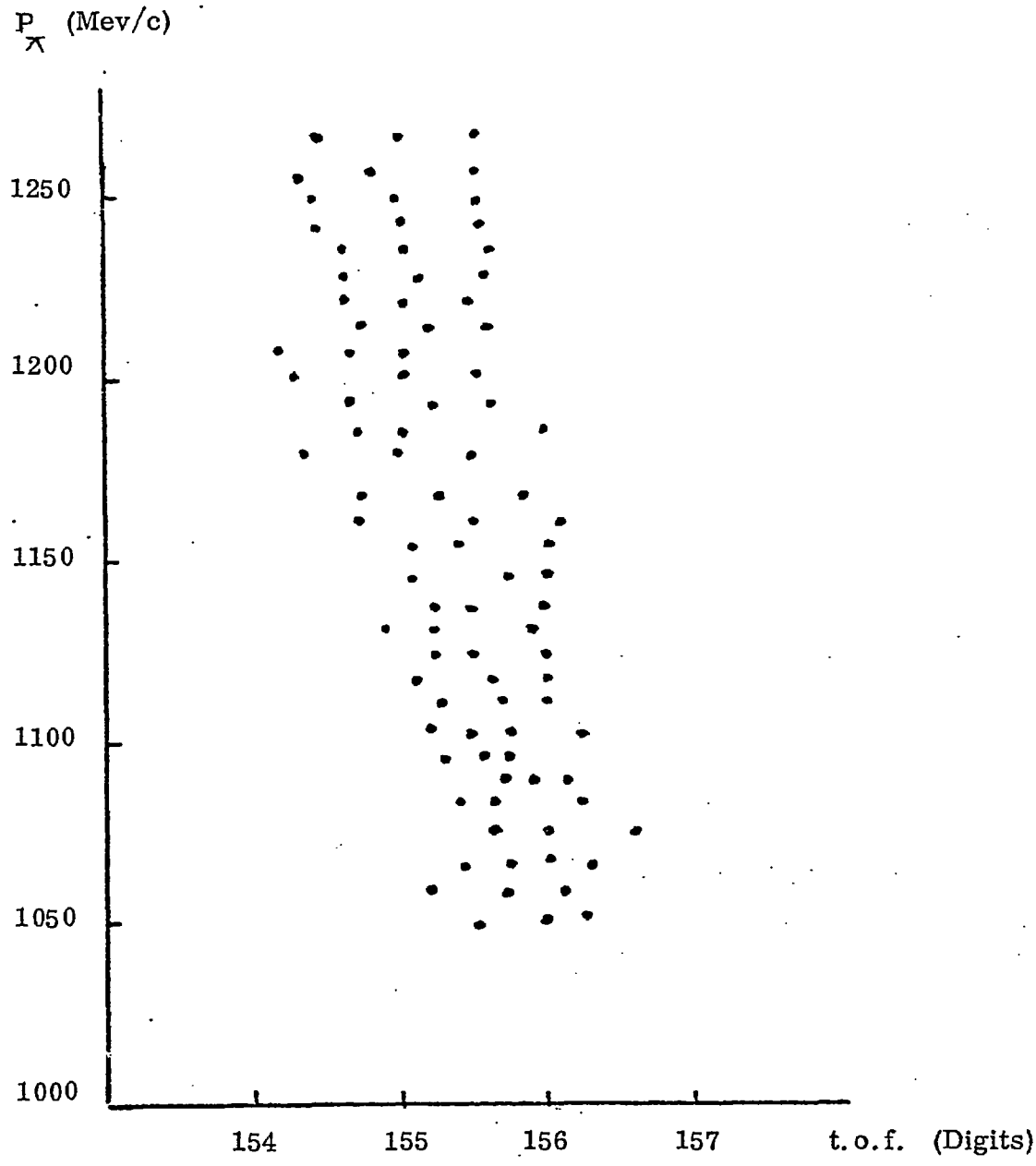

Fast peak position as a function of incident pion momentum.

Fig (5 - 1)

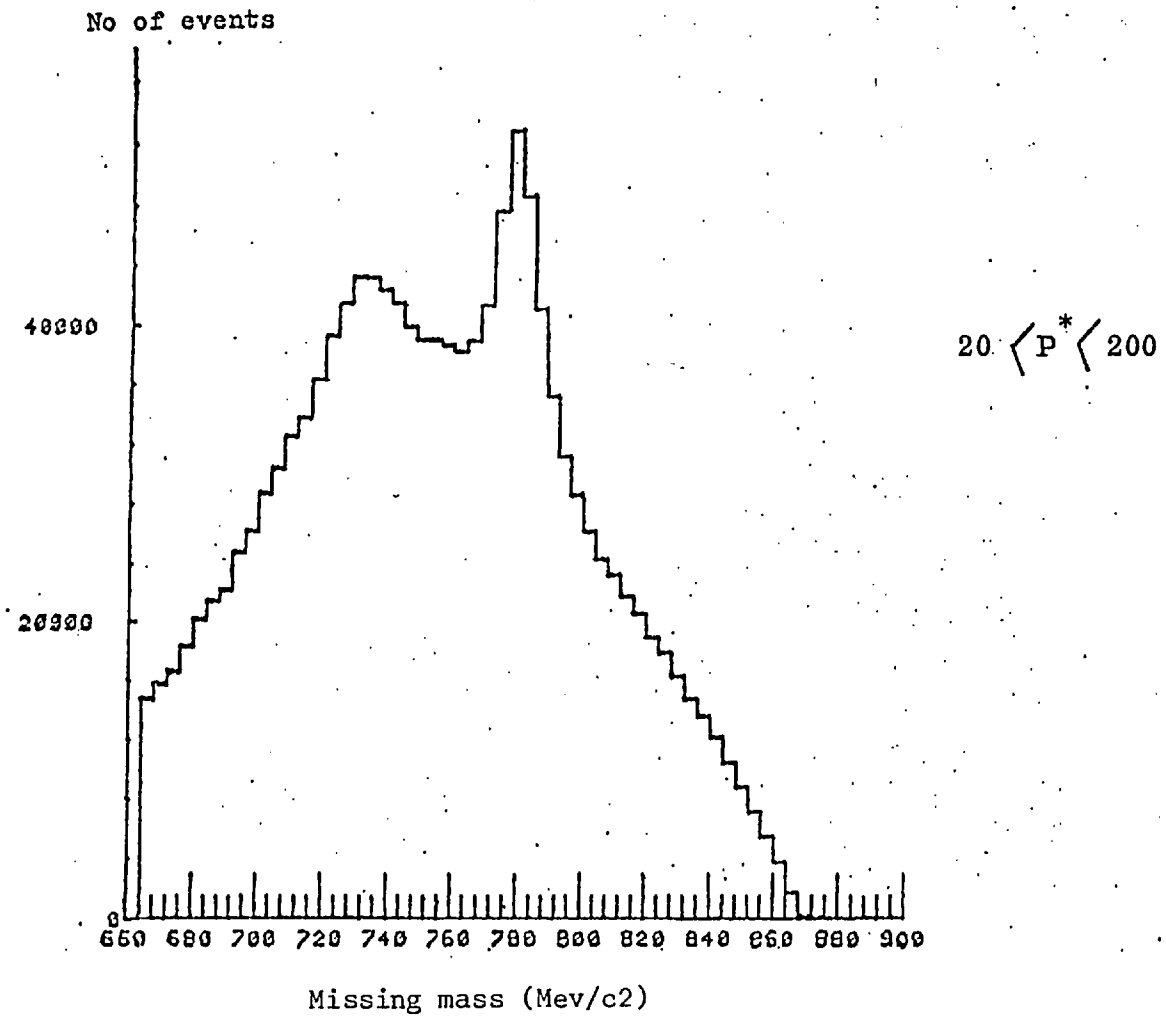

Missing mass spectrum normalised to 100 million beam pions for the total number of events in this experiment.

Fig (5-2)

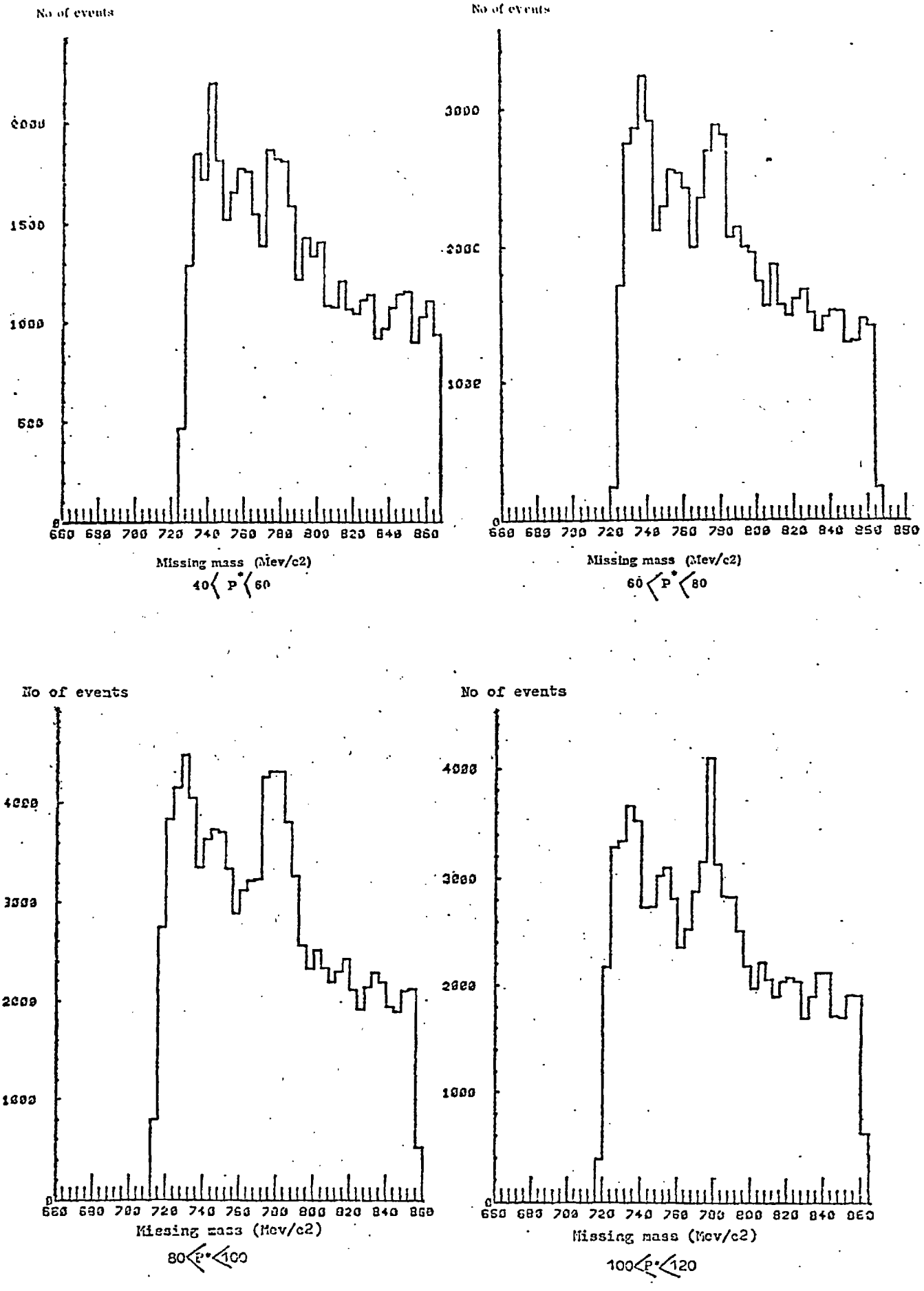

Missing mass spectra normalised to 100 million beam pions for the different p* intervals.

Fig(5-2)

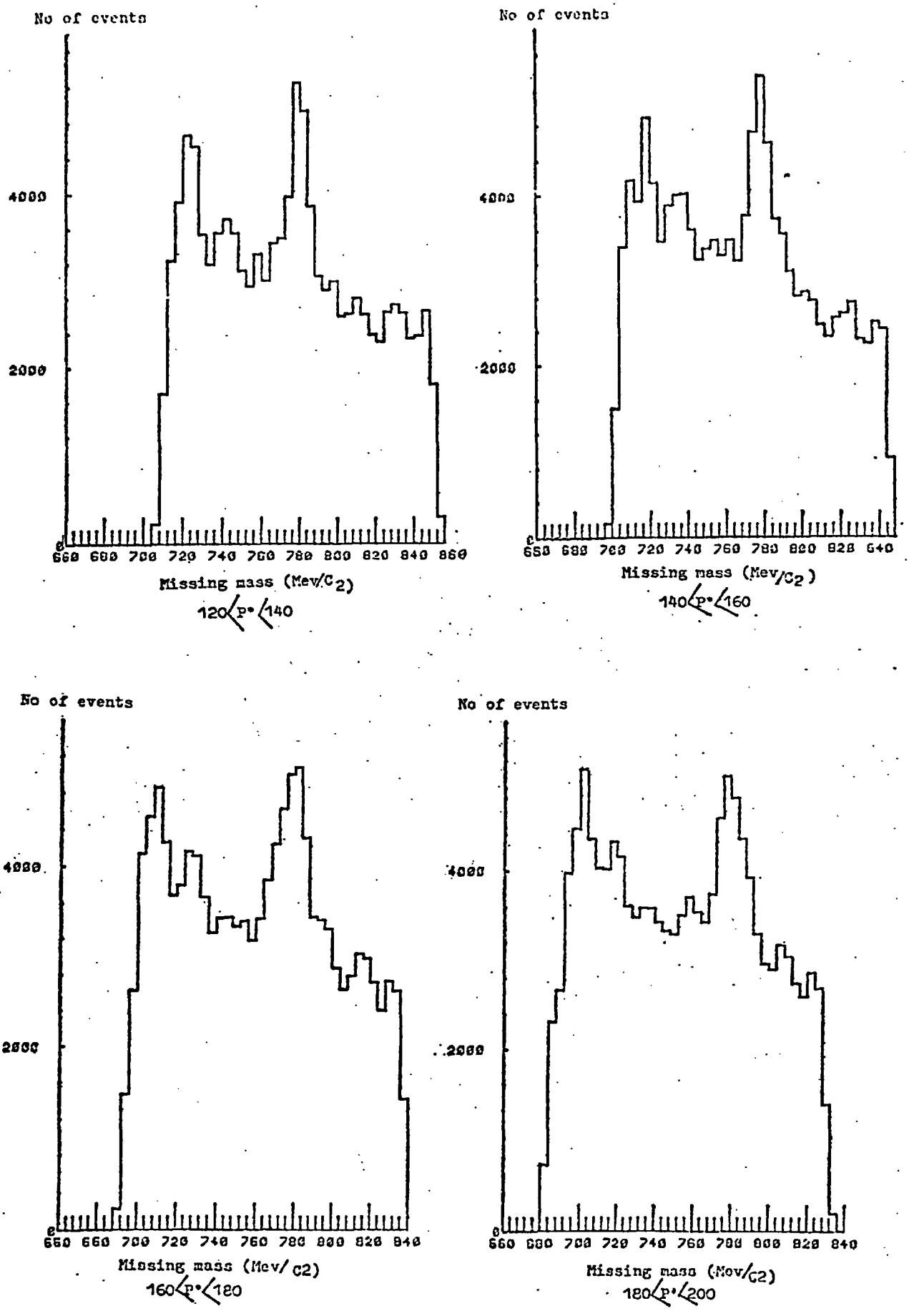

Missing mass spectra normalised to 100 million beam pions for the different p* intervals.

Fig(5-2)

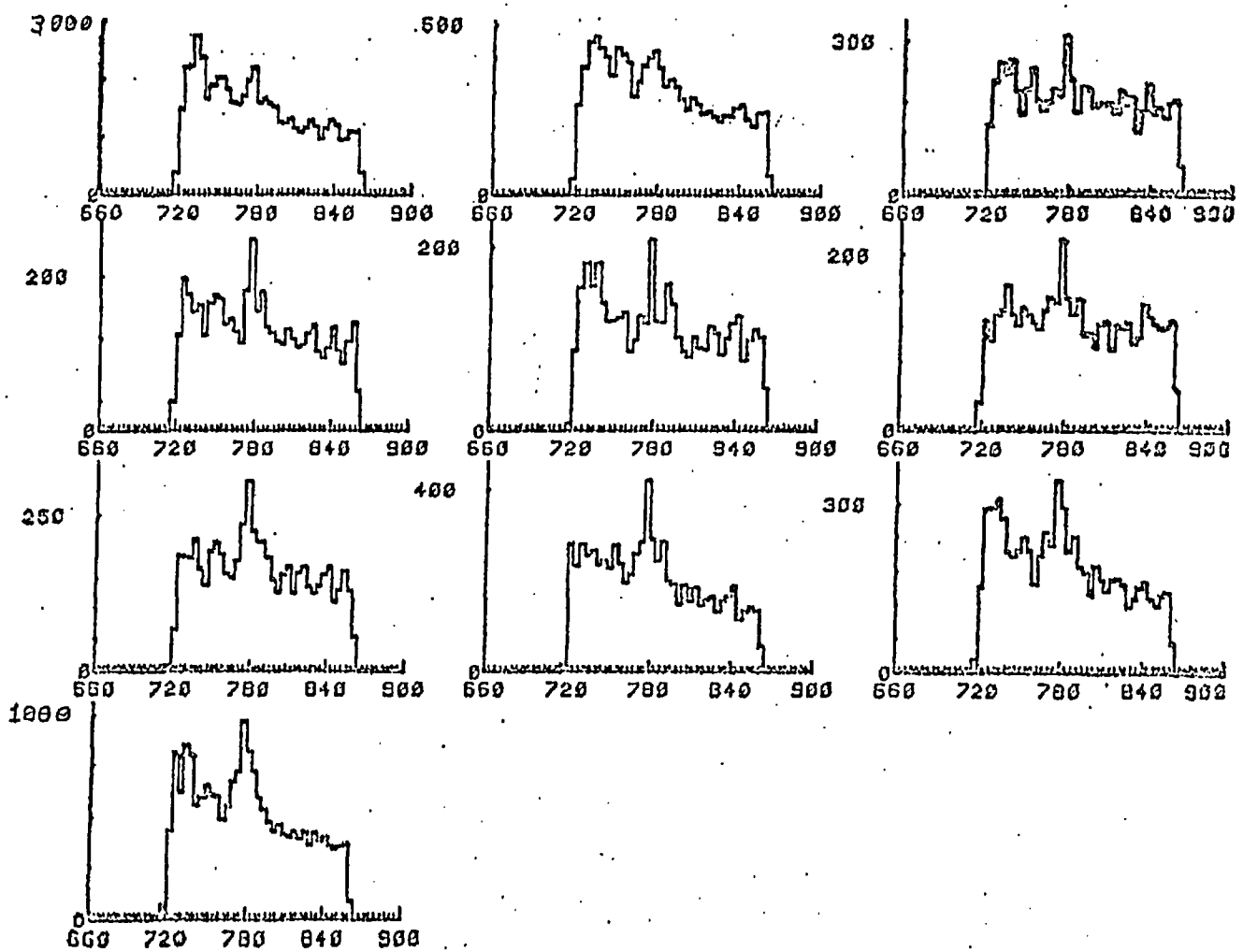

Missing mass spectra normalised to 100 million beam pions for the 10 CMS angular regions at 80 < p* < 100.

Fig (5-2)

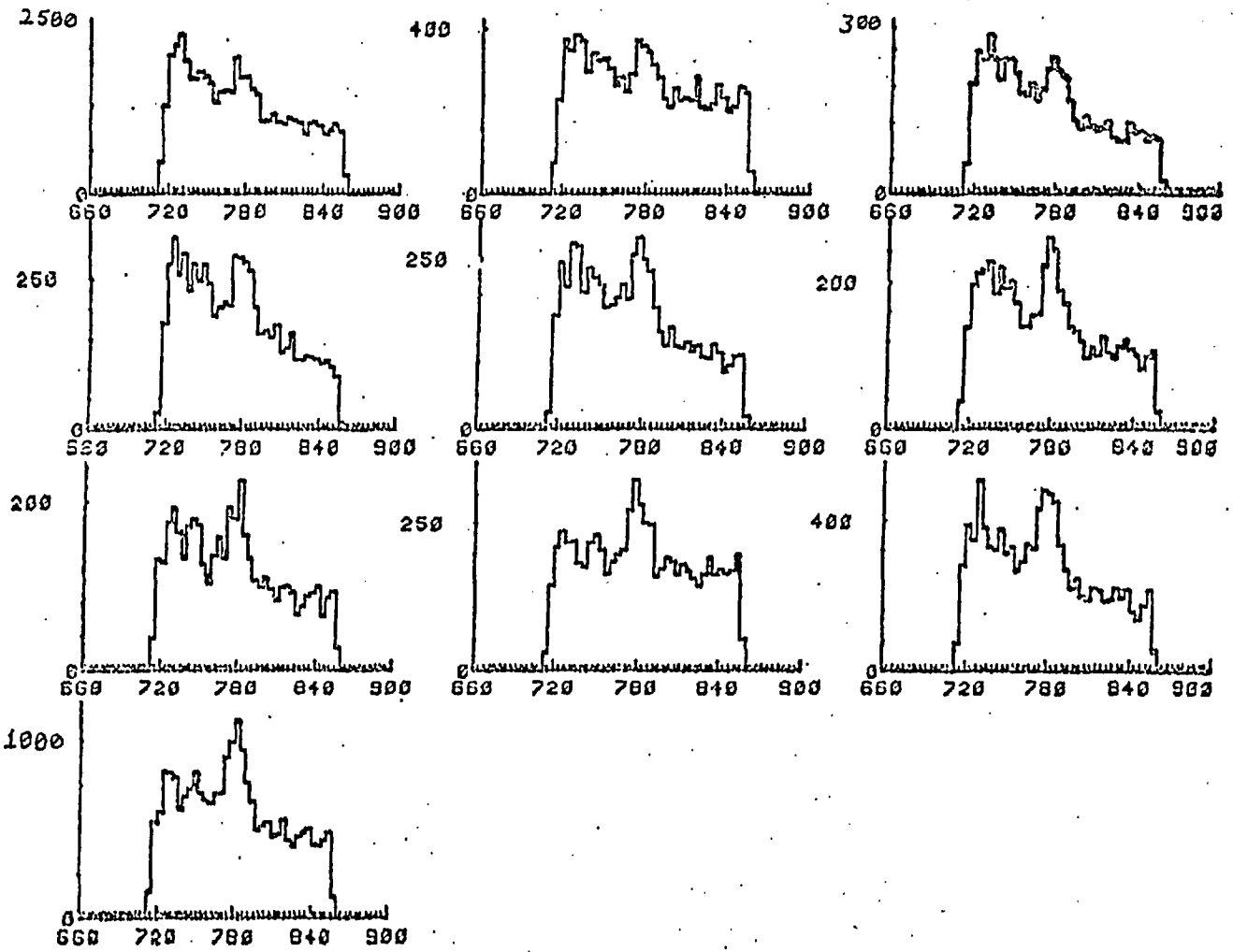

Missing mass spectra normalised to 100 million beam pions for the 10 CMS angular regions at $100 < p^{*} < 120$.

Fig (5-2)

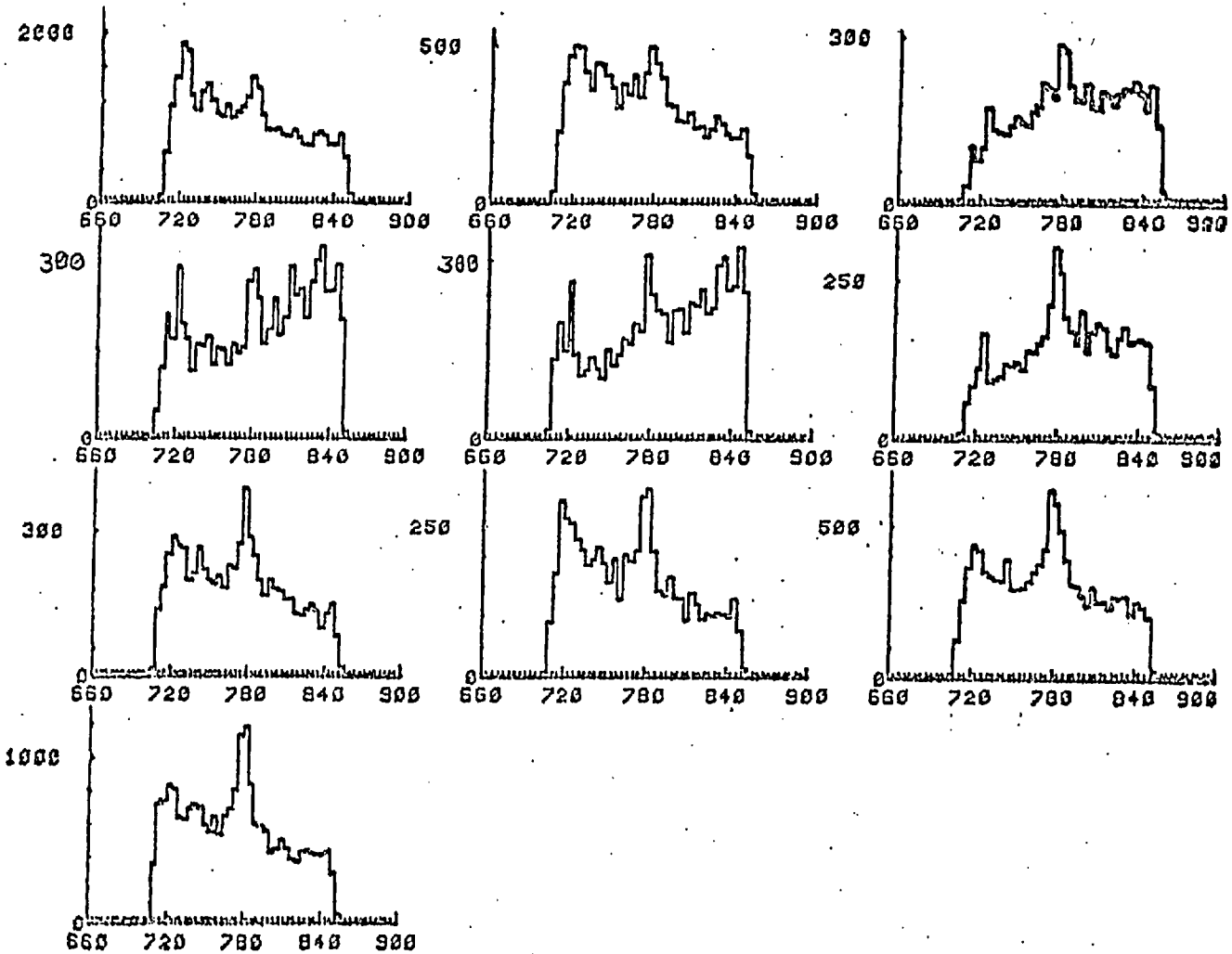

Missing mass spectra normalised to 100 million beam pions for the 10 CMS angular regions at $120 < p^* < 140$.

Fig (5-2)

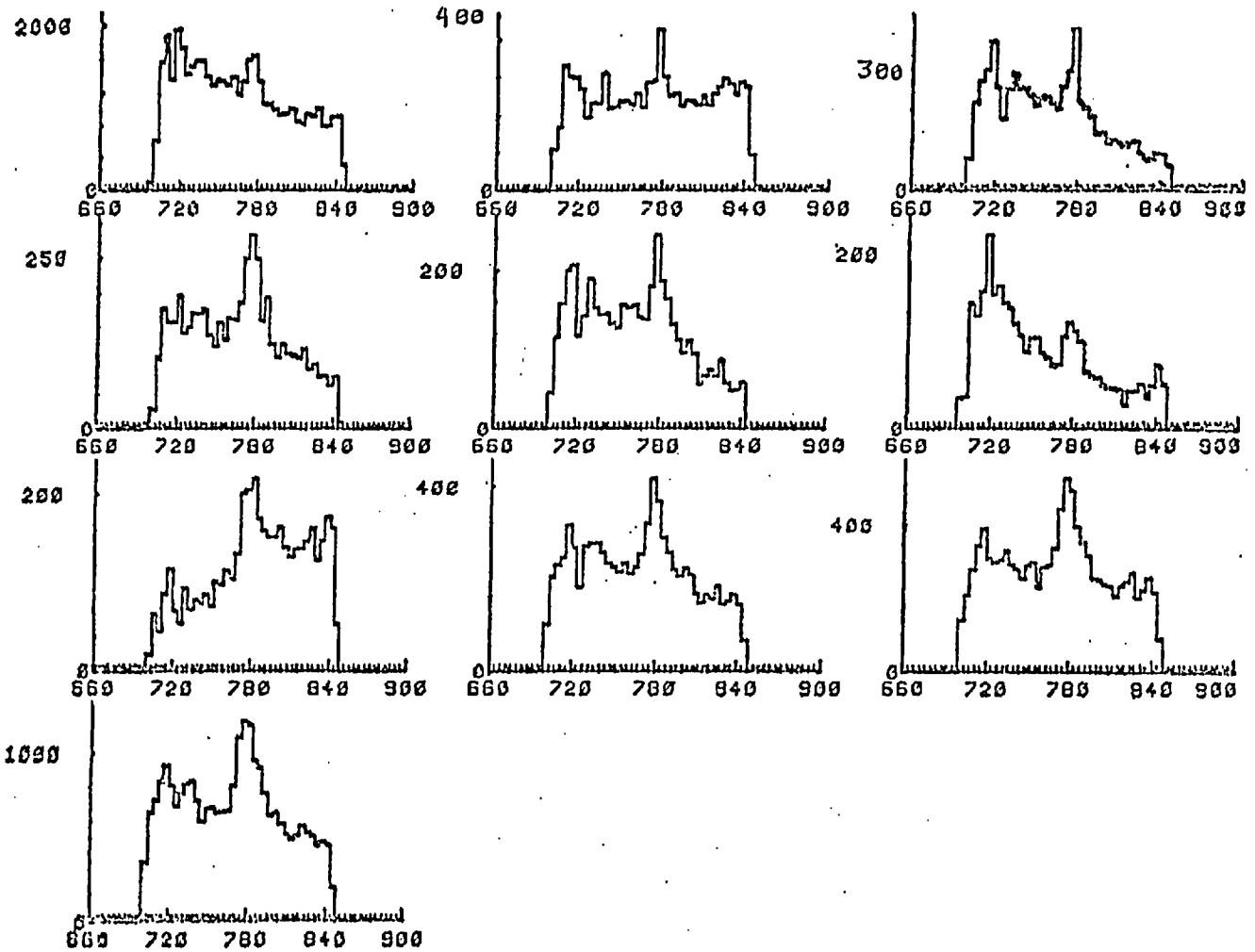

Missing mass spectra normalised to 100 million beam pions for the 10 CMS angular regions at 140 < p* < 160.

Fig (5-2)

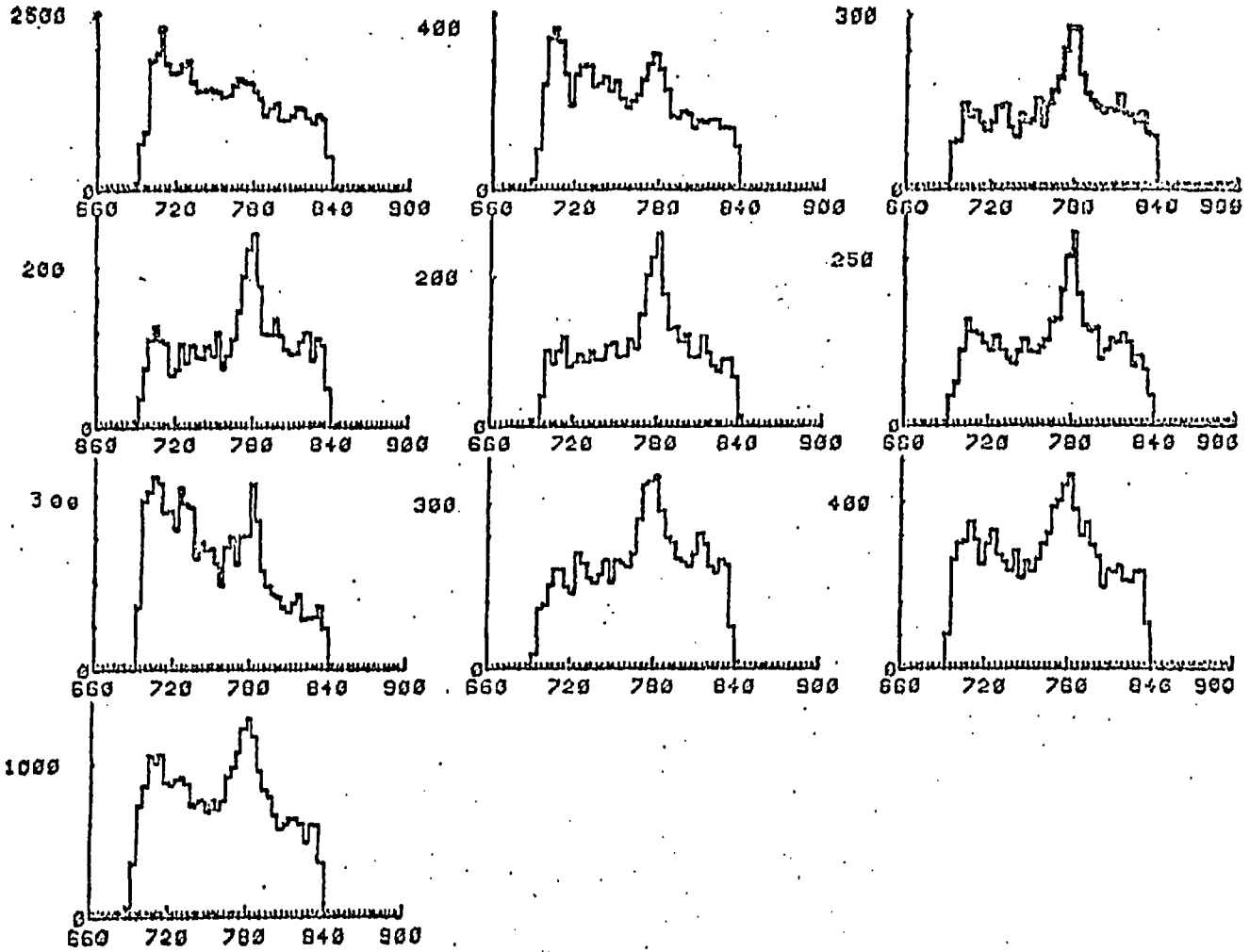

Missing mass spectra normalised to 100 million beam pions for the 10 CMS angular regions at $160 < p^* < 180$.

Fig (5-2)

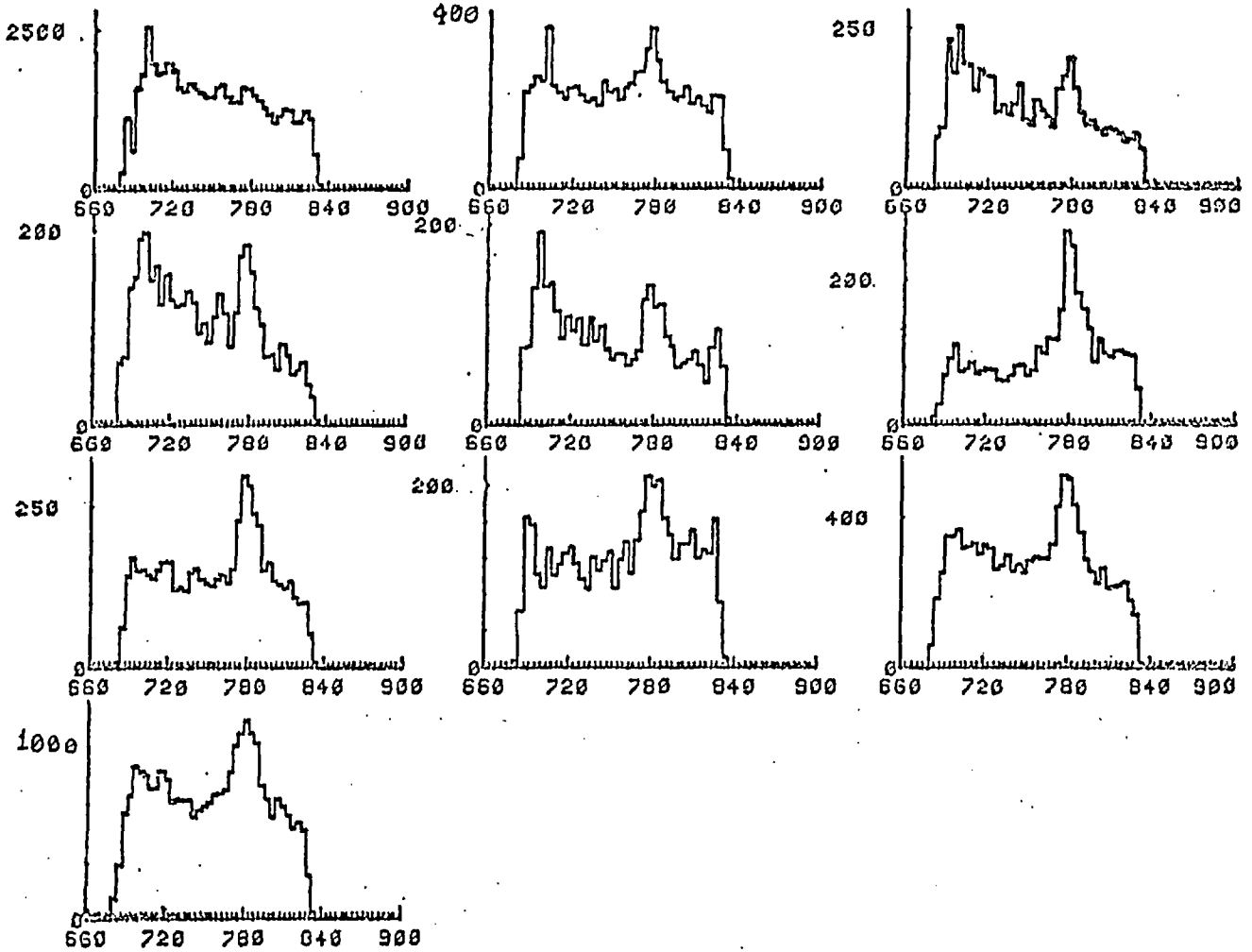

Missing mass spectra normalised to 100 million beam pions for the 10 CMS angular regions at 180 < p* < 200.

Fig(5-2)

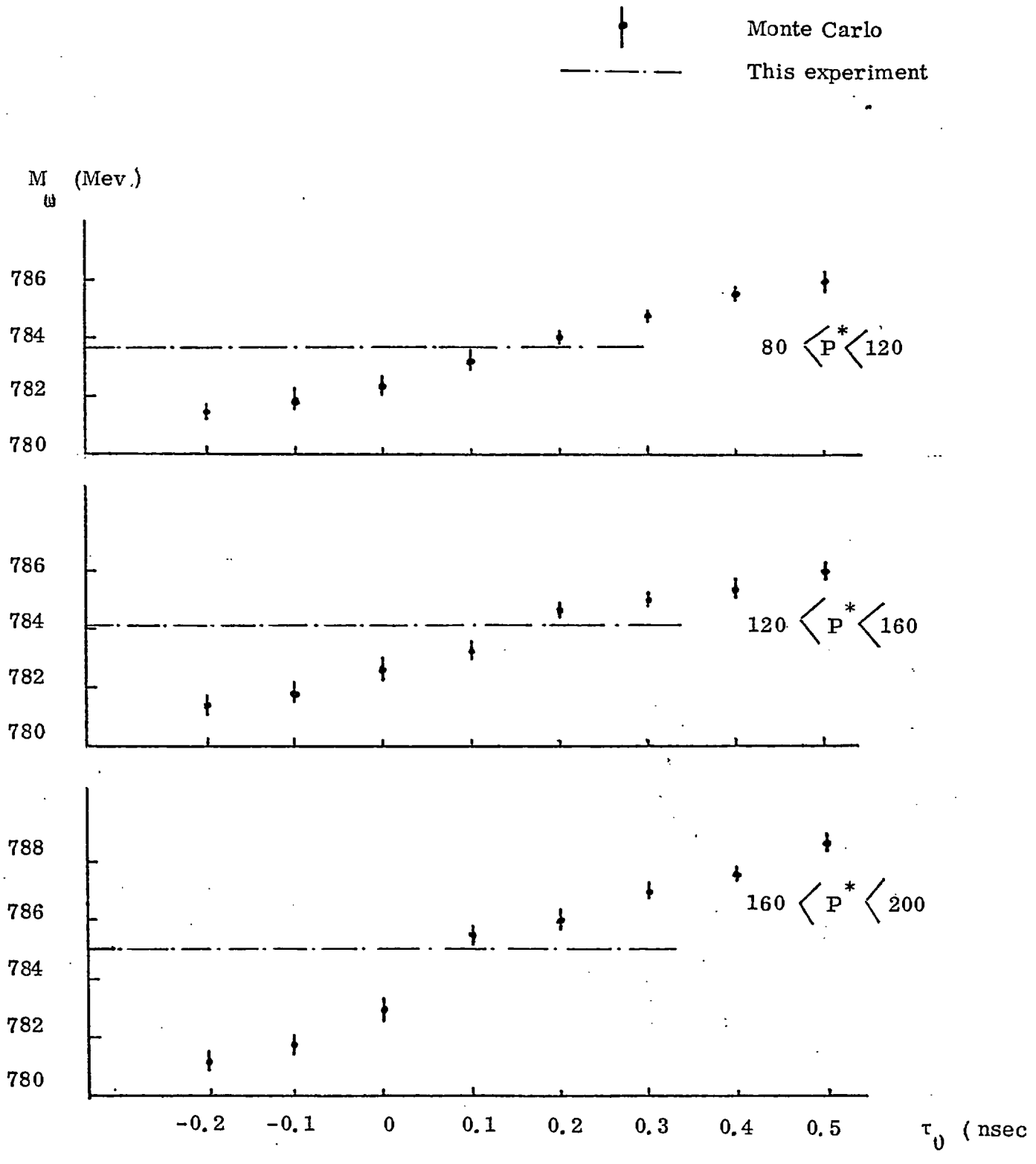

Variation of the peak position of the ω mass versus neutron t.o.f. shift for angular region $-1 < \cos\theta^* < -0.8$.

Fig (5 - 3)

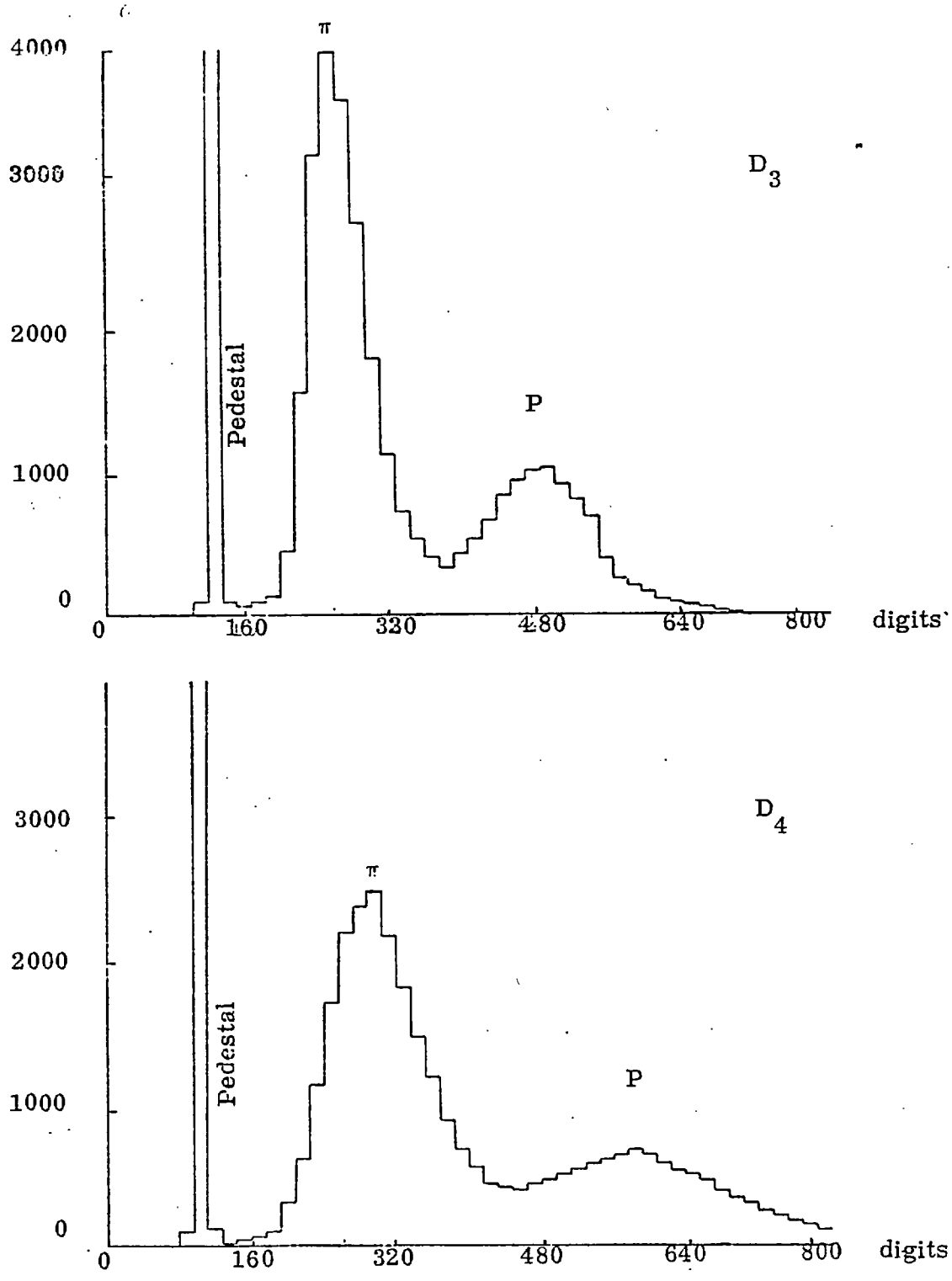

Pulse height distribution of π and p for D_3 and D_4

Fig (5-4)

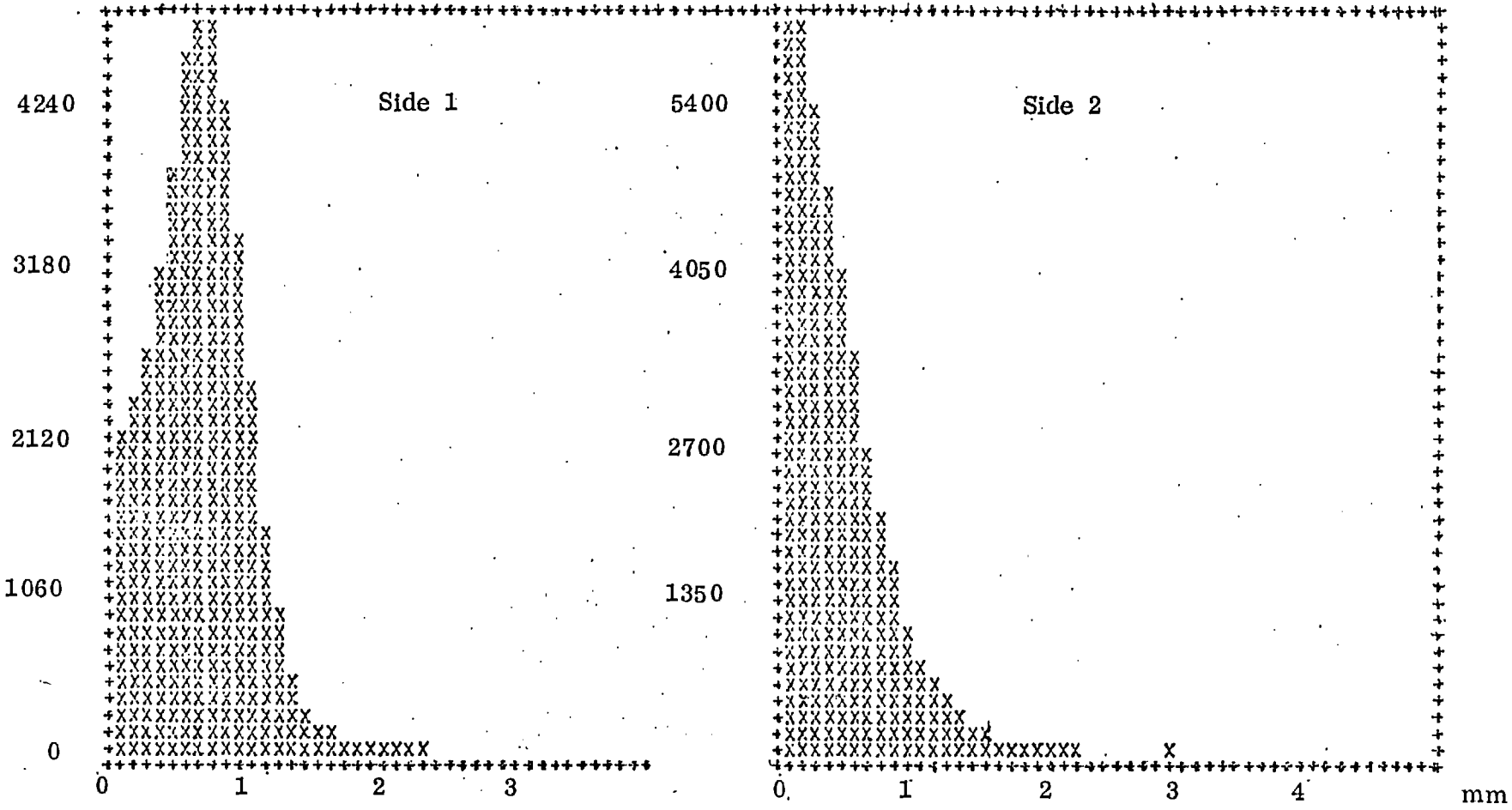

Distribution of the rms deviation from the fitted line in tack construction for side 1 and side 2 .

Fig (5 - 5)

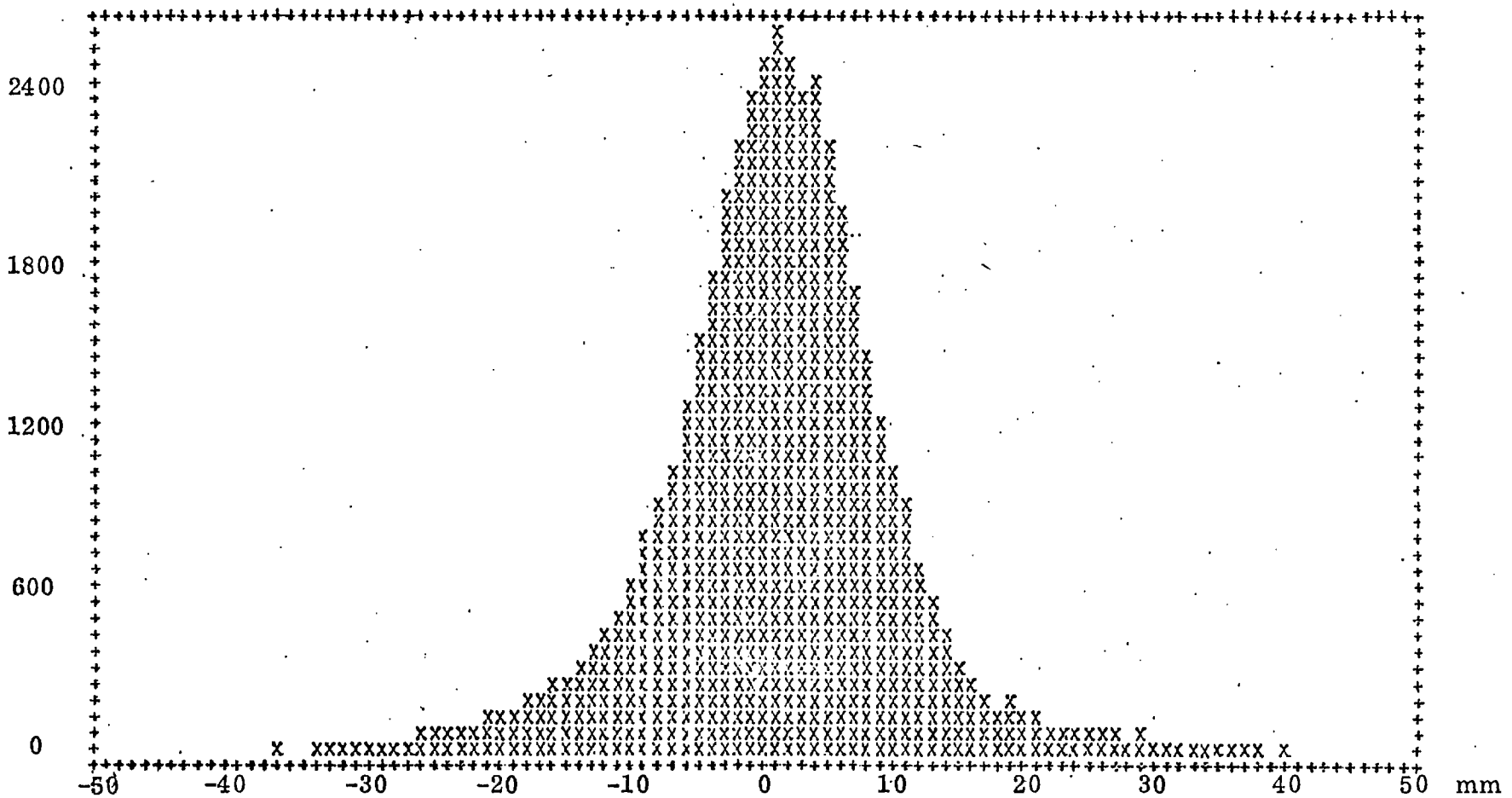

Distribution of the difference of the intersections of the scattered particles with the beam track .

Fig (5 - 6)

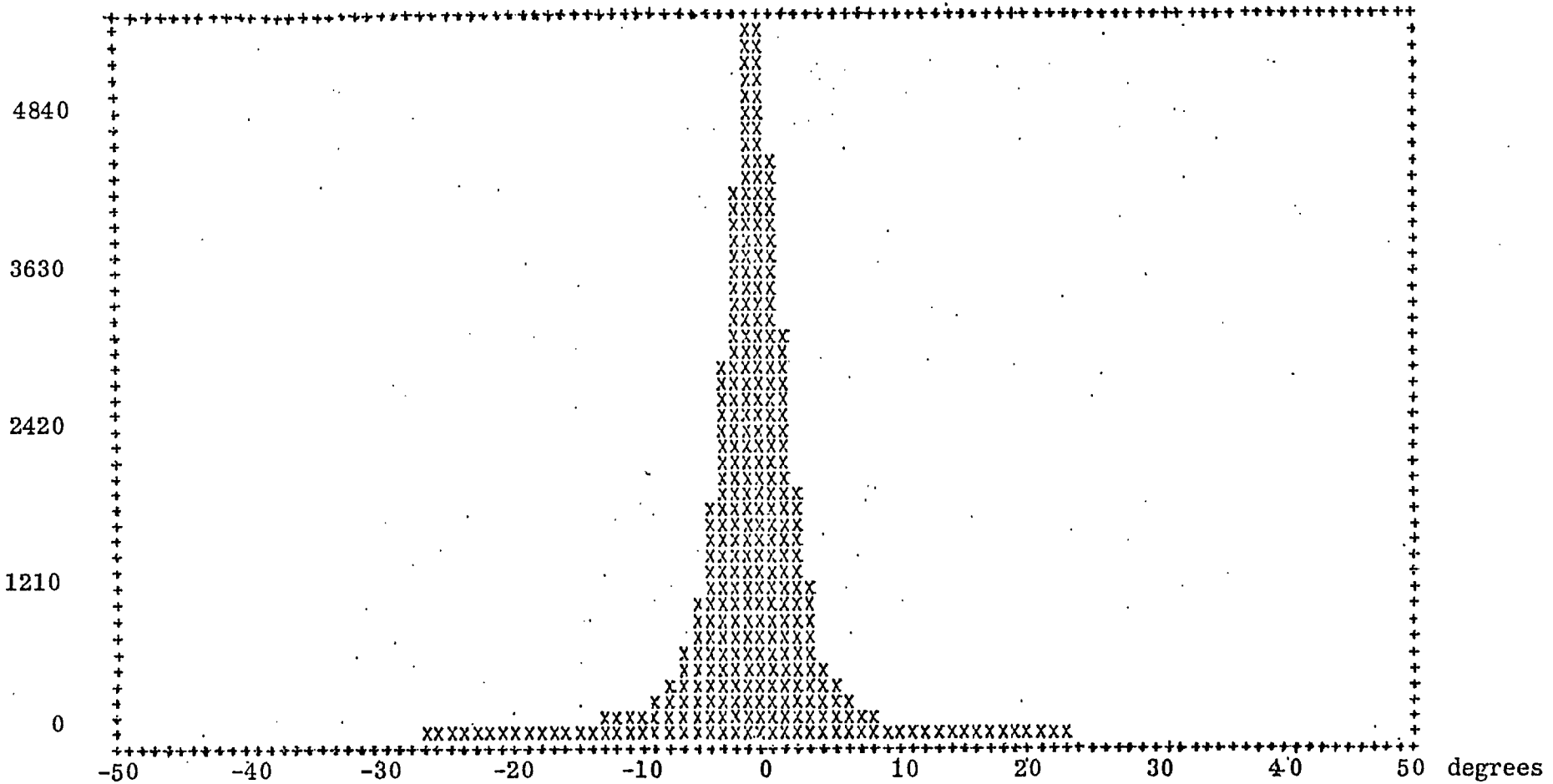

Distribution of the acoplanarity of the scattered particles in the XY plane .

Fig (5 - 7)

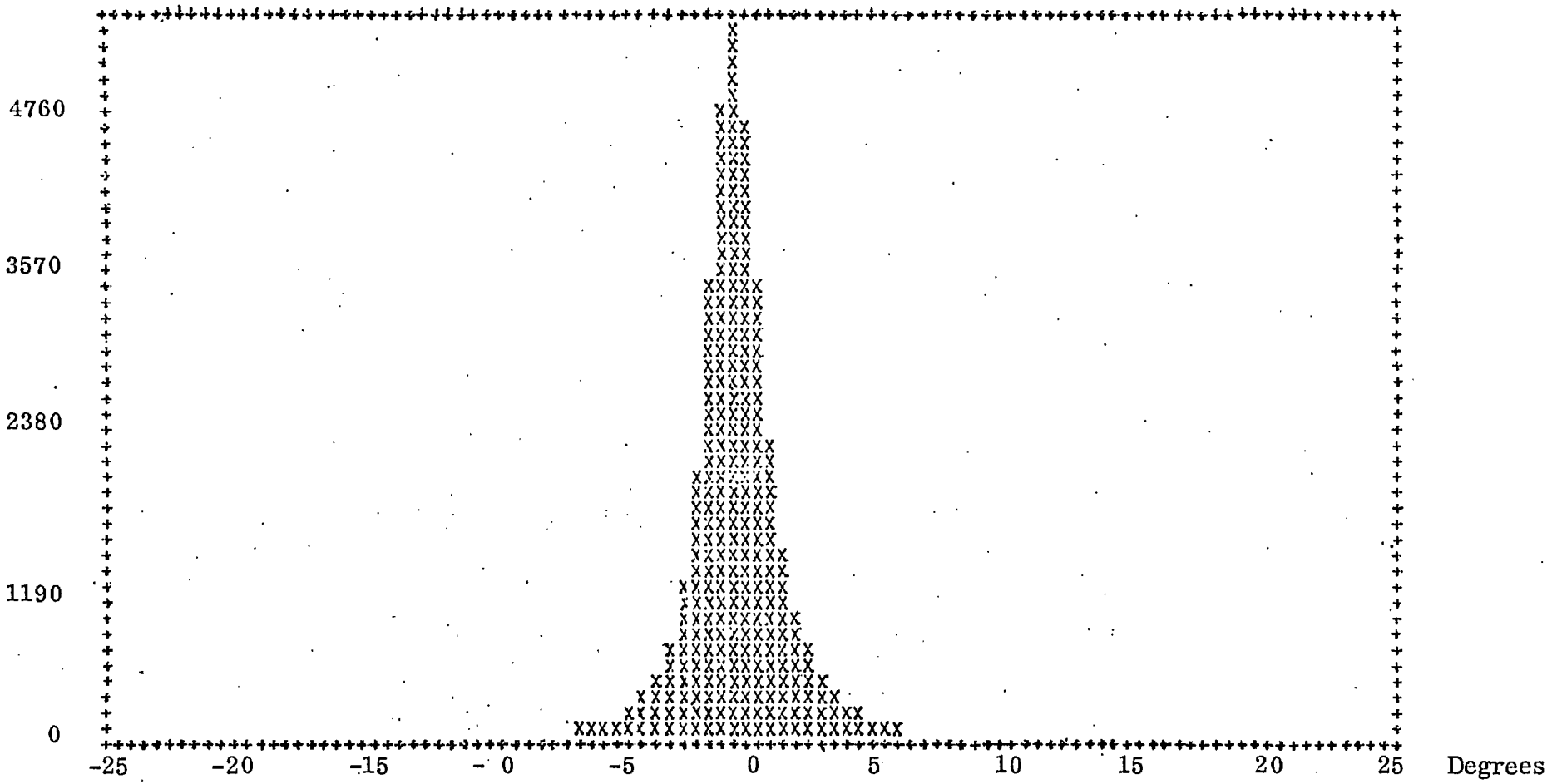

Distribution of the $(\theta^{*}_{\pi} - \theta^{*}_{p})$

Fig (5 - 8)

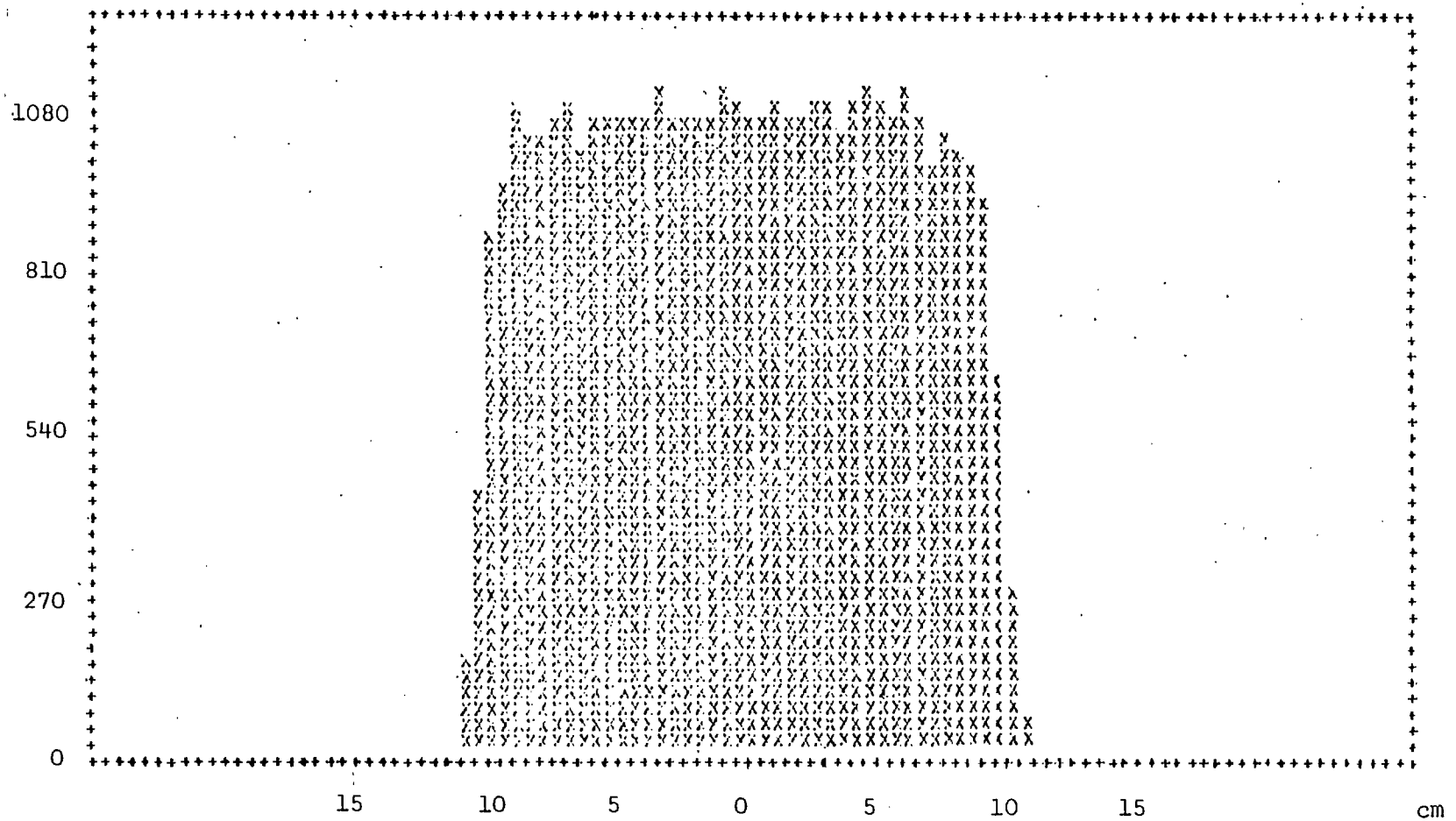

Distribution of the point of interaction in the liquid hydrogen.

Fig(5-9)

6 RESULTS

(6-1) ω Production Results.

Data were collected for a range of incident momentum corresponding to intervals of p* between p*= 20 Mev/c and p*=200 Mev/c, and grouped in 10 intervals of 20 Mev/c wide, which covered the whole CMS angular region. In each p* interval the data were subgrouped in 10 regions of COS θ*, each having a width of 0.2. There were 100 missing mass spectra covering different intervals of p*, and COSθ*.

The ω mass and width were deduced by fitting a Monte-Carlo generated ω distribution to the data for each missing mass spectrum. In this Monte-Carlo, described in detail in chapter (5-2-4), an initial assumption was made that the ω cross-sectic rises linearly with p* and that there was an isotropic angular distribution in the CMS.

(6-1-1) Mass Of The ω.

In each p* intervals the 10 missing mass spectra from the different regions of COS θ* were combined to increase the statistics.

Each of these missing mass spectra was fitted with a third order Polynomial representing the background together with a Breit-Wigner resonance with two varying parameters M, and Γ, the mean mass and width of the ω meson respectively.

The method of fitting of data to the Monte-Carlo was as follows;

Using a fixed value of Γ, the values of χ^2 corresponding to different values of M, were determined and the value of M, giving the least value of χ^2 was found. Fixing this value of M, the value of Γ, was varied until another minimum in χ^2 was found, and this procedure repeated until the change in the value of M, observed by any further iteration, was less than 0.1 Mev/c2. Fig(6-1) shows a typical fit. The variation of

the ω mass as a function of p^* is plotted in Fig(6-2). This suggests that the mass of the ω meson is independent of p^* which is consistent with the result of the $\pi 7$ experiment. The weighted mean of 11 points in Fig(6-2) is 783.0 ± 0.2 Mev/c2, and the χ^2 for the hypothesis of no p^* dependence was 4.1 for 10 degrees of freedom.

The systematic error comes from the uncertainty in the measurement of the absolute value of the central momentum . It was estimated to be ± 0.03% which corresponded to ± 0.2 Mev/c2. By quadratically adding the systematic error to the statistical error the result for the ω mass is;

$$M_{\omega} = 783.0 \pm 0.35 \text{ Mev/c2}$$

The above value of the ω mass is in good agreement with the world average figure of 782.6 ± 0.3 Mev/c2, {see Fig(6-3)}.

(6-1-2) Width Of The ω.

The ω width was determined at various p^* intervals. In each p^* interval the best fitted value of Γ was found from the missing mass spectrum in the COS θ^* region, where the missing mass resolution was small compared to the width of the ω . A Breit-Wigner resonance together with a three term Polynomial representing the backgroundwas used. The variation of χ^2 as a function of Γ, was obtained with the ω mass fixed at a value found from the previous stage. The variation of Γ as a function of p^* is plotted in Fig(6-4) where the error bars represent only the statistical error. The weighted mean value of the width derived from all the data points is 9.9 ± 0.35 Mev/c2 which has a χ^2 value of 13.7 for 9 degrees of freedom. Using a different order polynomial for the background, had no significant effect on this result.

There is also an additional contribution to the error of the ω width caused by uncertainty in the mass resolution. This systematic error

comes from the uncertainties in measurement of the absolute momentum, neutron time of flight and neutron angle, A value of 0.24 Mev/c^2 for the systematic error in Γ_ω was obtained, { detailed calculation of the systematic error in the Γ_ω is given in Ref(17) }. Thus the final result for the width of ω is;

$$\Gamma_\omega = 9.9 \pm 0.42 \text{ Mev/}c^2$$

This result is in good agreement with the world average value of 10.05 ± 0.33 Mev/c^2. Table(I) shows the variation of the ω mass and width for this experiment.

(6-1-3) The ω Cross-section.

The cross-section can in principle be found directly from the area under the ω resonance signal in the missing mass spectra. The acceptance of the neutron counters, however, was found to be strongly dependent on the values of p^*, and COS θ^*, used. Because of this problem we deduced the cross-section by the fitting the missing mass spectra with those generated by the Monte-Carlo programme. In the Monte-Carlo it was assumed that the cross-section rises linearly with p^*, i.e., $\sigma=Ap^*$, where σ is the cross-section and A is a constant factor. A two term polynomial represented the background.

The ratio of the experimental missing mass signal to the Monte-Carlo signal gave the value A, in the expression $\sigma=Ap^*$.

The following systematic effects were taken into account and used to adjust the values of the cross-section;

(I) Contamination of the beam by particles other than negative pions (mostly μ mesons) ; +4 ± 1% ,{this figure is taken from the investigation regarding the beam contamination, carried out at the π7 beam Ref(17) }.

(II) Loss of neutrons interacting in the 10 cm long hydrogen target (i.e., half the length of the target) + 2 mm scintillator (P counter) + 6.15 meters air : +2 ± 1% ;

(III) Attenuation of the pion beam through interactions in the hydrogen target(calculated for half the length of the hydrogen target) : +2 ± 1% ;

(IV) Target empty correction; A hydrogen out run showed that some events attributed to ω production off free hydrogen were interactions with free protons in the melinex end caps of the hydrogen flask and also in the scintillation counters: -2 ± 1% ;

The above effects lead to a correction factor of 1.06 ± 0.02. Thus the total systematic uncertainty in the cross-section was ±2%, which should be combined with the 5% error coming mainly from uncertainty in the absolute neutron counter efficiency and also 8% error coming from the uncertainty in the rejection of events from the "Ambiguous" type neutrons.

By quadratically adding the above contributions, we obtain a total systematic uncertainty of 10%. The resulting cross-sections, divided by p*, are shown as a function of p*. in Fig(6-5). Table(II) shows the values of A and σ at different p* intervals.

A comparison between the result of this experiment and the π7 result Fig(1-2), shows a very good agreement.

The total cross-section for ω production is plotted in Fig(6-6). In addition to this experiment, there exist three sets of data[18,19], on ω production and these are also shown in this plot. The agreement between our data points and those of the other experiments justifies the earlier assumption which was made regarding the efficiency of the neutron counters.

(6-1-4) Differential Cross-sections.

The differential cross-section $\frac{d\sigma}{d\Omega}$, for each interval of p*, and Cos θ*, was deduced from the missing mass spectra in the same way as described in section (6-1-3).

The Cross-sections for ω production, corrected for systematic errors, for values of p* between 20 Mev/c and 200 Mev/c, in intervals of 20 Mev/c and COS θ* intervals of 0.2 are listed in table (III) and shown in Fig. (6-7).

To determine which angular momenta are present in production, the measured differentialCross-sections $\frac{d\sigma}{d\Omega}$, were expanded in terms of Legendre polynomial series in the form;

$$\frac{d\sigma}{d\Omega}(\theta^*) = \sum_{\ell=0}^{n} C_\ell \, P_\ell (\cos\theta^*) \qquad (6\text{-}1)$$

where θ*, is the CMS scattering angle. Values of the coefficients C_ℓ , were obtained from a least squares fitting programme. The values of the coefficients C_ℓ , obtained at each P* interval are listed in Table(IV). Also listed in this table are the χ^2 values obtained. The theoretical curves obtained from Eq(6-1) for the best fit are also plotted in Fig(6-7).

Fig. (6-8) gives the behaviour of the coefficients C_ℓ , as functions of P*. The values of the ratios of the Legendre polynomial coefficients C_1/C_o, and C_2/C_o, from the fits to the angular distributions as functions of P*, are shown in Fig. (6-9), and listed in table (V).

(6-2) π^-P Elastic Scattering Results

In this section we present the preliminary results of measurements of the π^-P elastic scattering Cross-section.

Data were collected across the ω production threshold covering a range in momentum from $P\pi$ = 1.010 Gev/c to $P\pi$ = 1.170 Gev/c, and in CMS angle from cos θ *= -0.64 to cos θ * = 0.86.

The differential Cross-section in the above momentum and angular ranges were measured in momentum intervals of 0.37 Mev/c and cos θ^* intervals of 0.1.Our data were normalized to existing published data Ref (2), and a constant normalization factor of 1.3 was found. This rather large factor mainly comes from the inefficiency of the drift chamber system together with the rejection of elastic events in the several cuts imposed in the off-line analysis. The factor was found to be independent of $P\pi$, and θ *, and this is supported by a comparison between our angular distribution and that from Ref.(20) both at $P\pi$ = 1.101 Gev/c is shown in Fig. (6-12) where it is seen that the agreement between these two experiments is very good.

(6-2-1) Differential Cross-Sections

The measured differential Cross-sections for π^-P elastic scattering are listed in table (VI), where the errors quoted are statistical only. In Fig. (6-10), these differential Cross-sections for various CMS angular regions are plotted as a function of pion momentum.

The behaviour of the cross-section in the first forward angular region i.e., 0.76 < COS θ^* < 0.86 shows an oscillating structure of magnitude about 4% of the cross-section, repeating itself every 10 Mev/c over the range of the momemtum covered. Further investigation of the non-elastic events which were rejected by the various cuts imposed, showed a similar behaviour. Subsequently we realised that the calculated acceptance factor of the drift chambers used in this particular angular region was slightly inaccurate. A more accurate analysis of the data which

is in progress, but not completed yet, shows a smoother behaviour. However, the preliminary results are presented in this work and there is sufficient evidence to show that this structure is not a genuine one and is produced by the analysis programme.

The angular distributions in 3.92 Mev/c intervals of P_π are presented in Fig. (6-11).

Since our data do not cover the full angular range in the CMS, and as the latter figure shows that the cross-section in the uncovered region varies smoothly, the data from Ref. (20), have been used in the following fit to the angular distribution of this experiment.

The smooth curves represent the best fit to the data points by an expansion in a Legendre polynomial series Eq. (6-1). Up to 7th order were found to be sufficient to fit the data. The higher order 8th term did not improve the values of χ^2 and no significant changes were observed in the values of the coefficients C_ℓ, obtained from the lower order fit.

The values of the Legendre polynomial coefficients C_ℓ as functions of p_π are given in table (Vii), and shown in Fig. (6-13).

The total elastic Cross-section was determined from the Legendre polynomial coefficients, fitted to the data points, using the relation;

$$\sigma_{el} \text{ (Tot)} = 4 \cdot \pi \cdot C_0$$

and is shown in Fig. (6-14).

The forward Cross-section may be extrapolated from the Legendre polynomial coefficients according to;

$$\frac{d\sigma}{d\Omega} \ (\theta^* = 0^\circ) = \sum_{\ell=0}^{n} C_\ell$$

The values were determined and are shown in Fig(6-15).

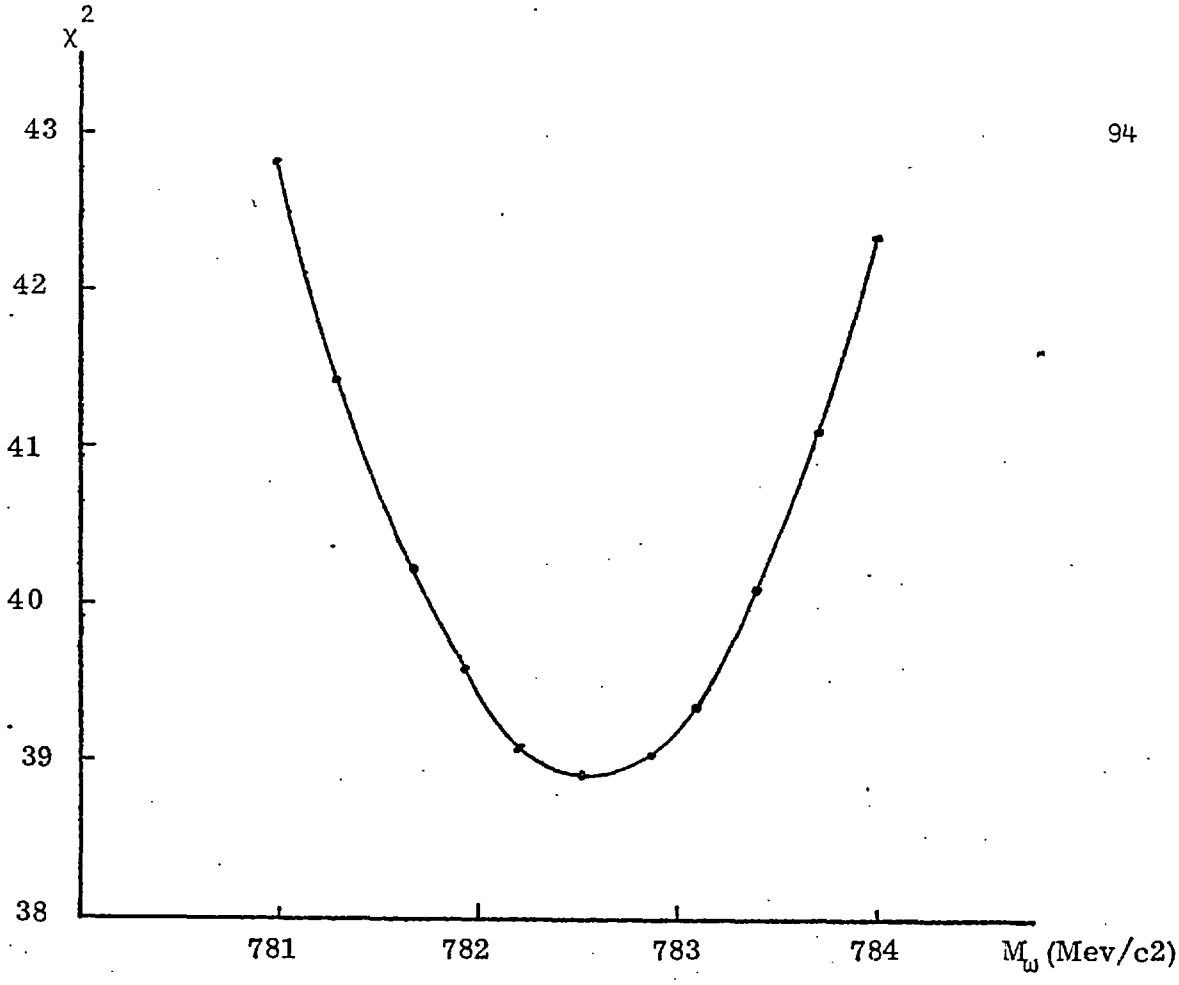

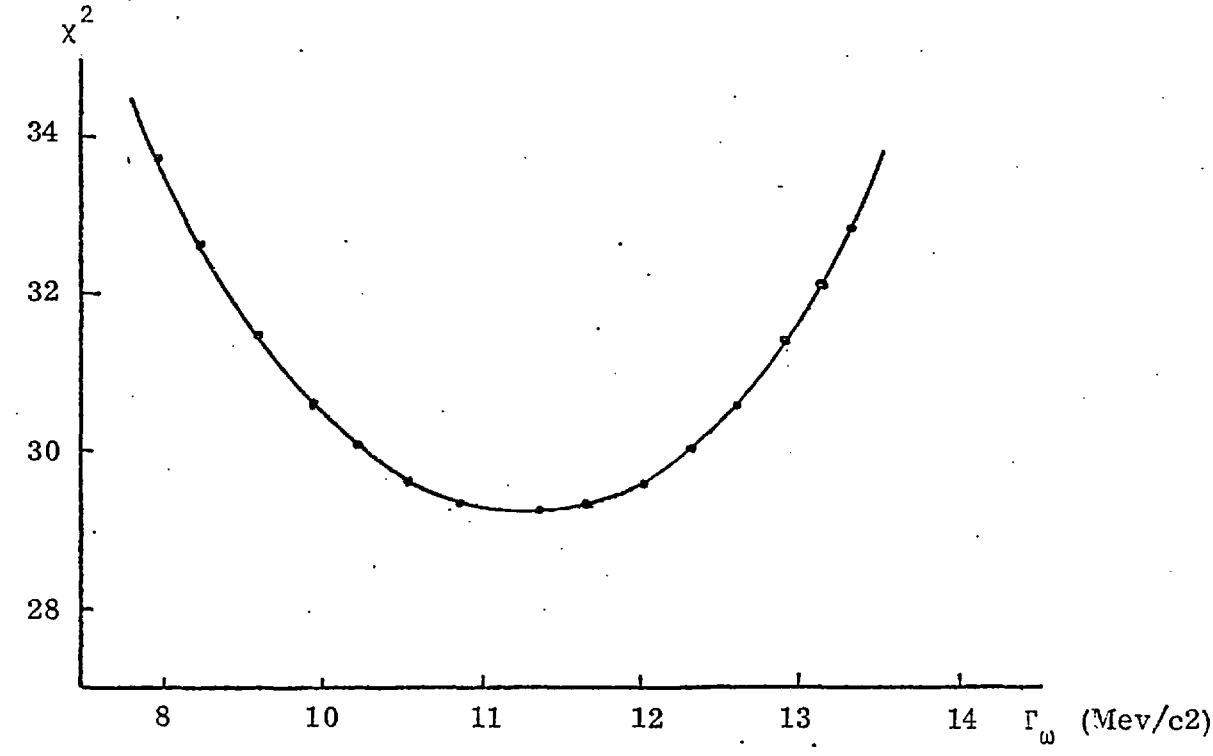

χ^2 versus mass and width of the ω .

Fig(6-1)

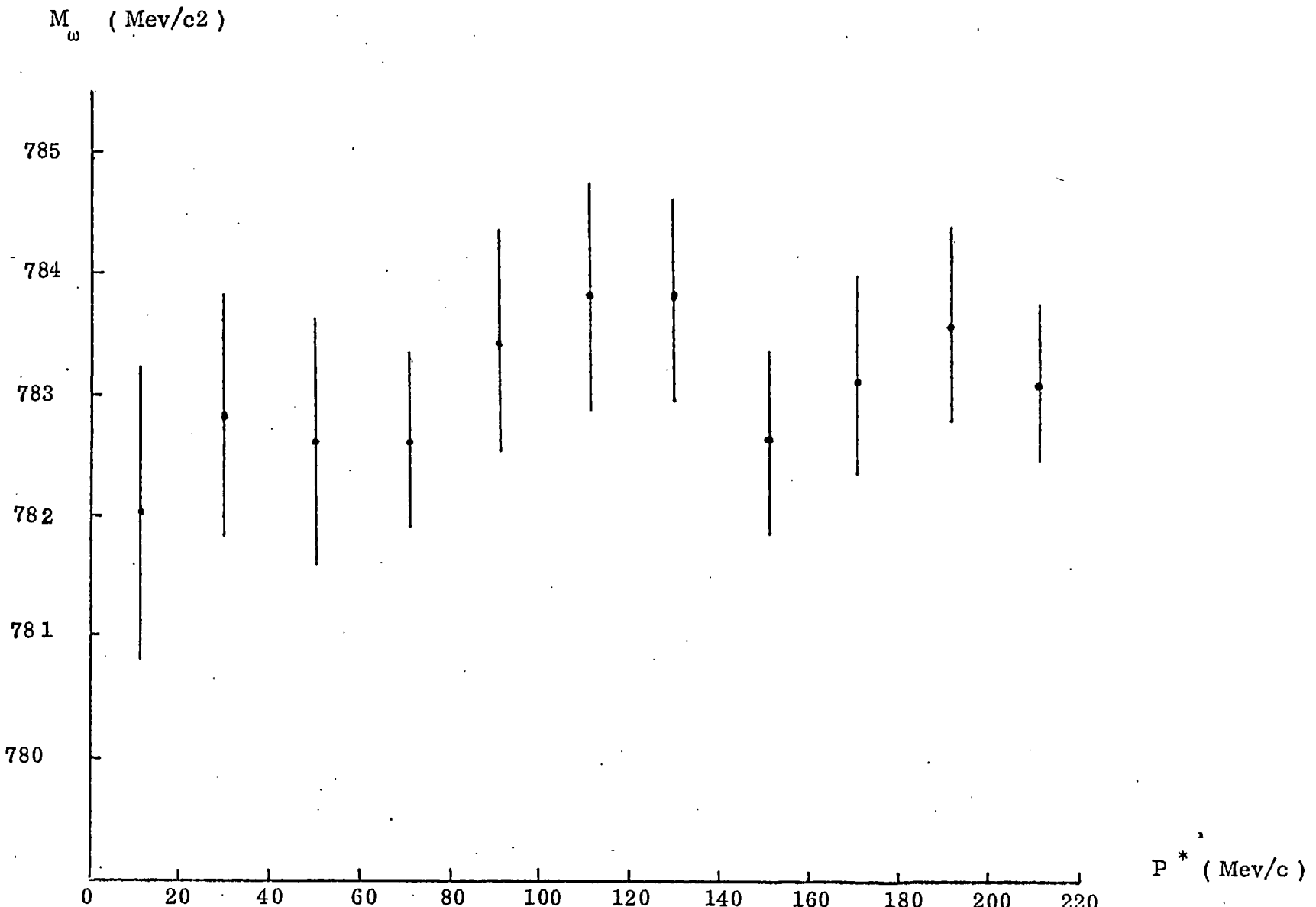

Mass of the ω plotted as a function of P^*

Fig (6 - 2)

$\omega(783)$

I OMEGA(783,JPC=1--) I=0

I OMEGA MASS (MEV)

	64 (779.4)	(1.4)	ARMENTERO	62	HBC	0.0 PBAR P K1K1.	2/74
	930 (783.0)	(1.0)	ALFF	62	HBC	2.3-2.9 PI+P	. 2/74
	56 (784.0)	(1.0)	ARMENTERO	63	HBC	0.0 PBAR P	. 2/74
	220 (781.0)	(2.0)	KRAEMER	64	CBC	1.2 PI+D	. 2/74
	170 (785.6)	(1.2)	MILLER D	65	HBC	SEEN WITH K+K-	. 2/74
	666 (784.0)	(1.0)	JAMES	66	HBC	2.1 PI+P	. 2/74
	2159 783.4	0.7	BALTAY	67	HBC	0.0 PBAR P	2/74
	155 (779.5)	(1.5)	BARASH	67	HBC	0.0 PBAR P K1K1.	2/74
	(784.8)	(1.1)	KEY	69	HBC	? PI-P	. 2/74
	2400 782.4	0.5	BIZZARRI	69	HBC	0 PBAR P	5/67
	750 784.1	1.2	ABRAMOVIC	70	HBC	3.9 PI- P	2/74
	784.0	0.7	ATHERTON	70	HBC	3.6 PBAR P, 7 PI.	2/74
F	(783.2)	(1.5)	BIGGS	70	CNTR	PHOTOPRODUCTION	2/74
F	FROM OMEGA-PHO INTERFERENCE IN THE PI+PI- MASS SPECTRUM						
F	ASSUMING OMEGA WIDTH 12.6 MEV.						
	260 (781.0)	12.0)	CASON	70	HBC	5.0 PI-P,4PI	. 2/74
	250 (784.1)	(1.1)	DANBURG	70	DBC	1.2 PI+ D	. 2/74
	500 (784.1)	(1.1)	DANBURG	70	CBC	1.4 PI+ D	. 2/74
	400 (784.1)	(1.1)	DANBURG	70	DBC	1.7 PI+ D	. 2/74
	580 (784.1)	(1.1)	DANBURG	70	DBC	1.9 PI+ D	. 2/74
	400 (783.1)	(1.1)	DANBURG	70	CBC	2.1 PI+ D	. 2/74
	250 (785.1)	(2.1)	DANBURG	70	CBC	2.3 PI+ D	. 2/74
	248 783.4	1.0	BIZZARRI	71	HBC	0.0 P PBAR K+K-	11/71
	510 781.0	0.6	BIZZARRI	71	HBC	0.0 P PBAR K1K1	11/71
C	4270 (784.1)	(0.3)	COYNE	71	HBC	3.7 PI+ P	11/71
C	FROM TOTAL SAMPLE OF COYNE 71. THEY OBSERVE AN IMPORTANT						
C	CORRELATION BETWEEN SIGMA OF EXP. RESOLUTION AND THE MEAS. MASS.						
D	783.7	1.0	COYNE	71	HBC	3.7 PI+ P	11/71
D	FROM BEST-RESOLUTION SAMPLE OF COYNE 71						11/71
	349 (784.0)	(1.4)	MATTHEWS	71	DBC	6.95 PI+ D	. 2/74
	418 782.5	0.8	AGUILAR	72	HBC	3.9,4.6 K- P	12/72
S	10000 (782.4)	10.5)	BINNIE	73	CNTR	PI-P, OMEGA N	12/75*
A	BINNIE 73 SUPERSEDED BY KEYNE 76						
S	4800 782.0	0.8	OREN	74	HBC	2.3 PBAR P,5PI	12/75*
S	ERROR INCLUDES 0.5 MEV MASS SCALE ERROR						
	29300 (782.9)	10.3)	ROOS	74	RVUE	0-3.6 PBAR P	12/75*
S	10000 782.4	0.5	KEYNE	76	CNTR	PI-P, OMEGA N	12/75*
S	OBSERVED BY THRESHOLD-CROSSING TECHNIQUE. MASS RESOL.=4.8 MEV FWHM						
	AVG 782.61	0.30	AVERAGE (ERROR INCLUDES SCALE FACTOR OF 1.4)				
	STUDENT 782.66	0.27	AVERAGE USING STUDENT10TH/I.11) -- SEE TEXT				

(SEE IDEOGRAM BELOW)

WEIGHTED AVERAGE = 782.61 ± 0.30
ERROR SCALED BY 1.4

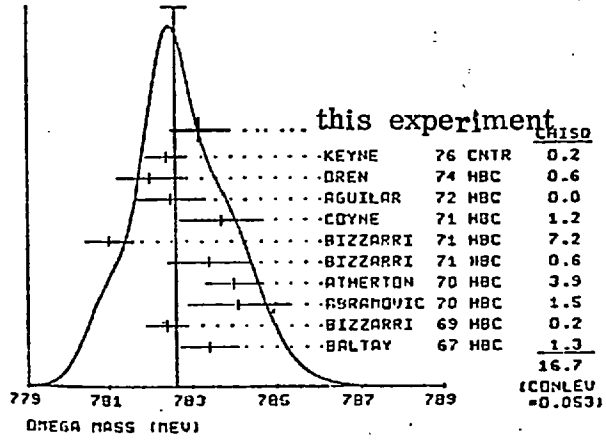

This plot is reproduced from reference (6)

Fig (6 - 3)

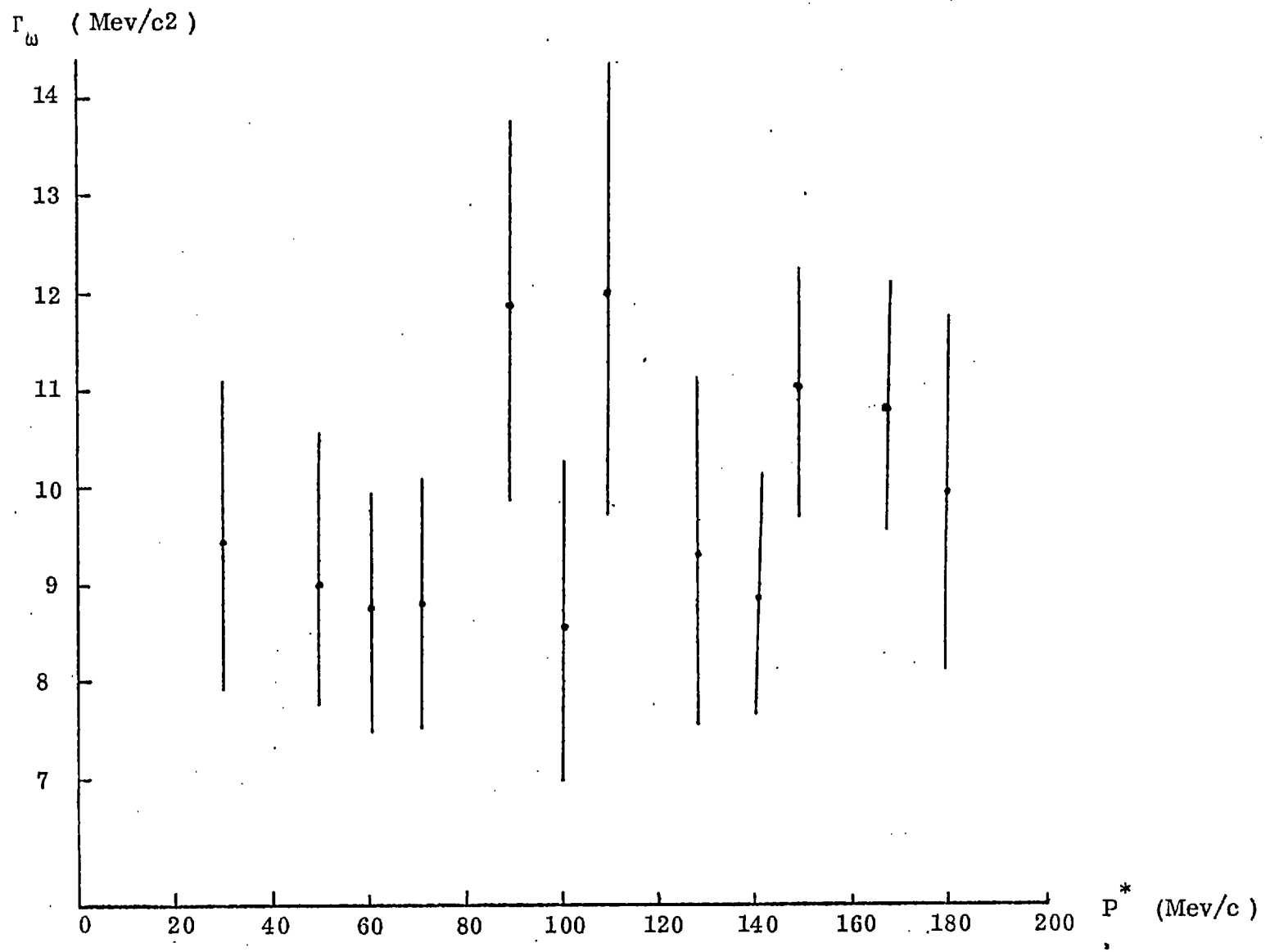

Width of the ω plotted as a function of P^* .

Fig (6 - 4)

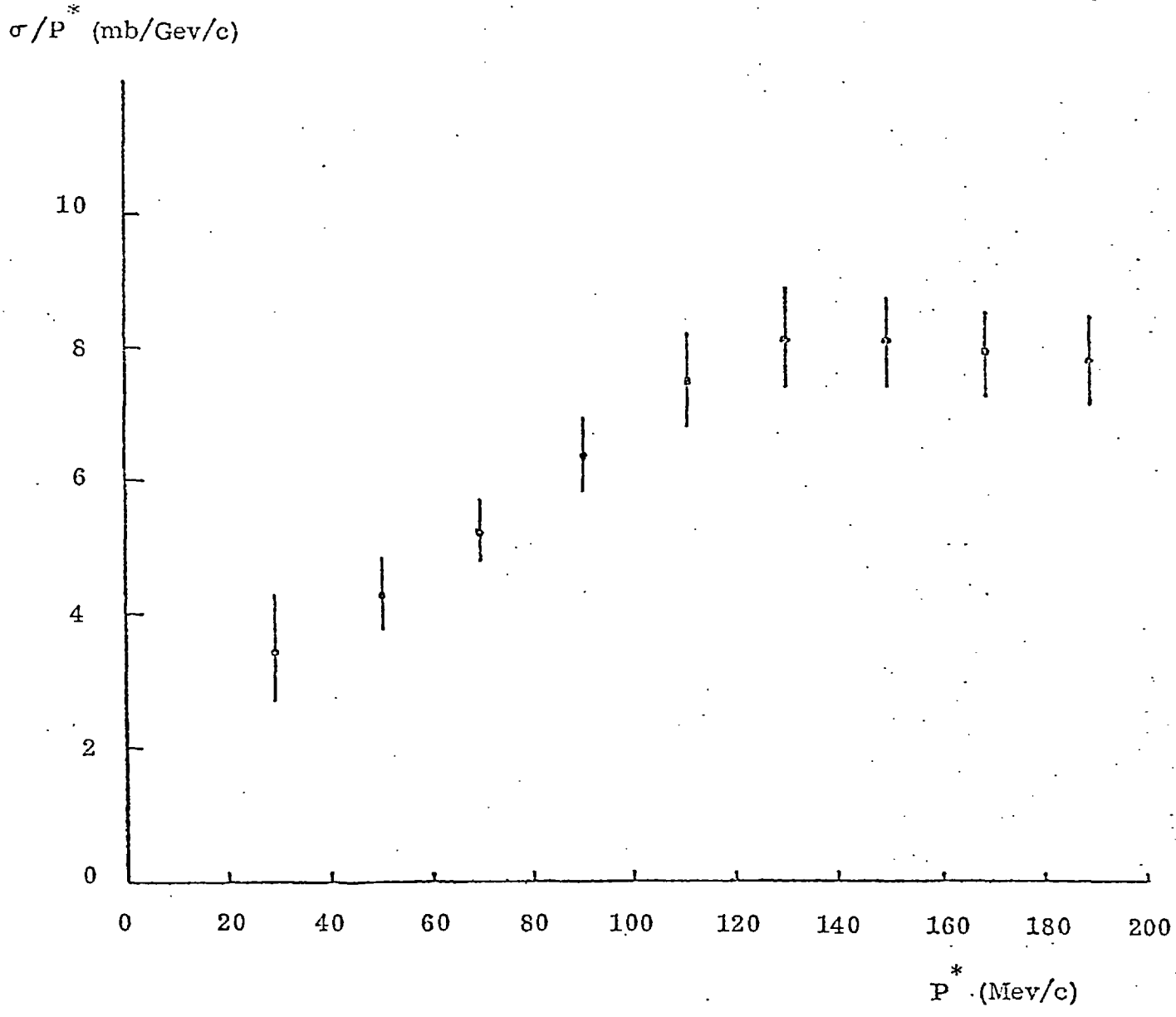

The behaviour of σ/p^* as a function of p^* for ω production in $\pi^- p \rightarrow \omega n$.

Fig(6-5)

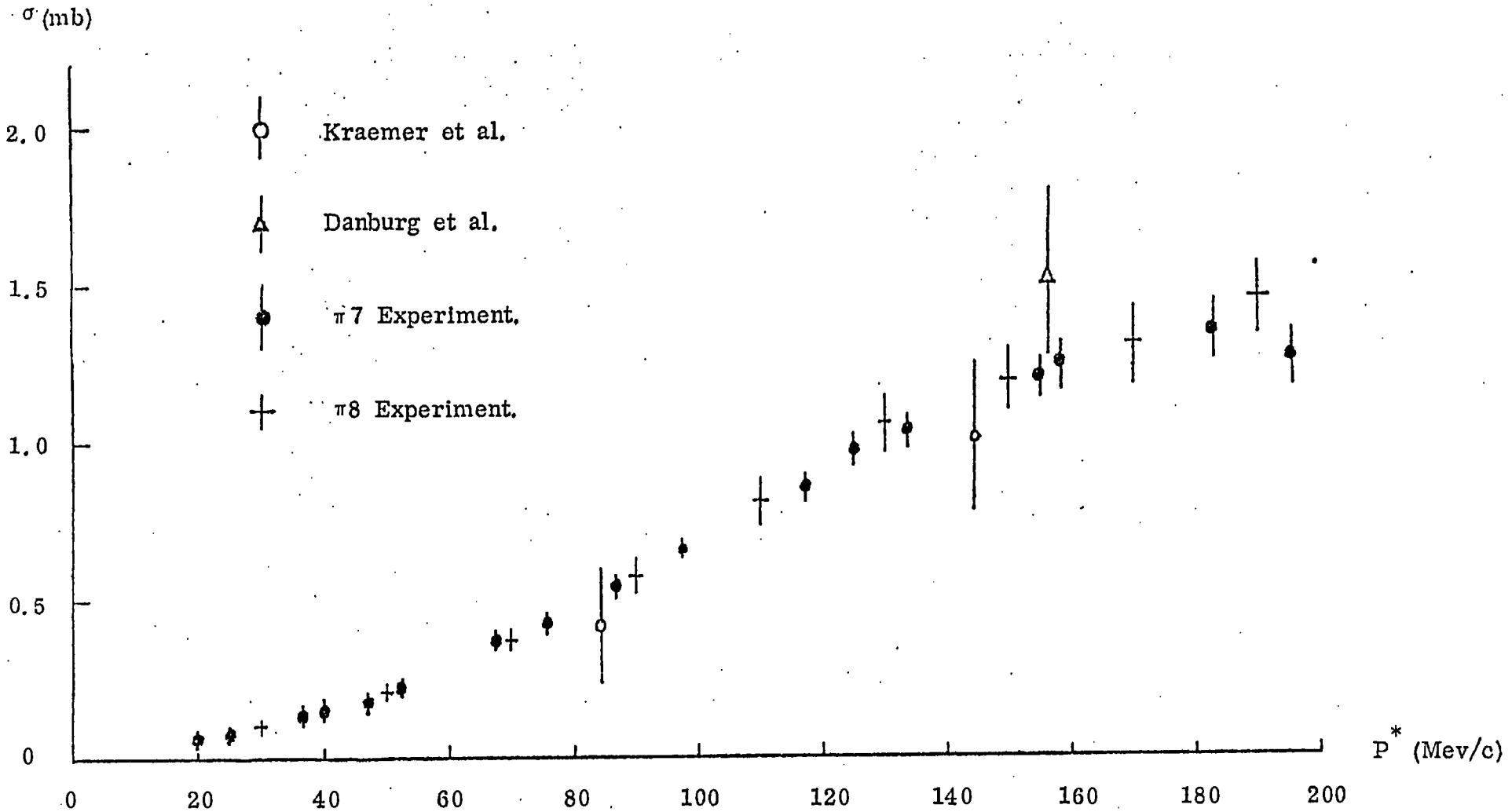

The total cross section of the ω production as a function of P^*.

Fig (6 - 6)

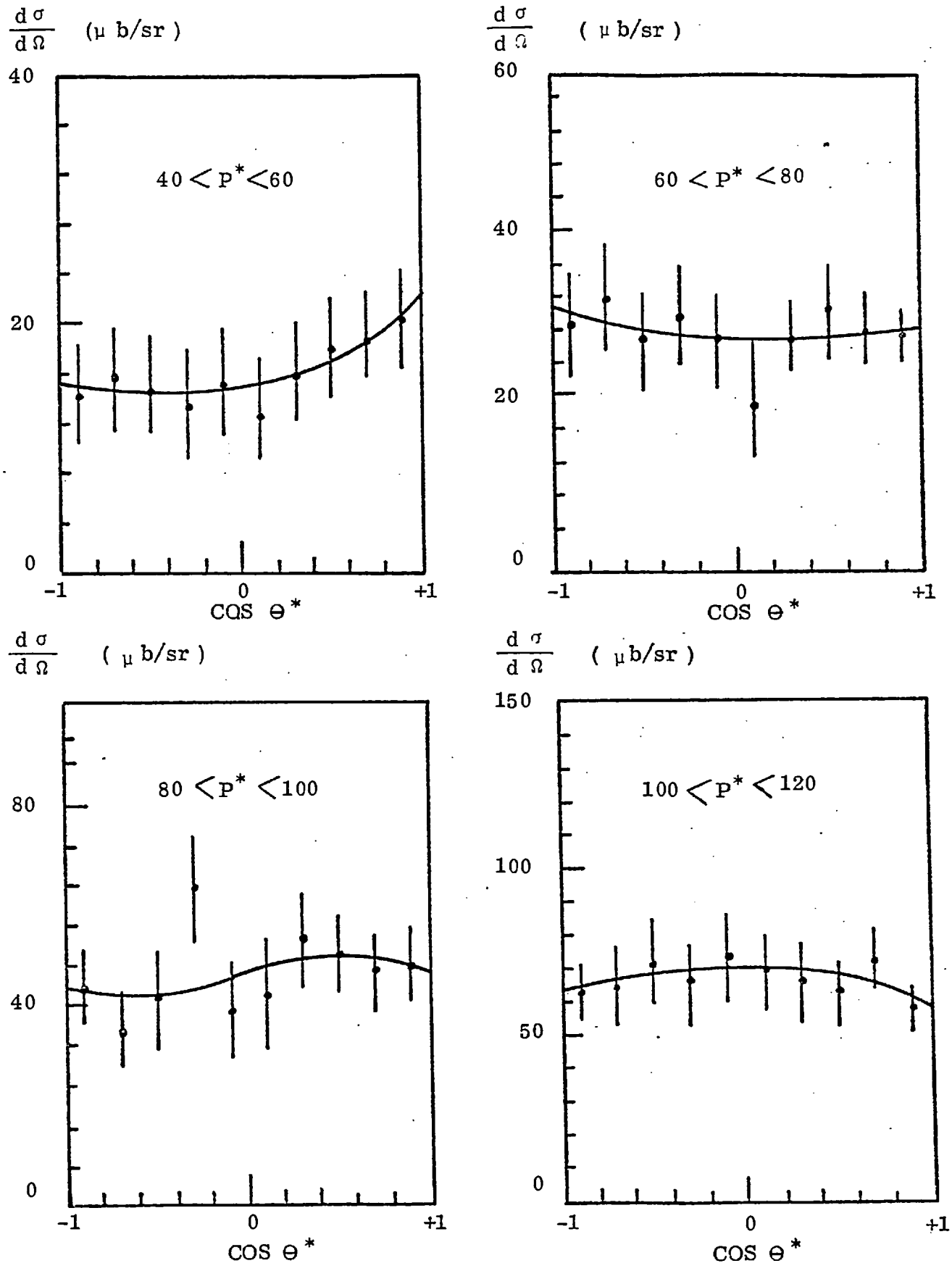

Angular distribution of the ω production in the reaction $\bar{\pi}^- + P \longrightarrow \omega + n$.

Fig (6 - 7)

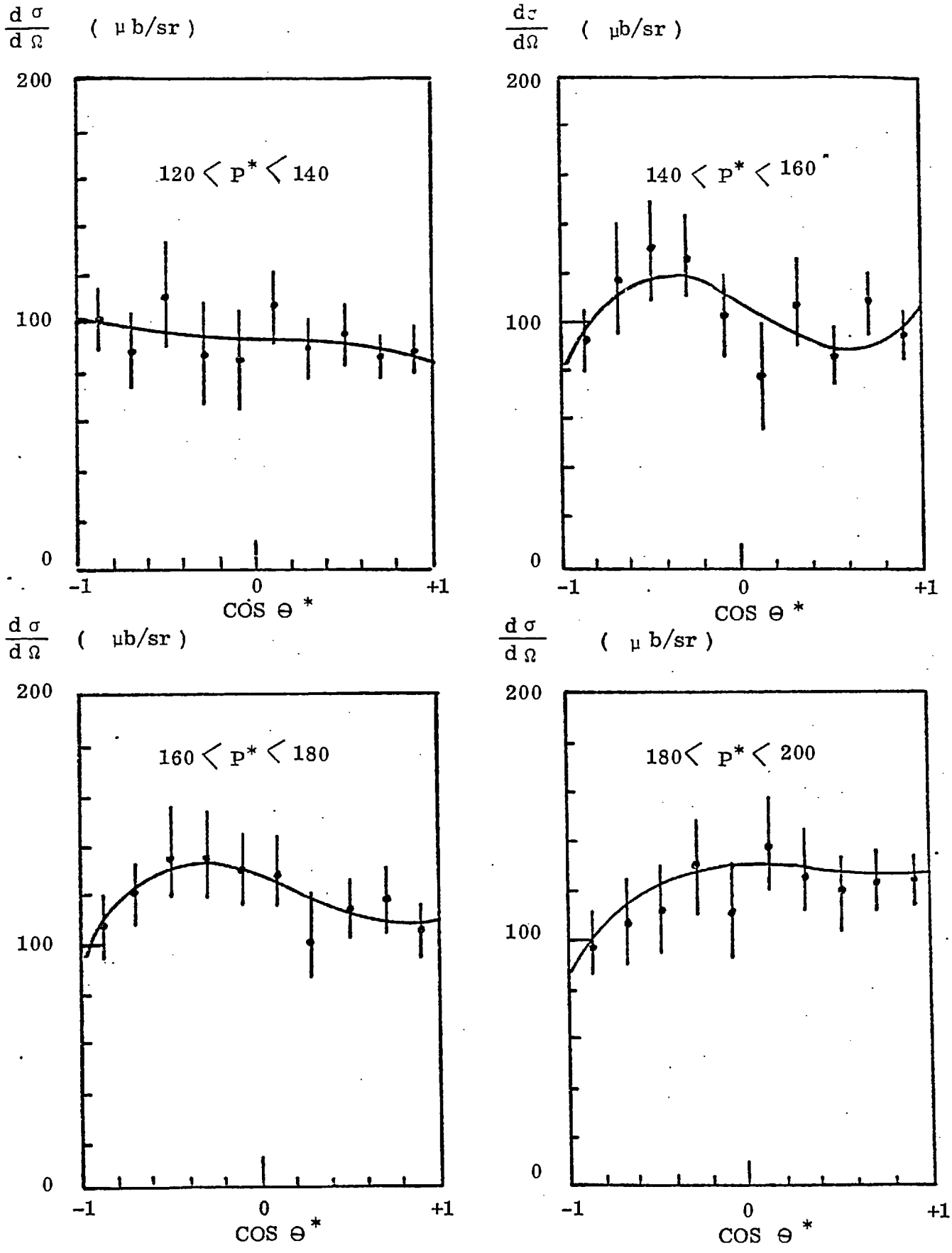

Angular distribution 0f the ω production in the reaction $\pi^- + P \longrightarrow \omega + n$.

Fig (6 - 7)

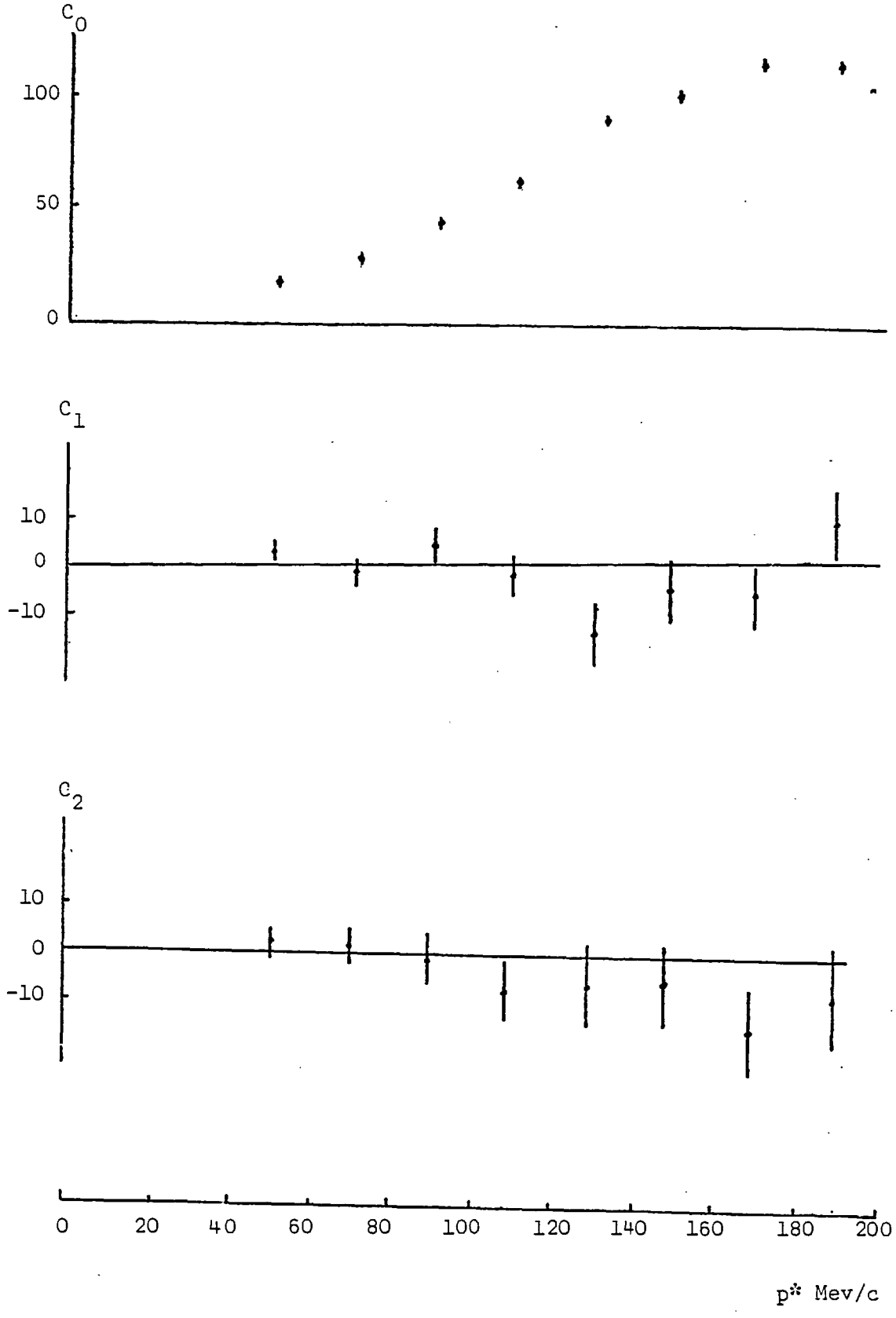

Legendre polynomial coefficients obtained by fits to $\pi^- p \rightarrow \omega n$ differential cross-sections as a function of p*.

Fig(6-8)

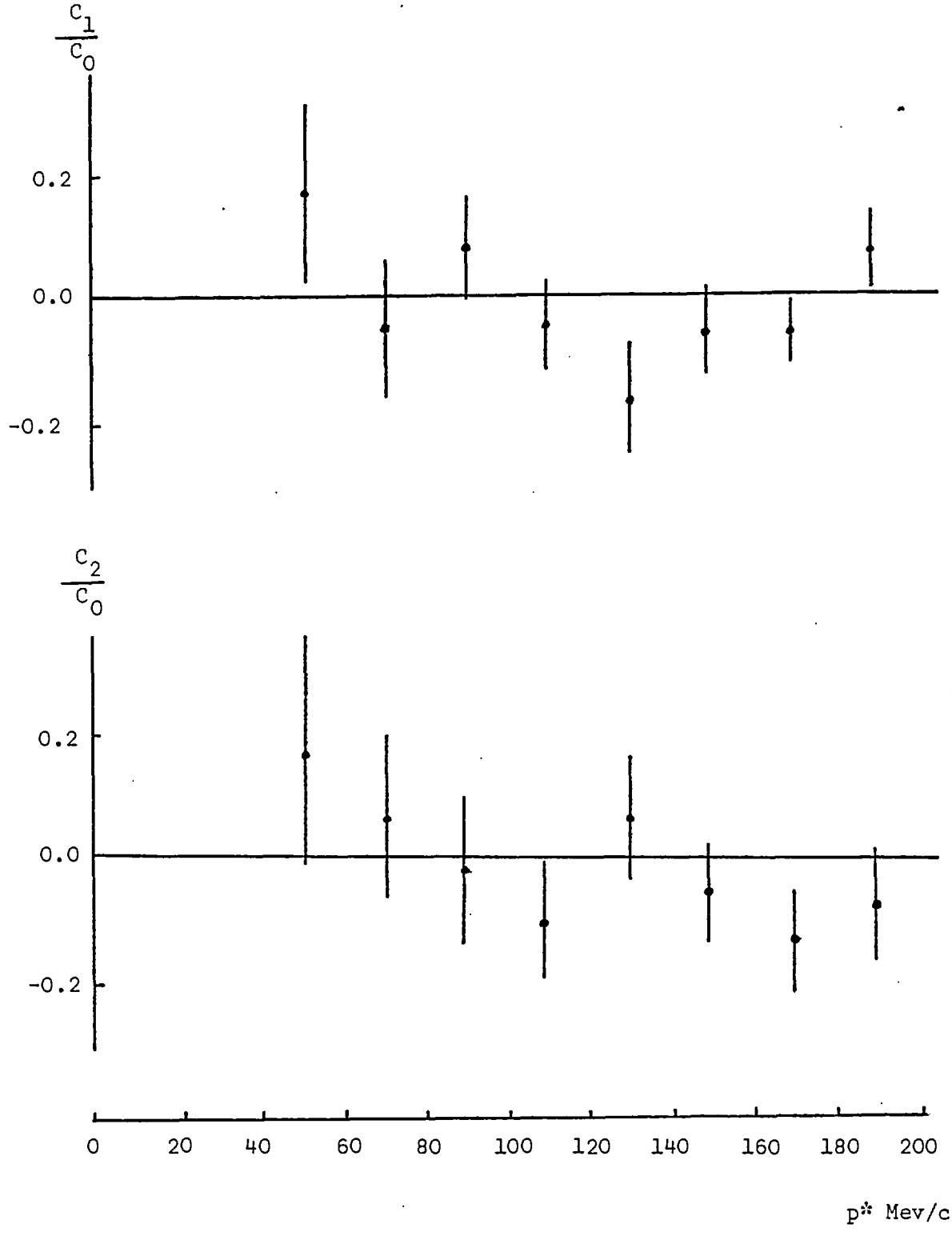

Ratios of the Legendre polynomial coefficients to C_0 from fits to the differential cross-section as a function of p*.

Fig(6-9)

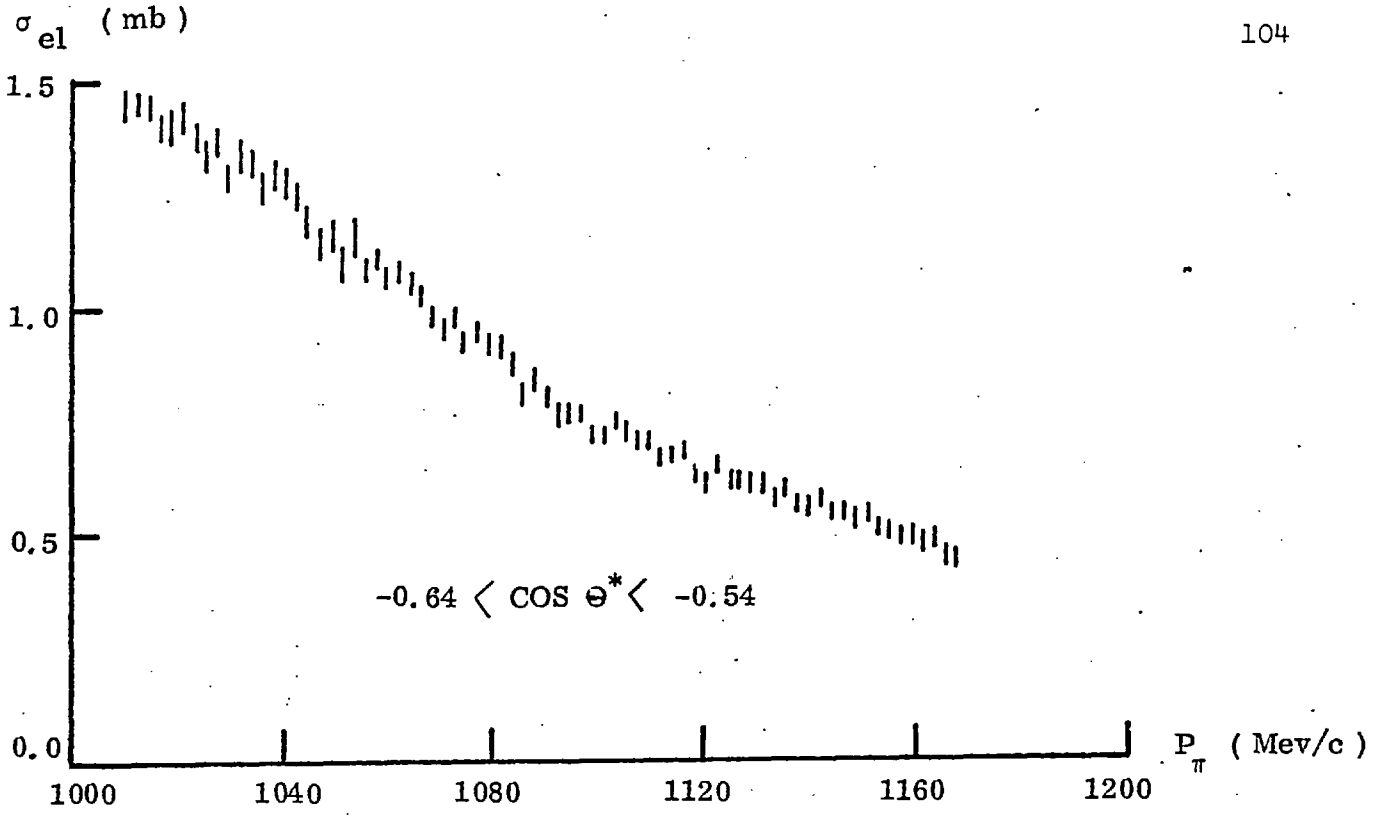

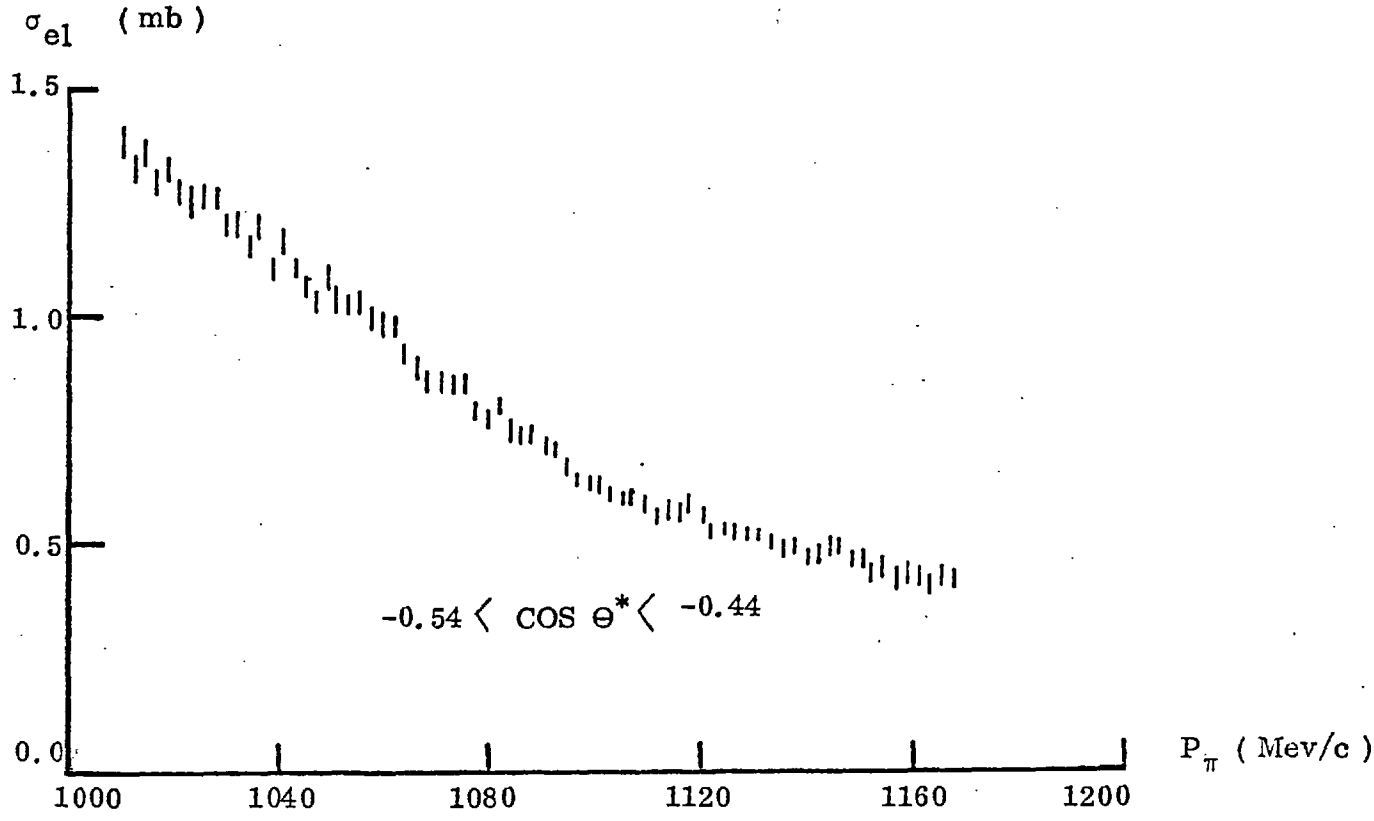

$\pi^- P$ elastic cross-sections as a function of p_{π^-} .

Fig (6 - 10)

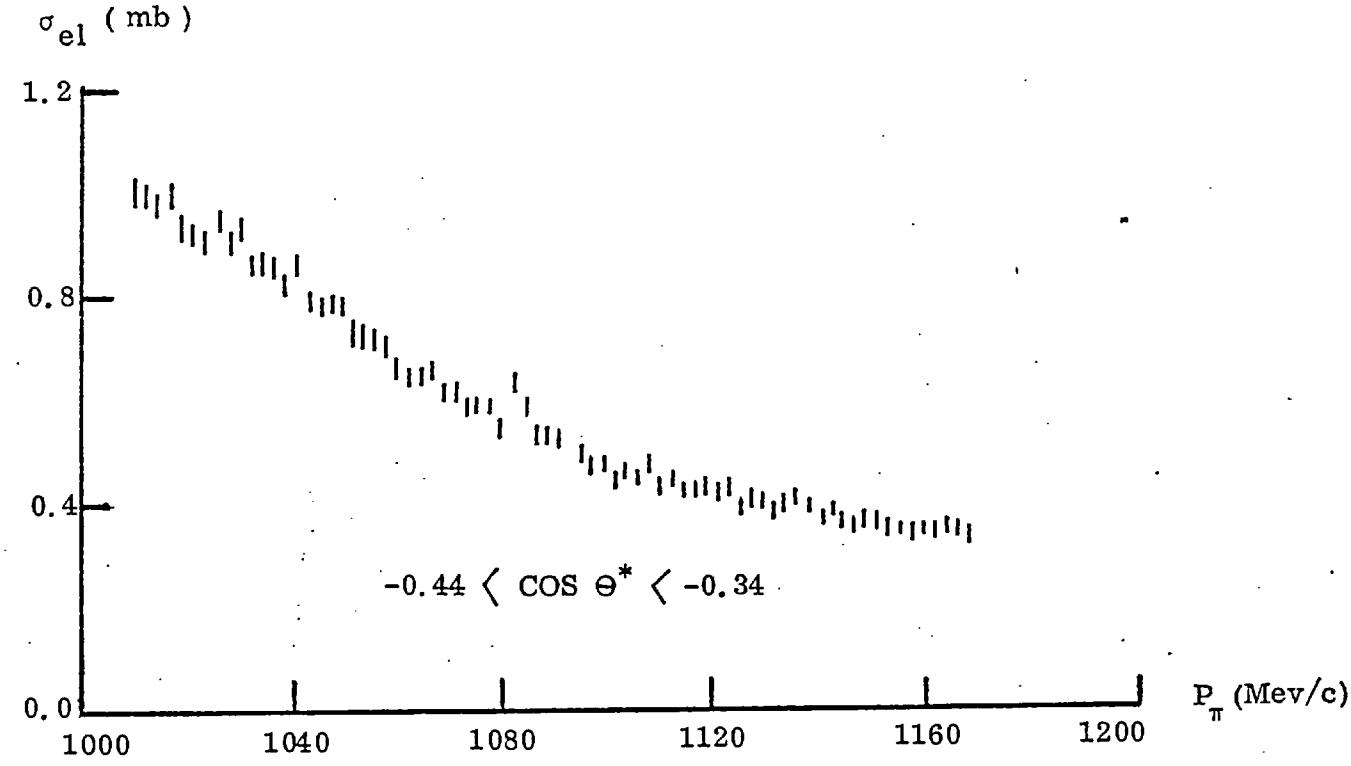

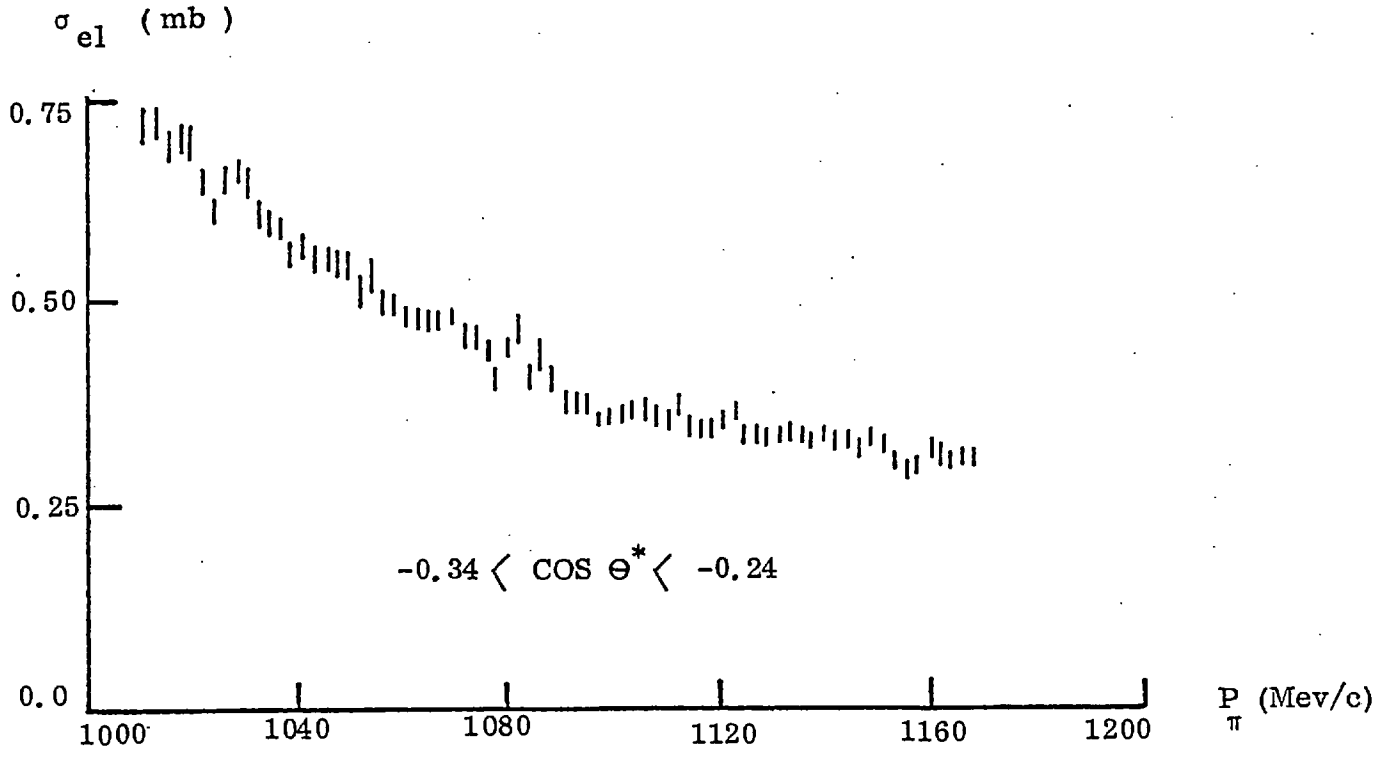

π^- P elastic cross-sections as a function of P_{π^-}

Fig (6 - 10)

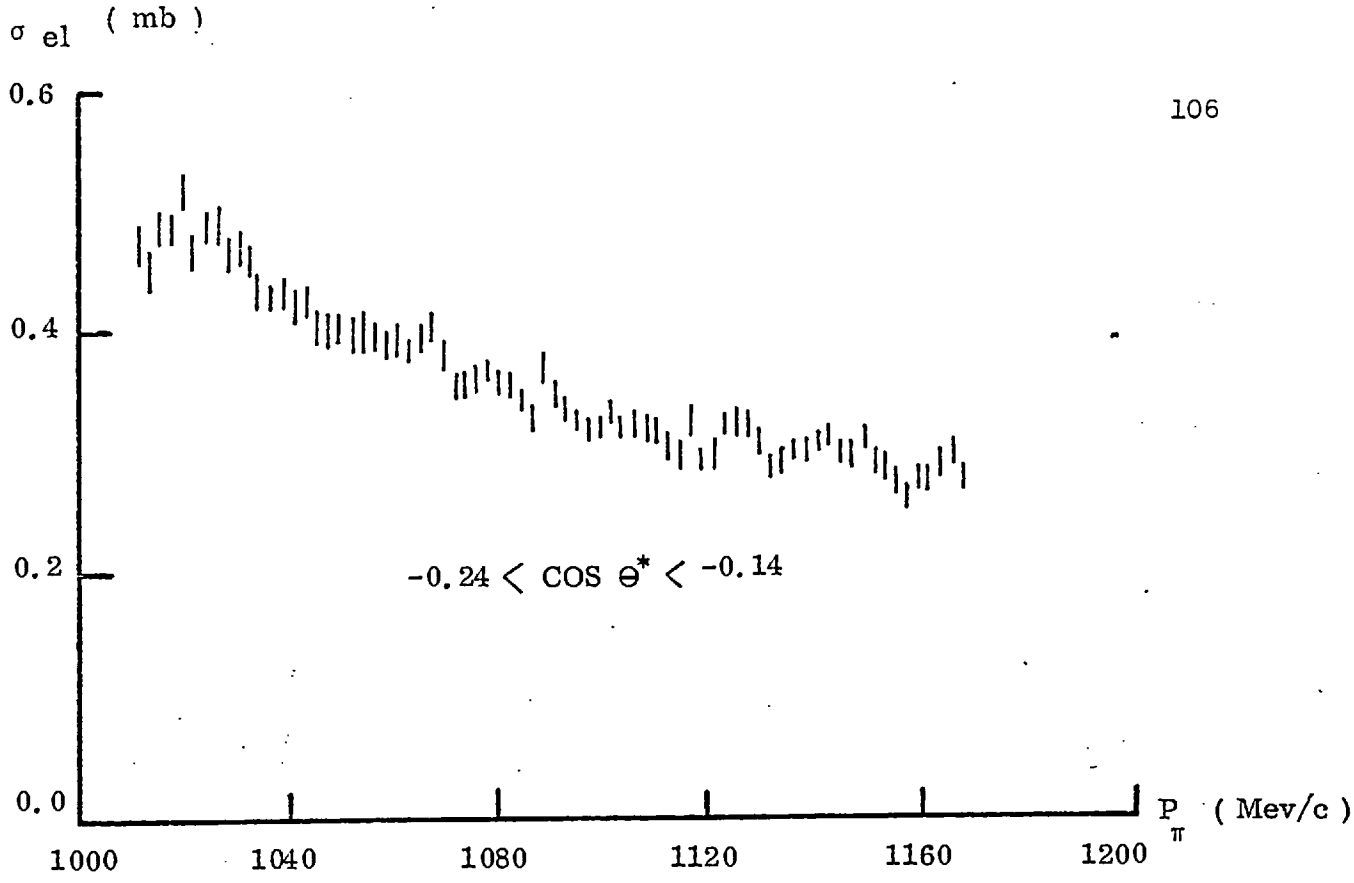

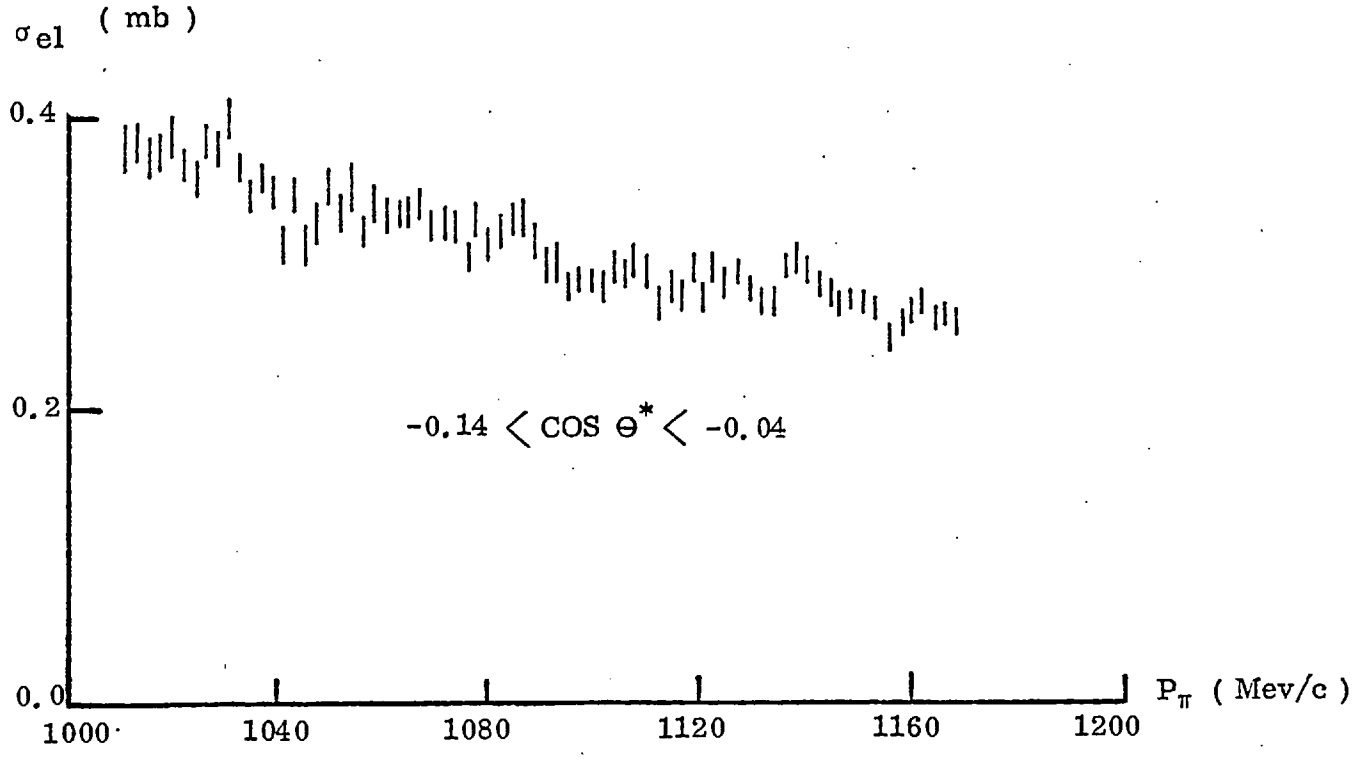

$\pi^- P$ elastic cross-sections as a function of P_{π^-}.

Fig (6 - 10)

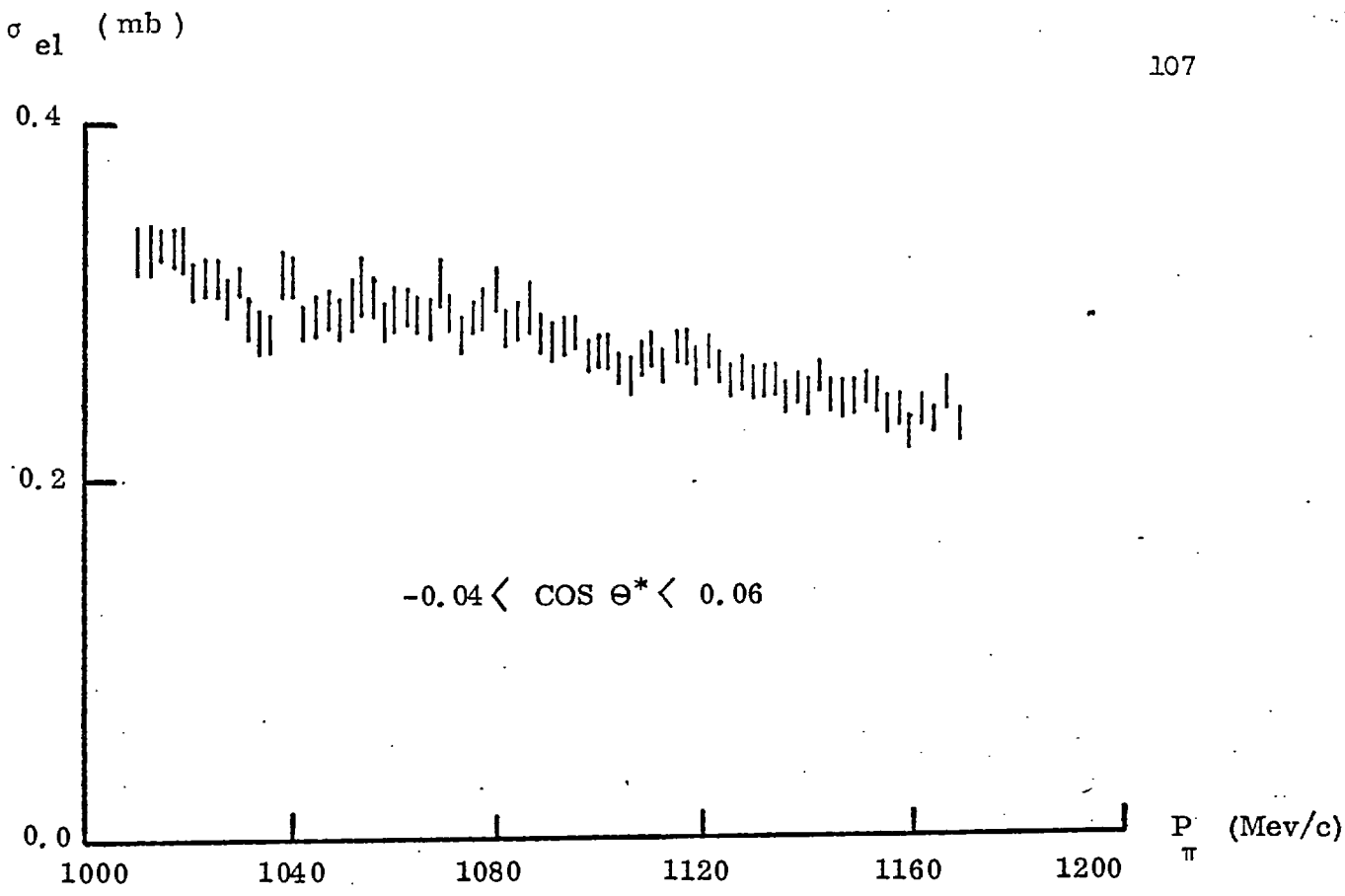

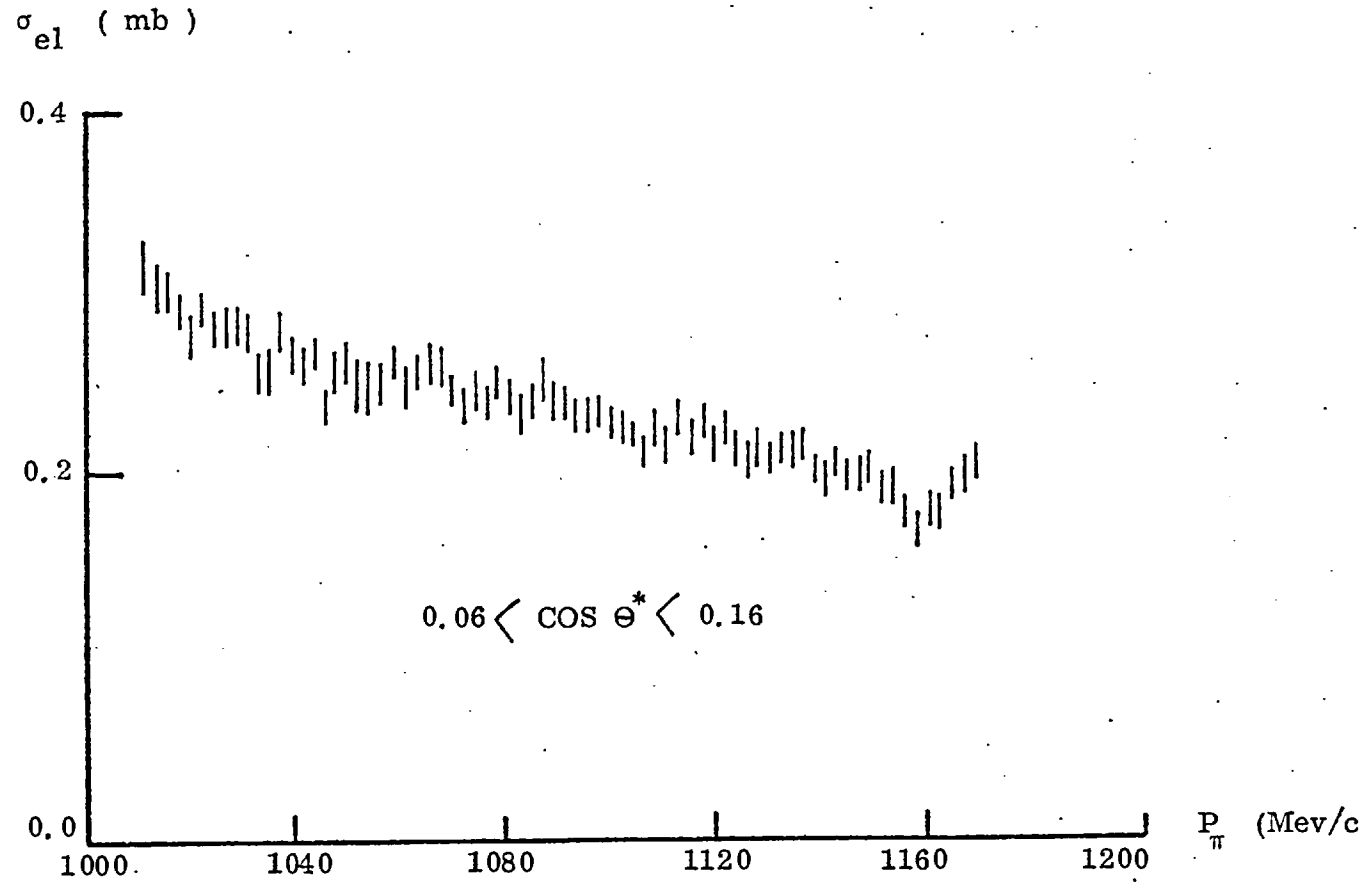

$\pi^- P$ elastic cross-sections as a function of P_{π^-}.

Fig (6 - 10)

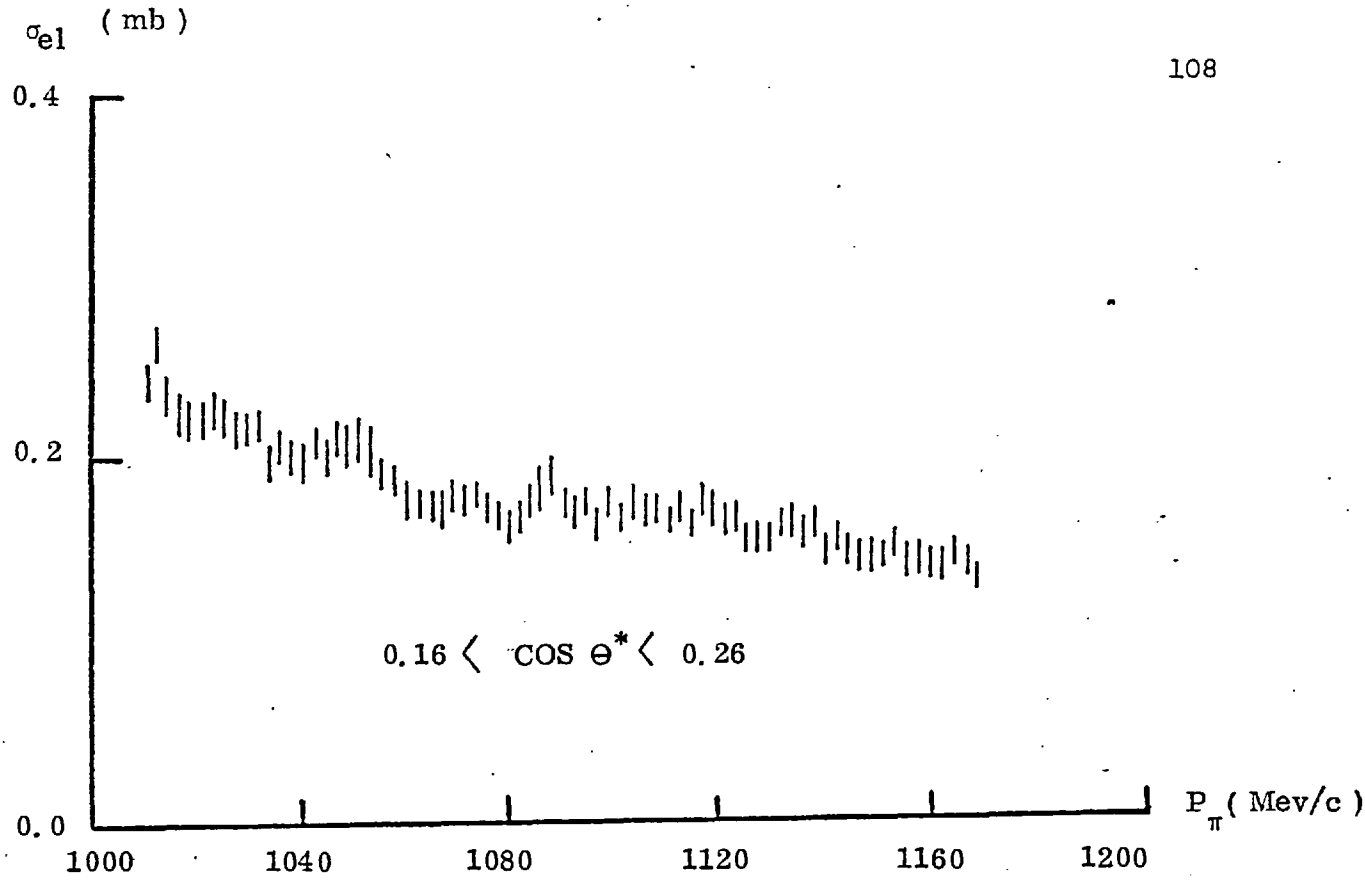

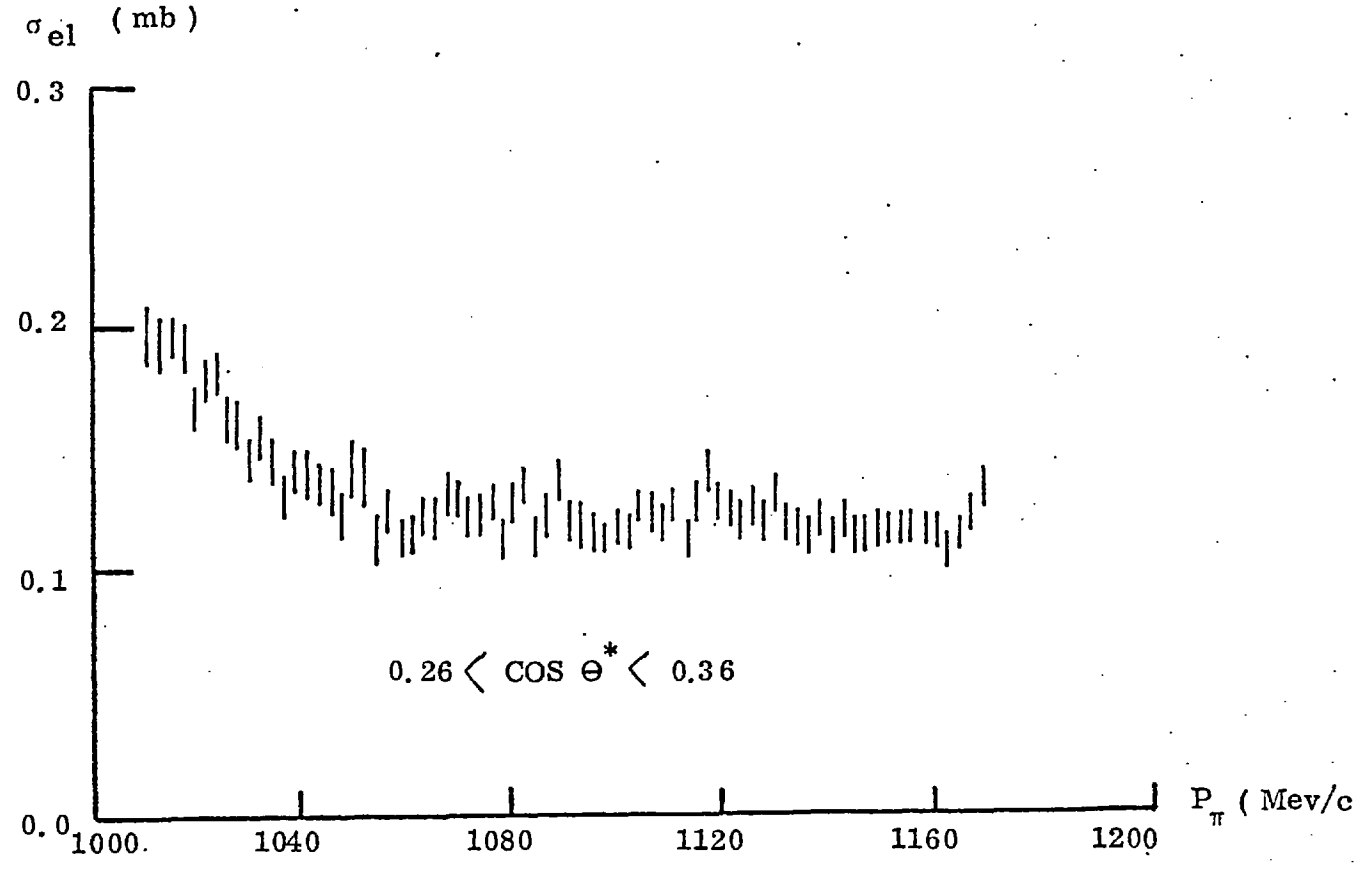

$\pi^- P$ elastic cross-sections as a function of P_{π^-} .

Fig (6 - 10)

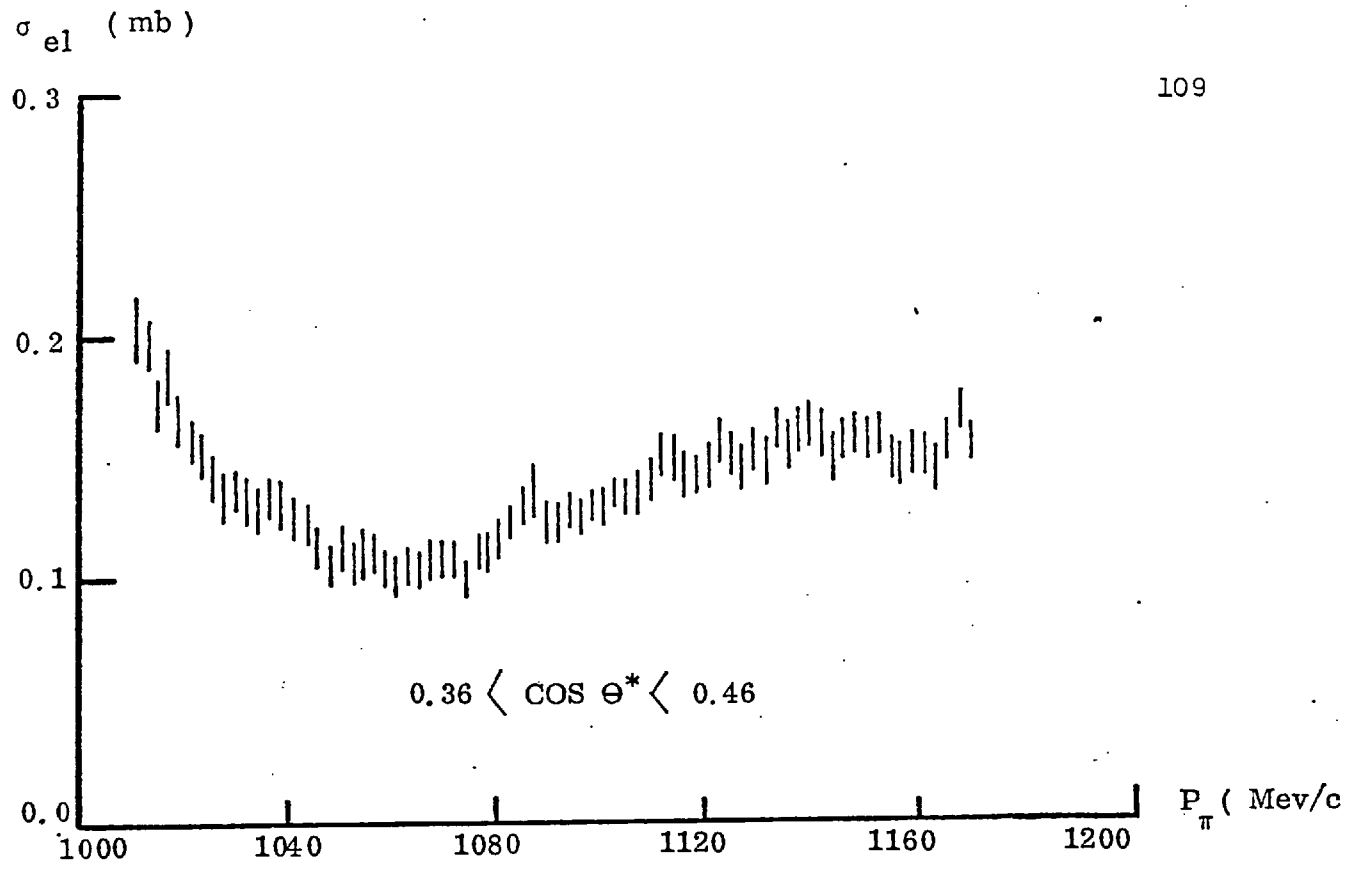

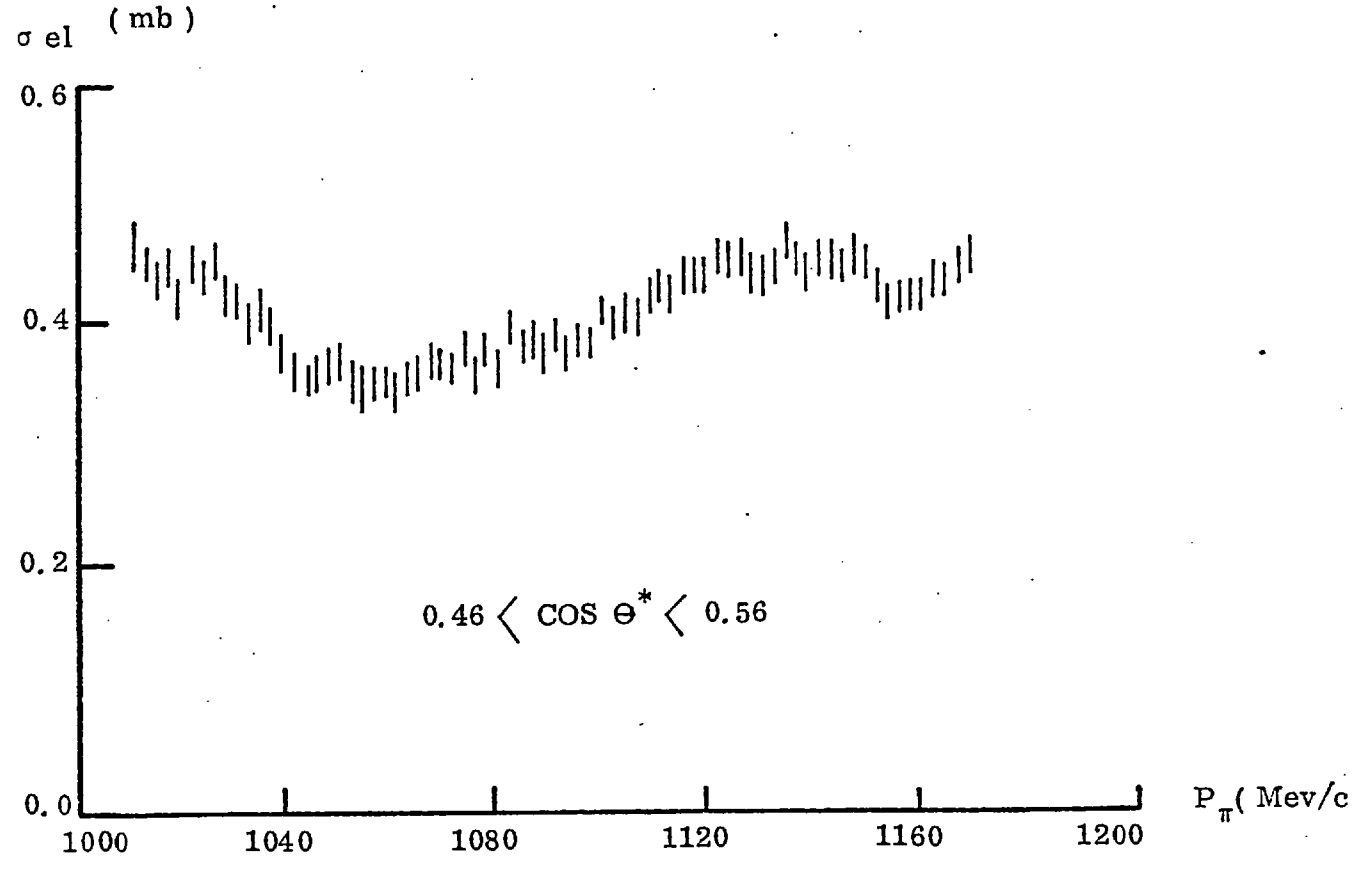

$\pi^- P$ elastic cross-sections as a function of P_{π^-} .

Fig (6 - 10)

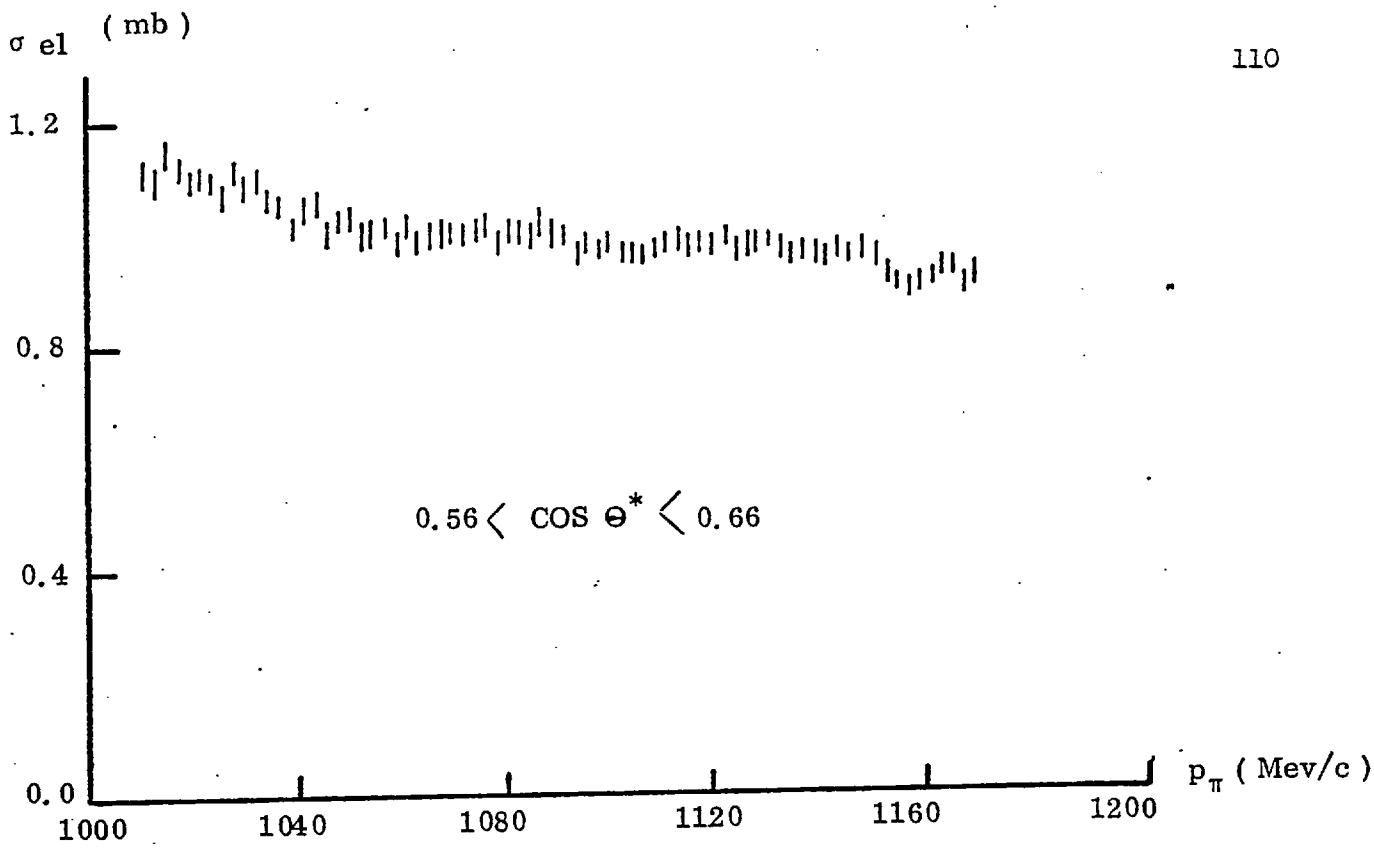

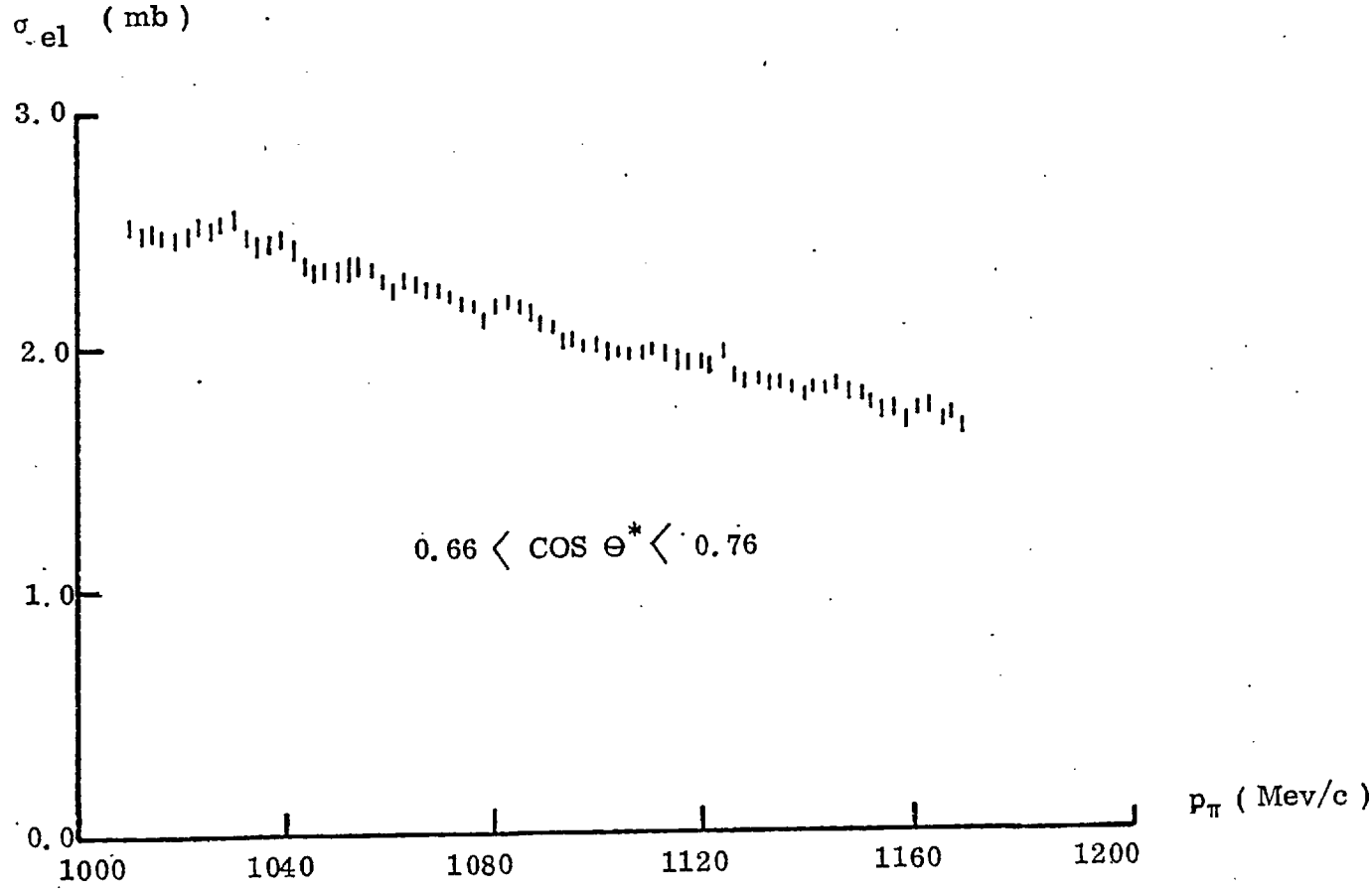

$\pi^- P$ elastic cross-sections as a function of P_{π^-}.

Fig (6 - 10)

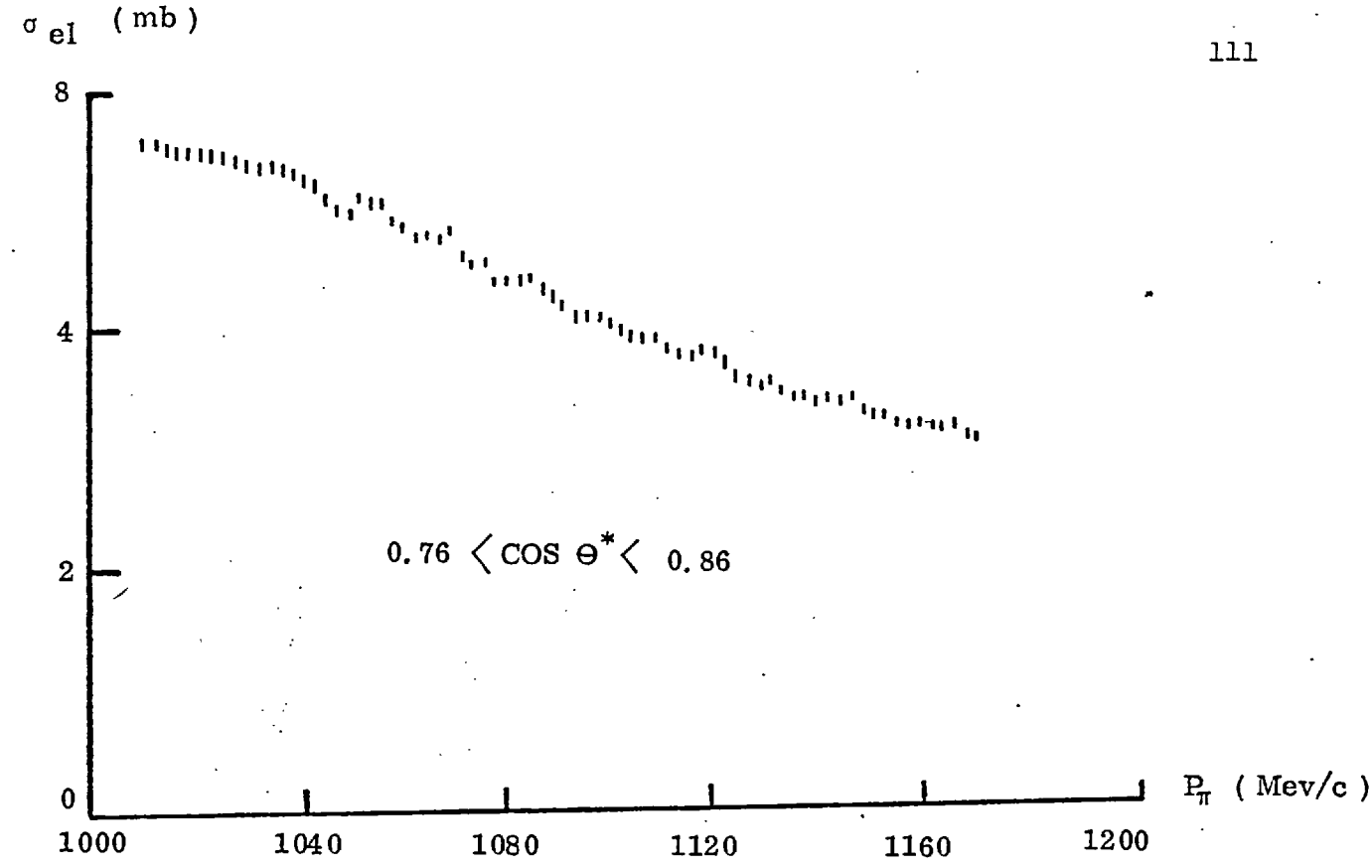

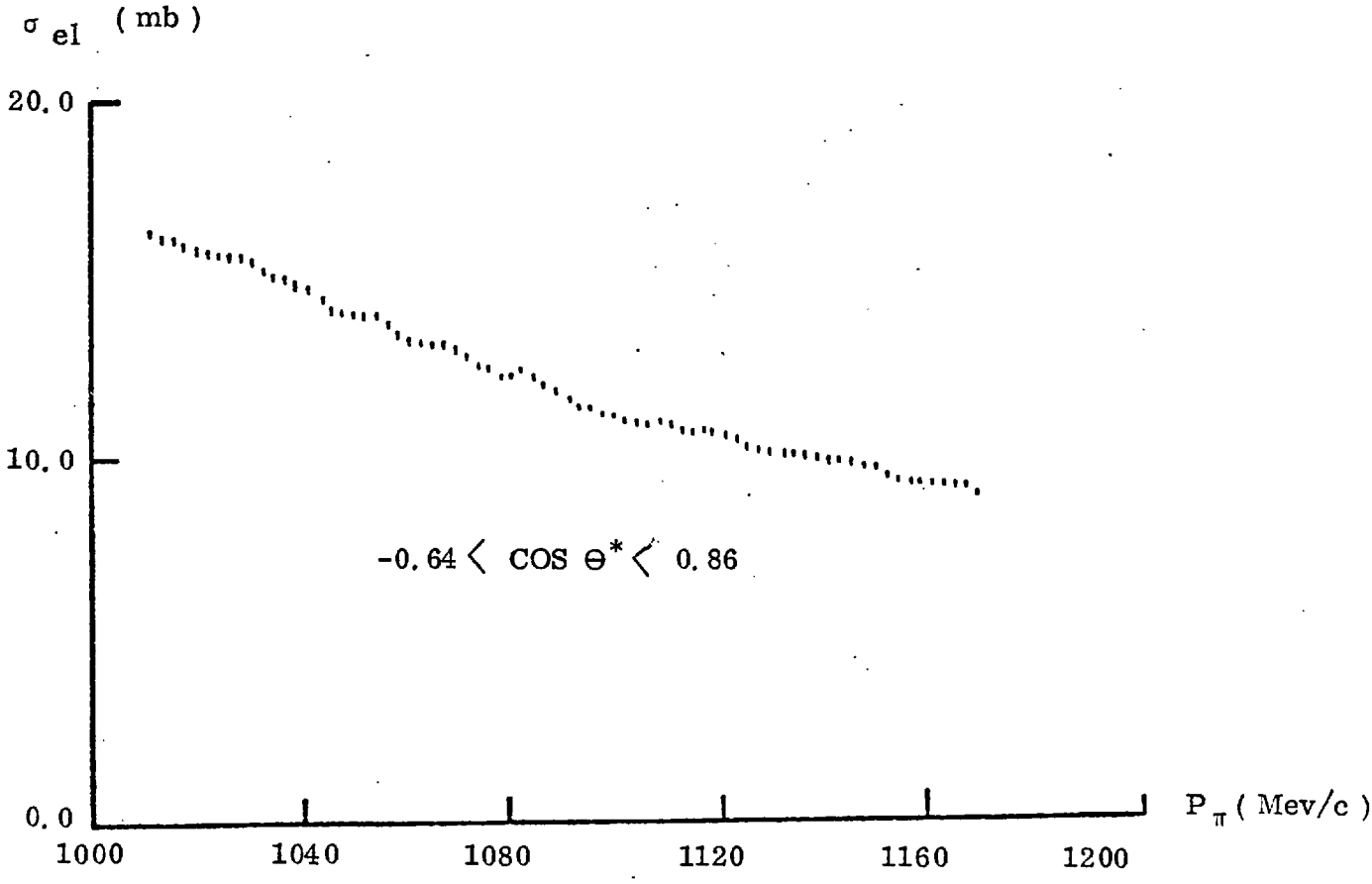

$\pi^- P$ elastic cross-sections as a function of P_{π^-} .

Fig (6 - 10)

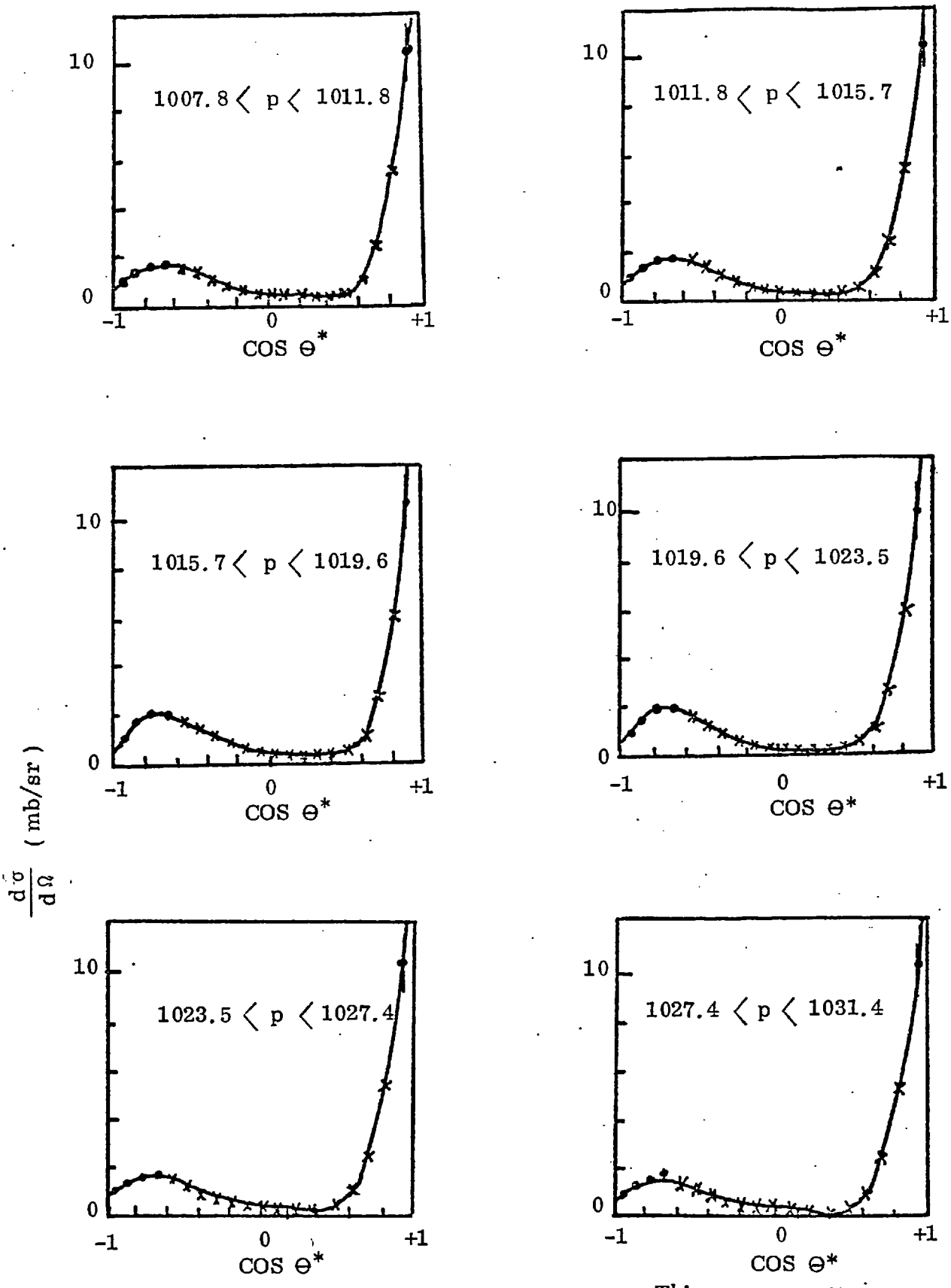

$\bar{\pi}P$ differential cross-section .

Fig (6 - 11)

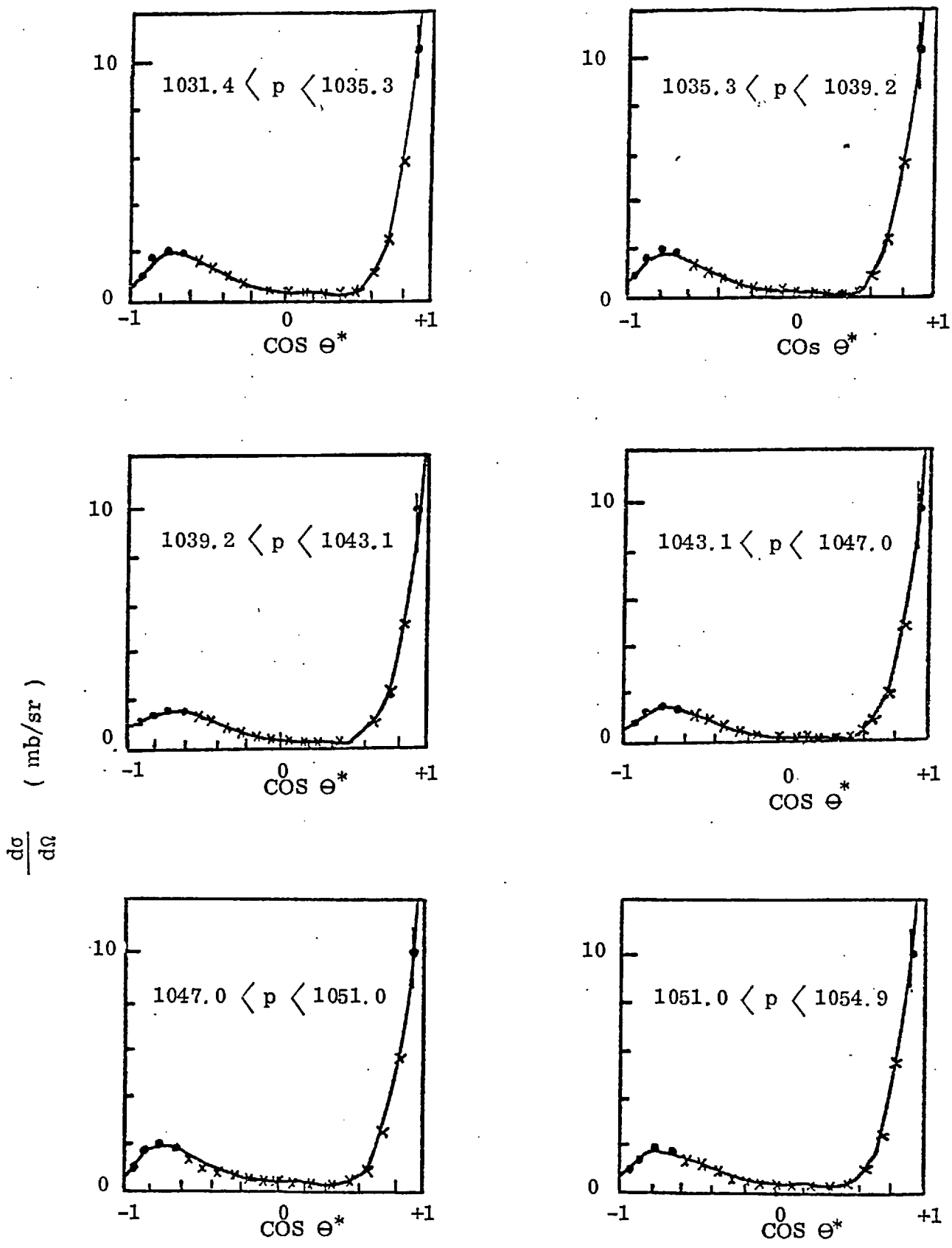

$\bar{\pi}P$ differential cross-section .

This exp x

Ref (20) •

Fig (6 - 11)

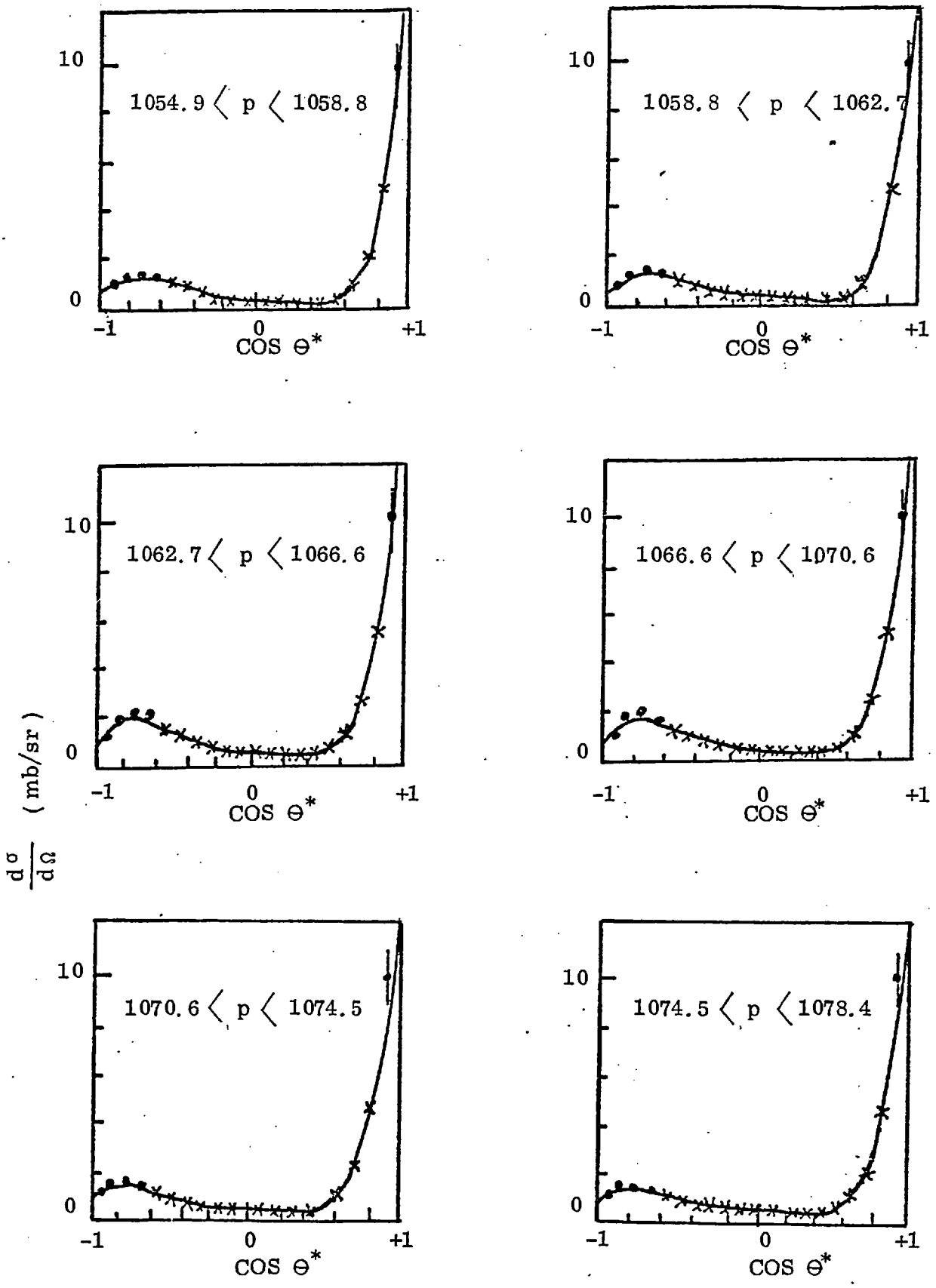

$\pi^- P$ differential cross-section . This exp x

Ref (20) •

Fig (6 - 11)

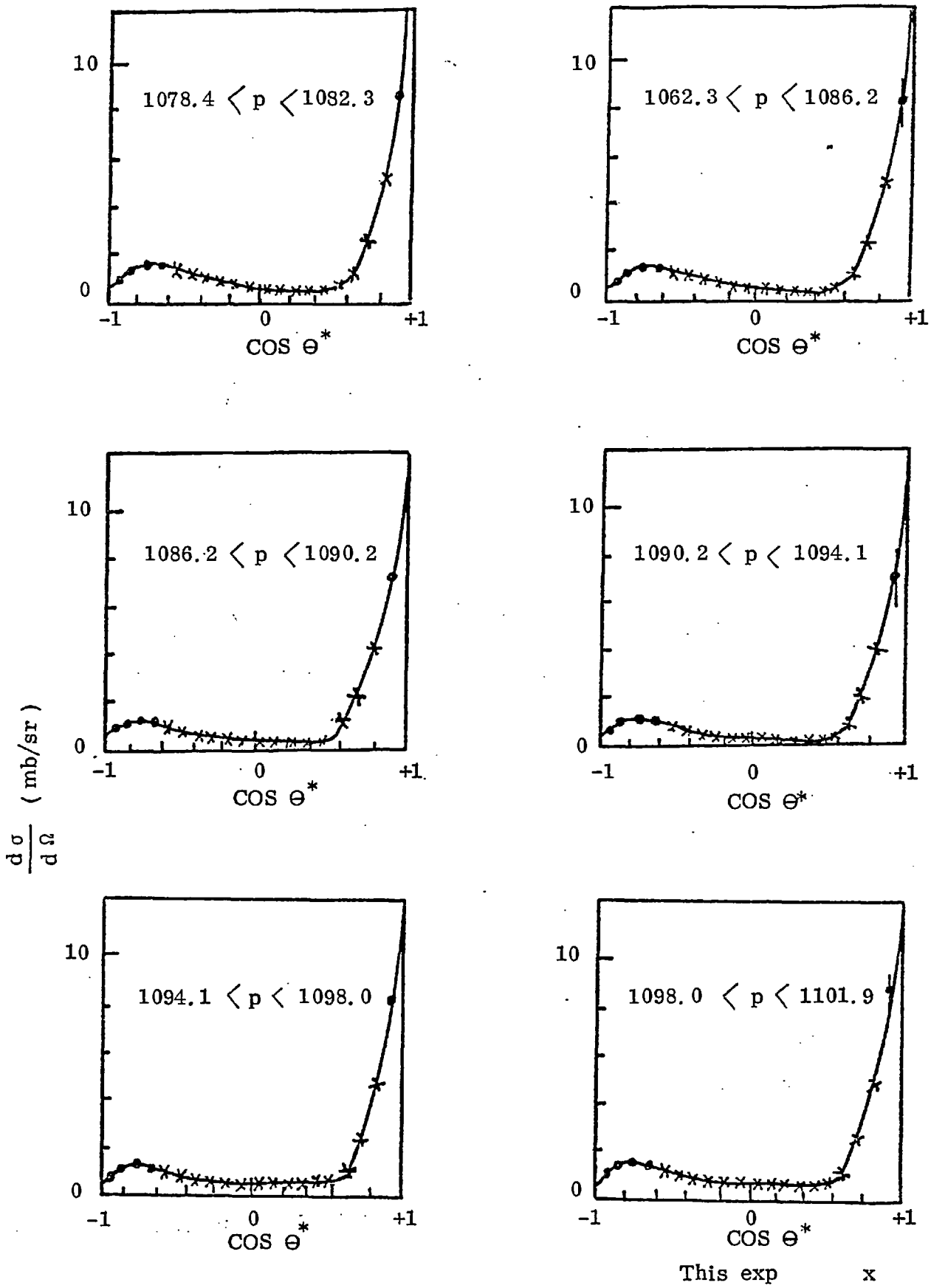

$\pi^- P$ differential cross-section .

Fig (6 - 11)

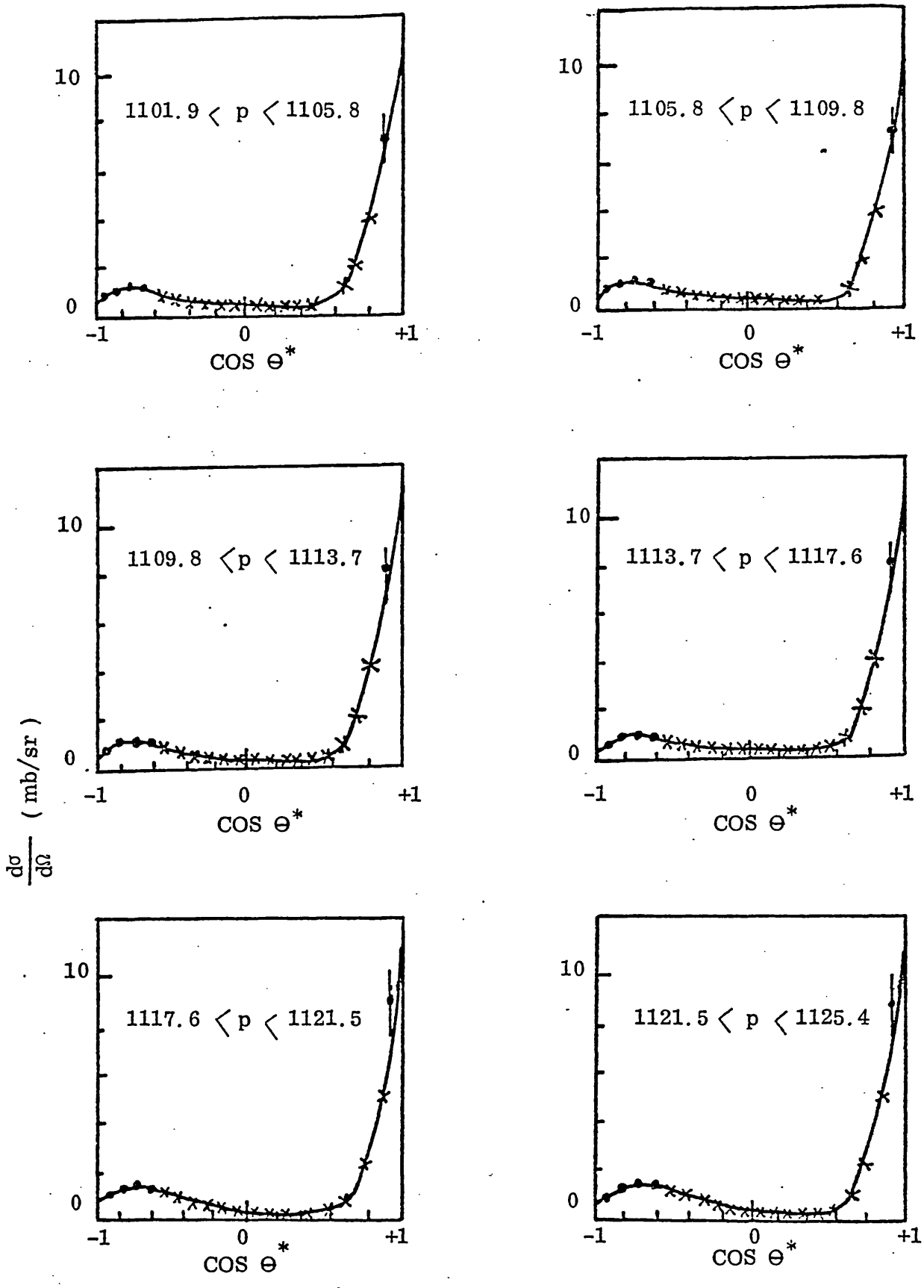

$\pi^- P$ differential cross-section .

Fig (6 - 11)

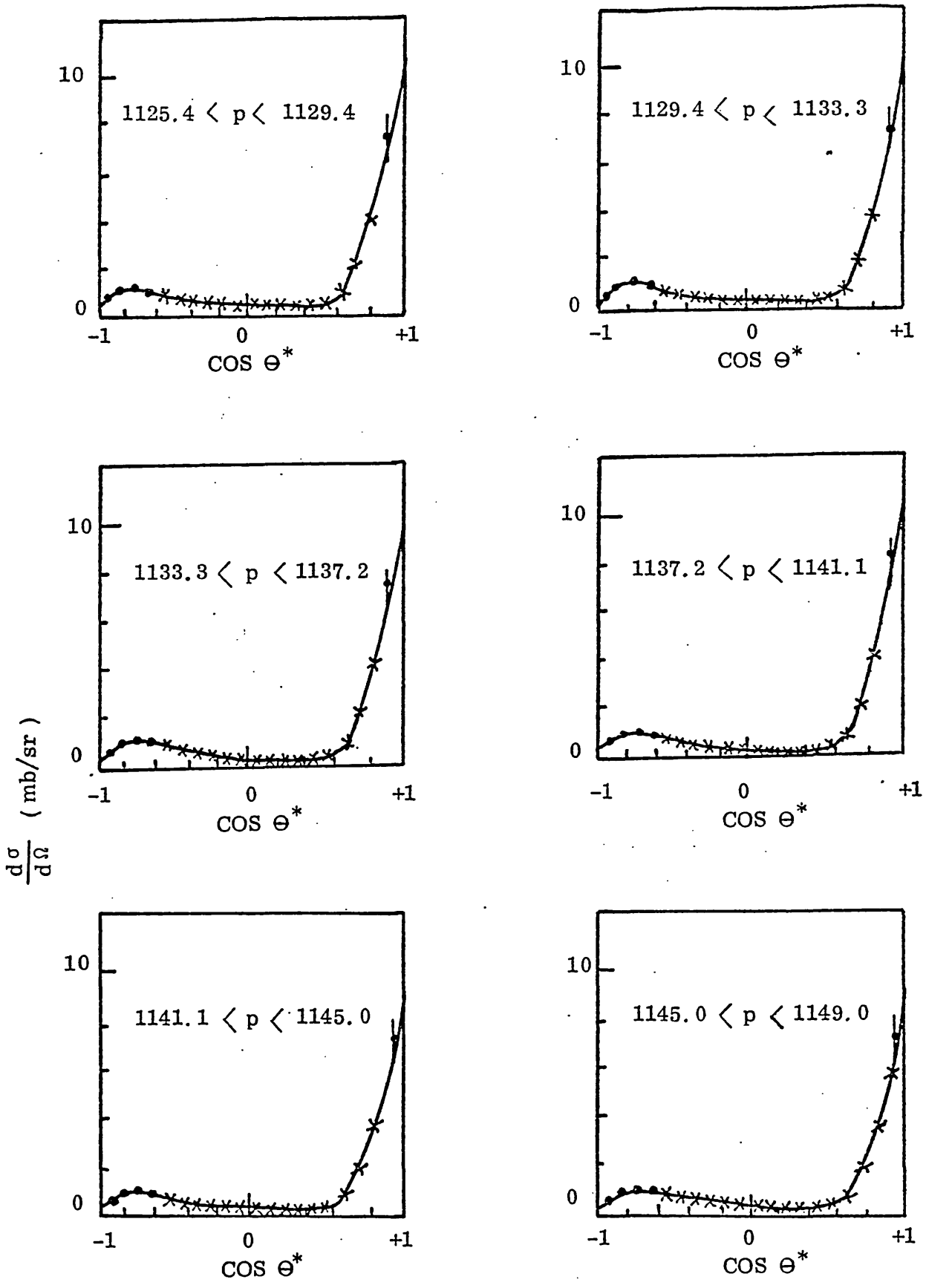

$\bar{\pi}$P differential cross-section .

Fig (6 - 11)

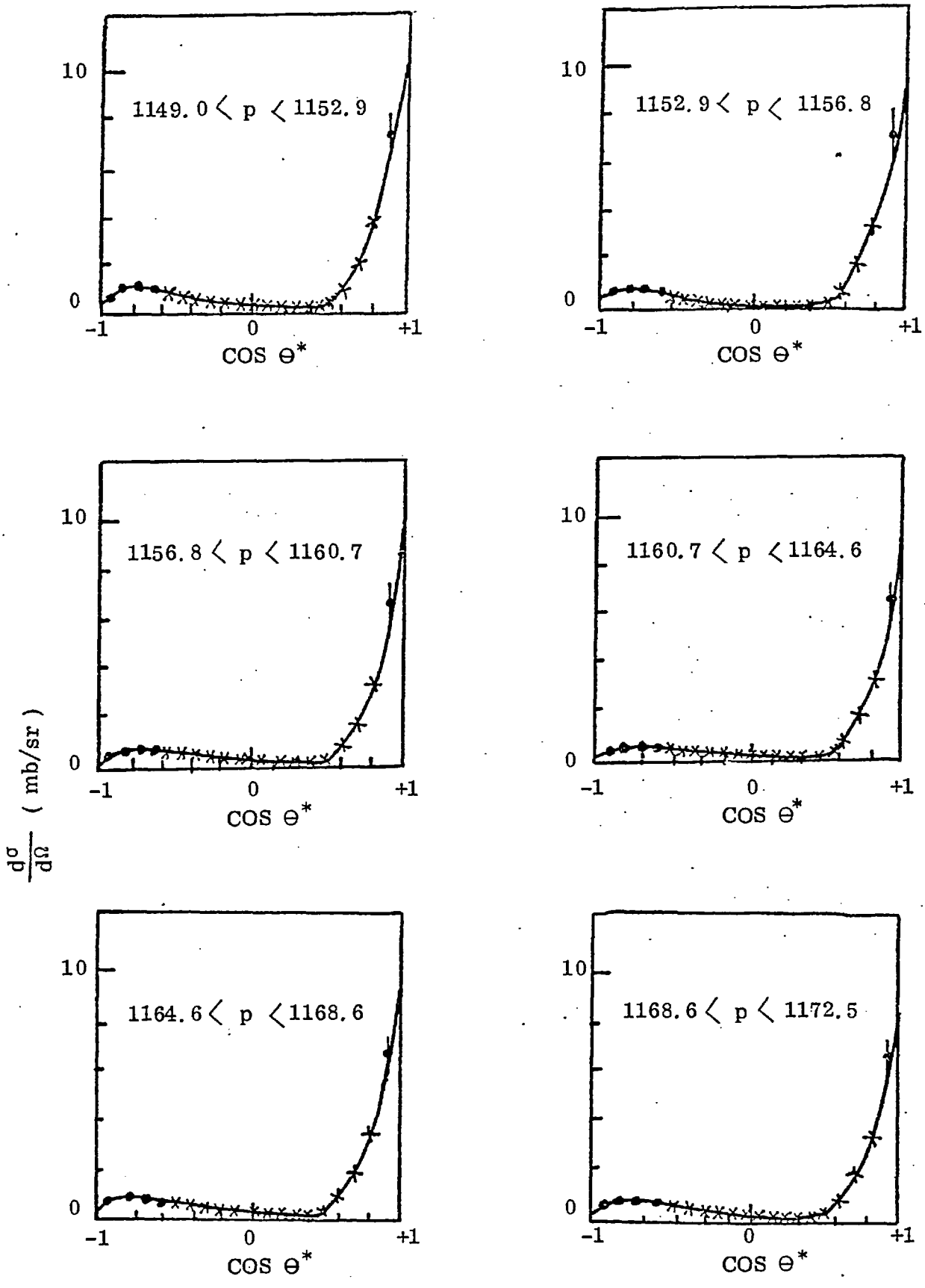

$\bar{\pi}P$ differential cross-section .

Fig (6 - 11)

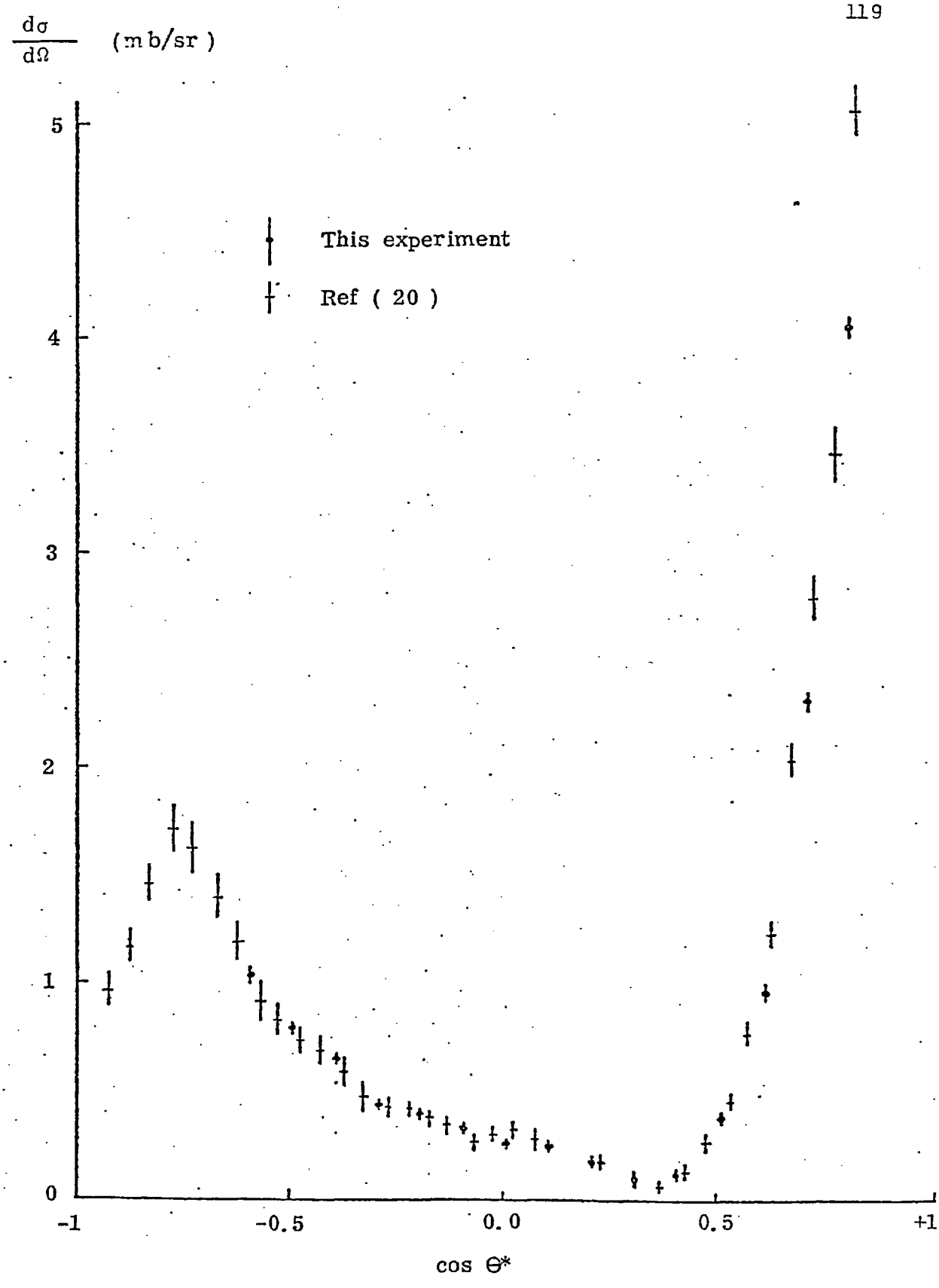

A comparison of the angular distribution of the π^-p elastic differential cross-section at p_π=1.101 Gev/c, between this experiment and that of Ref(20).

Fig(6-12)

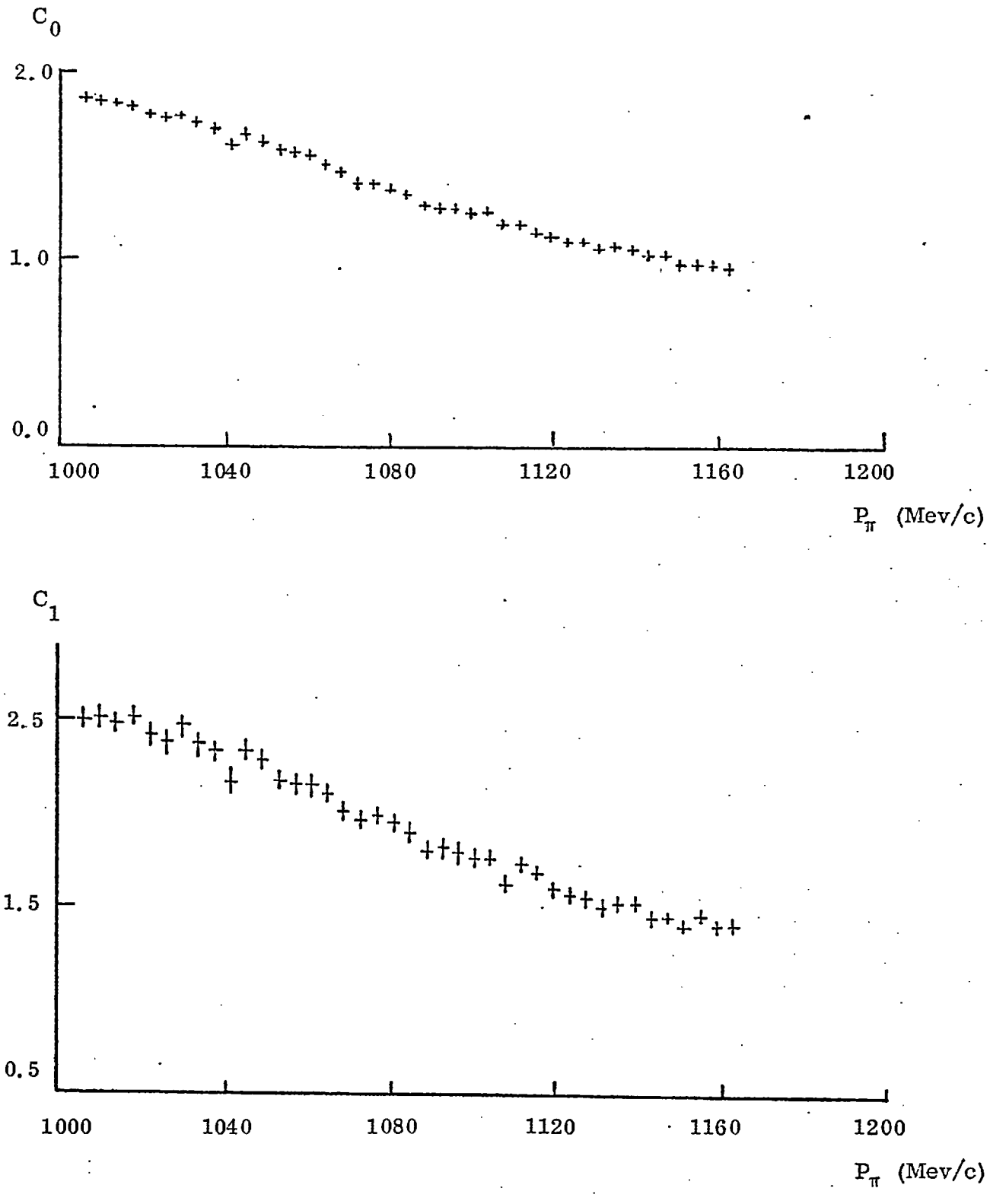

Legendre coefficients from fits to $\pi^- P$ elastic differential cross sections.

Fig (6-13)

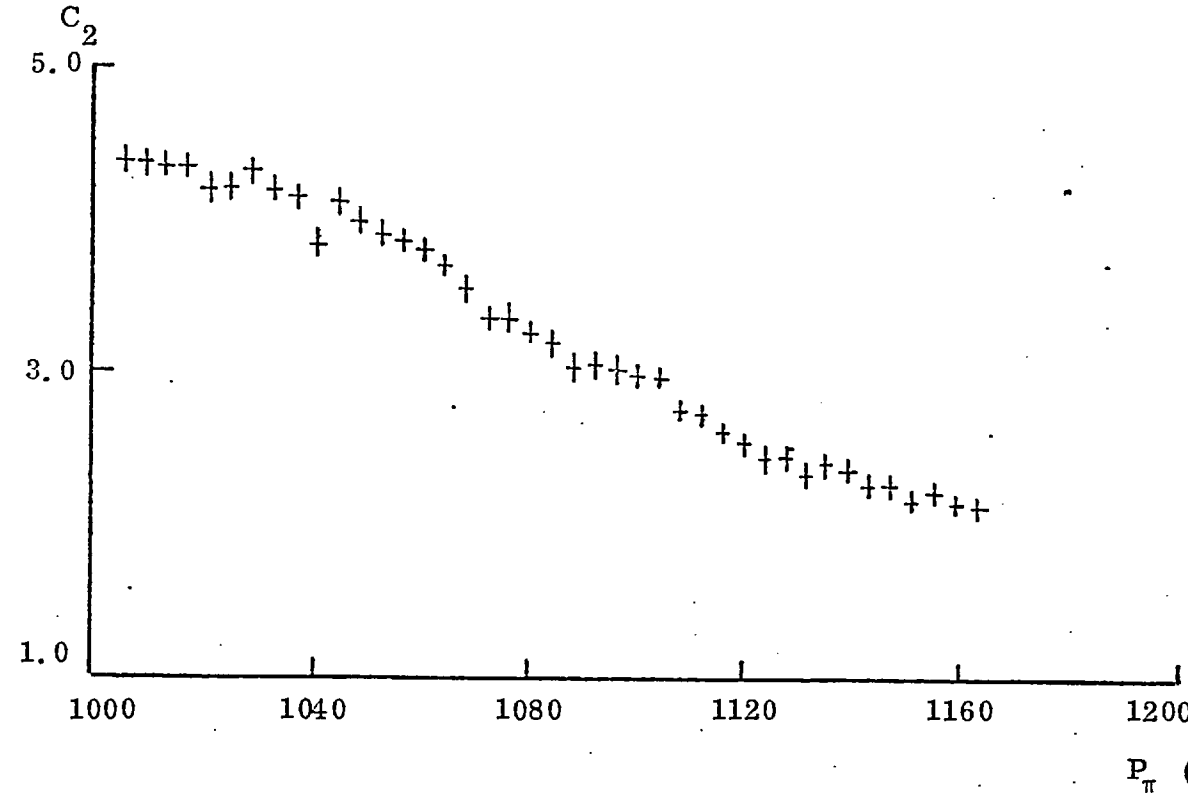

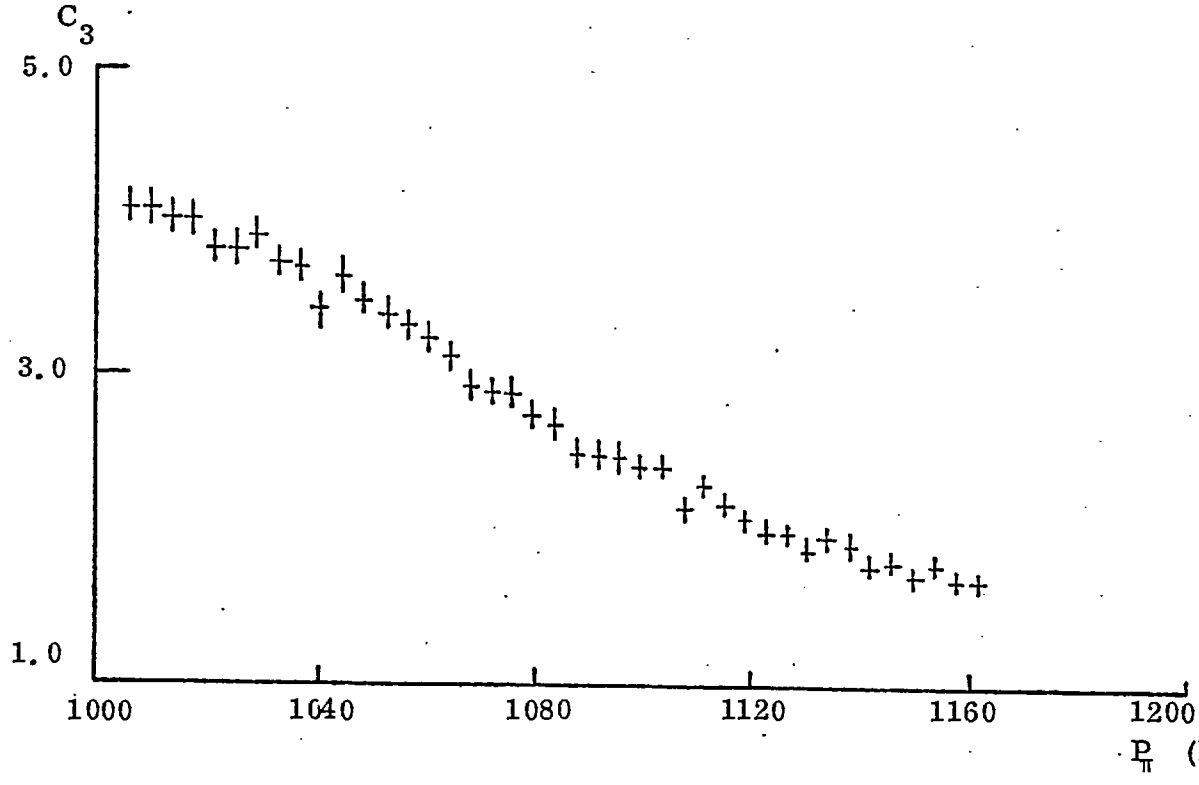

Legendre coefficients from fits to $\pi^- P$ elastic differential cross sections .

Fig (6-13)

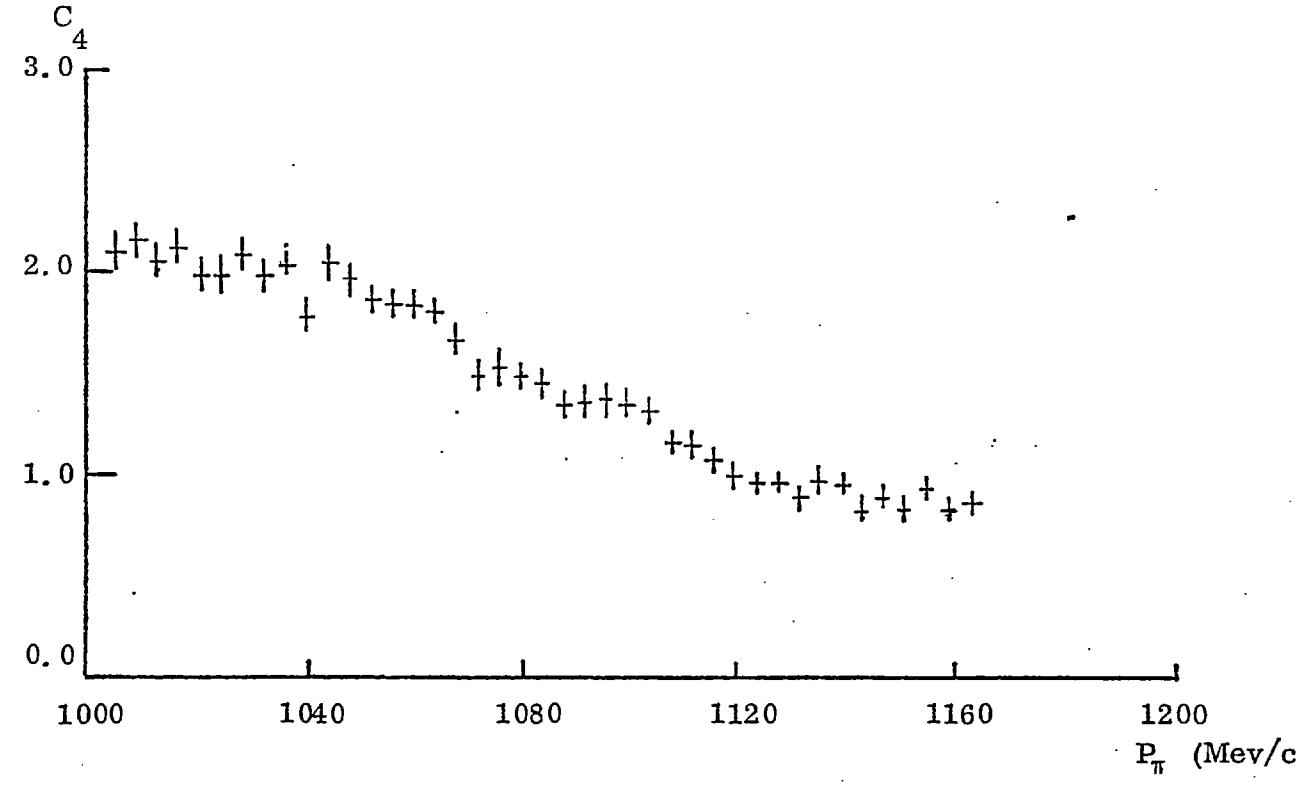

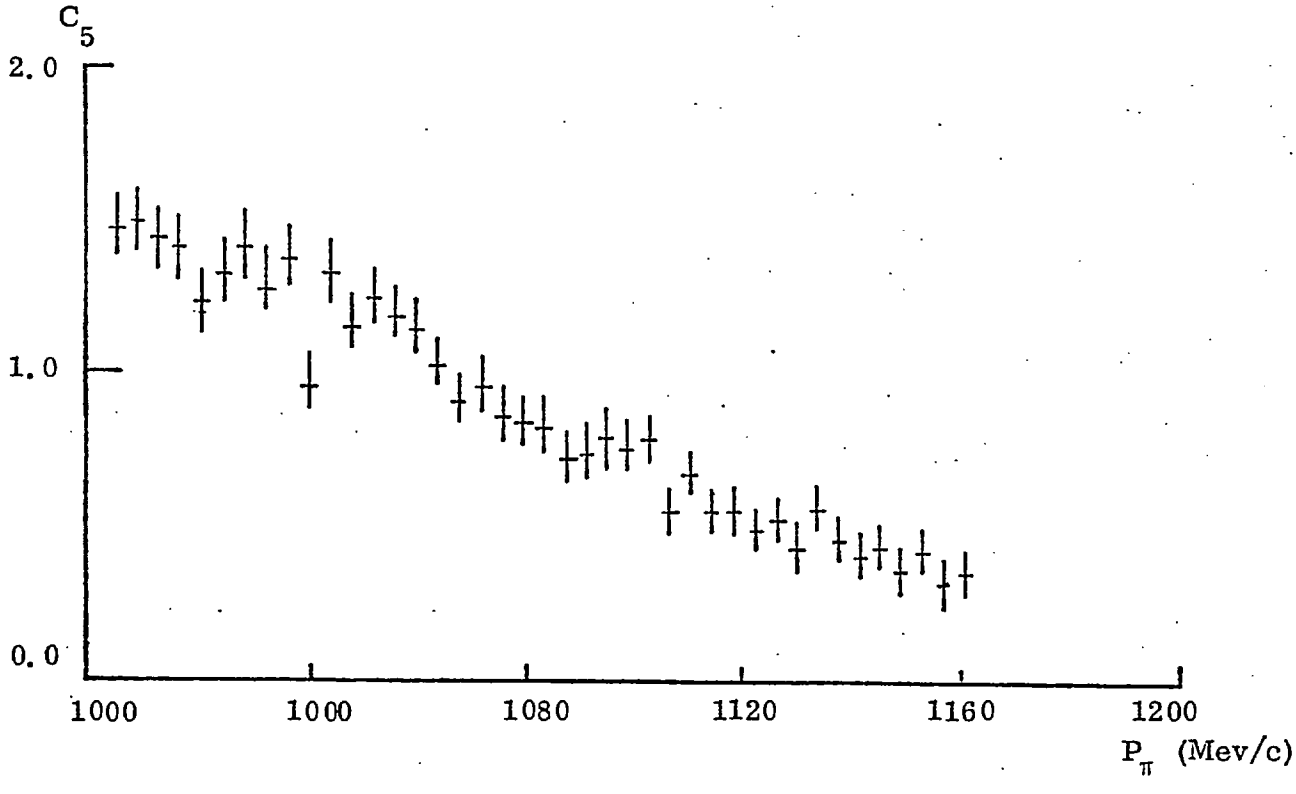

Legendre coefficients from fits to $\pi^- P$ elastic differential cross sections.

Fig (6-13)

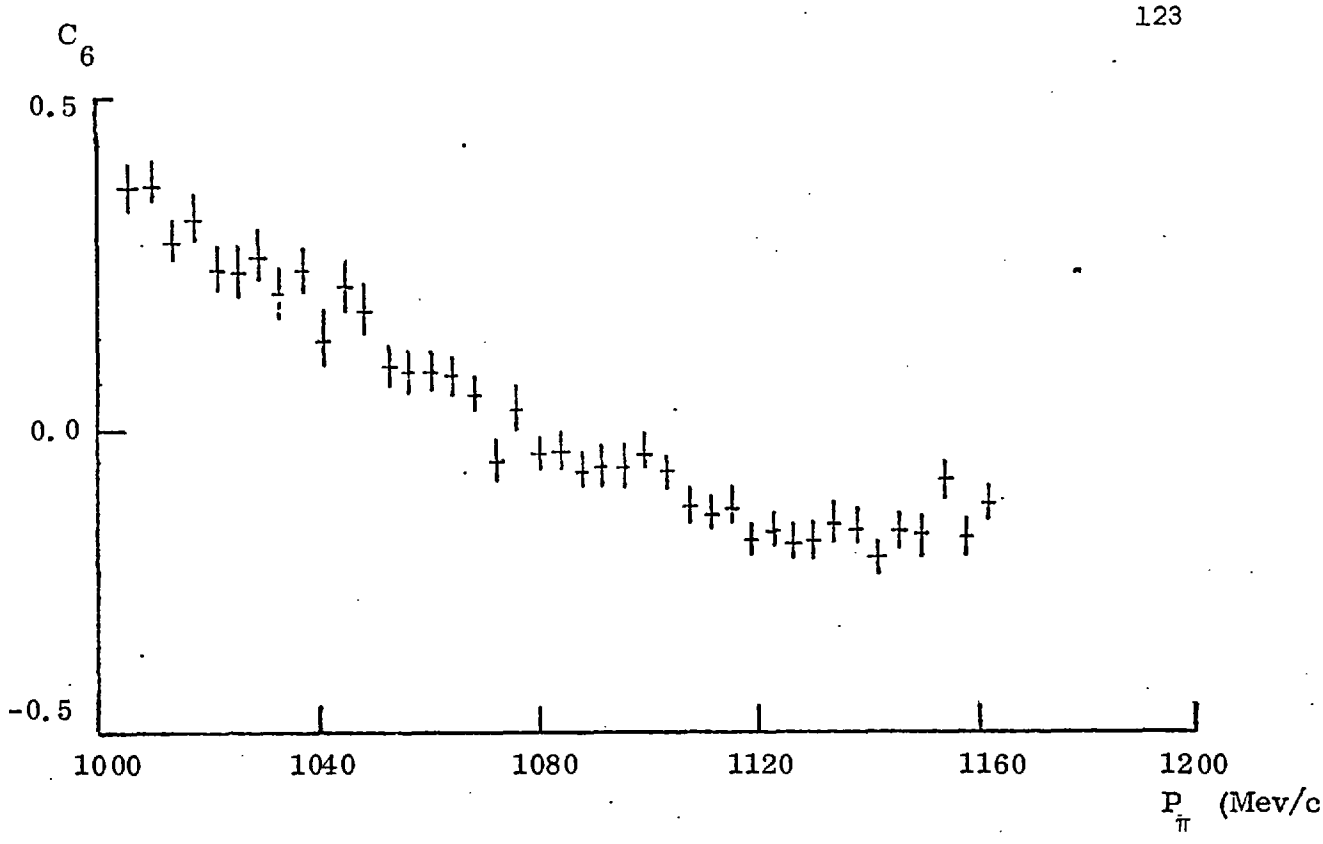

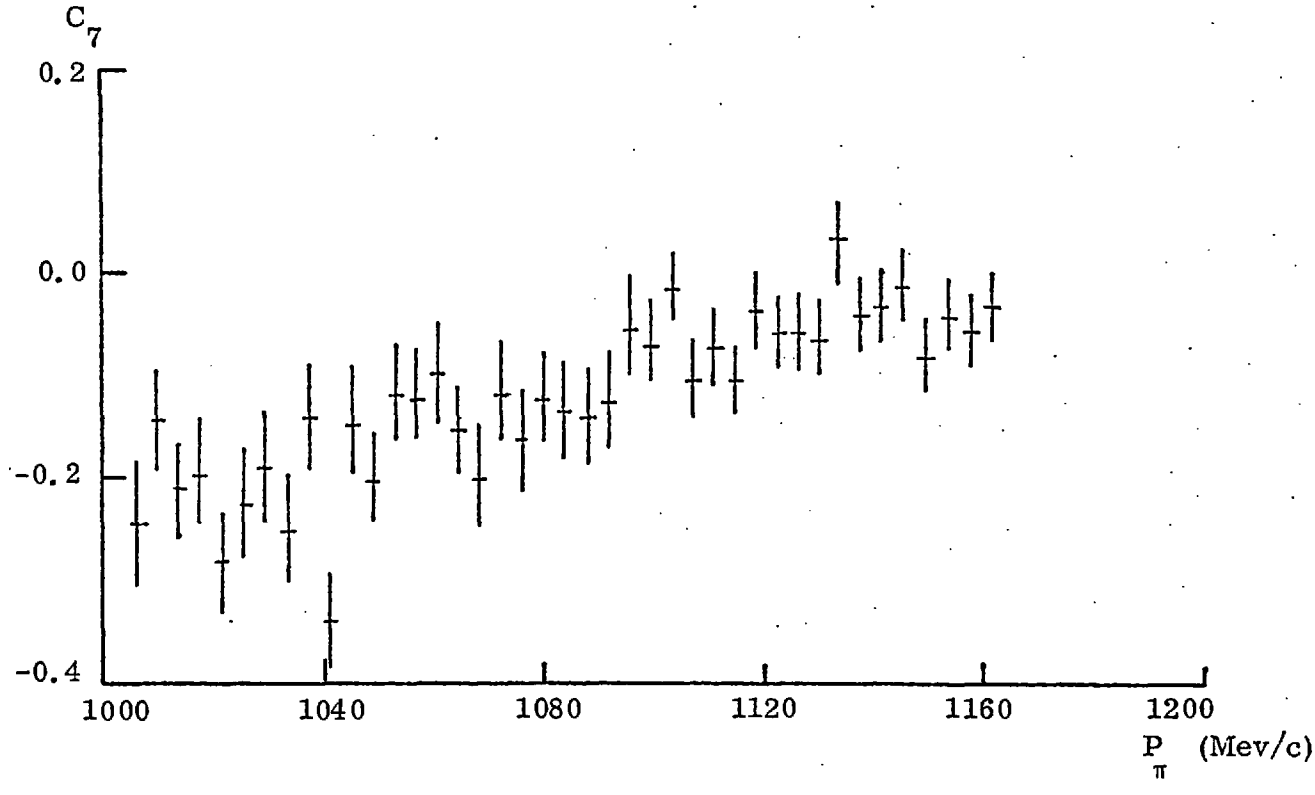

Legendre coefficients from fits to $\pi^- P$ elastic differential cross sections.

Fig (6-13)

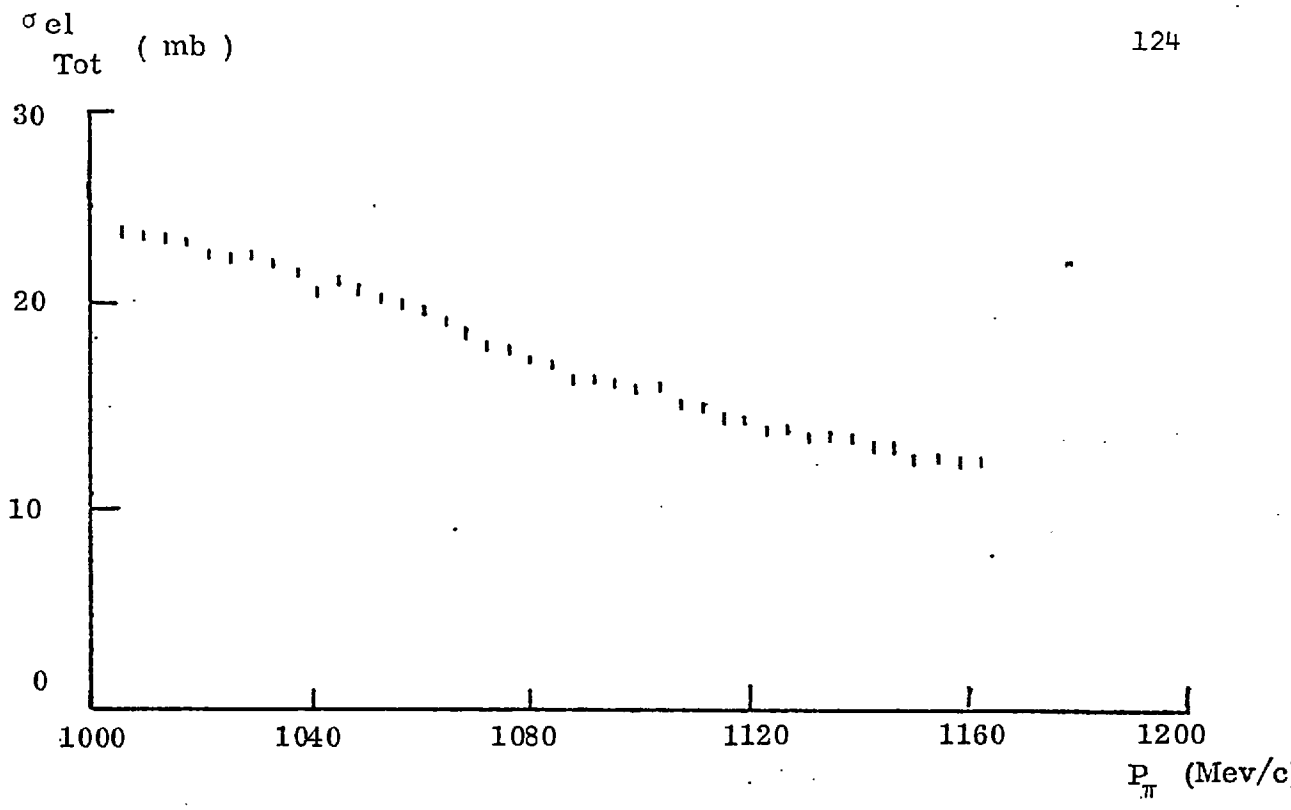

Total $\pi^- p$ elastic cross-sections .

Fig (6-14)

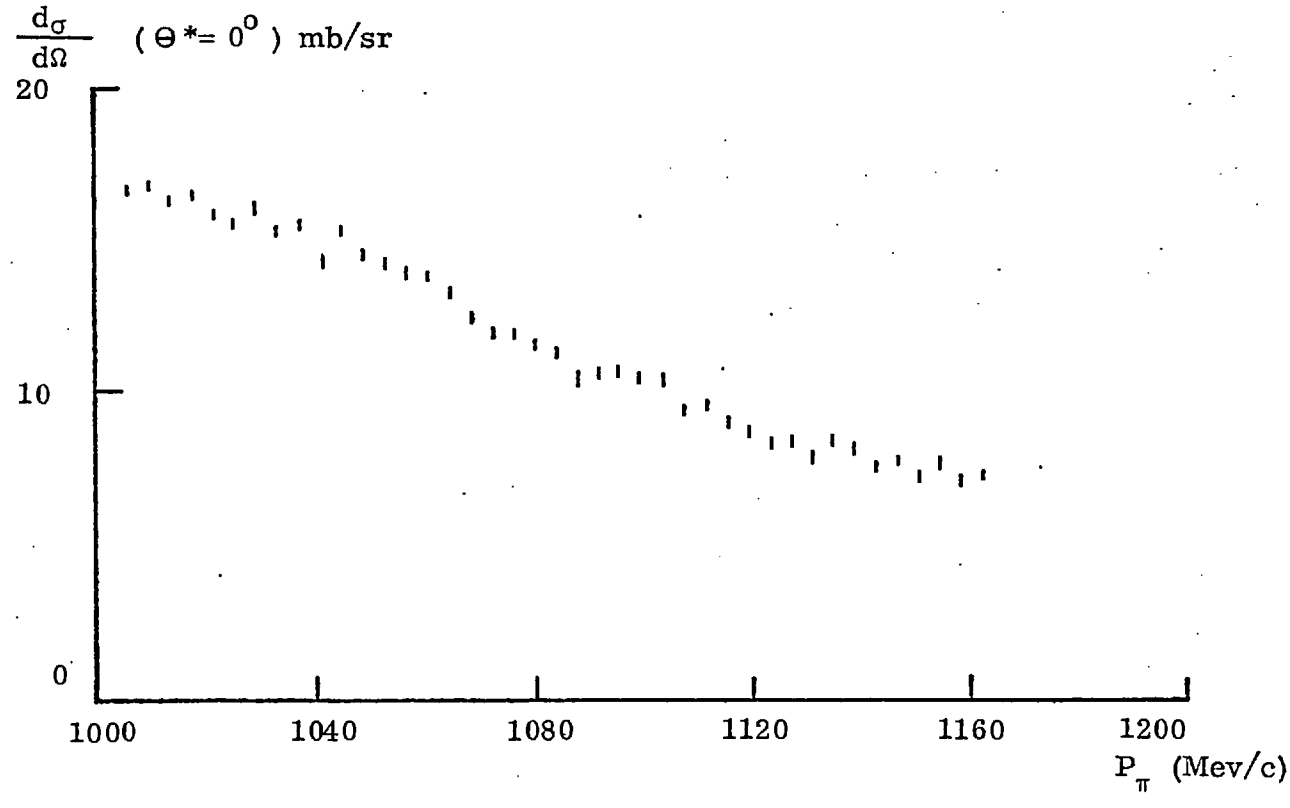

Forward $\pi^- P$ elastic cross-sections measured in this experiment .

Fig (6-15)

Table I

Variation of the mass and width of the ω with P^* .

P^* Mev/c	M_ω Mev/c2	Γ_ω Mev/c2
0 - 20	782.0 ± 1.2	9.5 ± 1.6
20 - 40	782.8 ± 1.0	9.5 ± 1.6
40 - 60	782.6 ± 1.0	9.0 ± 1.3
60 - 80	782.6 ± 0.6	8.8 ± 1.3
80 - 100	783.4 ± 0.9	11.9 ± 2.0
100 - 120	783.8 ± 0.9	12.0 ± 2.2
120 - 140	783.8 ± 0.8	9.3 ± 1.9
140 - 160	782.6 ± 0.7	11.0 ± 1.2
160 - 180	783.6 ± 0.8	10.9 ± 1.3
180 - 200	783.2 ± 0.6	9.8 ± 1.1
200 - 220	783.2 ± 0.6	9.8 ± 1.1

Table II

Variation of σ and σ/P^* for ω production with P^*.

P^* Mev/c	$A=\frac{\sigma}{P*}\ \frac{mb}{Gev/c}$	σ μb
20 - 40	3.53 ± 0.80	106 ± 24
40 - 60	4.28 ± 0.50	214 ± 25
60 - 80	5.35 ± 0.50	374 ± 35
80 - 100	6.24 ± 0.61	577 ± 55
100 - 120	7.49 ± 0.71	824 ± 78
120 - 140	8.20 ± 0.70	1066 ± 92
140 - 160	8.02 ± 0.70	1203 ± 106
160 - 180	7.80 ± 0.72	1326 ± 120
180 - 200	7.80 ± 0.70	1482 ± 133

Table III

Differential cross-sections for ω production.

$\cos\theta^*$	$\frac{d\sigma}{d\Omega}$ μb/sr $40 < P^* < 60$	$\frac{d\sigma}{d\Omega}$ μb/sr $60 < P^* < 80$	$\frac{d\sigma}{d\Omega}$ μb/sr $80 < p^* < 100$
-1.0 -0.8	14.3 ± 4.3	28.2 ± 6.7	44.7 ± 6.5
-0.8 -0.6	15.9 ± 4.4	31.7 ± 6.7	35.0 ± 7.9
-0.6 -0.4	15.1 ± 4.0	26.7 ± 6.1	41.4 ± 10.0
-0.4 -0.2	13.1 ± 4.8	29.5 ± 6.1	63.4 ± 12.0
-0.2 0.0	15.2 ± 4.4	26.7 ± 6.5	38.6 ± 9.4
0.0 0.2	12.4 ± 4.5	18.4 ± 6.9	41.5 ± 10.6
0.2 0.4	15.9 ± 4.0	26.7 ± 4.2	53.0 ± 9.4
0.4 0.6	17.9 ± 4.0	30.0 ± 6.1	50.1 ± 7.1
0.6 0.8	19.0 ± 3.3	27.3 ± 4.4	45.8 ± 7.1
0.8 1.0	19.9 ± 4.0	26.7 ± 3.3	48.0 ± 6.4

Table III (continued)

Differential cross-sections for ω production.

$\cos\theta^*$	$\frac{d\sigma}{d\Omega}$ μb/sr $100 < P^* < 120$	$\frac{d\sigma}{d\Omega}$ μb/sr $120 < P^* < 140$	$\frac{d\sigma}{d\Omega}$ μb/sr $140 < P^* < 160$
-1.0 -0.8	63.0 ± 7.9	103.5 ± 11.5	95.5 ± 11.9
-0.8 -0.6	64.4 ± 12.0	87.9 ± 14.5	121.7 ± 27.0
-0.6 -0.4	72.6 ± 11.0	110.5 ± 23.8	133.7 ± 20.4
-0.4 -0.2	64.7 ± 12.0	85.5 ± 21.1	128.9 ± 16.7
-0.2 0.0	73.5 ± 13.0	82.7 ± 20.1	105.0 ± 10.7
0.0 0.2	68.3 ± 10.5	105.8 ± 13.5	78.8 ± 20.4
0.2 0.4	64.7 ± 12.0	87.8 ± 12.5	108.5 ± 19.1
0.4 0.6	61.3 ± 8.8	61.3 ± 8.8	87.0 ± 10.8
0.6 0.8	71.8 ± 9.0	71.8 ± 9.0	109.9 ± 13.1
0.8 1.0	56.5 ± 6.2	86.9 ± 9.2	95.5 ± 8.4

Table III (continued)

Differential cross-sections for ω production.

$\cos\theta^*$	$\frac{d\sigma}{d\Omega}$ μb/sr $160 < P^* < 180$	$\frac{d\sigma}{d\Omega}$ μb/sr $180 < P^* < 200$
-1.0 -0.8	108.2 ± 12.2	110.5 ± 15.0
-0.8 -0.6	121.2 ± 10.8	111.9 ± 18.1
-0.6 -0.4	136.0 ± 17.5	115.0 ± 18.3
-0.4 -0.2	136.0 ± 17.3	133.1 ± 19.6
-0.2 0.0	129.8 ± 14.9	113.5 ± 19.6
0.0 0.2	128.9 ± 14.7	141.2 ± 19.1
0.2 0.4	99.3 ± 16.2	130.0 ± 16.3
0.4 0.6	112.2 ± 12.2	119.1 ± 16.7
0.6 0.8	117.8 ± 12.1	125.3 ± 12.1
0.8 1.0	102.8 ± 10.5	125.3 ± 10.5

TABLE IV

Legendre polynomial coefficients. $d\sigma/d\Omega = \Sigma_\ell C_\ell P_\ell$ (COS θ^*).

p^* Mev/c	C_0	C_1	C_2	χ^2
40 - 60	15.9±1.3	2.8±2.2	2.7±3.0	0.67
60 - 80	27.3±1.8	-1.4±3.0	1.7±3.7	2.17
80 - 100	45.6±2.7	3.82±3.9	-1.1±5.7	5.0
100 - 120	65.8±3.2	-2.6±4.6	-7.1±6.3	1.9
120 - 140	85.9±4.2	-14.6±6.3	6.0±8.8	9.7
140 - 160	103.4±4.5	-6.2±6.9	-5.4±8.7	8.7
160 - 180	118.9±4.3	-6.8±6.5	-15.4±9.3	3.6
180 - 200	122.4±5.2	8.2±7.8	-8.3±10.9	1.5

TABLE V

Ratios of the Legendre polynomial coefficients.

p* Mev/c	C_1/C_0	C_2/C_0
40 - 60	0.17±0.14	0.17±0.19
60 - 80	-0.05±0.11	0.06±0.13
80 - 100	0.08±0.08	-0.02±0.12
100 - 120	-0.04±0.07	-0.10±0.09
120 - 140	-0.17±0.08	0.07±0.10
140 - 160	-0.06±0.7	-0.05±0.08
160 - 180	-0.06±0.05	-0.13±0.08
180 - 200	0.07±0.06	-0.07±0.09

Table VI

COS Θ^*		1007.8 < P_π < 1011.8 MEV/C		1011.8 < P_π < 1015.7 MEV/C		1015.7 < P_π < 1019.6 MEV/C	
		$d\sigma/d\Omega$ mb/sr	ERROR mb/sr	$d\sigma/d\Omega$ mb/sr	ERROR mb/sr	$d\sigma/d\Omega$ mb/sr	ERROR mb/sr
+.86	+.76	5.558	0.056	5.499	0.047	5.410	0.047
+.76	+.66	2.499	0.033	2.487	0.027	2.480	0.027
+.66	+.56	1.107	0.021	1.121	0.018	1.094	0.018
+.56	+.46	0.458	0.015	0.435	0.012	0.428	0.012
+.46	+.36	0.211	0.010	0.187	0.008	0.182	0.008
+.36	+.26	0.204	0.010	0.195	0.008	0.172	0.008
+.26	+.16	0.272	0.011	0.241	0.009	0.216	0.008
+.16	+.06	0.307	0.012	0.302	0.010	0.284	0.009
+.06	-0.04	0.329	0.012	0.315	0.010	0.326	0.010
-0.04	-0.14	0.379	0.013	0.373	0.010	0.382	0.011
-0.14	-0.24	0.479	0.014	0.465	0.012	0.497	0.012
-0.24	-0.34	0.721	0.018	0.697	0.015	0.700	0.015
-0.34	-0.44	1.005	0.021	0.977	0.017	0.954	0.017
-0.44	-0.54	1.363	0.025	1.331	0.021	1.290	0.021
-0.54	-0.64	1.441	0.027	1.467	0.023	1.401	0.023

$\pi^- P$ differential cross-sections.

Table VI (continued)

COS Θ^*		1019.6 $<P_\pi<$ 1023.5 MEV/C		1023.5 $<P_\pi<$ 1027.4 MEV/C		1027.4 $<P_\pi<$ 1031.4 MEV/C	
		$d\sigma/d\Omega$ mb/sr	ERROR mb/sr	$d\sigma/d\Omega$ mb/sr	ERROR mb/sr	$d\sigma/d\Omega$ mb/sr	ERROR mb/sr
+.86	+.76	5.480	0.045	5.439	0.049	5.371	0.044
+.76	+.66	2.464	0.026	2.490	0.029	2.541	0.026
+.66	+.56	1.111	0.017	1.082	0.019	1.100	0.017
+.56	+.46	0.439	0.012	0.440	0.013	0.415	0.011
+.46	+.36	0.148	0.007	0.144	0.007	0.135	0.006
+.36	+.26	0.174	0.007	0.168	0.008	0.151	0.007
+.26	+.16	0.227	0.008	0.214	0.009	0.214	0.008
+.16	+.06	0.283	0.009	0.276	0.010	0.278	0.009
+.06	0.04	0.312	0.009	0.307	0.010	0.314	0.009
-0.04	-0.14	0.370	0.010	0.370	0.011	0.391	0.010
-0.14	-0.24	0.476	0.011	0.481	0.013	0.467	0.011
-0.24	-0.34	0.644	0.014	0.630	0.015	0.651	0.013
-0.34	-0.44	0.917	0.016	0.933	0.018	0.908	0.016
-0.44	-0.54	1.301	0.020	1.231	0.021	1.220	0.019
-0.54	-0.64	1.409	0.022	1.348	0.024	1.332	0.021

π^-P differential cross-sections.

Table VI (continued)

COS θ*		1031.4 < P_π < 1035.3 MEV/C		1035.3 < P_π < 1039.2 MEV/C		1039.2 < P_π < 1043.1 MEV/C	
		dσ/dΩ mb/sr	ERROR mb/sr	dσ/dΩ mb/sr	ERROR mb/sr	dσ/dΩ mb/sr	ERROR mb/sr
+.86	+.76	5.260	0.048	5.370	0.045	5.259	0.047
+.76	+.66	2.445	0.028	2.435	0.026	2.442	0.028
+.66	+.56	1.080	0.019	1.047	0.017	1.058	0.018
+.56	+.46	0.390	0.012	0.398	0.011	0.361	0.011
+.46	+.36	0.128	0.007	0.137	0.007	0.123	0.007
+.36	+.26	0.158	0.008	0.135	0.007	0.135	0.007
+.26	+.16	0.206	0.008	0.196	0.008	0.197	0.008
+.16	+.06	0.255	0.009	0.283	0.009	0.258	0.009
+.06	0.04	0.291	0.010	0.284	0.009	0.307	0.010
-0.04	-0.14	0.347	0.011	0.346	0.010	0.329	0.010
-0.14	-0.24	0.441	0.012	0.408	0.011	0.426	0.012
-0.24	-0.34	0.604	0.014	0.579	0.013	0.549	0.013
-0.34	-0.44	0.856	0.017	0.841	0.016	0.835	0.017
-0.44	-0.54	1.174	0.020	1.164	0.019	1.133	0.020
-0.54	-0.64	1.334	0.023	1.276	0.021	1.281	0.022

$\bar{\pi}P$ differential cross-sections.

Table VI (continued)

COS Θ^*		1043.1 < P_π < 1047.0 MEV/C		1047.0 < P_π < 1051.0 MEV/C		1051.0 < P_π < 1054.9 MEV/C	
		$d\sigma/d\Omega$ mb/sr	ERROR mb/sr	$d\sigma/d\Omega$ mb/sr	ERROR mb/sr	$d\sigma/d\Omega$ mb/sr	ERROR mb/sr
+.86	+.76	5.092	0.044	4.963	0.046	5.045	0.058
+.76	+.66	2.269	0.025	2.343	0.027	2.334	0.034
+.66	+.56	1.018	0.017	1.046	0.018	0.984	0.022
+.56	+.46	0.358	0.011	0.365	0.011	0.351	0.014
+.46	+.36	0.116	0.006	0.107	0.006	0.110	0.008
+.36	+.26	0.136	0.007	0.131	0.007	0.130	0.008
+.26	+.16	0.201	0.008	0.212	0.008	0.198	0.010
+.16	+.06	0.247	0.008	0.268	0.009	0.239	0.011
+.06	-0.04	0.292	0.009	0.286	0.009	0.306	0.012
-0.04	-0.14	0.329	0.010	0.339	0.010	0.337	0.013
-0.14	-0.24	0.415	0.011	0.396	0.011	0.397	0.014
-0.24	-0.34	0.550	0.013	0.537	0.013	0.521	0.015
-0.34	-0.44	0.760	0.015	0.776	0.016	0.730	0.019
-0.44	-0.54	1.080	0.018	1.048	0.019	1.044	0.024
-0.54	-0.64	1.217	0.021	1.150	0.021	1.136	0.026

π^- P differential cross-sections.

Table VI (continued)

COS Θ*		1054.9 <P_{π^-}< 1058.8 MEV/C		1058.8 <P_{π^-}< 1062.7 MEV/C		1062.7 <P_{π^-}< 1066.6 MEV/C	
		$d\sigma/d\Omega$ mb/sr	ERROR mb/sr	$d\sigma/d\Omega$ mb/sr	ERROR mb/sr	$d\sigma/d\Omega$ mb/sr	ERROR mb/sr
+.86	+.76	5.009	0.047	4.859	0.044	4.774	0.039
+.76	+.66	2.327	0.028	2.209	0.026	2.269	0.023
+.66	+.56	1.016	0.018	0.997	0.017	0.975	0.015
+.56	+.46	0.348	0.011	0.343	0.011	0.350	0.010
+.46	+.36	0.109	0.006	0.098	0.006	0.100	0.005
+.36	+.26	0.121	0.007	0.112	0.006	0.121	0.006
+.26	+.16	0.202	0.009	0.175	0.007	0.177	0.007
+.16	+.06	0.246	0.009	0.258	0.009	0.251	0.008
+.06	-0.04	0.302	0.010	0.286	0.009	0.293	0.008
-0.04	-0.14	0.334	0.011	0.338	0.010	0.333	0.009
-0.14	-0.24	0.396	0.012	0.385	0.011	0.387	0.010
-0.24	-0.34	0.513	0.013	0.464	0.012	0.478	0.011
-0.34	-0.44	0.714	0.016	0.671	0.015	0.635	0.013
-0.44	-0.54	1.013	0.019	0.974	0.018	0.924	0.015
-0.54	-0.64	1.092	0.021	1.090	0.020	1.068	0.018

π^- P differential cross-sections.

Table VI (continued)

COS Θ^*		1066.6 $< P_\pi <$ 1070.6 MEV/C		1070.6 $< P_\pi <$ 1074.5 MEV/C		1074.5 $< P_\pi <$ 1078.4 MEV/C	
		$d\sigma/d\Omega$ mb/sr	ERROR mb/sr	$d\sigma/d\Omega$ mb/sr	ERROR mb/sr	$d\sigma/d\Omega$ mb/sr	ERROR mb/sr
+.86	+.76	4.742	0.042	4.663	0.038	4.541	0.039
+.76	+.66	2.251	0.025	2.223	0.023	2.169	0.024
+.66	+.56	1.023	0.017	0.986	0.015	1.005	0.015
+.56	+.46	0.372	0.011	0.359	0.010	0.368	0.010
+.46	+.36	0.116	0.006	0.100	0.005	0.111	0.006
+.36	+.26	0.132	0.007	0.119	0.006	0.125	0.006
+.26	+.16	0.174	0.007	0.177	0.007	0.187	0.007
+.16	+.06	0.257	0.009	0.235	0.008	0.243	0.008
+.06	-0.04	0.298	0.009	0.296	0.008	0.285	0.008
-0.04	-0.14	0.329	0.010	0.327	0.009	0.308	0.009
-0.14	-0.24	0.392	0.011	0.363	0.009	0.353	0.009
-0.24	-0.34	0.472	0.012	0.456	0.011	0.441	0.011
-0.34	-0.44	0.637	0.014	0.606	0.012	0.589	0.013
-0.44	-0.54	0.863	0.016	0.846	0.015	0.837	0.015
-0.54	-0.64	1.022	0.019	0.962	0.017	0.943	0.017

π^- P differential cross-sections.

Table VI (continued)

COS θ*		1078.4 <P_π< 1082.3 MEV/C		1082.3 <P_π< 1086.2 MEV/C		1086.2 <P_π< 1090.2 MEV/C	
		dσ/dΩ mb/sr	ERROR mb/sr	dσ/dΩ mb/sr	ERROR mb/sr	dσ/dΩ mb/sr	ERROR mb/sr
+.86	+.76	4.390	0.038	4.396	0.039	4.294	0.046
+.76	+.66	2.134	0.023	2.167	0.023	2.135	0.028
+.66	+.56	0.987	0.016	0.990	0.016	1.004	0.019
+.56	+.46	0.369	0.010	0.387	0.010	0.386	0.013
+.46	+.36	0.111	0.006	0.122	0.006	0.129	0.007
+.36	+.26	0.120	0.006	0.124	0.006	0.122	0.007
+.26	+.16	0.169	0.007	0.165	0.007	0.177	0.008
+.16	+.06	0.243	0.008	0.234	0.008	0.247	0.010
+.06	-0.04	0.298	0.009	0.292	0.009	0.291	0.010
-0.04	-0.14	0.326	0.009	0.318	0.009	0.326	0.011
-0.14	-0.24	0.363	0.010	0.342	0.009	0.341	0.011
-0.24	-0.34	0.412	0.010	0.454	0.011	0.410	0.013
-0.34	-0.44	0.566	0.012	0.612	0.013	0.536	0.015
-0.44	-0.54	0.780	0.015	0.768	0.015	0.714	0.017
-0.54	-0.64	0.933	0.017	0.910	0.017	0.822	0.019

π^-p differential cross-sections.

Table VI (continued)

COS θ^*		1090.2 < P_π < 1094.1 MEV/C		1094.1 < P_π < 1098.0 MEV/C		1098.0 < P_π < 1101.9 MEV/C	
		$d\sigma/d\Omega$ mb/sr	ERROR mb/sr	$d\sigma/d\Omega$ mb/sr	ERROR mb/sr	$d\sigma/d\Omega$ mb/sr	ERROR mb/sr
+.86	+.76	4.211	0.040	4.043	0.039	4.058	0.023
+.76	+.66	2.083	0.024	2.026	0.024	2.018	0.017
+.66	+.56	1.004	0.017	0.979	0.016	0.971	0.012
+.56	+.46	0.375	0.011	0.372	0.011	0.389	0.008
+.46	+.36	0.124	0.006	0.123	0.006	0.181	0.005
+.36	+.26	0.127	0.006	0.116	0.006	0.110	0.004
+.26	+.16	0.180	0.007	0.168	0.007	0.171	0.005
+.16	+.06	0.238	0.008	0.228	0.008	0.232	0.006
+.06	-0.04	0.272	0.009	0.278	0.009	0.266	0.006
-0.04	-0.14	0.305	0.009	0.295	0.009	0.284	0.006
-0.14	-0.24	0.353	0.010	0.333	0.010	0.318	0.007
-0.24	-0.34	0.393	0.011	0.373	0.010	0.356	0.007
-0.34	-0.44	0.517	0.012	0.488	0.012	0.470	0.009
-0.44	-0.54	0.707	0.015	0.686	0.014	0.636	0.011
-0.54	-0.64	0.822	0.017	0.760	0.016	0.750	0.012

$\bar{\pi}$ P differential cross-sections.

Table VI (continued)

COS θ^*		1101.9 $<P_\pi<$ 1105.8 MEV/C		1105.8 $<P_\pi<$ 1109.8 MEV/C		1109.8 $<P_\pi<$ 1113.7 MEV/C	
		$d\sigma/d\Omega$ mb/sr	ERROR mb/sr	$d\sigma/d\Omega$ mb/sr	ERROR mb/sr	$d\sigma/d\Omega$ mb/sr	ERROR mb/sr
+.86	+.76	3.971	0.028	3.885	0.030	3.890	0.033
+.76	+.66	1.971	0.017	1.964	0.018	1.972	0.021
+.66	+.56	0.959	0.012	0.960	0.013	0.968	0.014
+.56	+.46	0.406	0.008	0.391	0.009	0.430	0.010
+.46	+.36	0.133	0.005	0.133	0.005	0.148	0.006
+.36	+.26	0.115	0.004	0.124	0.005	0.124	0.005
+.26	+.16	0.162	0.005	0.172	0.006	0.159	0.006
+.16	+.06	0.223	0.006	0.211	0.006	0.216	0.007
+.06	-0.04	0.273	0.006	0.252	0.007	0.274	0.008
-0.04	-0.14	0.285	0.007	0.293	0.007	0.301	0.008
-0.14	-0.24	0.327	0.007	0.311	0.007	0.318	0.008
-0.24	-0.34	0.353	0.007	0.365	0.008	0.353	0.009
-0.34	-0.44	0.448	0.009	0.454	0.009	0.453	0.010
-0.44	-0.54	0.626	0.010	0.593	0.011	0.609	0.012
-0.54	-0.64	0.727	0.012	0.733	0.012	0.712	0.014

$\bar{\pi}$p differential cross-sections.

Table VI (continued)

COS Θ*		1113.7 < P_π < 1117.6 MEV/C		1117.6 < P_π < 1121.5 MEV/C		1121.5 < P_π < 1125.4 MEV/C	
		dσ/dΩ mb/sr	ERROR mb/sr	dσ/dΩ mb/sr	ERROR mb/sr	dσ/dΩ mb/sr	ERROR mb/sr
+.86	+.76	3.743	0.034	3.793	0.032	3.708	0.034
+.76	+.66	1.946	0.021	1.949	0.020	1.920	0.021
+.66	+.56	0.985	0.015	0.982	0.014	0.930	0.015
+.56	+.46	0.426	0.011	0.440	0.010	0.443	0.011
+.46	+.36	0.145	0.006	0.141	0.006	0.153	0.006
+.36	+.26	0.111	0.005	0.137	0.005	0.117	0.005
+.26	+.16	0.161	0.006	0.168	0.006	0.163	0.006
+.16	+.06	0.225	0.007	0.226	0.007	0.218	0.007
+.06	-0.04	0.262	0.008	0.276	0.007	0.253	0.008
-0.04	-0.14	0.275	0.008	0.284	0.007	0.282	0.008
-0.14	-0.24	0.300	0.008	0.314	0.008	0.287	0.008
-0.24	-0.34	0.360	0.009	0.344	0.008	0.344	0.009
-0.34	-0.44	0.438	0.010	0.417	0.009	0.422	0.010
-0.44	-0.54	0.556	0.012	0.572	0.011	0.565	0.012
-0.54	-0.64	0.668	0.014	0.674	0.013	0.623	0.014

π^- P differential cross-sections.

Table VI (continued)

COS θ^*		1125.4 < P_π < 1129.4 MEV/C		1129.4 < P_π < 1133.3 MEV/C		1133.3 < P_π < 1137.2 MEV/C	
		$d\sigma/d\Omega$ mb/sr	ERROR mb/sr	$d\sigma/d\Omega$ mb/sr	ERROR mb/sr	$d\sigma/d\Omega$ mb/sr	ERROR mb/sr
+.86	+.76	3.557	0.030	3.474	0.033	3.490	0.029
+.76	+.66	1.933	0.019	1.867	0.021	1.834	0.018
+.66	+.56	0.963	0.013	0.978	0.015	0.970	0.013
+.56	+.46	0.459	0.010	0.430	0.011	0.435	0.009
+.46	+.36	0.146	0.006	0.148	0.006	0.149	0.005
+.36	+.26	0.119	0.005	0.124	0.006	0.117	0.005
+.26	+.16	0.158	0.006	0.144	0.006	0.157	0.005
+.16	+.06	0.209	0.006	0.211	0.007	0.211	0.005
+.06	-0.04	0.259	0.007	0.247	0.008	0.258	0.007
-0.04	-0.14	0.289	0.007	0.283	0.008	0.274	0.007
-0.14	-0.24	0.320	0.008	0.317	0.009	0.290	0.007
-0.24	-0.34	0.350	0.008	0.329	0.009	0.330	0.008
-0.34	-0.44	0.413	0.009	0.397	0.010	0.385	0.009
-0.44	-0.54	0.511	0.010	0.525	0.012	0.509	0.010
-0.54	-0.64	0.649	0.012	0.594	0.013	0.616	0.012

$\bar{\pi}$ p differential cross-sections.

Table VI (continued)

COS θ*		1137.2 < P_{π} < 1141.1 MEV/C		1141.1 < P_{π} < 1145.0 MEV/C		1145.0 < P_{π} < 1149.0 MEV/C	
		$d\sigma/d\Omega$ mb/sr	ERROR mb/sr	$d\sigma/d\Omega$ mb/sr	ERROR mb/sr	$d\sigma/d\Omega$ mb/sr	ERROR mb/sr
+.86	+.76	3.389	0.031	3.356	0.031	3.386	0.030
+.76	+.66	1.849	0.020	1.792	0.019	1.812	0.019
+.66	+.56	0.948	0.014	0.956	0.014	0.954	0.014
+.56	+.46	0.466	0.011	0.450	0.010	0.444	0.010
+.46	+.36	0.159	0.006	0.158	0.006	0.150	0.006
+.36	+.26	0.113	0.005	0.114	0.005	0.115	0.005
+.26	+.16	0.161	0.006	0.155	0.006	0.154	0.005
+.16	+.06	0.216	0.007	0.194	0.006	0.203	0.006
+.06	-0.04	0.249	0.007	0.248	0.007	0.247	0.007
-0.04	-0.14	0.286	0.008	0.301	0.008	0.279	0.007
-0.14	-0.24	0.297	0.008	0.309	0.008	0.308	0.008
-0.24	-0.34	0.335	0.009	0.330	0.008	0.328	0.008
-0.34	-0.44	0.404	0.010	0.375	0.009	0.382	0.009
-0.44	-0.54	0.487	0.011	0.480	0.010	0.476	0.010
-0.54	-0.64	0.586	0.012	0.566	0.012	0.560	0.012

$\bar{\Pi}$ p differential cross-sections.

Table VI (continued)

COS θ^*		1149.0 < P_π < 1152.9 MEV/C		1152.9 < P_π < 1156.8 MEV/C		1156.8 < P_π < 1160.7 MEV/C	
		$d\sigma/d\Omega$ mb/sr	ERROR mb/sr	$d\sigma/d\Omega$ mb/sr	ERROR mb/sr	$d\sigma/d\Omega$ mb/sr	ERROR mb/sr
+.86	+.76	3.284	0.030	3.236	0.029	3.130	0.033
+.76	+.66	1.799	0.019	1.785	0.019	1.725	0.021
+.66	+.56	0.969	0.014	0.944	0.014	0.896	0.015
+.56	+.46	0.453	0.010	0.436	0.010	0.409	0.011
+.46	+.36	0.159	0.006	0.166	0.006	0.144	0.007
+.36	+.26	0.111	0.005	0.114	0.005	0.115	0.005
+.26	+.16	0.142	0.006	0.144	0.005	0.148	0.005
+.16	+.06	0.198	0.007	0.197	0.006	0.186	0.007
+.06	-0.04	0.247	0.007	0.243	0.007	0.241	0.008
-0.04	-0.14	0.271	0.008	0.281	0.007	0.253	0.008
-0.14	-0.24	0.295	0.008	0.298	0.008	0.281	0.009
-0.24	-0.34	0.324	0.008	0.323	0.008	0.290	0.009
-0.34	-0.44	0.355	0.009	0.365	0.009	0.347	0.010
-0.44	-0.54	0.481	0.011	0.460	0.010	0.437	0.011
-0.54	-0.64	0.548	0.012	0.534	0.011	0.512	0.013

$\bar{\pi}$ p differential cross-sections .

TABLE V II

	C0	C1	C2	C3	C4	C5	C6	C7	X2
1007.8<P<1011.8	1.89±0.02	2.60±0.05	4.48±0.09	4.23±0.10	2.21±0.08	1.53±0.10	0.49±0.04	-0.23±0.06	45.61
1011.8<P<1015.7	1.86±0.02	2.52±0.06	4.40±0.09	4.12±0.11	2.07±0.10	1.47±0.11	0.39±0.05	-0.24±0.06	52.09
1015.7<P<1019.6	1.85±0.02	2.52±0.05	4.40±0.07	4.12±0.10	2.13±0.07	1.49±0.10	0.40±0.04	-0.14±0.05	37.15
1019.6<P<1023.5	1.83±0.02	2.48±0.05	4.36±0.07	4.05±0.10	2.03±0.07	1.44±0.10	0.30±0.04	-0.21±0.05	92.46
1023.5<P<1027.4	1.82±0.02	2.52±0.06	4.37±0.09	4.04±0.10	2.10±0.08	1.41±0.10	0.35±0.04	-0.20±0.05	65.49
1027.4<P<1031.4	1.78±0.02	2.43±0.06	4.20±0.09	3.85±0.10	1.95±0.08	1.20±0.10	0.26±0.04	-0.28±0.05	50.47
1031.4<P<1035.3	1.75±0.02	2.39±0.05	4.21±0.09	3.84±0.10	1.95±0.09	1.33±0.11	0.25±0.04	-0.23±0.06	43.10
1035.3<P<1039.2	1.77±0.02	2.48±0.05	4.32±0.09	3.94±0.09	2.06±0.09	1.41±0.10	0.28±0.04	-0.19±0.05	74.44
1039.2<P<1043.1	1.73±0.02	2.37±0.05	4.20±0.08	3.76±0.10	1.95±0.07	1.27±0.10	0.22±0.04	-0.25±0.05	36.66
1043.1<P<1047.0	1.69±0.02	2.33±0.06	4.16±0.08	3.73±0.10	2.02±0.07	1.38±0.10	0.26±0.04	-0.14±0.05	64.34
1047.0<P<1051.0	1.59±0.02	2.16±0.06	3.80±0.08	3.30±0.10	1.73±0.07	0.91±0.10	0.14±0.04	-0.37±0.05	57.74
1051.0<P<1054.9	1.67±0.02	2.34±0.05	4.13±0.09	3.67±0.10	2.03±0.08	1.33±0.11	0.23±0.04	-0.15±0.06	33.93
1054.9<P<1058.8	1.63±0.02	2.28±0.05	3.99±0.08	3.50±0.09	1.94±0.08	1.15±0.09	0.19±0.04	-0.22±0.05	50.33
1058.8<P<1062.7	1.59±0.02	2.17±0.05	3.92±0.07	3.41±0.09	1.84±0.06	1.24±0.09	0.09±0.03	-0.12±0.05	75.71
1062.7<P<1066.6	1.57±0.02	2.16±0.05	3.86±0.07	3.34±0.09	1.82±0.06	1.19±0.09	0.08±0.03	-0.12±0.05	46.34
1066.6<P<1070.6	1.56±0.02	2.15±0.05	3.81±0.08	3.26±0.09	1.81±0.07	1.14±0.09	0.09±0.03	-0.10±0.05	43.79
1070.6<P<1074.5	1.51±0.02	2.11±0.05	3.71±0.06	3.14±0.08	1.77±0.06	1.02±0.08	0.08±0.03	-0.16±0.04	62.90
1074.5<P<1078.4	1.46±0.02	2.01±0.05	3.55±0.08	2.95±0.09	1.64±0.07	0.91±0.09	0.05±0.03	-0.20±0.05	69.12
1078.4<P<1082.3	1.40±0.02	1.97±0.05	3.35±0.08	2.90±0.09	1.47±0.07	0.96±0.09	-0.06±0.03	-0.12±0.05	39.41
1082.3<P<1086.2	1.40±0.02	1.99±0.05	3.34±0.08	2.89±0.09	1.50±0.08	0.86±0.09	0.02±0.04	-0.17±0.05	38.78
1086.2<P<1090.2	1.36±0.02	1.95±0.05	3.25±0.06	2.76±0.08	1.46±0.06	0.84±0.09	-0.05±0.03	-0.12±0.04	25.00

Legendre polynomial coefficients from fits to the $\pi^- p$ elastic differential cross-section.

Table VII (continued)

	C0	C1	C2	C3	C4	C5	C6	C7	X2
1094.1<P<1098.0	1.28±0.02	1.80±0.05	3.04±0.08	2.51±0.09	1.32±0.07	0.72±0.09	-0.08±0.03	-0.14±0.05	51.53
1098.0<P<1101.9	1.27±0.02	1.82±0.05	3.05±0.08	2.50±0.09	1.34±0.08	0.74±0.10	-0.07±0.04	-0.13±0.05	69.08
1101.9<P<1105.8	1.26±0.02	1.79±0.06	3.02±0.10	2.48±0.10	1.34±0.09	0.79±0.11	-0.07±0.05	-0.05±0.06	90.54
1105.8<P<1109.8	1.24±0.02	1.76±0.05	2.98±0.06	2.43±0.08	1.32±0.06	0.75±0.08	-0.05±0.03	-0.07±0.04	59.58
1109.8<P<1113.7	1.25±0.02	1.75±0.04	2.97±0.06	2.42±0.07	1.29±0.06	0.79±0.07	-0.08±0.03	-0.01±0.04	59.31
1113.7<P<1117.6	1.17±0.02	1.63±0.04	2.75±0.06	2.15±0.07	1.13±0.06	0.55±0.07	-0.13±0.03	-0.10±0.04	63.52
1117.6<P<1121.5	1.17±0.02	1.73±0.04	2.73±0.06	2.30±0.07	1.11±0.06	0.67±0.07	-0.15±0.03	-0.07±0.04	80.45
1121.5<P<1125.4	1.13±0.02	1.68±0.04	2.61±0.06	2.18±0.07	1.05±0.06	0.56±0.07	-0.14±0.03	-0.11±0.03	72.06
1125.4<P<1129.4	1.11±0.02	1.60±0.04	2.54±0.06	2.09±0.08	0.97±0.06	0.56±0.08	-0.19±0.03	-0.04±0.04	59.44
1129.4<P<1133.3	1.08±0.02	1.56±0.04	2.45±0.06	2.01±0.07	0.94±0.06	0.50±0.07	-0.17±0.03	-0.06±0.04	63.71
1133.3<P<1137.2	1.08±0.02	1.55±0.04	2.46±0.06	2.01±0.07	0.94±0.06	0.54±0.07	-0.19±0.03	-0.06±0.04	71.61
1137.2<P<1141.1	1.05±0.02	1.50±0.04	2.35±0.07	1.90±0.08	0.80±0.06	0.44±0.08	-0.19±0.03	-0.06±0.04	69.53
1141.1<P<1145.0	1.06±0.02	1.52±0.04	2.41±0.07	1.97±0.08	0.96±0.07	0.56±0.08	-0.16±0.03	0.04±0.04	67.54
1145.0<P<1149.0	1.04±0.01	1.52±0.04	2.38±0.05	1.93±0.07	0.93±0.05	0.47±0.07	-0.17±0.03	-0.04±0.04	76.41
1149.0<P<1152.9	1.01±0.02	1.44±0.04	2.27±0.06	1.80±0.08	0.82±0.06	0.42±0.07	-0.22±0.03	-0.03±0.04	69.20
1152.9<P<1156.8	1.01±0.02	1.45±0.04	2.28±0.06	1.82±0.08	0.87±0.06	0.44±0.07	-0.17±0.03	-0.01±0.04	47.70
1156.8<P<1160.7	0.96±0.02	1.40±0.04	2.17±0.06	1.73±0.07	0.82±0.06	0.37±0.07	-0.18±0.03	-0.08±0.04	34.35
1160.7<P<1164.6	0.97±0.02	1.46±0.04	2.24±0.06	1.81±0.07	0.92±0.05	0.44±0.07	-0.09±0.03	-0.04±0.04	81.94
1164.6<P<1168.6	0.95±0.02	1.41±0.04	2.15±0.06	1.70±0.07	0.81±0.06	0.33±0.07	-0.18±0.03	-0.06±0.04	40.68
1168.6<P<1172.5	0.95±0.02	1.41±0.04	2.15±0.06	1.71±0.06	0.85±0.05	0.36±0.06	-0.13±0.03	-0.03±0.03	52.32
1172.5<P<1176.4	0.88±0.02	1.28±0.04	1.94±0.06	1.49±0.06	0.74±0.05	0.26±0.06	-0.15±0.03	-0.05±0.03	104.37

Legendre polynomial coefficients from fits to the $\pi^- p$ elastic differential cross-section.

7. ANALYSIS OF THE RESULTS

7-1 Behaviour Of The ω Cross-section.

The differential Cross-sections as a function of Cos θ* for ω production are shown in Fig(6-7).

In attempting to understand the ω production mechanism, one can make use of different models and apply them to the Cross-section behaviour.

One approach is to try to describe the behaviour of the Cross-section using a complex scattering length theory described in chapter(1-3). Using this approach, the Cross-section is given by;

$$\sigma = \frac{4\pi}{k^2} \cdot \frac{gbp^{2\ell+1}}{(1+bp^{2\ell+1})^2 + (ap^{2\ell+1})^2} \qquad (7\text{-}1)$$

Where the quantity p is;

$$p = \frac{p^*}{\sqrt{1 + (p^* r)^2}}$$

and where k is the CMS momentum corresponding to the initial state, p^* is the final state CMS momentum, ℓ is the orbital angular momentum of the final state system, r is the radius of the interaction, a is the real part and b is the imaginary part of the scattering length and g is a positive number less than one which measures the $\pi^- p \to \omega n$ coupling. For a given angular momentum, there are four parameters, i.e., a,b,r, and g to be determined in a fit to the Cross-section by Eq(7-1).

The finite radius of the interactions puts a limit on the angular momentum ℓ, such that $\ell \lesssim \frac{p^*}{m_\pi}$. Therefore one would expect ω's to be produced in an S-wave for $p^* \lesssim 140$ Mev/c .

Fits to the Cross-section have been attempted using both S-wave and

P-wave scattering lengths. Fig(7-1) contains all the existing Cross-section data up to p^*=200 Mev/c, the dashed curve is the best S-wave fit for $p^* < 140$ Mev/c and the solid curve shows a fit from a combination of S-wave and P-waves. It is seen from these fits that neither an S-wave nor a P-wave scattering length hypothesis can explain the behaviour at the threshold.

Another approach to fitting the Cross-section is to assume that the ω-n final state results from the decay of an N* resonance, i.e.;

$$\pi^- p \rightarrow N^* \rightarrow \omega\, n$$

Consider first an S-wave production of the ω-n system through the decay of an N* resonance. Those N* baryon resonances which could decay to an S-wave ω-n system could only be S_{11} and D_{13} . Therefore an attempt was made to fit the data with an S-wave Breit-Wigner resonance of form;

$$\sigma = \frac{2\pi(J+1/2)}{3k^2} \cdot \frac{\Gamma_{\pi p}\,\Gamma_{\omega n}}{(E-E_R)^2 + \frac{1}{4}(\Gamma_{\pi p}+\Gamma_{\omega n}+\Gamma_o)^2} \qquad (7\text{-}2)$$

Where E_R is the resonance energy, E is the CMS total energy, k is the the CMS momentum of the incident particles and $\Gamma_{\pi p}$, and $\Gamma_{\omega n}$, and Γ_o are the partial widths to the elastic, ωn, and all the other channels respectively. The values of $\Gamma_{\pi p}$, and Γ_o are functions of k^* (CMS momentum of the corresponding channel), or k^{*3} depending on whether an S or D wave N* is postulated. k^*, however,varies by only 3% over the p^* range from threshold to 200 Mev/c and they have been taken as constants. For S-wave production of the ω one has $\Gamma_{\omega n} = cp^*$, where c is a constant and p^* is the CMS momentum of ωn channel.

The parameters E_R, $\Gamma_{\pi p}$, Γ_o and c were varied until the best fits for S_{11} and D_{13} were obtained and shown in Fig(7-2). It is clear that the Cross-section can not be explained as an S-wave decay product of an N* baryon resonance, the basic problem is that to achieve a rapid change of σ/p^* at

low p* a small total width is required which also produces a rapid fall in σ/p^* above the peak in contradiction with the data.

The possibility was considered that the ωn final state was in a P-wave state through the decay of an N* resonance. The possible resonances which are allowed to decay in to a P-wave ωn system are P_{11}, P_{13}, and F_{15}. An attempt was made to fit the data with a P-wave N* resonance plus an S-wave scattering length.

The S-wave contribution to the Cross-section was assumed to be proportional to P* (equivalent to an S-wave scattering length) and the P-wave to be represented by a Breit-Wigner resonance, Thus the Cross-section is of the form;

$$\sigma = ap^* + \frac{2/3(J+1/2)\pi}{3k^2} \cdot \frac{\Gamma_{\pi p} \cdot \Gamma_{\omega n}}{(E-E_R)^2 + \frac{1}{4}(\Gamma_{\pi p} + \Gamma_o + \Gamma_{\omega n})^2} \qquad \text{(Eq.(7-3)}$$

The symbols are defined as before but the partial width $\Gamma_{\omega n}$ now incorporates the Blatt-Weisskopf barrier factor and is given by;

$$\Gamma_{\omega n} = \frac{\gamma (p^* r)^3}{1+(p^* r)^2} \qquad \text{(Eq.(7-4)}$$

Where r is the radius of the interaction, p* is the CMS momentum of the ω n channel and γ is a constant.

Parameters a, γ, E_R, $\Gamma_{\omega p}$, and Γ_o for various fixed values of r (from 0.5 to 2.5 fermi) were varied until the best fit to the data was obtained. Equally good fits were obtained for values of J=1/2,3/2 or 5/2, and Table(IIX) shows some of the results for J=1/2, where the values of χ^2 are for 36 degrees of freedom.

This table shows that the value of χ^2 is insensitive to changes of 100 Mev/c2 in, E_R, γ, or $\Gamma_{\pi p}$ and that the shape of the fitted curve

depends mainly on the barrier factor.

To demonstrate this insensitivity, the values of the parameters corresponding to the lowest values of χ^2 were roughly averaged and gave E_R = 1720 Mev/c2, $\Gamma_{\pi p}$=150 Mev/c2, Υ=100 Mev/c2, and r=1.2 fermi. Γ_o and a were allowed to vary and Fig(7-3) shows the result of the fit which gave a value of χ^2 = 18 .

A comparison between the S and P wave contributions to the Cross-section shows the P-wave contribution is quite large, dominating over the S-wave even at very low p* (table IX). This large P-wave contribution is an indication that a P-wave N* resonance is possibly responsible for ω production.

As far as the total cross-section is concerned there is no evidence for preference of any of the total angular momentum values J of the N* resonance.

7-2 Angular Distribution Of The ωn System.

As has already been described in section(1-3), there are only seven amplitudes from all the possible S and P-wave combinations which could contribute to the angular distribution shown expanded in Eq(1-29). This suggests that combinations of amplitudes (SS11) + (PP13) or (DS33) + (PP11), lead to an isotropic angular distribution while the combinations (SS11) + (PP13) + (PP33) + (FP53) or (DS33) + (PP31) + (PP11), produce no P_1(COS θ*) term in the angular distribution although they produce a P_2(COS θ*) term.

The values of the ratio of the Legendre polynomial coefficients from the fit to the angular distribution, as a function of p*, are shown in Fig(6-9). The values of the ratios C_1/C_o and C_2/C_o which represent the contributions from the P_1(COS θ*) and P_2(COS θ*) term in the Cross-section

respectively are consistent with zero, (their maximum values are less than 0.15). Therefore, it is not unreasonable to assume that the angular distribution is isotropic. Then the allowed amplitudes are; (SS11) + (PP13) or (DS33) + (PP11). It must be pointed out that even though each of the above combinations leads to an isotropic angular distribution only one of the above combinations could be responsible for the isotropic production of the ωn system. For both of the above combinations, the final state P-wave component is linked to an initial $\pi^- p$ state of J=1/2 and L=1, associated with a P_{11} . However, the P_{11} resonance would be expected to contribute to both the PP11 and PP13 amplitudes and thus would lead to a $P_1(\cos\theta^*)$ term in the angular distribution through S-P interference. The isotropic distribution implies therefore, that either the PP11 or PP13 together with the corresponding final state S-wave is suppressed.

A theoretical prediction of an N* baryon resonance decay involving a vector meson based on the ℓ-broken $SU(6)_W$ model was presented by W.P. Petersen and et al[21]. Their model predicted the dominent spin of the ρn system for the decay of the $P_{11}(1780)$ in $\pi^- p$ collisions, which was found to be in agreement with the experimental data[22]. They also predicted that a spin of s=3/2 would be dominant in the reaction $\pi p \to P_{11}(1780) \to \omega n$ and the ratio of the amplitudes PP13/PP11 would be 97% / 3% .Therefore, based on this prediction, there is a theroretical justification for the suppression of the PP11 final state amplitude in the decay of a P_{11} resonance into an ωn system.

A further consideration is to keep the prohibition on the $P_1(\cos\theta^*)$ term but allow a $P_2(\cos\theta^*)$ term to be present in the angular distribution as our data possibly requires. In such a case the combinations of amplitudes

which lead to the absence of the $p_1(\cos\theta^*)$ term are (SS11) + (PP13) + (PP33) + (FP53) or (DS33) + (PP11) + (PP31). The initial state $\pi^- p$ system could have L=1, J=3/2 or L=3, J=5/2, which correspond to N* resonance in P_{13} and F_{15} states.

The P_{13} suffers from two difficulties. The first one is the same as the P_{11}, that is, the prohibition of $P_1(\cos\theta^*)$ term requires the suppresion of one of the amplitudes that the resonance can feed,i.e., either PP13, or PP33. Assuming that this was theoretically justified a second difficulty arises because both of these two amplitudes would produce a large $P_2(\cos\theta^*)$ term in the angular distribution (see appendix I)., whilst our data indicate a contribution of less than 15±15 % .

The F_{15} can only produce one amplitude and so does not suffer the first difficulty of the P_{13}, but again it would produce a large $P_2(\cos\theta^*)$ term.

Thus neither P_{13} nor F_{15} could be a possible N* resonance candidate for ω production.

A possible alternative to the models which have been used to examine the ω production mechanism, is a final state interaction model. The average separation of the ω and n at the decay for p* = 31 Mev/c, is equal to a pion compton wavelength. A possible effect which might introduce a significant change in the Cross-section in region of low p* is a final state interaction between the neutron and a pion from the ω decay products. This model was examined in some detail in Ref(2). The drop in the Cross-section could be understood by this model. However, if it is so, the final state interaction effect would be much stronger in the $\pi^+\pi^-\pi^o$ than in the $\pi^o\gamma$ decay channels and resulting from this one would expect to see the $\frac{\pi^-\pi^+\pi^o}{\pi^o\gamma}$ branching ratio increasing with p*, while such an effect has not been observed. In addition a final state interaction could also lead to the distortion of the ω mass spectrum and

again no such effect is seen.

There has been a suggestion that ρ meson exchange in the t-channel could account for the drop in the production Cross-section near threshold. A detailed calculation of the ρ exchange model showed that it could only account for a few % of the drop in the Cross-section [2].

7-3 Analysis of the $\pi^- p$ Elastic Results.

The results of the elastic scattering Cross-section measurement are now examined.

7-3-1 Cusp Effect

It should be mentioned that the elastic scattering data was part of a series of measurements to study possible structure at the η,ω, and X^o thresholds. In the course of the work a cusp was observed in the elastic scattering Cross-section at the η threshold and the result of this measurement is published elsewhere [16]. In this work, however, only the data which correspond to the ω meson threshold is presented.

The results of the measurements of the elastic cross-sections, angular distributions and the Legendre polynomial coefficients from fits to the angular distributions are shown in Figs. (6-10) to (6-15).

A feature of data is that the Cross-section shows neither any structure at the ω production threshold (E_t), nor any narrow resonance over the energy range which has been covered.

The fact that we have not observed any structure at the production threshold, is not very surprising and can be explained. The physical quantities characterising the scattering process are singular at the threshold of a new reaction channel. The singularity in the Cross-section which is associated with threshold "distributes itself", over the elastic scattering

Cross-section and the Cross-section of the reaction channels, thus two conclusions follow; (1) Near the threshold E_t for the ω production, there are anomalies not only in the scattering Cross-section, but in the Cross-section of all the other reaction channels, whose threshold energy E_t' lies below E_t; (2) As the number of competing reaction channels increases, the anomaly in the elastic Cross-section decreases. The magnitude depends on the details of the situation, but the decrease need not be small. However, the nature of the singularity does not change, and whether or not it can be observed depends on the precision of the measurement. This argument holds only when the width of the resonance is small; if the resonance is wide, then the anomaly in the Cross-section will be smeared out and it will not be possible to observe it.

The threshold energy for ω production in $\bar{\pi}p$ collisions is E_t = 1.722 Gev. In addition to ω production there are a large number of final states Kinematically allowed, such as $\bar{\pi}p \to n\rho$, $K^o \Lambda^o$, $K^o \Sigma^o$ and multi-pion final states. The other more important aspect of the ω meson is that the width (Γ_ω = 10 Mev/c^2), is large compared to that of η(Γ_η = 2.6 Kev/c^2). Therefore, it is believed that these two characteristics of ω meson production smear out the anomaly in the elastic channel and thus make it unobservable as a cusp.

7-3-2 The effect of the opening of the ω threshold on the elastic channel.

For an unpolarised target the differential cross section of the recoil nucleon expressed in terms of the non-spin-flip amplitude $f(\theta^*,k)$ and the spin-flip amplitude $g(\theta^*,k)$

$$\frac{d\sigma}{d\Omega} = |f(\theta^*,k)|^2 + |g(\theta^*,k)|^2 \qquad (7\text{-}5)$$

The $f(\theta^*,k)$ and $g(\theta^*, k)$ amplitude can be expanded as a sum of partial waves. For each value of ℓ , the orbital angular momentum of the system, there are two values of the total angular momentum, i.e., $J = \ell + 1/2$ and $J = \ell - 1/2$ and both terms appear in the summation. The expansion is given by

$$f(\theta^*,k) = \lambda \Sigma_\ell \; (\ell+1) T_{\ell+}(k) + \ell \, T_{\ell-}(k) \cdot P_\ell(\cos\theta^*)$$

$$g(\theta^*,k) = i\lambda \Sigma_\ell \; T_\ell(k) + T_\ell(k) \; P^1_\ell(\cos\theta^*) \qquad (7\text{-}6)$$

where $P^1_\ell(\cos\theta^*) = \sin\theta^* \, (dp_\ell / d\cos\theta^*)$ are the first associated Legendre functions and $P_\ell(\cos\theta^*)$ are the Legendre polynomials, $\lambda = 1/k$ is the wavelength and $T_{\ell\pm}$ are the partial wave amplitudes, defined by;

$$T_{\ell\pm} = \frac{1}{2i} \left(\eta_{\ell\pm 1/2} \, e^{2i\delta_{\ell\pm 1/2}} - 1\right) \qquad (7\text{-}7)$$

For $\ell\pm$ the convention adopted is S,P,D,F,G,H for ℓ = 0,1,2,3,4,5 with subscripts 2I and 2J, $(\ell_{2I\,2J})$, so D_{13} is $\ell = 2$, $I = 1/2$, $J = 3/2$.

Considering the two isopin state I=1/2 and I=3/2, and using the above convention $f(\theta^*, k)$, and $g(\theta^*, k)$ can be written as;

$$f(\theta^*,k) = \frac{1}{6\,ik} \{ (2S_{11} + S_{31}) + (2P_{11} + 4P_{13} + P_{31} + 2P_{33}) \cos\theta^*$$
$$+ (4D_{13} + 6D_{15} + 2d_{33} + 3D_{35}) \, (3/2 \cos^2\theta^* - 1/2)$$
$$+ (6F_{15} + 8F_{17} + 4F_{37}) \, (5/2 \cos^3\theta^* - 3/2 \cos) + \ldots \}$$

and

$$g(\theta^*,k) = -\frac{1}{6k} \{ P_{33} + 2P_{13} - P_{31} - 2P_{11}) \sin\theta^*$$
$$+ 3(D_{35} + 2D_{15} - D_{33} - 2D_{13}) \sin\theta^* \cos\theta^*$$
$$+ 3/2 \, (F_{37} + 2F_{17} - F_{35} - 2F_{15}) \, (5\cos^2\theta^* - 1) \sin\theta^*$$
$$+ \ldots \} \qquad (7\text{-}8)$$

where the amplitudes are given by Eq(7-7), e.g., for S_{11} we have

$\eta_{S_{11}} e^{2i\delta_{11}} - 1.$

An attempt has been made to investigate the effect of the production of the ω meson on the elastic scattering channel. For this purpose we have used the results of a phase shift analysis Cern Experimental (1969) [24]. As they have only six data points at about 40 Mev/c apart in the range of the momentum which has been covered by our experiment we averaged their data and an interpolation has been made to calculate the phase shift parameters at every 4 Mev/c .

The prediction of the elastic scattering cross-section from the phase shift results for a number of angular regions are shown in Fig(7-4). The agreement between our data and the prediction of the phase shift analysis is very good and justifies our normalisation.

Although we would not expect to see any cusp behaviour the opening of the ω-n channel could affect the elastic cross-section significantly. In order to calculate what effect this could have had we have estimated values that the elastic cross-section would have taken had there been no ω production.

To calculate this effect two assumptions were made; first that ω production only couples to the elastic channel and second that only S_{11} and P_{11} - waves are present. The P_{13}, D_{13}, and F_{15} as already discussed are suppressed.

To do this we need the (S_{11} and P_{11}) cross-section as a function of p_π, however, Table(IX) gives them as a function of the centre of mass momentum

(p^*).

These were calculated at a particular value of p_π , by;

a) Choosing a series of ω masses over its width according to a Breit-Wigner distribution.

b) For each mass calculating the corresponding p^* and therefore, the cross-section.

c) Determining the weighted cross-section corresponding to p_π .

Having calculated the ω cross-section as a function of p_π, then the effect in the elastic channel was determined at each value of p_π ;

i) Calculating the elastic S_{11} and P_{11} -waves cross-sections from the phase shift analysis.

ii) Increasing the elastic cross-section by the corresponding amounts calculated above.

iii) Recalculating the phase shift absorption parameters.

iv) Determining the difference between the old and new phase shift predictions.

These are ploted in Fig(7-4). It is seen from this plot that changes in the slope of the cross-section in a number of angular regions are quite significant. These rather large changes suggest that the assumption which has been made in our calculation, i.e., that ω production only comes from the elastic channel, is not true and therefore, the other inelastic channels are also affected by ω meson production.

The other feature of the elastic scattering result is the absence of

any narrow resonance over the range of energy covered. Although there is a sign of an enhancment at total centre of mass energy E = 1.717 Gev, it is only observed in two regions of Cos θ^* ,{ $-0.34 < \cos\theta^* < -0.24$, and $-0.44 < \cos\theta^* < -0.34$ }, with a width of a few Mev/c^2 and a height of not more than two standard deviations. This ,however, is a very narrow and small bump and is most likely a statistical fluctuation. To get an idea how a very narrow resonance would look like in the elastic channel, a small loop in the S_{11} - wave Argand plot was imposed between two consecutive data points of Ref(24), and the resulting elastic cross-section was then calculated. The Argand diagram for this wave and the predicted cross-section behaviour in only one angular region are shown in Fig(7-5). The effect of imposing a loop was similar in the other angular regions. Therefore, because of absence of such a very characteristic behaviour in our data , the possibility is rejected that a narrow N* resonance coupling strongly to the elastic channel causes the rapid rise in the cross-section of the ω production near its threshold.

7-4 Conclusion.

To conclude our results, we now summarize the ω production analysis and try to find an answer to the question " How is the ω produced ".

It has been shown that the production of the ω meson can not be understood either by elastic scattering length theory or by a ρ meson exchange in the t-channel. The final state interaction model could explain the drop in the cross-section at low p*, but the other aspects of the production behaviour completely reject this model. The resonance model, however, has shown that an N* resonance in the P_{11}, state with parameters of $E_R = 1720 \pm 100$ Mev/c^2, $\Gamma_{\pi p} = 150 \pm 100$ Mev/c^2, and $\gamma = 100 \pm 100$ Mev/c^2 can explain both the behaviour of the ω production cross-section and its angular distribution.

The nearest well-established $\pi^- p$ resonance with these quantum numbers is the P_{11} with mass range of 1640 - 1800 Mev/c^2 and width of between 100 and 300 Mev/c^2. These characteristics of the observed N* resonance are quite within the range of the obtained fitted parameters in our result. Therefore it is very likely that the ω meson is produced mainly through the P-wave decay of this P_{11} resonance.

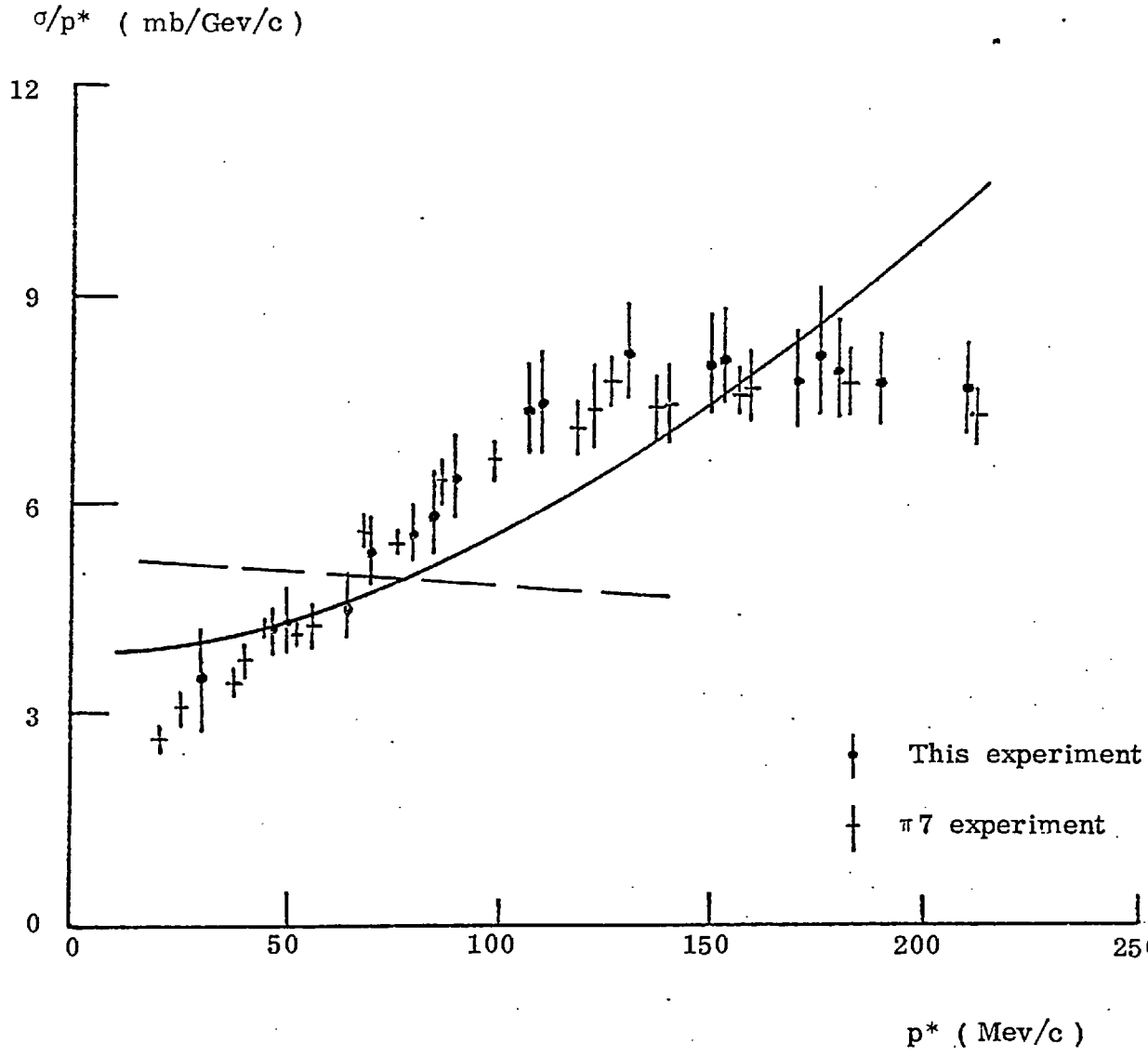

The cross-section data fitted using scattering length theory. The broken curve shows an S-wave fit for $p^* < 140$ Mev/c, the solid curve is for P-wave.

Fig (7-1)

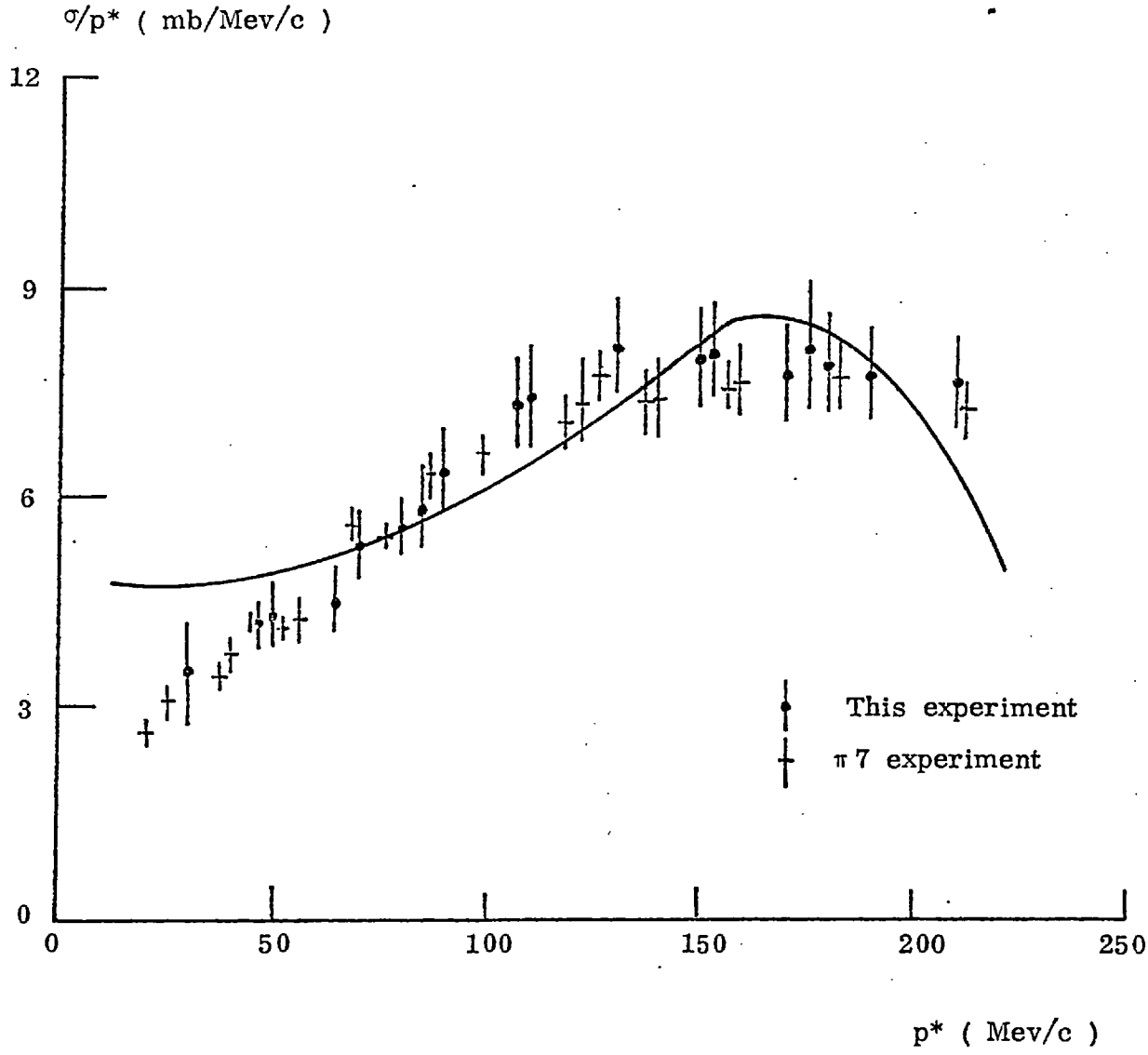

The cross-section data fitted by an N* resonance model. The curve shows an S-wave N* fit.

Fig (7-2)

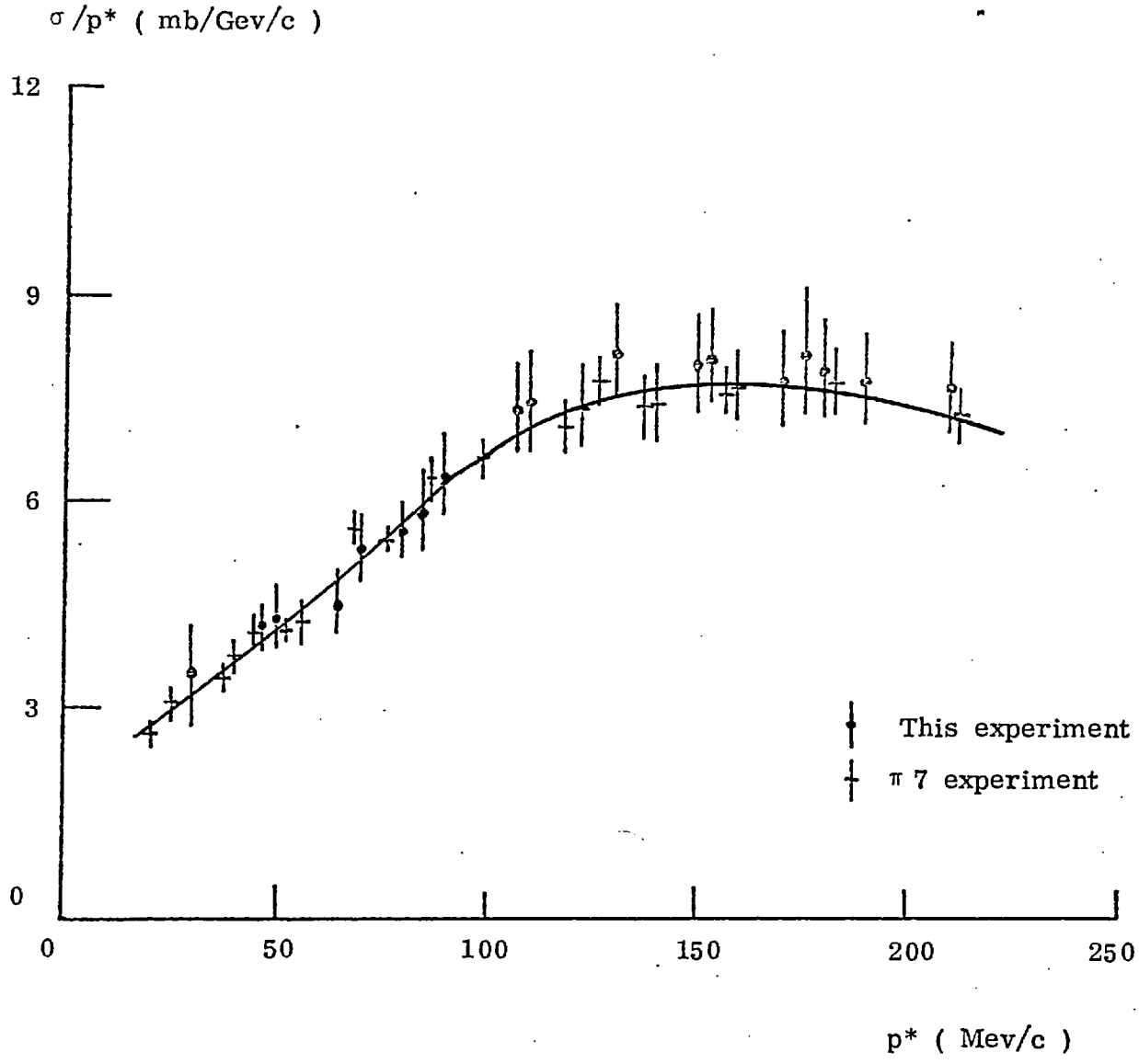

The cross-section data fitted by an N* resonance model. The curve shows a P-wave N* plus a constant σ/p^* contribution.

Fig (7-3)

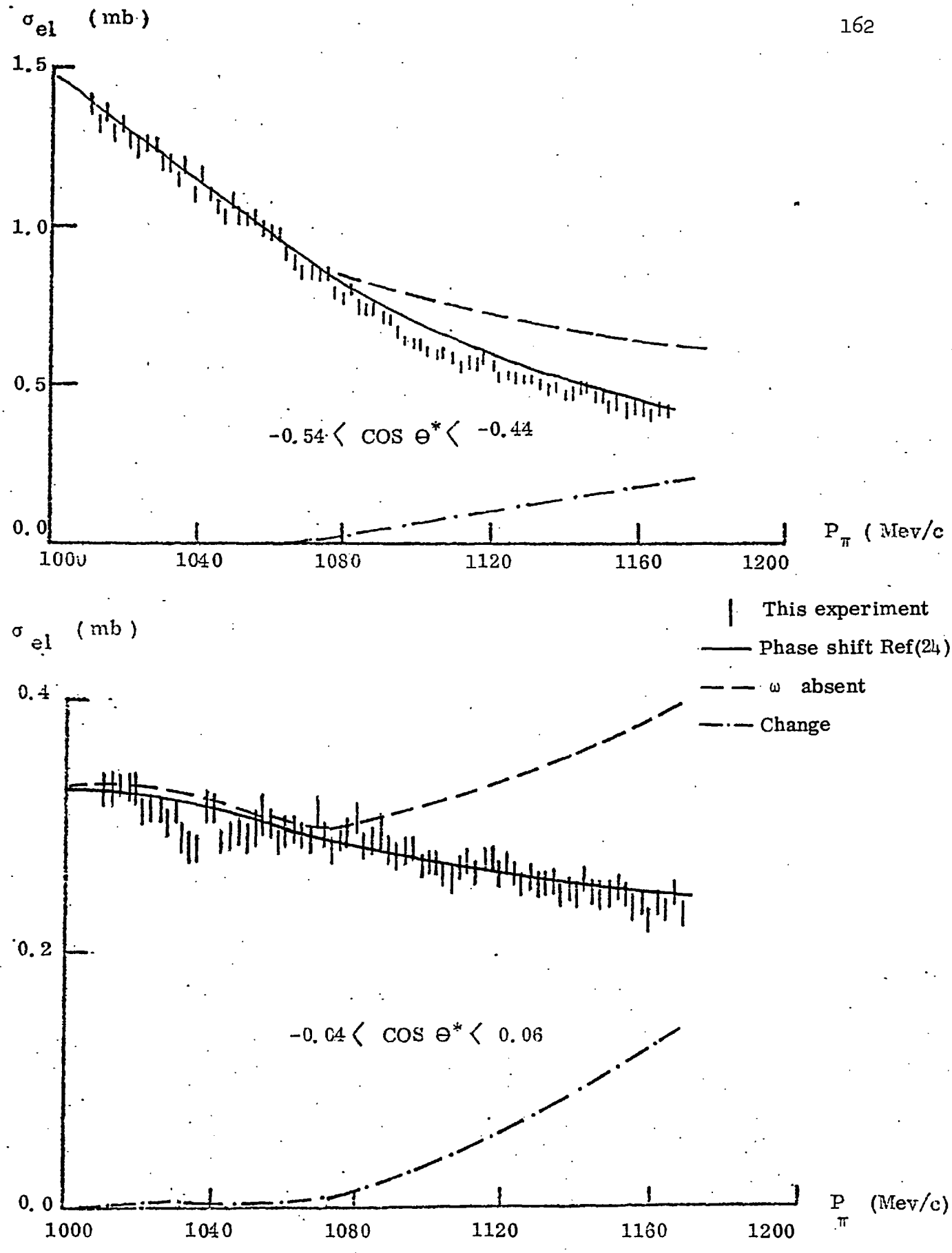

Comparison between the result of the πp elastic cross-section from this experiment and the prediction from phase shift analysis of Ref(23).

Fig (7-4)

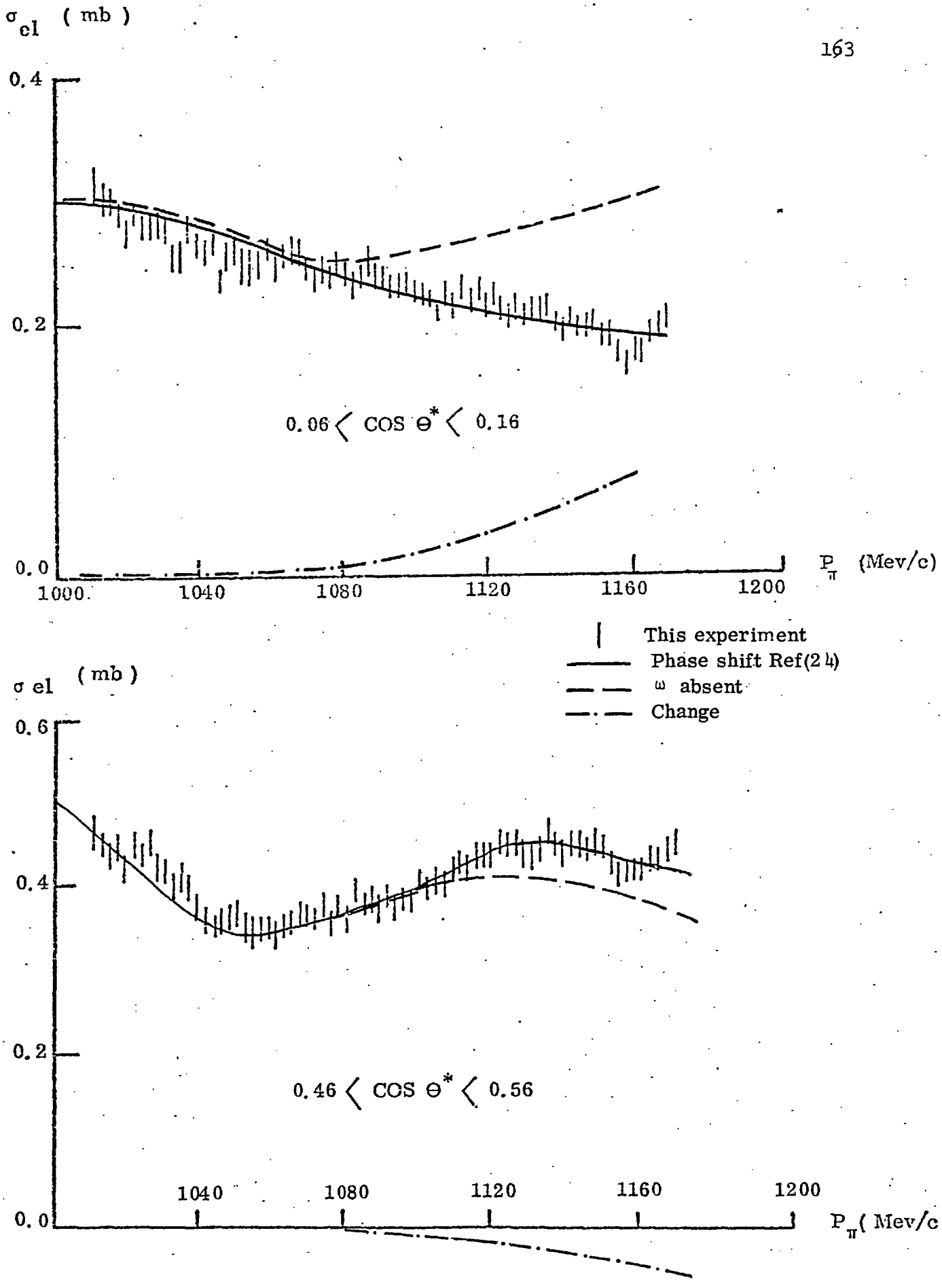

Comparison between the result of the πp elastic cross-section from this experiment and the prediction from phase shift analysis of Ref(23).

Fig(7-4)

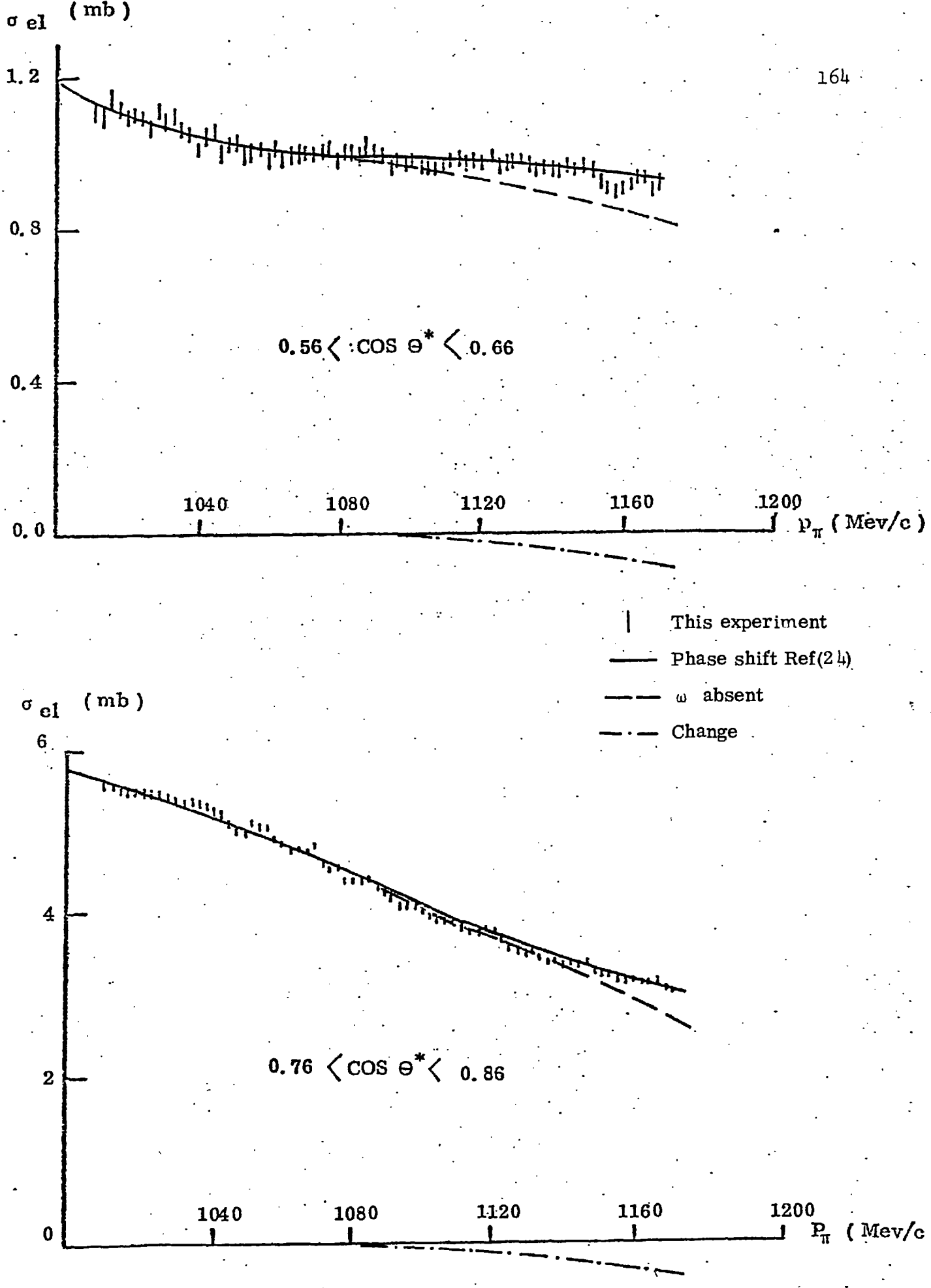

Comparison between the result of the πp elastic cross-section from this experiment and the prediction from phase shift analysis of Ref(23).

Fig (7-4)

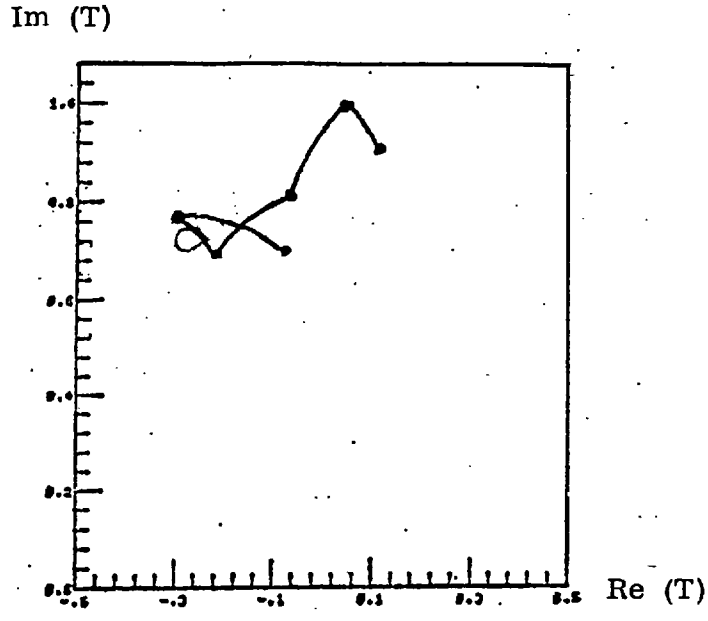

Arg and plot for S_{11}

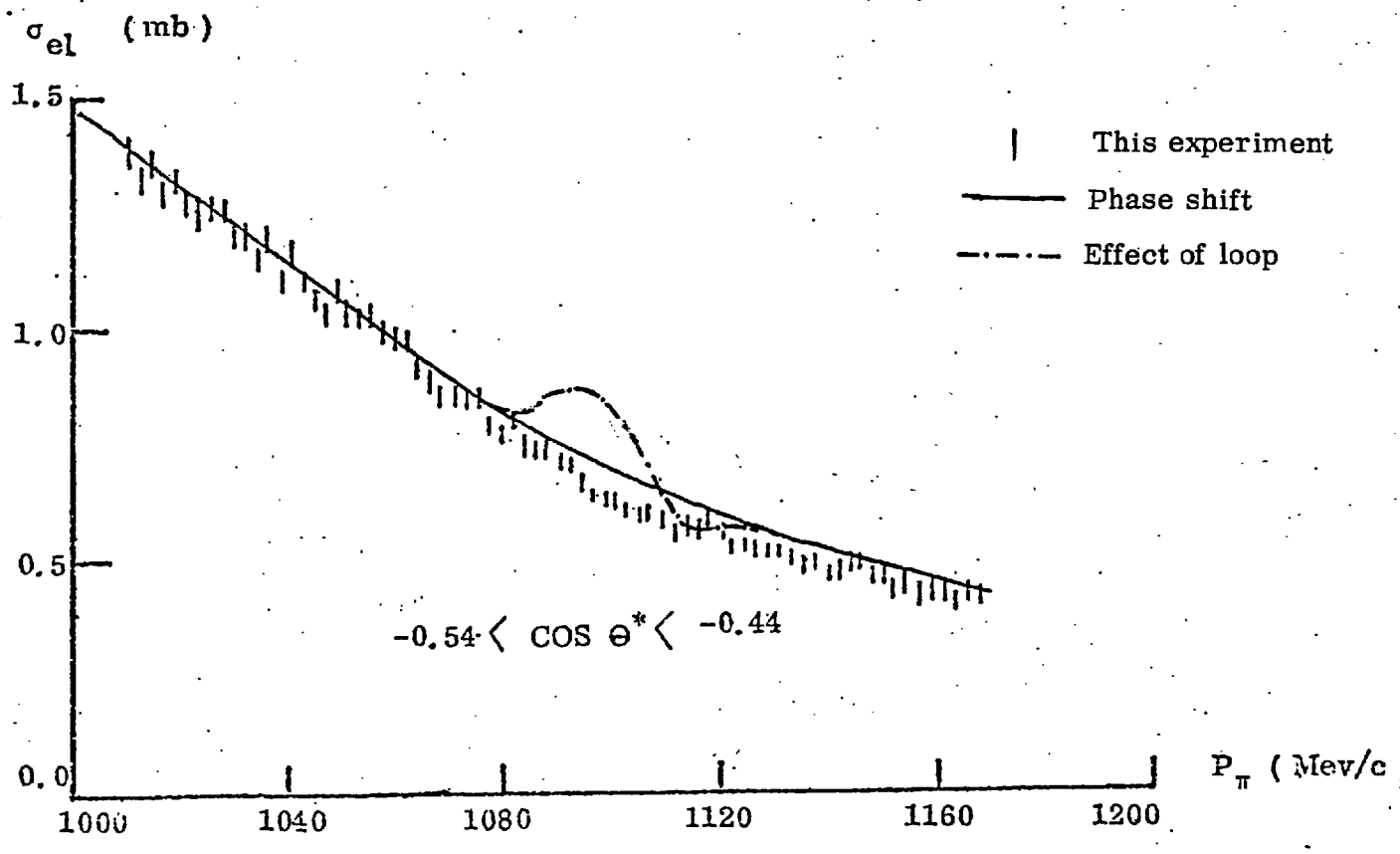

$\pi^- p$ elastic cross-section as a function of pion momentum.

Fig (7-5)

TABLE(IIX)

J = 1/2

r Fermi	E_R Mev/c2	γ Mev/c2	Γ_{el} Mev/c2	Γ_o Mev/c2	Γ * Mev/c2	σ_{el} ** mb	χ^2
0.5	1680	70	85	0.3	87	1.8	19.5
0.8	1660	240	115	0.5	128	2.8	19
1.0	1640	185	150	6.0	174	2.8	18
1.2	1650	125	250	50	320	1.0	18
1.5	1790	85	110	85	220	1.6	18.5
2.0	1710	45	340	17	380	0.1	27

* Γ is the total width and calculated for p*=100 Mev/c.

** σ_{el} is the calculated Cross-section for the elastic reaction at $E=E_R$.

TABLE IX

The results of fits to the ω production Cross-section data using an S-wave scattering length plus a p-wave N* resonance, i.e.; $\sigma = \sigma(\text{S-wave}) + \sigma(\text{p-wave})$.

P* Mev/c	σ_{data} μb	$\Delta\sigma_{data}$ μb	σ_{fit} μb	σ_{fit} (S-wave) μb	σ_{fit} (P-wave) μb
20	53	4	57	52	5
25	77	6	75	65	10
30	105	24	96	78	18
35	127	7	129	96	33
40	151	9	146	104	42
45	190	8	175	117	58
50	214	25	208	130	78
56	238	19	252	145	106
64	288	28	316	166	149
70	374	35	370	182	188
76	414	12	425	197	229
80	448	32	466	208	256
85	497	51	517	221	297
90	577	50	570	234	335
99	650	28	665	257	408
103	633	62	707	268	440

TABLE IX (continued)

P* Mev/c	σ_{data} μb	$\Delta\sigma_{data}$ μb	σ_{fit} μb	σ(S-wave) fit μb	σ (P-wave) fit μb
107	802	59	750	278	470
110	824	78	782	286	495
118	838	43	864	307	557
122	903	73	904	317	585
126	978	45	943	331	617
130	1066	91	981	338	643
137	1013	63	1046	356	689
140	1043	84	1072	364	708
150	1203	106	1155	390	765
157	1200	56	1209	408	800
170	1326	122	1297	442	855
180	1431	126	1357	468	889
190	1482	133	1411	494	917
196	1262	80	1440	510	930
210	1617	149	1503	546	955

APPENDIX

COEFFICIENTS FOR $d\sigma/d\Omega$

STATE 1	STATE 2	A0	A 1	A 2	A 3	A 4	A 5	A 6	A 7	A 8	A 9
00000101	00000101	1.000	0.0	0.0	0.0	0.0	0.0	0.0	0.0	0.0	0.0
00000101	01010101	0.0	2.000	0.0	0.0	0.0	0.0	0.0	0.0	0.0	0.0
00000101	01010301	0.0	4.000	0.0	0.0	0.0	0.0	0.0	0.0	0.0	0.0
00000101	02020301	0.0	0.0	4.000	0.0	0.0	0.0	0.0	0.0	0.0	0.0
00000101	02020501	0.0	0.0	6.000	0.0	0.0	0.0	0.0	0.0	0.0	0.0
00000101	03030501	0.0	0.0	0.0	6.000	0.0	0.0	0.0	0.0	0.0	0.0
00000101	03030701	0.0	0.0	0.0	0.0	8.000	0.0	0.0	0.0	0.0	0.0
00000101	04040701	0.0	0.0	0.0	0.0	0.0	8.000	0.0	0.0	0.0	0.0
00000101	04040901	0.0	0.0	0.0	0.0	0.0	0.0	10.000	0.0	0.0	0.0
00000101	05050901	0.0	0.0	0.0	0.0	0.0	0.0	0.0	10.000	0.0	0.0
01010101	01010101	1.000	0.0	0.0	0.0	0.0	0.0	0.0	0.0	0.0	0.0
01010101	01010301	0.0	0.0	4.000	0.0	0.0	0.0	0.0	0.0	0.0	0.0
01010101	02020301	0.0	4.000	0.0	0.0	0.0	0.0	0.0	0.0	0.0	0.0
01010101	02020501	0.0	0.0	0.0	6.000	0.0	0.0	0.0	0.0	0.0	0.0
01010101	03030501	0.0	0.0	6.000	0.0	0.0	0.0	0.0	0.0	0.0	0.0
01010101	03030701	0.0	0.0	0.0	0.0	8.000	0.0	0.0	0.0	0.0	0.0
01010101	04040701	0.0	0.0	0.0	8.000	0.0	0.0	0.0	0.0	0.0	0.0
01010101	04040901	0.0	0.0	0.0	0.0	0.0	10.000	0.0	0.0	0.0	0.0
01010101	05050901	0.0	0.0	0.0	0.0	10.000	0.0	0.0	0.0	0.0	0.0
01010301	01010301	2.000	0.0	2.000	0.0	0.0	0.0	0.0	0.0	0.0	0.0
01010301	02020301	0.0	0.800	0.0	7.200	0.0	0.0	0.0	0.0	0.0	0.0
01010301	02020501	0.0	7.200	0.0	4.800	0.0	0.0	0.0	0.0	0.0	0.0
01010301	03030501	0.0	0.0	1.714	0.0	10.286	0.0	0.0	0.0	0.0	0.0
01010301	03030701	0.0	0.0	10.286	0.0	5.714	0.0	0.0	0.0	0.0	0.0
01010301	04040701	0.0	0.0	0.0	2.667	0.0	13.333	0.0	0.0	0.0	0.0
01010301	04040901	0.0	0.0	0.0	13.333	0.0	6.667	0.0	0.0	0.0	0.0
01010301	05050901	0.0	0.0	0.0	0.0	3.636	0.0	16.364	0.0	0.0	0.0
02020301	02020301	2.000	0.0	2.000	0.0	0.0	0.0	0.0	0.0	0.0	0.0
02020301	02020501	0.0	0.0	1.714	0.0	10.286	0.0	0.0	0.0	0.0	0.0
02020301	03030501	0.0	7.200	0.0	4.800	0.0	0.0	0.0	0.0	0.0	0.0
02020301	03030701	0.0	0.0	0.0	2.667	0.0	13.333	0.0	0.0	0.0	0.0
02020301	04040701	0.0	0.0	10.286	0.0	5.714	0.0	0.0	0.0	0.0	0.0
02020301	04040901	0.0	0.0	0.0	0.0	3.636	0.0	16.364	0.0	0.0	0.0
02020301	05050901	0.0	0.0	0.0	13.333	0.0	6.667	0.0	0.0	0.0	0.0
02020501	02020501	3.000	0.0	3.429	0.0	2.571	0.0	0.0	0.0	0.0	0.0
02020501	03030501	0.0	0.514	0.0	3.200	0.0	14.286	0.0	0.0	0.0	0.0
02020501	03030701	0.0	10.286	0.0	8.000	0.0	5.714	0.0	0.0	0.0	0.0
02020501	04040701	0.0	0.0	1.143	0.0	4.675	0.0	18.182	0.0	0.0	0.0
02020501	04040901	0.0	0.0	14.286	0.0	9.351	0.0	6.364	0.0	0.0	0.0
02020501	05050901	0.0	0.0	0.0	1.818	0.0	6.154	0.0	22.028	0.0	0.0
03030501	03030501	3.000	0.0	3.429	0.0	2.571	0.0	0.0	0.0	0.0	0.0
03030501	03030701	0.0	0.0	1.143	0.0	4.675	0.0	18.182	0.0	0.0	0.0
03030501	04040701	0.0	10.286	0.0	8.000	0.0	5.714	0.0	0.0	0.0	0.0
03030501	04040901	0.0	0.0	0.0	1.818	0.0	6.154	0.0	22.028	0.0	0.0
03030501	05050901	0.0	0.0	14.286	0.0	9.351	0.0	6.364	0.0	0.0	0.0
03030701	03030701	4.000	0.0	4.762	0.0	4.208	0.0	3.030	0.0	0.0	0.0
03030701	04040701	0.0	0.381	0.0	2.182	0.0	6.593	0.0	22.844	0.0	0.0
03030701	04040901	0.0	13.333	0.0	10.909	0.0	9.231	0.0	6.527	0.0	0.0
03030701	05050901	0.0	0.0	0.866	0.0	3.237	0.0	8.485	0.0	27.413	0.0
04040701	04040701	4.000	0.0	4.762	0.0	4.208	0.0	3.030	0.0	0.0	0.0
04040701	04040901	0.0	0.0	0.866	0.0	3.237	0.0	8.485	0.0	27.413	0.0
04040701	05050901	0.0	13.333	0.0	10.909	0.0	9.231	0.0	6.527	0.0	0.0
04040901	04040901	5.000	0.0	6.061	0.0	5.664	0.0	4.848	0.0	3.427	0.0
04040901	05050901	0.0	0.303	0.0	1.678	0.0	4.615	0.0	10.750	0.0	32.653
05050901	05050901	5.000	0.0	6.061	0.0	5.664	0.0	4.848	0.0	3.427	0.0

States are labeled as; $L\ L'(2J)\ (2s')$

state 1	state 2	A0	A1	A 2	A 3	A 4	A 5	A6	A 7	A 8	A 9
00020103	00020103	1.000	0.0	0.0	0.0	0.0	0.0	0.0	0.0	0.0	0.0
00020103	01010103	0.0	2.000	0.0	0.0	0.0	0.0	0.0	0.0	0.0	0.0
00020103	01010303	0.0	-1.265	0.0	0.0	0.0	0.0	0.0	0.0	0.0	0.0
00020103	01030303	0.0	3.795	0.0	0.0	0.0	0.0	0.0	0.0	0.0	0.0
00020103	02000303	0.0	0.0	-2.828	0.0	0.0	0.0	0.0	0.0	0.0	0.0
00020103	02020303	0.0	0.0	2.828	0.0	0.0	0.0	0.0	0.0	0.0	0.0
00020103	02020503	0.0	0.0	-2.268	0.0	0.0	0.0	0.0	0.0	0.0	0.0
00020103	02040503	0.0	0.0	5.555	0.0	0.0	0.0	0.0	0.0	0.0	0.0
00020103	03010503	0.0	0.0	0.0	-4.648	0.0	0.0	0.0	0.0	0.0	0.0
00020103	03030503	0.0	0.0	0.0	3.795	0.0	0.0	0.0	0.0	0.0	0.0
00020103	03030703	0.0	0.0	0.0	-3.266	0.0	0.0	0.0	0.0	0.0	0.0
00020103	03050703	0.0	0.0	0.0	7.303	0.0	0.0	0.0	0.0	0.0	0.0
00020103	04020703	0.0	0.0	0.0	0.0	-6.414	0.0	0.0	0.0	0.0	0.0
00020103	04040703	0.0	0.0	0.0	0.0	4.781	0.0	0.0	0.0	0.0	0.0
00020103	04040903	0.0	0.0	0.0	0.0	-4.264	0.0	0.0	0.0	0.0	0.0
00020103	05030903	0.0	0.0	0.0	0.0	0.0	-8.165	0.0	0.0	0.0	0.0
00020103	05050903	0.0	0.0	0.0	0.0	0.0	5.774	0.0	0.0	0.0	0.0
01010103	01010103	1.000	0.0	0.0	0.0	0.0	0.0	0.0	0.0	0.0	0.0
01010103	01010303	0.0	0.0	-1.265	0.0	0.0	0.0	0.0	0.0	0.0	0.0
01010103	01030303	0.0	0.0	3.795	0.0	0.0	0.0	0.0	0.0	0.0	0.0
01010103	02000303	0.0	-2.828	0.0	0.0	0.0	0.0	0.0	0.0	0.0	0.0
01010103	02020303	0.0	2.828	0.0	0.0	0.0	0.0	0.0	0.0	0.0	0.0
01010103	02020503	0.0	0.0	0.0	-2.268	0.0	0.0	0.0	0.0	0.0	0.0
01010103	02040503	0.0	0.0	0.0	5.555	0.0	0.0	0.0	0.0	0.0	0.0
01010103	03010503	0.0	0.0	-4.648	0.0	0.0	0.0	0.0	0.0	0.0	0.0
01010103	03030503	0.0	0.0	3.795	0.0	0.0	0.0	0.0	0.0	0.0	0.0
01010103	03030703	0.0	0.0	0.0	0.0	-3.266	0.0	0.0	0.0	0.0	0.0
01010103	03050703	0.0	0.0	0.0	0.0	7.303	0.0	0.0	0.0	0.0	0.0
01010103	04020703	0.0	0.0	0.0	-6.414	0.0	0.0	0.0	0.0	0.0	0.0
01010103	04040703	0.0	0.0	0.0	4.781	0.0	0.0	0.0	0.0	0.0	0.0
01010103	04040903	0.0	0.0	0.0	0.0	0.0	-4.264	0.0	0.0	0.0	0.0
01010103	05030903	0.0	0.0	0.0	0.0	-8.165	0.0	0.0	0.0	0.0	0.0
01010103	05050903	0.0	0.0	0.0	0.0	5.774	0.0	0.0	0.0	0.0	0.0
01010303	01010303	2.000	0.0	-1.600	0.0	0.0	0.0	0.0	0.0	0.0	0.0
01010303	01030303	0.0	0.0	-2.400	0.0	0.0	0.0	0.0	0.0	0.0	0.0
01010303	02000303	0.0	1.789	0.0	0.0	0.0	0.0	0.0	0.0	0.0	0.0
01010303	02020303	0.0	1.431	0.0	-3.220	0.0	0.0	0.0	0.0	0.0	0.0
01010303	02020503	0.0	6.024	0.0	-4.590	0.0	0.0	0.0	0.0	0.0	0.0
01010303	02040503	0.0	0.0	0.0	-3.513	0.0	0.0	0.0	0.0	0.0	0.0
01010303	03010503	0.0	0.0	2.939	0.0	0.0	0.0	0.0	0.0	0.0	0.0
01010303	03030503	0.0	0.0	2.743	0.0	-5.143	0.0	0.0	0.0	0.0	0.0
01010303	03030703	0.0	0.0	7.967	0.0	-5.902	0.0	0.0	0.0	0.0	0.0
01010303	03050703	0.0	0.0	0.0	0.0	-4.619	0.0	0.0	0.0	0.0	0.0
01010303	04020703	0.0	0.0	0.0	4.057	0.0	0.0	0.0	0.0	0.0	0.0
01010303	04040703	0.0	0.0	0.0	4.032	0.0	-7.055	0.0	0.0	0.0	0.0
01010303	04040903	0.0	0.0	0.0	9.888	0.0	-7.191	0.0	0.0	0.0	0.0
01010303	05030903	0.0	0.0	0.0	0.0	5.164	0.0	0.0	0.0	0.0	0.0
01010303	05050903	0.0	0.0	0.0	0.0	5.311	0.0	-8.963	0.0	0.0	0.0
01030303	01030303	2.000	0.0	1.600	0.0	0.0	0.0	0.0	0.0	0.0	0.0
01030303	02000303	0.0	0.0	0.0	-5.367	0.0	0.0	0.0	0.0	0.0	0.0
01030303	02020303	0.0	1.073	0.0	4.293	0.0	0.0	0.0	0.0	0.0	0.0
01030303	02020503	0.0	-0.861	0.0	-3.442	0.0	0.0	0.0	0.0	0.0	0.0
01030303	02040503	0.0	7.026	0.0	3.513	0.0	0.0	0.0	0.0	0.0	0.0
01030303	03010503	0.0	0.0	-0.420	0.0	-8.398	0.0	0.0	0.0	0.0	0.0
01030303	03030503	0.0	0.0	2.057	0.0	5.143	0.0	0.0	0.0	0.0	0.0
01030303	03030703	0.0	0.0	-1.771	0.0	-4.426	0.0	0.0	0.0	0.0	0.0
01030303	03050703	0.0	0.0	9.897	0.0	3.959	0.0	0.0	0.0	0.0	0.0
01030303	04020703	0.0	0.0	0.0	-0.901	0.0	-11.269	0.0	0.0	0.0	0.0
01030303	04040703	0.0	0.0	0.0	3.024	0.0	6.047	0.0	0.0	0.0	0.0
01030303	04040903	0.0	0.0	0.0	-2.697	0.0	-5.394	0.0	0.0	0.0	0.0
01030303	05030903	0.0	0.0	0.0	0.0	-1.408	0.0	-14.084	0.0	0.0	0.0
01030303	05050903	0.0	0.0	0.0	0.0	3.983	0.0	6.971	0.0	0.0	0.0
02000303	02000303	2.000	0.0	0.0	0.0	0.0	0.0	0.0	0.0	0.0	0.0
02000303	02020303	0.0	0.0	-4.000	0.0	0.0	0.0	0.0	0.0	0.0	0.0
02000303	02020503	0.0	0.0	3.207	0.0	0.0	0.0	0.0	0.0	0.0	0.0
02000303	02040503	0.0	0.0	0.0	0.0	-7.856	0.0	0.0	0.0	0.0	0.0
02000303	03010503	0.0	6.573	0.0	0.0	0.0	0.0	0.0	0.0	0.0	0.0
02000303	03030503	0.0	0.0	0.0	-5.367	0.0	0.0	0.0	0.0	0.0	0.0
02000303	03030703	0.0	0.0	0.0	4.619	0.0	0.0	0.0	0.0	0.0	0.0
02000303	03050703	0.0	0.0	0.0	0.0	0.0	-10.328	0.0	0.0	0.0	0.0
02000303	04020703	0.0	0.0	9.071	0.0	0.0	0.0	0.0	0.0	0.0	0.0
02000303	04040703	0.0	0.0	0.0	0.0	-6.761	0.0	0.0	0.0	0.0	0.0
02000303	04040903	0.0	0.0	0.0	0.0	6.030	0.0	0.0	0.0	0.0	0.0
02000303	05030903	0.0	0.0	0.0	11.547	0.0	0.0	0.0	0.0	0.0	0.0
02000303	05050903	0.0	0.0	0.0	0.0	0.0	-8.165	0.0	0.0	0.0	0.0
02020303	02020303	2.000	0.0	0.0	0.0	0.0	0.0	0.0	0.0	0.0	0.0
02020303	02020503	0.0	0.0	2.291	0.0	-5.498	0.0	0.0	0.0	0.0	0.0
02020303	02040503	0.0	0.0	2.245	0.0	5.611	0.0	0.0	0.0	0.0	0.0
02020303	03010503	0.0	-1.315	0.0	-5.258	0.0	0.0	0.0	0.0	0.0	0.0
02020303	03030503	0.0	6.440	0.0	-1.073	0.0	0.0	0.0	0.0	0.0	0.0
02020303	03030703	0.0	0.0	0.0	3.079	0.0	-7.698	0.0	0.0	0.0	0.0
02020303	03050703	0.0	0.0	0.0	3.443	0.0	6.885	0.0	0.0	0.0	0.0
02020303	04020703	0.0	0.0	-2.592	0.0	-6.479	0.0	0.0	0.0	0.0	0.0
02020303	04040703	0.0	0.0	8.693	0.0	-1.932	0.0	0.0	0.0	0.0	0.0

state 1	state 2	A 0	A 1	A 2	A 3	A 4	A 5	A 6	A 7	A 8	A 9
02020303	04040903	0.0	0.0	0.0	0.0	3.837	0.0	-9.868	0.0	0.0	0.0
02020303	05030903	0.0	0.0	0.0	-3.849	0.0	-7.698	0.0	0.0	0.0	0.0
02020303	05050903	0.0	0.0	0.0	10.887	0.0	-2.722	0.0	0.0	0.0	0.0
02020503	02020503	3.000	0.0	1.224	0.0	-2.939	0.0	0.0	0.0	0.0	0.0
02020503	02040503	0.0	0.0	-1.800	0.0	-4.499	0.0	0.0	0.0	0.0	0.0
02020503	03010503	0.0	1.054	0.0	4.216	0.0	0.0	0.0	0.0	0.0	0.0
02020503	03030503	0.0	0.984	0.0	3.251	0.0	-8.537	0.0	0.0	0.0	0.0
02020503	03030703	0.0	9.523	0.0	1.234	0.0	-7.054	0.0	0.0	0.0	0.0
02020503	03050703	0.0	0.0	0.0	-2.760	0.0	-5.521	0.0	0.0	0.0	0.0
02020503	04020703	0.0	0.0	2.078	0.0	5.195	0.0	0.0	0.0	0.0	0.0
02020503	04040703	0.0	0.0	2.065	0.0	4.013	0.0	-11.499	0.0	0.0	0.0
02020503	04040903	0.0	0.0	12.663	0.0	0.377	0.0	-8.205	0.0	0.0	0.0
02020503	05030903	0.0	0.0	0.0	3.086	0.0	6.172	0.0	0.0	0.0	0.0
02020503	05050903	0.0	0.0	0.0	3.174	0.0	4.700	0.0	-14.421	0.0	0.0
02040503	02040503	3.000	0.0	3.061	0.0	1.653	0.0	0.0	0.0	0.0	0.0
02040503	03010503	0.0	0.0	0.0	-0.956	0.0	-11.952	0.0	0.0	0.0	0.0
02040503	03030503	0.0	0.753	0.0	3.513	0.0	6.274	0.0	0.0	0.0	0.0
02040503	03030703	0.0	-0.648	0.0	-3.024	0.0	-5.399	0.0	0.0	0.0	0.0
02040503	03050703	0.0	10.142	0.0	6.761	0.0	3.381	0.0	0.0	0.0	0.0
02040503	04020703	0.0	0.0	-0.141	0.0	-1.928	0.0	-15.746	0.0	0.0	0.0
02040503	04040703	0.0	0.0	1.581	0.0	4.656	0.0	7.042	0.0	0.0	0.0
02040503	04040903	0.0	0.0	-1.410	0.0	-4.153	0.0	-6.280	0.0	0.0	0.0
02040503	05030903	0.0	0.0	0.0	-0.344	0.0	-2.907	0.0	-19.427	0.0	0.0
02040503	05050903	0.0	0.0	0.0	2.430	0.0	5.756	0.0	7.850	0.0	0.0
03010503	03010503	3.000	0.0	2.400	0.0	0.0	0.0	0.0	0.0	0.0	0.0
03010503	03030503	0.0	0.0	-2.519	0.0	-6.299	0.0	0.0	0.0	0.0	0.0
03010503	03030703	0.0	0.0	2.168	0.0	5.421	0.0	0.0	0.0	0.0	0.0
03010503	03050703	0.0	0.0	0.0	0.0	-1.543	0.0	-15.428	0.0	0.0	0.0
03010503	04020703	0.0	9.937	0.0	4.968	0.0	0.0	0.0	0.0	0.0	0.0
03010503	04040703	0.0	0.0	0.0	-3.703	0.0	-7.407	0.0	0.0	0.0	0.0
03010503	04040903	0.0	0.0	0.0	3.303	0.0	6.606	0.0	0.0	0.0	0.0
03010503	05030903	0.0	0.0	13.553	0.0	5.421	0.0	0.0	0.0	0.0	0.0
03010503	05050903	0.0	0.0	0.0	0.0	-4.879	0.0	-8.538	0.0	0.0	0.0
03030503	03030503	3.000	0.0	1.886	0.0	-1.286	0.0	0.0	0.0	0.0	0.0
03030503	03030703	0.0	0.0	1.918	0.0	3.621	0.0	11.736	0.0	0.0	0.0
03030503	03050703	0.0	0.0	1.650	0.0	4.859	0.0	7.348	0.0	0.0	0.0
03030503	04020703	0.0	-0.869	0.0	-4.057	0.0	-7.244	0.0	0.0	0.0	0.0
03030503	04040703	0.0	9.719	0.0	3.024	0.0	-3.672	0.0	0.0	0.0	0.0
03030503	04040903	0.0	0.0	0.0	2.819	0.0	3.941	0.0	-14.851	0.0	0.0
03030503	05030903	0.0	0.0	-1.844	0.0	-5.432	0.0	-8.215	0.0	0.0	0.0
03030503	05050903	0.0	0.0	13.041	0.0	2.561	0.0	-4.647	0.0	0.0	0.0
03030703	03030703	4.000	0.0	3.175	0.0	-0.468	0.0	-4.040	0.0	0.0	0.0
03030703	03050703	0.0	0.0	-1.420	0.0	-4.182	0.0	-6.324	0.0	0.0	0.0
03030703	04020703	0.0	0.748	0.0	3.491	0.0	6.235	0.0	0.0	0.0	0.0
03030703	04040703	0.0	0.744	0.0	3.194	0.0	3.861	0.0	-15.405	0.0	0.0
03030703	04040903	0.0	12.766	0.0	5.697	0.0	-2.410	0.0	-9.089	0.0	0.0
03030703	05030903	0.0	0.0	1.587	0.0	4.675	0.0	7.071	0.0	0.0	0.0
03030703	05050903	0.0	0.0	1.633	0.0	4.323	0.0	4.000	0.0	-19.384	0.0
03050703	03050703	4.000	0.0	4.444	0.0	3.273	0.0	1.616	0.0	0.0	0.0
03050703	04020703	0.0	0.0	0.0	-0.355	0.0	-3.003	0.0	-20.034	0.0	0.0
03050703	04040703	0.0	0.582	0.0	2.857	0.0	6.043	0.0	7.976	0.0	0.0
03050703	04040903	0.0	-0.519	0.0	-2.548	0.0	-5.390	0.0	-7.114	0.0	0.0
03050703	05030903	0.0	0.0	-0.065	0.0	-0.804	0.0	-4.427	0.0	-24.519	0.0
03050703	05050903	0.0	0.0	1.278	0.0	3.980	0.0	7.155	0.0	8.669	0.0
04020703	04020703	4.000	0.0	4.082	0.0	2.204	0.0	0.0	0.0	0.0	0.0
04020703	04040703	0.0	0.0	-1.825	0.0	-5.377	0.0	-8.131	0.0	0.0	0.0
04020703	04040903	0.0	0.0	1.628	0.0	4.795	0.0	7.252	0.0	0.0	0.0
04020703	05030903	0.0	13.093	0.0	8.729	0.0	4.364	0.0	0.0	0.0	0.0
04020703	05050903	0.0	0.0	0.0	-2.806	0.0	-6.647	0.0	-9.064	0.0	0.0
04040703	04040703	4.000	0.0	3.537	0.0	0.601	0.0	-2.424	0.0	0.0	0.0
04040703	04040903	0.0	0.0	1.566	0.0	4.124	0.0	3.676	0.0	-19.559	0.0
04040703	05030903	0.0	-0.651	0.0	-3.194	0.0	-6.756	0.0	-8.917	0.0	0.0
04040703	05050903	0.0	12.881	0.0	6.775	0.0	0.0	0.0	-5.855	0.0	0.0
04040903	04040903	5.000	0.0	4.821	0.0	1.802	0.0	-2.094	0.0	-4.984	0.0
04040903	05030903	0.0	0.580	0.0	2.849	0.0	6.026	0.0	7.953	0.0	0.0
04040903	05050903	0.0	0.597	0.0	2.789	0.0	5.113	0.0	3.308	0.0	-24.116
05030903	05030903	5.000	0.0	5.556	0.0	4.091	0.0	2.020	0.0	0.0	0.0
05030903	05050903	0.0	0.0	-1.428	0.0	-4.450	0.0	-8.000	0.0	-9.692	0.0
05050903	05050903	5.000	0.0	5.051	0.0	2.517	0.0	-0.808	0.0	-3.427	0.0

ACKNOWLEDGEMENTS

I wish to thank Professor I. Butterworth for the opportunity to carry out research as a member of the High Energy Nuclear Physics group at Imperial College, London.

I would like to express my gratitude to Dr. D.M. Binnie and Dr. D.A. Garbutt, for their supervision, guidance and encouragement throughout my research.

I am grateful to my colleagues; Dr. J. Carr, Dr. N.C. Debenham, Dr. W.G. Jones, Dr. J. Keyne, Dr. H.N. Sarma, Dr. I. Siotis, and Mr. P. Mossidis for the many discussions and suggestions.

I would also like to thank Mr. R. F. Hobbs, Mr. D.G. Miller and Mr. J. Hiddlestone for their assistance during the preparation and running the experiment.

REFERENCES

1 D.M. Binnie et al, Phys. Rev., D8, 2789 (1973).

2 J. Keyne et al, Phys. Rev., D14, 28 (1976).

3 A partial wave analysis of the reaction $\pi p \rightarrow \pi\pi p$ in the C.M. Energy Range 1300-2000 Mev. Cashmore et al, Purdue Conference April 1973.

4 A. Brandstetter, S.M. Deen and P.J. Litchfield, Ruth. Lab. Report RHEL/R 224 (1971).

5 R.J. Cashmore, A.J.G. Hey and P.J. litchfield, Nucl. Phys. B98, 237 (1975).

6 Particle Data Group, T.G. Trippe et al, Rev. Mod. Phys., 105 (1976).

7 R. Dalitz and S. Taun, Ann. Phys., 10, 307 (1960).

8 M.H. Ross and G.L. Shaw, Ann. Phys., 13, 147 (1961).

9 W.G. Jones, Private communication.

10 E. P. Wigner, Phys. Rev., 73, 1002 (1948).

11 R.K. Adair, Phys. Rev., 111, 632 (1958).

12 I.A. Baz, Sovt. Phys., 6, 709 (1958).

13 I.A. Baz, L.B. Okun, Sovt. Phys., JETP, 8,526 (1958).

14 D.M. Binnie and A. Duane, Nucl. Inst. Meth. 77, 329 (1970).

15 J.Keyne, Ph.D. thesis, The University of London (1973).

16 H.N. Sarma, Ph.D. thesis, The University of London (1976).

17 C.A. Baker et al, Nucl. Instr. Meth., 59, 125 (1968).

18 J.S. Danburg et al, Phys, Rev., D2, 2564 (1970).

19 R. Kraemer et al, Phys. Rev., 136, 496 (1964).

20 P.C. Barber et al, Ruth. Lab. Report RL-74-087 (1974).

21 W.P. Petersen and J.L. Rosner, Phys. Rev., D7, 747 (1973).

22 J.M. Blatt, V.F. Weisskopf, Theoretical Nuclear Physics,

23 (J. Wiley and Sons Inc., New York, 1956).

24 πN Partial-wave amplitudes. D.J. Herdon et al.,
UCRL-20030 πN, February 1970.